Methanol and ethanol oxidation on carbon-supported platinum-based nanoparticles using a proton exchange membrane electrolysis cell

By

Ahmed Hashem Ali

February 2024

A thesis submitted to the School of Graduate Studies in partial fulfillment of the Doctor of Philosophy degree requirements.

Department of chemistry

Memorial University

St. John’s Newfoundland and Labrador

Abstract

Direct alcohol fuel cells (DAFC) have been extensively studied as energy conversion devices. The most extensively studied alcohol is methanol, which has a higher anodic oxidation rate than other alcohols because it does not need to dissociate a C-C bond in order to oxidize completely to CO_2. However, recent research has focused on ethanol, which has several advantages over methanol, such as its high energy density, low crossover rate, and low toxicity. Ethanol would be a promising fuel if it could completely oxidize to CO_2 to generate 12 electrons.

Our research aimed to develop high-activity catalysts that are more effective and give higher CO_2 faradaic yields compared to the most effective and widely known PtRu catalyst. Electrolysis cells are used instead of fuel cells to evaluate our prepared anodic catalysts to avoid chemical reactions between ethanol and oxygen.

In this study, we have prepared Pt-based core-shell nanoparticles with PtRu and Ru cores and Pt at the surface in different amounts (PtRu@Pt and Ru@Pt). These catalysts were prepared using the polyol method without adding stabilizers that would block the surface and decrease alcohol oxidation activity. We investigated the effect of Pt thickness on Ru and PtRu cores by conducting cyclic voltammetry (CV) at ambient temperature and in a proton exchange membrane electrolysis cell (PEMEC) at 80°C. The results indicate that methanol and ethanol oxidation selectivity to form CO_2 increased with increasing Pt shell thickness. As compared to PtRu, $PtRu@Pt_{1.7}$ had a higher selectivity for complete ethanol oxidation, while $Ru@Pt_{0.6}$ had a higher activity for methanol oxidation.

In many studies, Rh has been shown to increase the selectivity of Pt for oxidizing ethanol to CO_2. The Rh@Pt core-shell catalysts were prepared in an alkaline medium using ethanol as the

reducing agent. Electrochemical results indicate that Rh@Pt with half a monolayer of Pt would be a highly effective catalyst for direct ethanol fuel cells.

Furthermore, PtRh nanoparticles were investigated for methanol and ethanol oxidation reactions. The catalysts were synthesized using formic acid as a reducing agent. According to the PEMEC study, $Pt_{3.0}Rh$ demonstrated the best ethanol oxidation selectivity relative to Pt and PtRu at most applied potentials.

Acknowledgements

My sincere appreciation goes out to those who have shown me favor, support, and confidence.

First and foremost, Prof. Peter Pickup, I would like to express my sincere gratitude to my supervisor, who guided, instructed, trusted, and motivated me. The feedback you provided enabled me to deepen and refine my research, and the results presented in my thesis would not have been possible without you.

I would like to thank my supervisory committee members, Prof. Jane Stockmann and Prof. Graham J. Bodwell, for their valuable advice, support, and time they have dedicated throughout my Ph.D. program.

I want to thank my Ph.D. examiners (prof. Viola Ingrid Birss, prof. Christina Bottaro, and prof. Christopher M. Kozak) for taking the time to read my thesis carefully and give me such valuable feedback. Their suggestions greatly improved my thesis.

Moreover, I would like to express my appreciation to the Department of Chemistry, School of Graduate Studies (SGS), Graduate Students' Union (GSU), Memorial University of Newfoundland, Natural Science and Engineering Research Council of Canada for their financial support of this research, and the technical service staff at MUN for their high level of technical support.

I would also like to thank my lab mates and friends for making this experience so pleasant.

Thank you to my family for their support, prayers, and encouragement in helping me achieve my goals. It is especially my daughters, Rulan and Nellie, who inspire me to strive to become someone they are proud of.

Last but not least, I would like to dedicate this thesis to my wife, who has shown me patience, love, support, and help throughout my life.

Finally, I would like to thank everyone who has made the process easy and fun.

Table of contents

Chapter 6: Methanol and ethanol oxidation on carbon-supported platinum-rhodium alloy nanoparticles using a proton exchange membrane electrolysis cell 142

List of Tables

List of Figures

List of Abbreviation and Symbols

A	Area
a	Lattice parameter
AA	Acetic acid
AAL	Acetaldehyde
ACL	Anodic catalyst layer
AFC	Alkaline fuel cell
BP	Bipolar plate
C	Concentration
ca.	Approximately
CB	Carbon black – Vulcan XC 72R
CCL	Cathodic catalyst layer
CFP	Carbon fiber paper
CL	Catalyst layer
CSN	Core-shell nanoparticles
CV	Cyclic voltammetry
d	Diameter
DAFC	Direct alcohol fuel cells
DEFC	Direct ethanol fuel cells
DEMS	Differential electrochemical mass spectroscopy
DHE	Dynamic hydrogen electrode

DFT	Density functional theory
DMFC	Direct methanol fuel cells
E	Potential
e^-	Electron
ECSA	Electrochemically active surface area
EDX	Energy dispersive X-ray spectroscopy
E_f	Forward anodic peak potential
EG	Ethylene glycol
e.g.	For example,
EOR	Ethanol oxidation reaction
eq.	Equation
et al.	And others
F	Faraday constant
F_i	Faradaic yield of product i
FTIR	Fourier transform infrared spectroscopy
GDL	Gas diffusion layer
HFC	Hydrogen fuel cells
HOR	Hydrogen oxidation reaction
HPLC	High performance liquid chromatography
i.e.	In other words,
ICE	Internal combustion engine
m	Mass transport coefficient
MCFC	molten carbonate fuel cells

MEA	Membrane electrode assembly
ML	Monolayers
MOR	Methanol oxidation reaction
n	Electrons transferred in the reaction
NDIR	Non-dispersive infrared
NMR	Nuclear magnetic resonance
NP	Nanoparticles
NSERC	Natural Sciences and Engineering Research Council (of Canada)
OCP	Open circuit potential
ORR	Oxygen reduction reaction
PAFC	Phosphoric acid fuel cell
PEM	Proton exchange membrane
PEMEC	Proton exchange membrane electrolysis cells
PEMFC	Proton exchange membrane fuel cells
PTFE	Polytetrafluoroethylene
RHE	Reversible hydrogen electrode
SCE	Saturated calomel electrode
SEM	Scanning electron microscopy
SHE	Standard hydrogen electrode
SOFC	Solid oxide fuel cell
T	Temperature
TEM	Transmission electron microscopy

TGA	Thermogravimetric analysis
V	Voltage (volts)
vs	Versus
W_e	The required energy
x	Mole fraction
X(ad)	Species X adsorbed on the electrode surface
XRD	X-ray diffraction analysis
XPS	X-ray photoelectron spectroscopy
ε	Efficiency
λ	Wavelength
Θ	Diffraction angle
η	Overpotential
ν	Scan rate
Ω	Ohm

Chapter 1: Introduction

Currently, fossil fuels are the main source of energy in the world, and the combustion of these fuels causes the release of large quantities of greenhouse gases (mostly CO_2) (1-3). Furthermore, fossil fuel sources are diminishing (non-renewable), the cost of fossil fuels is rising constantly, and the annual consumption rate of fossil fuels is increasing alarmingly (4, 5). Our fossil fuel reserves are predicted to run out in this century, and this is based on scientific predictions, in which coal may last up to 114 years, oil up to 50 years, and natural gas up to 53 years (6). Therefore, governments and organizations are focusing on developing alternative energy sources to reduce their dependence on fossil fuels (7-13).

Renewable energy sources such as biomass, water, geothermal, wind, and solar are effective solutions to address these issues. Renewable energy sources are abundant, clean, and sustainable. In addition to reducing emissions and tackling climate change, they are reliable and cost-effective compared to traditional carbon-based energy sources.

Fuel cells are electrochemical devices that convert chemical energy into electricity. They are considered to be good sources of energy conversion (14-17). They can also be more energy efficient than internal combustion engines, emitting no harmful emissions when used (17).

Fuel cell technology is still in its infancy, but it is rapidly evolving and is expected to play a significant role in the automotive industry. Several companies, such as Toyota, Honda, Mercedes, and Hyundai, are developing fuel cell powered electric motors to replace conventional internal combustion engines in their vehicles (15, 17). Honda, for example, has introduced a fuel cell car called the Clarity Fuel Cell that runs on hydrogen as fuel and emits only water vapor as an exhaust (18). In addition to the Clarity Fuel Cell, Honda is also investigating the possibility of using bioethanol as a fuel source and has already released a few bioethanol-powered vehicles in Brazil (19).

In a fuel cell, chemical energy from a fuel is converted into electricity through electrochemical reactions, which is considered a static energy conversion device. Unlike a battery, it can be refilled with fuel and generate electricity continuously (20). One of the most common types of fuel cells is the hydrogen fuel cell, which operates on the principle of electrochemically reacting oxygen and hydrogen molecules (the fuel) to produce electricity and water. In order to facilitate these half-reactions, a catalytic material, such as platinum metal, is required (21-23). As a result of this catalytic material, the fuel cell can generate electricity more efficiently and reliably by speeding up the reaction. An electric motor or other devices will then be driven by the electricity that has been generated.

1.1. A brief history of fuel cells

Sir William Robert Grove demonstrated the fuel cell concept in 1839 (24, 25). The development of fuel cells in the early 20th century was slower than that of high-performance combustion engines. Fuel cell principles were extensively researched during the second half of the 20th century. Thomas Bacon invented the first fully functional alkaline fuel cells (AFC) in 1932 (26). Baur and Preis operated the first solid oxide fuel cell (SOFC) at 1000 °C in 1937 (27). A polymer exchange membrane fuel cell (PEMFC) was developed in 1955 by Willard Thomas Grub as a solution to other fuel cells' problems (28).

NASA used AFC and PEMFC for space vessel applications in the 1960s to provide electricity, water, and heat (29). Researchers focused on developing other types of fuel cells due to oil shortages, such as phosphoric acid fuel cells (PAFC) (30). The first hydrogen fuel cell vehicle was introduced by General Motors (GM) in 1966 (31). In 1993, Ballard developed a hydrogen PEMFC bus capable of reaching 72 kilometers per hour (32). In 2007, fuel cells, especially PEMFCs, became commercially available in various applications (33).

The use of liquid fuels such as methanol and ethanol has been widely developed as they have a higher volumetric energy density than hydrogen and are easier to transport and store. Direct methanol fuel cells (DMFC) and direct ethanol fuel cells (DEFC) are two examples of the types of direct liquid fuel cells (34). Several companies, such as SMART, MTI, Samsung, Casio, and Toshiba, conducted extensive research on cellular phones, laptops, and battery chargers based on direct methanol fuel cells (35).

Liquid ethanol has been mentioned as an alternative fuel in limited applications due to its poor performance compared to hydrogen and methanol (36). Offenburg students demonstrated the first DEFC-powered vehicle in 2007 (37). Moreover, during the Shell Eco-marathon Asia 2018, the Indian team (BITS Pilani) constructed 100% ethanol-fueled cars (38). Bioethanol was used as a fuel source for Nissan Motor's Solid Oxide Fuel Cell (SOFC) in 2020 (39).

1.2. Proton exchange membrane fuel cells (PEMFC)

As shown in Figure 1.1, there are six different types of fuel cells. The main differences between these cells are the electrolytes, operating temperatures, ions transferred, fuel used on the anode, and oxidizers used on the cathode (40). They are classified into solid oxide fuel cells (SOFC), molten carbonate fuel cells (MCFC), proton (polymer) electrolyte membrane fuel cells (PEMFC), direct methanol fuel cells (DMFC), phosphoric acid fuel cells (PAFC), and alkaline fuel cells (AFC). Direct ethanol fuel cells (DEFC) are another type that will be discussed later. There are some similarities in its operating conditions, components, and mechanism with DMFC. The only difference between them is in the fuel used and the way it is oxidized.

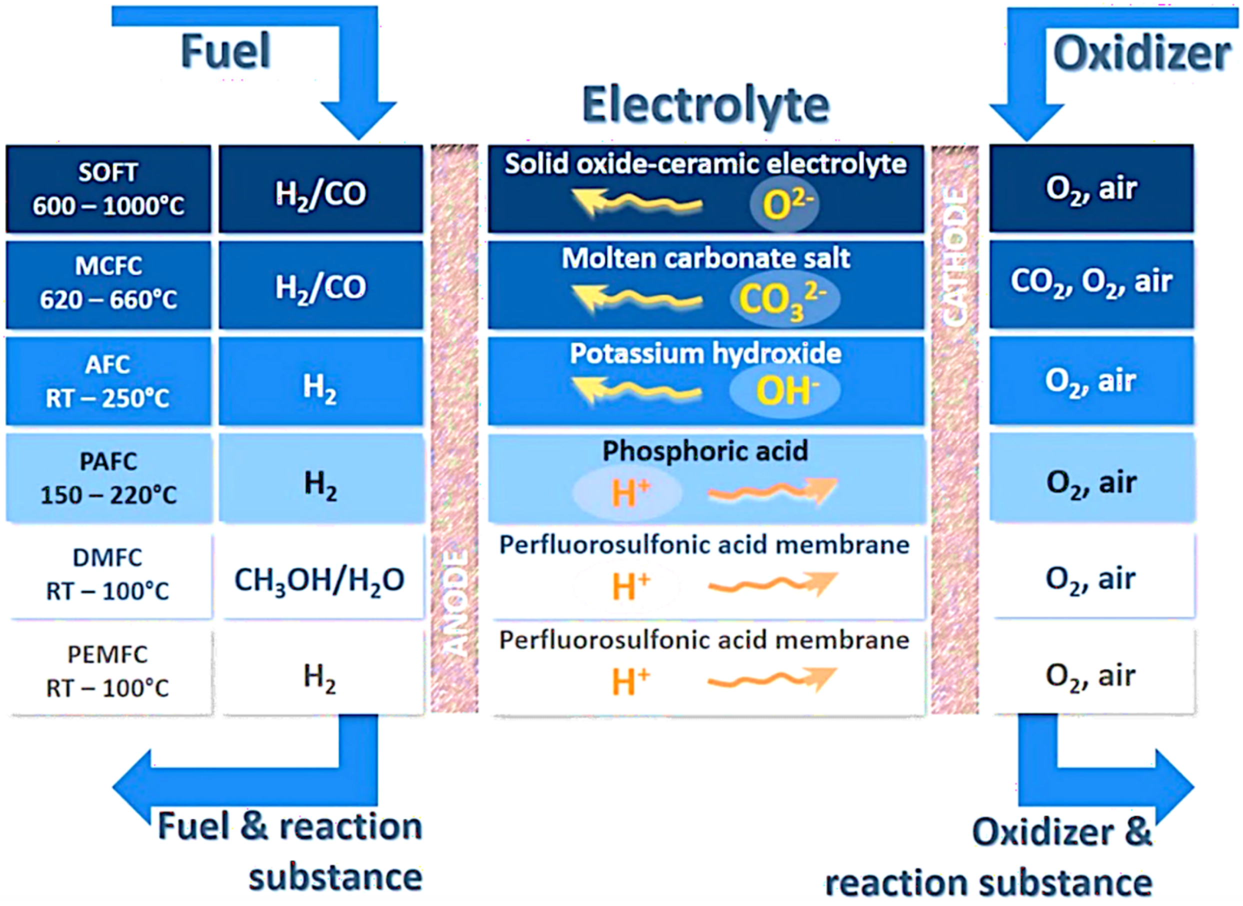

Figure 1.1. A schematic diagram of various types of fuel cells, their arrangement depends on the operational temperature, in which RT represents the room temperature, reprinted from (40). The review is published under the terms of the Creative Commons Attribution License.

Polymer electrolyte membrane fuel cells are regarded as one of the most promising sustainable energy conversion devices (40-42). They are attractive for commercial applications because of their high efficiency, low maintenance, favorable power density (10-500 W/kg), quick start-up, low environmental impact, and ability to run on different fuels such as hydrogen, methanol, and ethanol (42, 43). The PEMFC are also cost-efficient and environmentally friendly energy conversion sources. They have several applications, from transportation to portable devices to stationary energy production (42, 43).

The schematic diagram of the PEMFC is shown in Figure 1.2. The Membrane electrode assemblies (MEAs) of PEMFCs are made up of five components: proton exchange membranes (PEM), anode and cathode catalyst layers (CL), and anode and cathode gas diffusion layers (GDL). MEA are sandwiched between bipolar plates (BP), followed by current collectors, and then compression plates. Gaskets (silicone rubber) were used between the GDL and BP to seal effectively and prevent gas leakage.

The polymer exchange membrane (PEM) is considered the heart of this fuel cell. It facilitates proton transfer between the cell's electrodes during the redox reaction, acting as a solid electrolyte. Nafion (perfluorosulfonic acid-based) membranes have been widely used in PEMFC due to their high proton conductivity at low temperatures, chemical stability, and low fuel permeability. However, they suffer from many limited characteristics, such as low proton conductivity (above 80 °C) and membrane degradation at high temperatures (above 150 °C), leading to the release of corrosive and toxic gases that pollute the fuel cell and the surrounding environment (44).

Fuel oxidized at the anodic catalyst produces protons and electrons consumed by oxygen reduction at the cathodic catalyst. It is common to use Pt-based catalysts in PEMFC because they have low overpotentials and high catalytic activities for the hydrogen oxidation reaction (HOR) and the oxygen reduction reaction (ORR) compared to alternatives (45). Additionally, they can withstand harsh acidic environments inside PEMFC (46). Pt-based catalysts consist of Pt-based nanoparticles supported on carbon-based (e.g., carbon black) or non-carbon-based supports (e.g.

gold). Research continues to be conducted on improving catalyst stability and activity in PEMFC to boost fuel cell efficiency (45, 46).

A GDL plays a significant role in removing heat and water generated during the redox reactions, transporting current to collector plates, and distributing reactant gases to the catalyst surface. The most commonly used GDL is a carbon fiber paper coated with polytetrafluoroethylene (PTFE) (47).

Bipolar plates facilitate the flow of water and heat inside the cell, distribute fuel gas and air uniformly in the cell, and conduct electric current between cells in fuel cell stacks. In most BP, graphite is one of the most common materials (48).

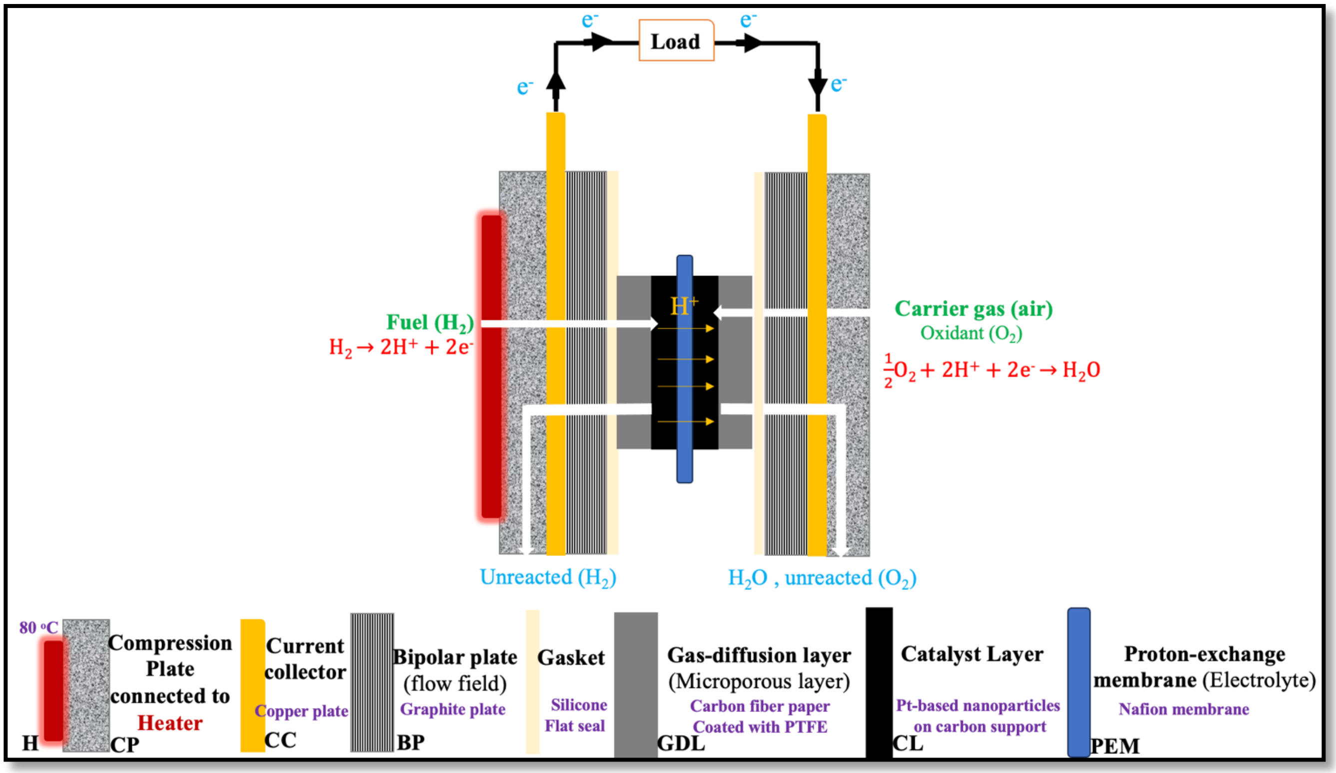

Figure 1.2. A schematic diagram of a single-cell H_2-fueled proton exchange membrane fuel cell, showing its components and operation mechanisms.

Hydrogen is the most common fuel used in fuel cells. The mechanism of cell operation can be seen in Figure 1.2. The fuel hydrogen is oxidized on the anodic catalyst's surface, which generates protons that are transferred to the cathode through a solid polymer electrolyte membrane (typically Nafion). In contrast, electrons are transferred (generating electrical current) to cathodes through the load. An oxidizer (normally oxygen) reacts with the transferred electrons and protons to produce water on the surface of a cathodic catalyst. There are many advantages associated with H_2-fueled PEMFC, which include zero CO_2 emissions, reliable power sources, quick start-up, easy refueling, and reasonable durability (49). The H_2-fueled PEMFC have two to three times higher power density and efficiency compared to internal combustion engines (ICE) (46).

Commercializing H_2-fueled PEMFC presents some challenges, including producing pure hydrogen gas, flammability, and difficulty transporting and storing hydrogen fuel (34, 50). As a result of these factors, researchers have been increasingly investigating alcohols as alternative fuels, such as methanol, ethanol, propanol, ethylene glycol, and glycerol, to assist in the development of a new type of PEMFC called direct alcohol fuel cells (DAFC) (34, 50).

1.3. Direct methanol fuel cell (DMFC)

Methanol is easier to transport and store than hydrogen and has a higher volumetric energy density. In addition, methanol is an environmentally friendly alternative to traditional fossil fuels because it can be produced from renewable resources (51).

As shown in Figure 1.3, the direct methanol fuel cell is similar in its operation and mechanism to the H_2-fueled PEMFC. The anodic catalyst layer oxidizes methanol to produce CO_2, six electrons, and six protons. Protons are transferred to the cathode through the PEM, while electrons are transferred externally through the load. These electrons and protons are consumed in the cathodic layer during oxygen reduction reaction (ORR). Therefore, the only difference between a DMFC and H_2-fueled PEMFC is the fuel used and how it is oxidized on the anodic catalyst layer (ACL).

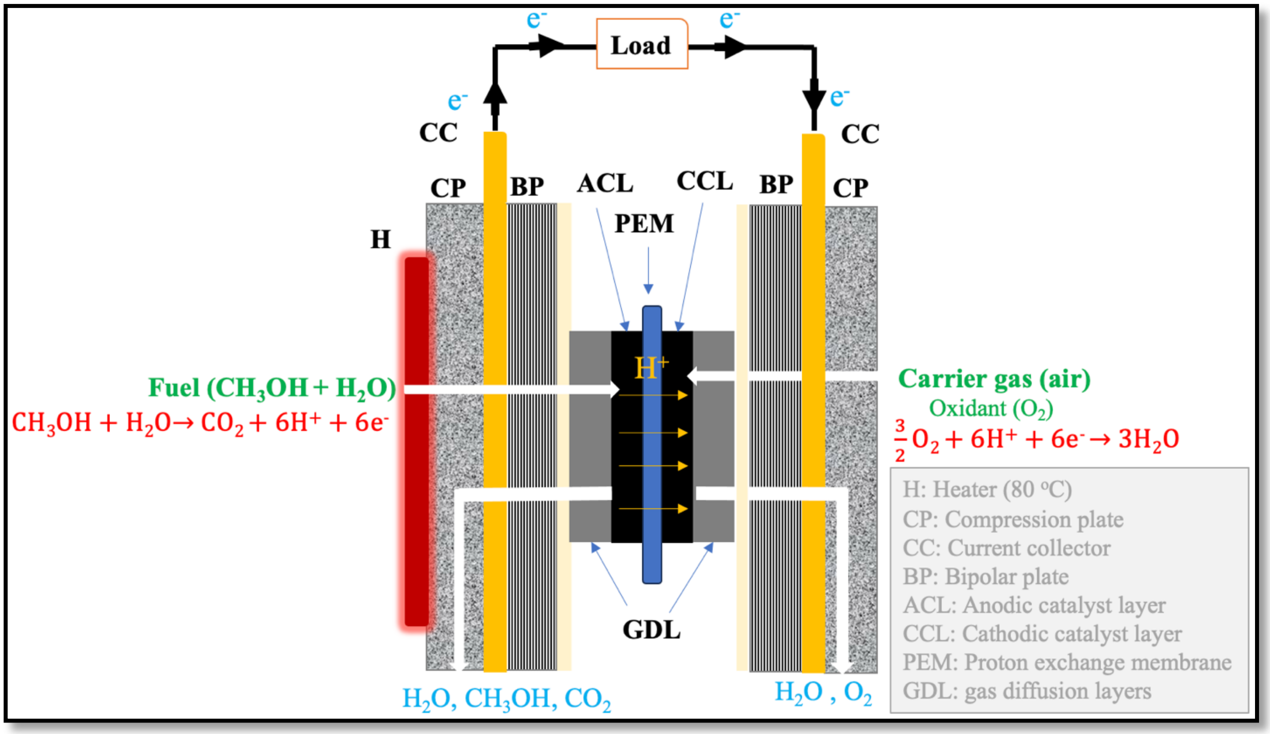

Figure 1.3. A schematic diagram of a direct methanol fuel cell.

1.3.1. Electrochemical oxidation of methanol on the surface of platinum

Pt is the most common anodic catalyst used for facilitating methanol oxidation. Several factors affect methanol oxidation on the surface of Pt, including potential, temperature, and electrolyte pH (52). Figure 1.4 shows the mechanism of methanol oxidation on the surface of Pt in acidic media and the effect of potential on mechanism pathways derived from experimental evidence (52). As methanol on Pt surfaces is oxidized, a number of adsorbed (ad) intermediates are formed, with CO(ad) being the most stable and HCOO(ad) and HCHO(ad) being the least stable. CO_2 is the primary product in the solution phase, with formic acid and formaldehyde being minor products. HCHO(ad) or HCOO(ad) intermediates are responsible for producing CO_2 at potentials lower than 0.45 V vs a reversible hydrogen electrode (RHE) since CO(ad) is the most stable intermediate at low potentials. When CO becomes unstable at potentials higher than 0.45 V, CO_2 is formed from the CO pathway (52).

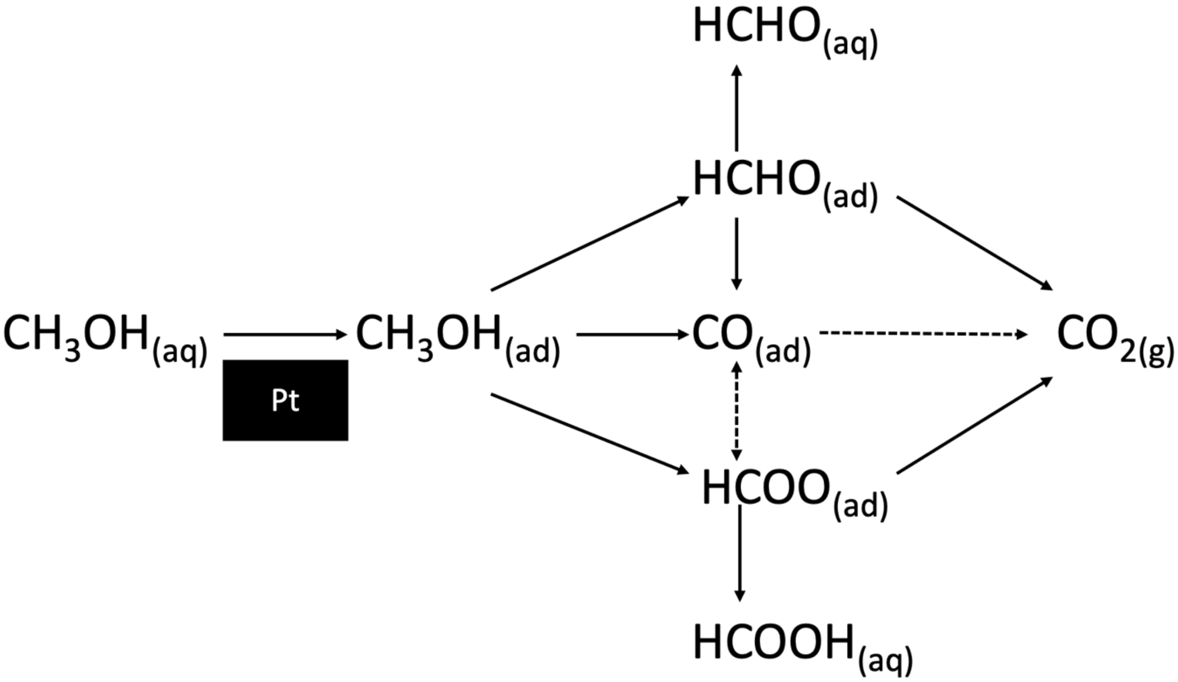

Figure 1.4. A schematic representation of the oxidation of methanol on a platinum catalyst surface. The dashed lines indicate that CO(ad) does not oxidize in potentials less than 0.45 V vs RHE.

During the oxidation of methanol, C-H and O-H bonds are activated on the surface sites of Pt, ultimately producing CO. A dual path of CO intermediate formation from methanol oxidation was confirmed by cyclic voltammetry, chronoamperometry, and DFT studies (53).

Figure 1.5, summarizes the dual mechanism for methanol oxidation to CO over Pt based on the DFT theory (53). The primary paths are shown in green, while the secondary paths are shown in black. At potentials lower than 0.35 V vs RHE, a sequence of C-H activation steps leads to the formation of the hydroxyl methylene (CHOH) intermediate, which then activates the O-H to form adsorbed CO (53). A higher potential will result in the activation of the O-H bond of methanol, followed by C-H bond activation that ultimately leads to the formation of formaldehyde (CH_2O), which may then be desorbable or continue to form a carbon monoxide (53).

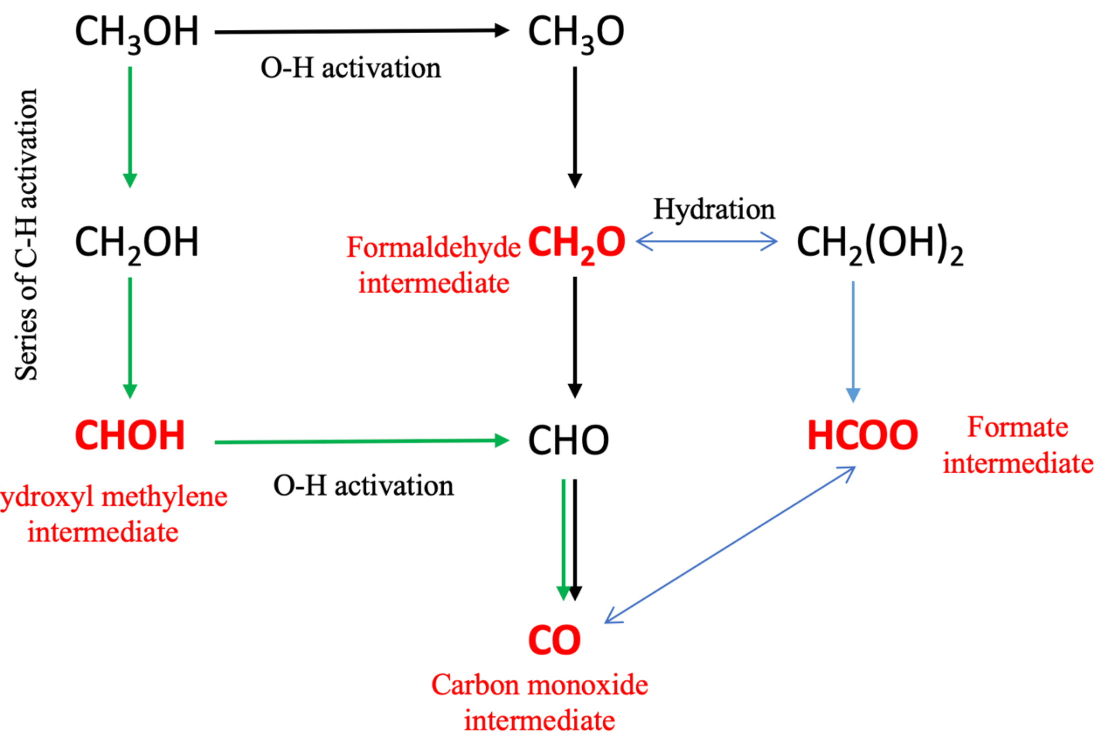

Figure 1.5. Dual mechanism of methanol oxidation to form CO on the surface of Pt, based on DFT calculation. Green lines represent the primary path of the first series of C-H activation, while the black lines are the path of the first O-H activation. The blue lines represent the way of formation of the formate intermediate.

Through an equilibrium process, the formaldehyde intermediate can be hydrated in solution to produce methanediol ($CH_2(OH)_2$). A dehydrogenation of methanediol in solution can produce formic acid, which dissociatively adsorbs on Pt to create adsorbed formate (HCOO) (52).

The methanol oxidation reaction (MOR) activity is determined by the removal of CO(ad) from the surface of Pt. Equations 1.1 and 1.2 show the steps involved in removing CO from Pt's surface. Firstly, Pt facilitates the dissociation of adsorbed H_2O into OH(ad). This step, however, required high potentials (above 0.60 V vs RHE) in acidic media. The strong CO-adsorption on Pt sites can make it difficult for water to adsorb (46). This explains the slow rate of the MOR on the surface of Pt in acidic media. The CO(ad) is then promoted and further oxidized to form CO_2 by OH(ad) on an adjacent Pt site (eq. 1.2)(51, 54, 55).

$$Pt + H_2O \rightarrow \quad Pt\text{-}OH + H^+ + e^- \qquad (1.1)$$

$$Pt\text{-}OH + Pt\text{-}CO \rightarrow 2Pt + CO_2 + H^+ + e^- \qquad (1.2)$$

1.3.2. Anodic catalysts for direct methanol fuel cells

Platinum plays a primary role in electrocatalysis of the MOR in acidic media in terms of activity, selectivity, and stability (51-53, 56). Platinum has outstanding thermal conduction, high electron mobility, and highly exposed active sites (51). However, its price and the poisoning of its surface by CO(ad) make researchers look for modifications to Pt catalysts to enhance the MOR activity (53, 56). Binary and ternary alloys of Pt with other metals, including Fe, Ni, Cu, Co, Ru, and Sn, are among the most effective ways of reducing Pt surface blocking (51-53, 56).

PtRu alloys are considered state-of-the-art anodic catalysts for DMFC (53, 56). By alloying Pt with Ru, platinum amounts are reduced, resulting in lower catalyst costs. Furthermore, their synergistic interactions allow CO to be removed from the catalyst surface more easily than pure Pt.

The MOR mechanism on the surface of PtRu is called the bi-functional mechanism (equations 1.3 - 1.5), in which, Pt forms the CO(ad) intermediate through the fast dehydrogenation of the adsorbed methanol on the Pt surface (eq. 1.3). Ruthenium is able to provide oxygen-containing species at more negative potentials (eq. 1.4), compared to platinum (eq. 1.1). In turn, these can oxidize CO at the adjacent platinum sites to form CO_2 (56).

$$Pt + CH_3OH \rightarrow Pt\text{-}CO + 4H^+ + 4e^- \quad (1.3)$$

$$Ru + H_2O \rightarrow Ru\text{-}OH + H^+ + e^- \quad (1.4)$$

$$Ru\text{-}OH + Pt\text{-}CO \rightarrow PtRu + CO_2 + H^+ + e^- \quad (1.5)$$

There are three types of synergistic interactions between Pt and Ru that promote the CO removal and increase the MOR activity: (I) bi-functional effects that arise from the oxidation of CO with hydroxyl groups on the active ruthenium on the surface of the catalyst(eq. 1.5); (II) ligand effects resulting from charge transfer from Ru (less electronegativity) to Pt (larger electronegativity), decreasing the vacant surface sites of Pt decrease the strength of the bonding between CO and Pt (51); (III) lattice strain that occurs when Ru atoms (smaller atomic radius) substitutes some Pt atoms from their lattice, changing the Pt-Pt interatomic distance and weakening the Pt-CO bond. Both ligand and strain effects control the d-band center of Pt. The downshift of the d-band center leads to a weakened bonding strength between Pt and oxygen-containing species CO and facilitates the CO removal; however, at the same time, this will decrease the rate of methanol dissociation. Enhanced MOR activity can be achieved by balancing the affinity between Pt and oxygen-containing carbon species (51).

PtRu alloy remains a costly catalyst despite MOR's high activity on its surface. Ru is also easily dissolved or corroded in acidic, high-temperature, and oxygen-rich environments, reducing its durability (57). Furthermore, the presence of Ru on the catalyst surface reduces the number of active Pt sites available for adsorbing alcohol molecules (57). Anodic catalyst modifications are underway improve DMFC performance and durability, as discussed in section 1.4.2.

1.3.3. Disadvantages of methanol as a fuel

Commercializing DMFC is difficult due to their low life cycle and high cost, as well as the fact that methanol itself is toxic and has a high crossover rate through the Nafion membrane (35).

The methanol crossover phenomenon is methanol diffusion from the anode to the cathode through the membrane without its oxidation on the surface of the anodic catalyst. Crossover of methanol is caused by the miscibility of methanol and water, as well as the inherent water-transport property of the Nafion membrane (35). By crossing the methanol to the cathode, it reacts chemically with oxygen, or is electrochemically oxidized on the surface of the cathodic catalyst layer. This results in a significant decrease in the cell voltage and lowers cell performance and efficiency compared to H_2-fueled PEMFC.

A further concern from the methanol crossover is the contamination of the cathodic catalyst layer with intermediates such as CO due to the MOR on its surface.

Compared to methanol, ethanol is a promising fuel source because it is higher in volumetric energy density, nontoxic, and readily available from renewable resources. Also, ethanol has a lower cross-over rate than methanol and, therefore, has less impact on cathode performance.

1.4. Direct ethanol fuel cell (DMFC)

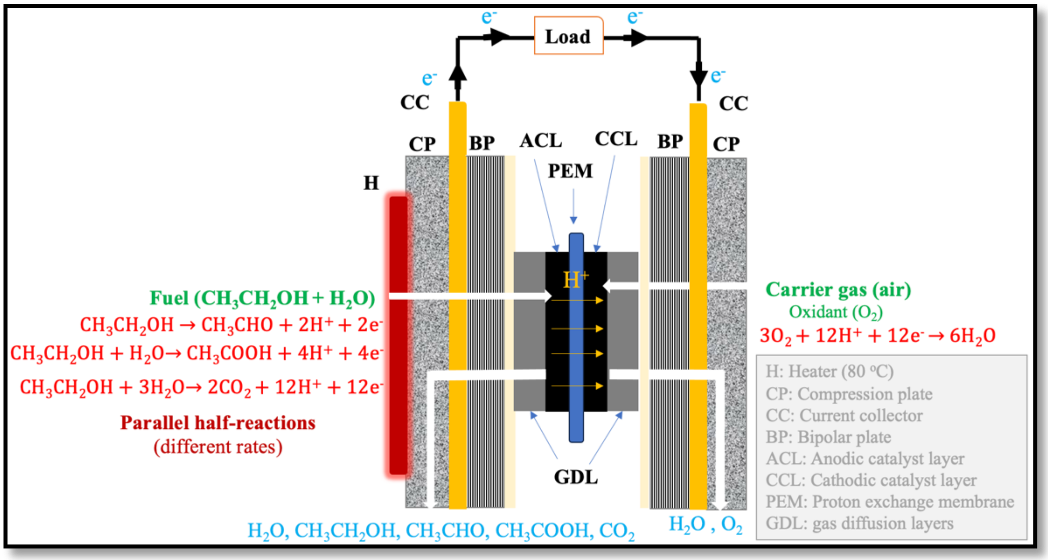

Figure 1.6. A schematic diagram of a direct ethanol fuel cell.

Direct ethanol fuel cell (DEFC) operates similarly to DMFC, as shown in Figure 1.6. The only difference between the two is the fuel used. In this case, ethanol is oxidized at the anodic catalyst surface, with three different half-reactions that are normally involved. This results in the formation of three products at variable rates (acetaldehyde, acetic acid, and carbon dioxide) and different stoichiometries (n), as shown in the equations for the three oxidation reactions in Figure 1.6. The anodic catalyst plays a vital role in controlling how fast each half-reaction occurs and the selectivity for each product formed.

1.4.1. Electrochemical oxidation of ethanol on the surface of platinum

Complex mechanisms are involved in the EOR. A summary of the basic mechanisms of EOR on Pt catalysts is presented in equations 1.7 - 1.14. These are based on computational calculations and experimental results from cyclic voltammetry, CO stripping, differential electrochemical mass spectroscopy (DEMS), Fourier-transform infrared spectroscopy (FTIR), and nuclear magnetic resonance (NMR) spectroscopy (55).

In general, it has been found that ethanol can oxidize in two different pathways, as shown in Figure 1.7. In the partial oxidation of ethanol (C2-mechanism), acetaldehyde and acetic acid are produced as products, and two or four electrons and protons are generated, respectively. In contrast, carbon dioxide is formed in the complete oxidation of ethanol (C1-mechanism), and 12 electrons and protons are generated. So, the efficiency of DEFC depends on the amount of CO_2(g) evolved from the complete oxidation of ethanol. The full oxidation of ethanol molecules requires not only breaking the O-H bond, as with methanol, but also breaking the C-C bond (58).

The average number of generated electrons (n_{av}) determines the current generated during ethanol oxidation since different possible products can be generated at different rates. Eq. 1.6 is used to calculate the n_{av}, depending on the concentration of each product.

$$n_{av} = \sum n_i x_i \qquad (1.6)$$

where, x_i is the mole fraction of each product from ethanol oxidation, and n_i is the number of generated electrons for each product, as shown in blue in Figure 1.7.

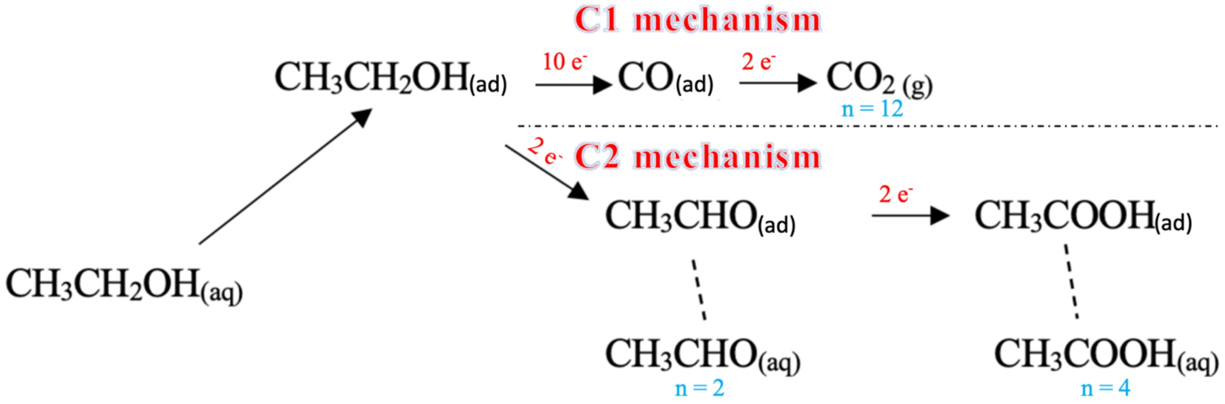

Figure 1.7. Schematic diagram of different pathways of ethanol oxidation (59).

Electrocatalytic oxidation of ethanol at Pt surfaces requires the ethanol molecule to be adsorbed first by oxidation of its α-hydrogen atom or hydrogen atom of its hydroxyl group, as shown in eq. 1.7 and eq. 1.8, respectively (55, 60).

$CH_3CH_2OH + Pt \rightarrow Pt\text{-}OCH_2CH_3 + H^+ + e^-$ (1.7)

$CH_3CH_2OH + Pt \rightarrow Pt\text{-}CH(OH)CH_3 + H^+ + e^-$ (1.8)

Following the easier C2 mechanism (no C-C bond dissociation), further oxidation of the initial species caused by ethanol adsorption leads to the formation of adsorbed Pt-$CHOCH_3$ species (eq. 1.9). With the aid of hydroxyl groups formed by water disassociation on the Pt surface (eq. 1.10), the Pt-$CHOCH_3$ species can be released from the surface and converted into acetaldehyde or further oxidized to acetic acid (eq. 1.11) (55, 60).

$Pt\text{-}OCH_2CH_3$ or $Pt\text{-}CH(OH)CH_3 \rightarrow Pt\text{-}CHOCH_3 + H^+ + e^-$ (1.9)

$Pt + H_2O \rightarrow Pt\text{-}OH + H^+ + e^-$ (1.10)

$Pt\text{-}CHOCH_3 + Pt\text{-}OH \rightarrow 2Pt + CH_3COOH + H^+ + e^-$ (1.11)

The other pathway (C1 mechanism) is completely oxidizing ethanol to carbon dioxide and generating 12 electrons. The C-C bond of ethanol must be broken in this reaction to produce adsorbed intermediates, including CH_x (ad) and CH_yO(ad) (eq. 1.12), which are further oxidized to carbon monoxide (eq. 1.13). CO(ad) species are oxidized to CO_2 by the hydroxyl groups on Pt surfaces (eq. 1.14) (55, 60).

However, the strongly adsorbed CO(ad) on the active site of Pt inhibits the complete oxidation of ethanol (C1 mechanism) because multiple Pt active sites are required to break the C-C bonds. This leads to an increase in the selectivity of incomplete ethanol oxidation to acetaldehyde and acetic acid since fewer active sites are required (55).

$$\text{Pt-OCH}_2\text{CH}_3 \text{ or Pt-CH(OH)CH}_3 \rightarrow \text{Pt-CH}_y\text{O} + \text{Pt-CH}_x + (5-x-y)\ \text{H}^+ + (5-x-y)\ \text{e}^- \qquad (1.12)$$

$$\text{Pt-CH}_y\text{O or Pt-CH}_x \rightarrow \text{Pt-CO} + (x + y)\ \text{H}^+ + (x + y)\ \text{e}^- \qquad (1.13)$$

$$\text{Pt-CO} + \text{Pt-OH} \rightarrow 2\text{Pt} + \text{CO}_2 + \text{H}^+ + \text{e}^- \qquad (1.14)$$

1.4.2. Anodic catalysts for direct ethanol fuel cells

Platinum catalysts remain the most efficient catalyst for the EOR in acidic media (57). However, although Pt has a high tendency for C-C bond dissociation in ethanol oxidation and increases selectivity for CO_2 generation as well as increasing electron generation, its slow EOR reaction rate due to CO poisoning prevents its commercialization as anodic catalyst for DEFC.

PtRu and PtSn are considered the best binary catalysts for the EOR (61-63). These alloys are able to remove CO from the Pt surface, giving them a high EOR activity. However, they are less capable than Pt of dissociating the C-C bond of ethanol, resulting in lower CO_2 selectivity, in which the major product from ethanol oxidation on the surface of PtRu is acetic acid (64).

Using PtRu in the form of core-shell structures increases EOR activity, selectivity for CO_2 generation, and catalyst durability (57).

Figure 1.8 shows the differences between bimetallic platinum-ruthenium alloys and core-shells. The catalytic activity of these core-shells depends on the interactions between the core and shell materials. Pt and Ru interact synergistically (strain, ligand, and bifunctional effects for sub-monolayers of Pt) to decrease Pt's d-band center, facilitating CO removal and enhancing EOR activity. The presence of only a few atomic monolayers (ML) of Pt on the surface increases CO_2 generation selectivity and decreases catalyst cost compared to Pt and PtRu. The Pt on the shell protects the active Ru on the core from dissolution, thus increasing the chemical stability of the catalyst (Chainmail effect) (57).

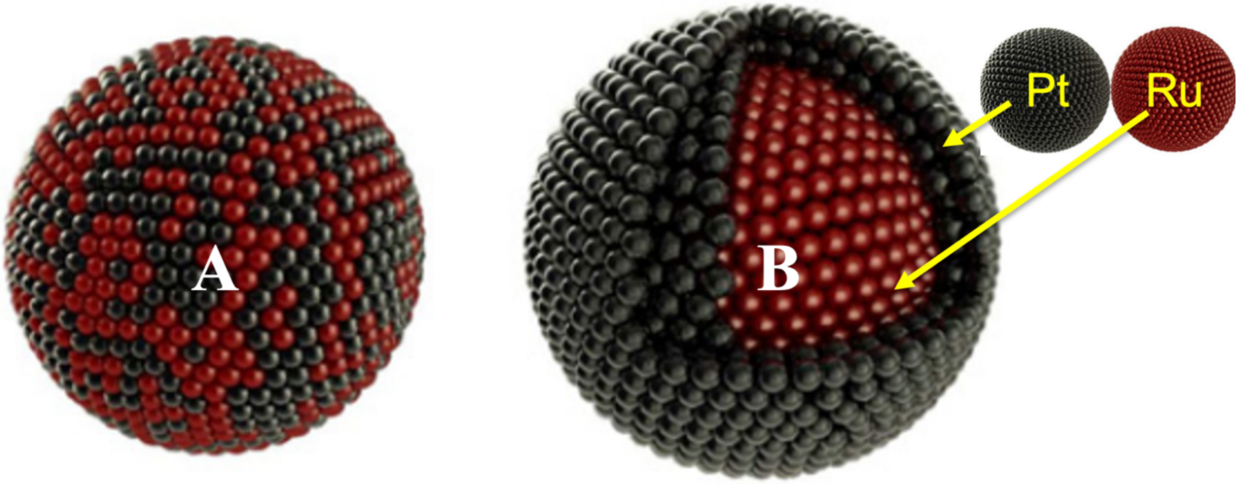

Figure 1.8. Various forms of bimetallic platinum ruthenium, including (A) alloys and (B) core-shell structures (58).

Hu et al. studied ethanol oxidation on Ru@Pt and standard PtRu at room temperature using cyclic voltammetry (0.5 M H_2SO_4 + 0.5 M ethanol with a scan rate of 50 mV s^{-1}) (65). They found that Ru@Pt had a higher peak current density (811 A g^{-1}) than PtRu (315 A g^{-1}), indicating better ethanol catalytic selectivity on Ru@Pt for CO_2 generation. Moreover, the Ru@Pt has a lower onset potential (0.54 V) than PtRu (0.61 V), suggesting that EOR on the core-shell structure has a higher catalytic activity (65).

According to Zou et al. all Ru@Pt of different Pt thicknesses have a higher current density than commercial PtRu for EOR. Further, they found that using Ru@Pt with crystalline Ru cores increased current density and decreased onset potentials compared to using amorphous Ru cores. Since Ru@Pt with an ordered Ru core does not have partial PtRu alloying at the Ru-Pt interface (well-defined boundaries). There is an increase in lattice strain in the Pt shell and a downshift in the d-band center. Thus, the Ru@Pt catalyst exhibits enhanced catalytic activity toward ethanol oxidation and increases CO_2 selectivity (66).

Effective core-shell nanoparticles (CSN) of low costs can be produced when precious metals like Pt, Pd, Au deposit on the surfaces of more active metals like Ru, Rh, Ni, Fe, and Co. The catalytic activity efficiency of these pairs is theoretically investigated using density functional theory, in which the d-band center model shows the ligand and strain effect between the core-shell, which helps design CSN with high activity and selectivity for ethanol oxidation (58).

In another direction, PtRh catalysts show higher selectivity for CO_2 generation than Pt (67-69). Rh facilitates C-C bond dissociation by forming an oxametallacyclic conformation with ethanol adsorbed on Rh (70). In spite of the fact that PtRh is more selective for CO_2 generation and stable under harsh conditions than PtRu, its kinetics remain slower (71, 72).

Kleber et al. compared carbon-supported PtRh catalysts with Pt in $HClO_4$ using differential electrochemical mass spectrometry (73). They found that these catalysts significantly increased CO_2 selectivity (73). Their CV results demonstrated a decrease in peak current density compared to Pt. Their explanation is that the Rh surface underwent a slow alcohol dehydrogenation reaction. Moreover, Rh was poisoned by CO more than Pt since the binding energy between Rh and CO is greater than that between Pt and CO (73). They suggested that alloying Ru or Sn with PtRh might increase the EOR activity and selectivity of CO_2 generation (73). Delpeuch et al. found that the kinetics of PtRh highly increased compared to Pt when the temperature was increased from ambient to 70 °C which is a typical operating temperature in PEMFC (74). Lima and Gonzalez found that Rh-Pt bimetallic's core-shell structure could increase the EOR rate and selectivity for CO_2 generation compared to their alloy structure (75).

EOR activity and selectivity were also improved by using ternary nanoalloys. Researchers focused on alloying a third active metal (such as Ni, Fe, Co, Cu) with the common Pt-based bimetallic nanometals (PtRu, PtSn, and PtRh). Adding a third metal reduces the amount of Pt and might enhance the C-C bond cleavage ability (62).

Wang et al. studied the EOR of PtRuNi/C and PtRu catalysts using cyclic voltammetry (76). Despite having the same onset potential, PRuNi had a much higher peak current density (higher selectivity for CO_2). According to their results, Ni weakens OH(ad) bonding to the surface of Ru at high potentials, improving the EOR activity (76).

Beyhan et al. studied the EOR on different PtSnM (M = Pb, Rh, Co, Ni) catalysts and compared the results with a standard PtSn catalyst (77). According to their polarization curves for DEFC, there was a significant improvement in current density and onset potential for the EOR for PtSnCo and PtSnNi trimetallic nanoparticles compared to PtSn (77). Ternary catalysts need to be further developed and studied for DEFC. It can be difficult to control particle size, crystallinity, and uniformity during preparation, as well as loss of active metals (62).

1.5. Platinum-based core-shell nanoparticles (CSN)

Researchers develop core-shell catalysts for the MOR and EOR by modifying the composition of both the core and shell, modifying the thickness of the Pt shell, and controlling their shape and size. In addition, they developed synthetic methods without stabilizers to produce highly effective, low-cost, small, and ultrathin core-shell catalysts. The stabilizers occupy the active sites of the catalyst, lowering its catalytic activity (57). Too thin a Pt shell will decrease the ability to adsorb alcohol, the selectivity of CO_2 generation, and the ability to preserve core materials. At the same time, too thick a shell cannot interact effectively with the core, increasing the activation energy required for the MOR and EOR due to CO poisoning (57).

1.5.1. A brief summary of CSN preparation

In order to reduce the costs, Pt-based catalysts should be prepared with a carbon black support since it has many advantages, including a high surface area, low cost, and easy availability (65). The preparation of Pt-based core-shell nanoparticles can be classified into two categories: top-down, which involves laser beam processing and mechanical methods. In contrast, the bottom-up approach consists of layer-by-layer coating, chemical reduction, electrochemical deposition, and sol-gel methods (63). Pt-based core-shell nanoparticles prepared from the bottom-up approach have several advantages over those prepared from the top-down, guaranteeing homogenous particles with few defects and controlling the Pt shell's thickness (63).

The simplest way to prepare a Pt-based core-shell is the reduction method, which is classified as a wet chemical synthesis method and relies on reducing metal ions using various reducing agents such as ethanol (78), formic acid (73), ethylene glycol (polyol method) (61, 79), and hydrogen (80). The reduction method can be categorized into a one-step method, when a platinum precursor is reduced and deposited on the surface of a commercial catalysts (61, 79), and a two-step method when we first reduce the metal ions of the core and then reduce the metal ions of the shell (63). The reduction method has some advantages because it is simple and allows control of the Pt shell composition and thickness.

However, the reduction method also has some problems, such as: (I) high temperatures are required to prevent galvanic displacement between Pt metal ions and more active core metals. However, the high temperatures could produce an amorphous core. (II) A long time is required to confirm that the reduction is complete. (III) There is a requirement for a capping agent (stabilizing agent) that helps to form nanoparticles of uniform size, provides stability, and prevents agglomeration of prepared nanoparticles. Polyvinyl pyrrolidone (PVP) is usually used as a capping agent (63).

The acidic treatment of binary alloys containing Pt and other reactive metals, such as Ni, Cu, and Fe, can also form Pt-based core-shell catalysts. It was found that adding $HClO_4$ (aq), acetic acid (aq), or H_2SO_4 (aq) to this type of binary alloy for 2-6 hours dissolves the metals with higher affinity for the acid, leaving behind the metals (Pt) with a lower affinity. This process is known as selective dissolution (81).

Electrochemical synthesis is another technique used to prepare Pt-based CSN. The most common electrochemical synthesis method is galvanic displacement. In this process, sacrificial Cu is first deposited on the core's surface to form a monolayer of Cu. After immersion in a solution of $PtCl_4$, a core@Cu monolayer spontaneously displaced the Cu ($E^\circ_{Cu2+/Cu}$ = 0.30 V) and Pt^{4+} ($E^\circ_{Pt4+/Pt}$ = 1.44 V) to form a core@Pt monolayer. The method works well for preparing a uniform shell thickness with control over the thickness of Pt and the size of nanoparticles (81).

1.5.2. A brief summary of CSN physical characterization

Various physical techniques are used to characterize the fabricated Pt-based core-shell nanoparticles. The main techniques are thermal gravimetric analysis (TGA), X-ray diffraction (XRD), transmission electron microscopy (TEM), energy dispersive X-ray spectroscopy with scanning electron microscopy (EDX-SEM) and X-ray photoelectron spectroscopy (XPS).

Thermal gravimetric analysis provides information about metal loading and carbon support percentages, as well as measures the thermal stability of the carbon support of the catalyst (82). EDX is used to determine the metals present in the formed core-shell catalysts and to measure their mass percentages and atomic ratios (61).

The TEM technique can be used to obtain a clear image of a formed core-shell nanoparticle that can be used to determine their homogeneity, morphology, and size of both the core and CSN. Evidence for the formation of core-shell catalyst can be obtained from the observation of nanoparticles that are larger than the core nanoparticles. Furthermore, the TEM should show an increase in the core shell's size as the Pt shell's thickness increases. Measured sizes matching calculated sizes, providing strong evidence for Pt deposition on the surface of the core without significant core dissolution (61).

X-ray diffraction is used to deduce the formation of Pt on the core surface. Pure Pt has an FCC structure with four characteristic diffraction peaks corresponding to lattice planes (111), (200), (220), and (311) at positions close to 40°, 46°, 68°, and 82°, respectively. Pt's diffraction peak (111) can be used to calculate its crystal size (d) (61). XRD allows for analyzing core-shell interactions, such as measuring the compression strain in the lattice of the Pt shell using the Pt (200) diffraction peaks (83).

Alayoglu et al. could distinguish between PtRu alloy and Ru@Pt nanoparticles from their XRD profiles (84). PtRu and Ru@Pt exhibit FCC diffraction peaks for the Pt; however, the peaks are shifted to higher angles than pure Pt due to the compressed lattice caused by Pt and Ru interactions. Nevertheless, the Ru@Pt core-shell structure had a distinct shoulder adjacent to the diffraction peak Pt (111) resulting from the amorphous Ru core. As a result of this extra reflection, the Ru@Pt pattern differs from that of pure Pt and PtRu alloy (84).

The XPS technique is a surface analysis in which materials are exposed to an X-ray beam, and their kinetic energy and electron escape rates are measured from its top 1 to 10 nm (85). So, Pt growth on the core surface can be identified by comparing the Pt-shell/core atomic ratios obtained from XPS and EDX. EDX involves the focus of a high-energy beam of electrons into the sample being studied to induce the emission of characteristic X-rays from a depth of 1 to 3 μm. The Pt-shell/core atomic ratio measured by XPS is higher than that measured by EDX, indicating that such growth has occurred (61, 79). Moreover, XPS allowed a clear understanding of the interaction between the core and shell (83).

1.6. Proton exchange membrane electrolysis cells (PEMEC)

A proton exchange membrane (PEM) electrolysis cell can be used to evaluate core-shell nanoparticles as the anodic catalysts for DEFC by measuring both the rate and stoichiometry (n_{av}) ethanol oxidation as a function of potential. A PEMEC is similar to the fuel cell in term of the components, the operation process, and the anodic reactions (Figure 1.9). They differ only in the cathodic reaction, where nitrogen is used to replace airflow, resulting in a reduction of the transferred protons to hydrogen gas, with the cathode acting as a dynamic hydrogen electrode (DHE).

The aim of removing oxygen is to evaluate the anodic catalyst efficiency since alcohol reacts chemically with oxygen when it crosses to the cathode, and this effect negatively affects the cathodic potentials and cell efficiency. It is possible to test many catalysts in the same run using a multi-anode PEMEC (86). The current flows in this cell due to alcohol oxidation at the surface of the anodic catalyst. This current is measured at different potentials, which results in a current-potential (I-V) curve, namely a polarization curve. At high potentials, the average number of electrons (n_{av}) that can evolve during the ethanol oxidation on the surface of each anode can be calculated (eq. 1.15) (61). In equation 1.15, I_{lim} is the limiting current, m is the mass transport coefficient, A is the electrode surface area, and C is bulk concentration.

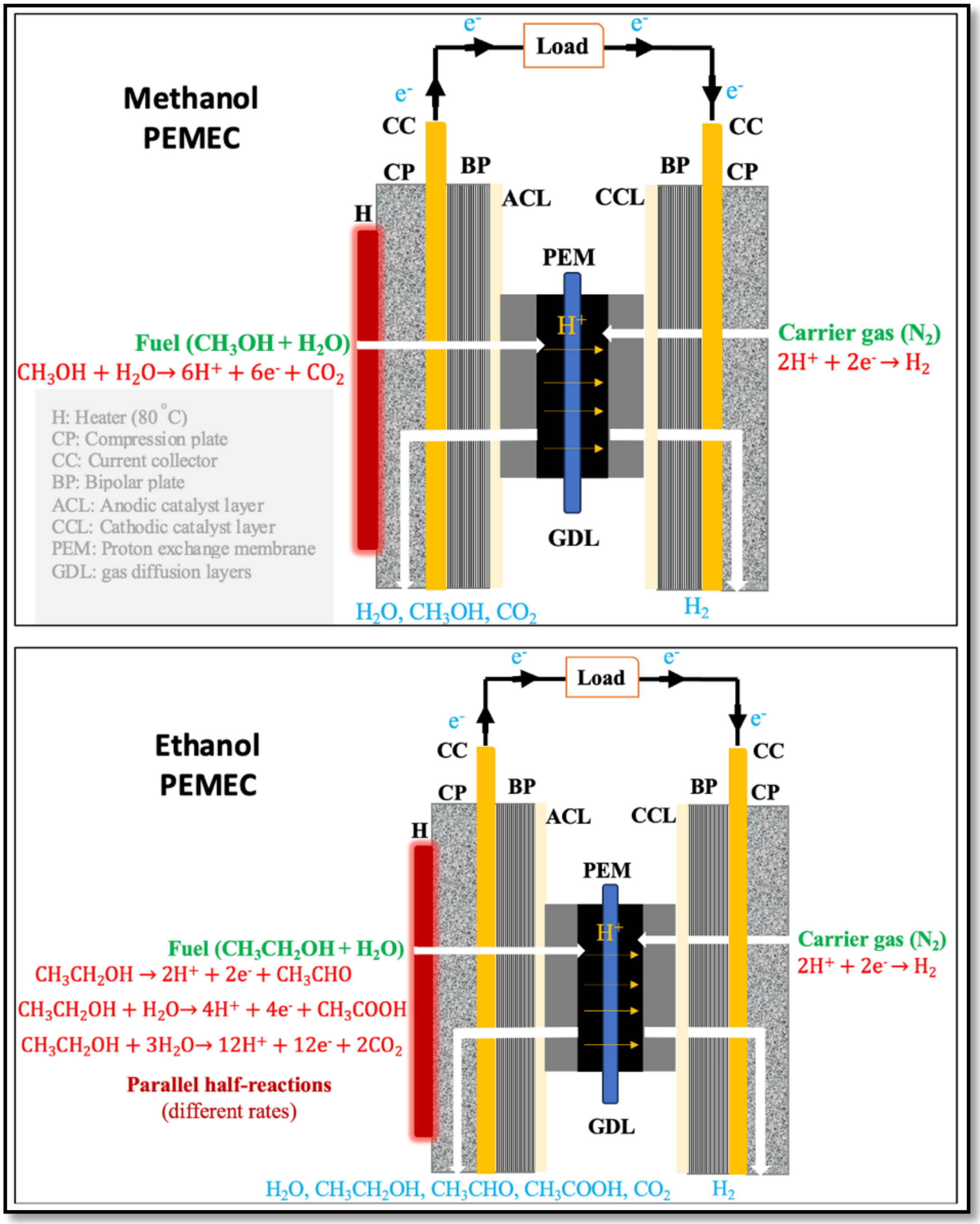

Figure 1.9. A schematic diagram of methanol and ethanol proton exchange membrane electrolysis cells (PEMEC).

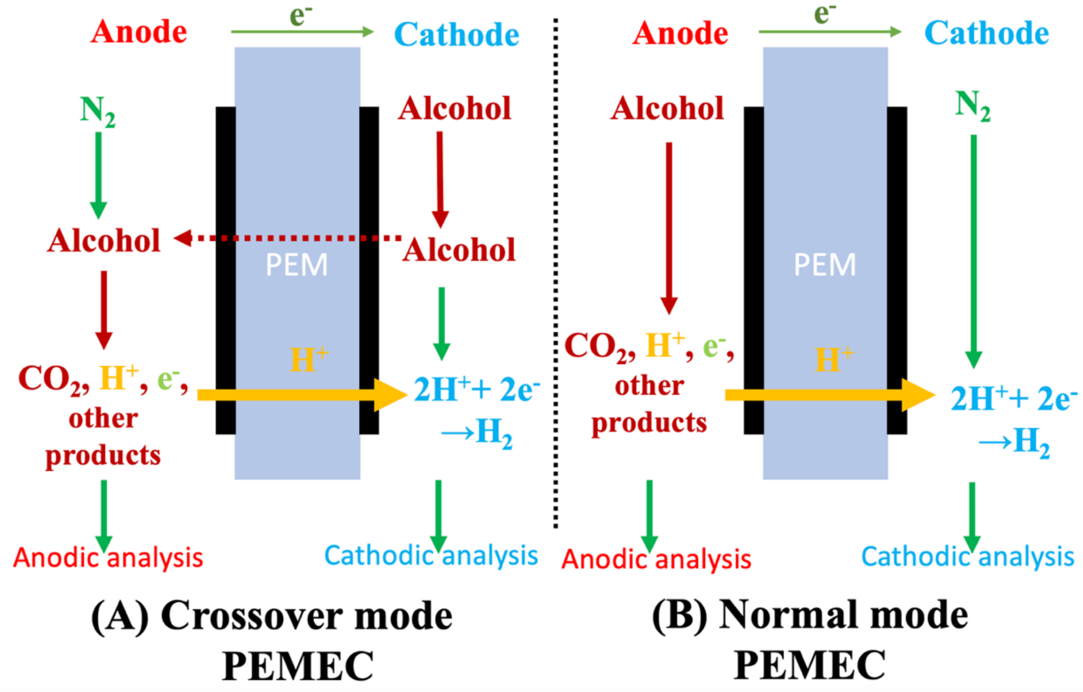

Figure 1.10. Schematic diagrams of the two configuration modes of the PEMEC employed in this work.

Two different modes can be applied based on the required study, as illustrated in Figure 1.10. These modes are crossover mode (Figure 1.10A) or anode polarization (normal) mode (Figure 1.10B). Anode has a positive potential relative to a cathode in both modes for oxidizing alcohol (methanol or ethanol). Protons are reduced to hydrogen gas in the cathode. So, the cathode acts as a dynamic hydrogen electrode (DHE) in both electrolysis modes. In order to control the diffusion of ethanol to the anode, the cell was operated in crossover mode. Consequently, steady-state polarization curves with mass transport regions were obtained (86). Normal mode evaluates the catalytic activity for MOR and EOR for the prepared catalysts as it would be in a real fuel cell (Figure 1.9), where a crossover effect of alcohol is considered (86).

El-Sawy et al. studied the catalytic activity of Ru@Pt and Rh@Pt catalysts of different Pt thicknesses using PEMEC (64). Their polarization curves for the oxidation of 0.1 M ethanol at $Ru_{54}@Pt_{46}$, $Rh_{54}@Pt_{46}$, $Rh_{46}@Pt_{54}$, $Rh_{40}@Pt_{60}$, and Pt catalysts in crossover mode are shown in Figure 1.11 (64). The $Ru_{54}@Pt_{46}$ shows a higher ethanol oxidation activity than its counterparts at potentials below 0.50 V vs DHE. In contrast, at a potential above 0.50 V, Pt has the highest activity. All Rh@Pt catalysts showed lower ethanol oxidation activities at all potentials compared to the Pt, and $Ru_{45}@Pt_{46}$. Moreover, changing the thickness of the Pt shell did not affect the ethanol oxidation activity. Equation 1.15 was used to calculate the n_{av} over the mass transport region (indicated in blue). The values of n_{av} decrease from 0.60 V to 0.90 V due to an increasing ratio of acetic acid to carbon dioxide (64). All the Rh@Pt catalysts formed acetic acid above 0.60 V vs DHE, as shown by the value of n_{av}, which was nearly constant and close to 4. Furthermore, the Rh forms hydroxides on the surface of catalysts at low applied potentials. These facilitate the oxidation of the $CHOCH_3$ intermediate to acetic acid (eq. 1.11).

$$I_{lim} = n_{av}FmAC \qquad (1.15)$$

As such, they suggested that $Ru_{54}@Pt_{46}$ is suitable to be employed in DEFC, especially at low applied potential, while none of the Rh@Pt are appropriate for utilization in DEFC at any potential.

The concentration of each product in the exhaust from a PEMFC at the given potential reflects the anodic catalyst's ability for ethanol oxidation and electricity generation. The main technique employed to analyze the products that result from the PEMEC in our group is proton NMR spectroscopy (87, 88). This technique measures the concentration of products by comparing each product's H-peaks with the internal standard (fumaric acid) peak. This internal standard has a singlet peak at 7.72 ppm, whereas the residual ethanol has a triplet peak at 1.10 ppm. In addition, acetaldehyde has a doublet peak at 2.15 ppm, while acetic acid has a singlet peak at 2.01 ppm.

On the other hand, the CO_2 products can be determined using a commercial non-dispersive infrared (NDIR) detector during the I-V analysis. The value of n_{av} at different potential values can be determined using equation 1.6. The significance of calculating the n_{av} is evaluating the efficiency of the anodic catalyst for ethanol oxidation at each potential for a DEFC. The faradaic efficiency can be calculated through equation 1.16, where the 12 in the denominator represents the maximum number of electrons that can be formed due to ethanol oxidation.

$$Faradic\ efficiency\ (\varepsilon_F)_{(at\ given\ potential)} = \frac{n_{av}}{12} \qquad (1.16)$$

In order for the DEFC to perform well, it is necessary to have high faradaic efficiency. The anodic catalyst plays a critical role in achieving a high level of performance from a cell. Specifically, the catalyst should be highly active and highly selective in terms of ethanol oxidation. In addition, it should also be able to tolerate high concentrations of ethanol and be stable over a wide range of temperatures. It is also important that the catalyst be both low-cost and non-toxic. Additionally, the catalyst should resist corrosion and have a low environmental impact (89).

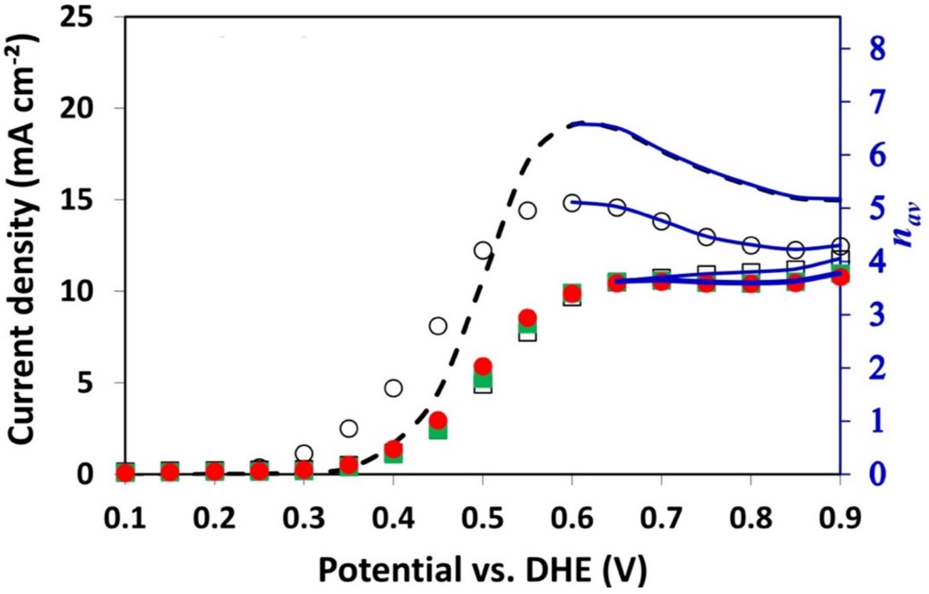

Figure 1.11. Polarization curves for 0.1 M ethanol oxidation at 80 ^{0}C using Ru$_{54}$@Pt$_{46}$ (O), Rh$_{54}$@Pt$_{46}$ (▢), Rh$_{46}$@Pt$_{54}$ (🟩), Rh$_{40}$@Pt$_{60}$(🔴) and Pt/C as anodes in PEMEC and the blue lines show the valid range, reprinted from (64). Open access article distributed under the Creative Commons Attribution 4.0 License.

1.7. Performance and efficiency of DEFC

An evaluation of a fuel cell's performance can be based on the potential current output (polarization curve). A typical polarization curve of a low-temperature PEMFC is shown in Figure 1.12 (90). The thick black line at the top represents the reversible cell potential (E_{rev}), which considers the maximum fuel cell potential. E_{rev} is the difference between the electrode potentials calculated from the Nernst equation during thermodynamically reversible conditions with no current flowing in the cell. The open circuit potential (OCP) is the experimental potential difference between electrodes when no current flows. Because of the crossover of ethanol, the OCP is lower than the E_{rev} in Figure 1.12, which can be attributed to a mixed potential.

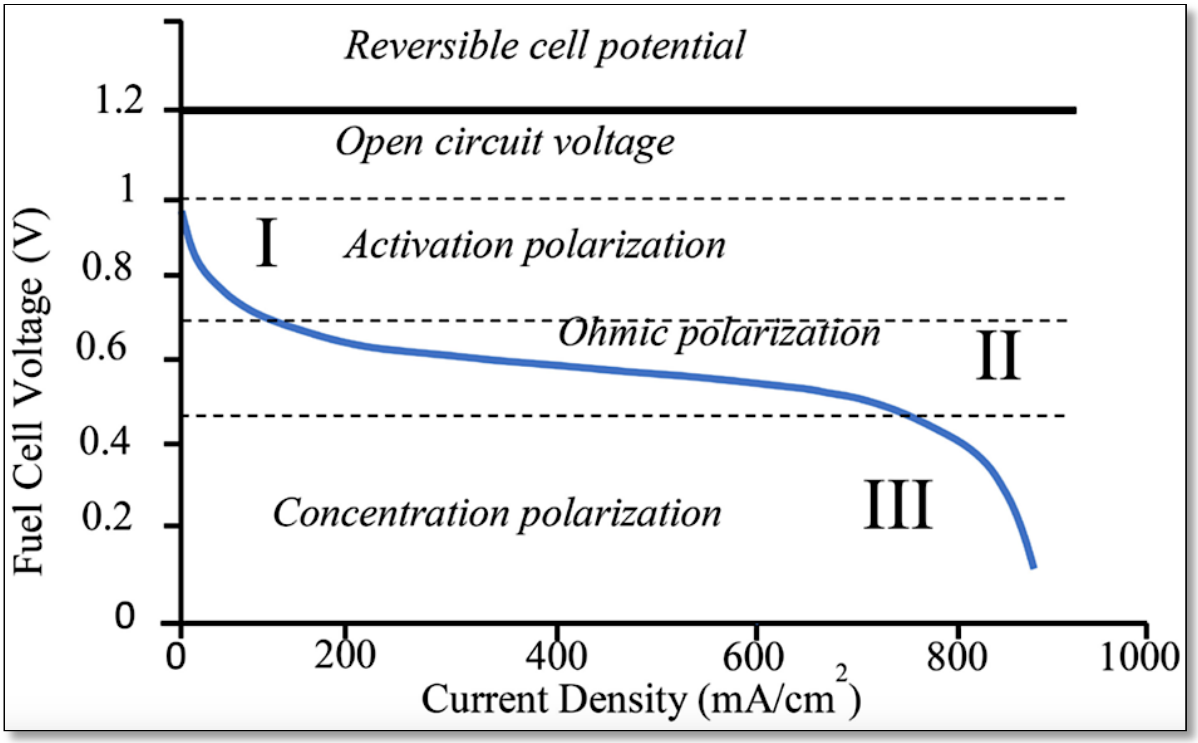

Figure 1.12. A typical polarization curve of a low-temperature PEMFC, reprinted from (90). A Creative Commons Attribution International License has been applied to this work (CC BY 4.0).

OCP is measured experimentally instead of $E°_{cell}$ and E_{rev} being calculated theoretically using thermodynamic data. The cell potential (E_{cell}) is the cell's potential under non-standard conditions (measured value). Overpotential is the difference between the actual potential (E_{cell}) and the E_{rev} (91, 92).

The polarization curve can be divided into three regions: (I) The activation polarization (the low current region) is controlled by the slow kinetics of the EOR and ORR, which the Tafel equation can model. (II) The ohmic polarization (the intermediate current region) comes from the ohmic resistance of the membrane and mainly from proton conduction. (III) The concentration polarization (high current region) shows a significant drop in the cell potential due to the mass transport resistance of the fuel and oxidant to the catalyst surface through the diffusion layer (90, 93).

In order to achieve the best performance, a fuel cell must have the lowest overpotential and the highest limiting current. Fuel cell performance is reduced due to activation polarization, ohmic resistance polarization, and concentration polarization. The DEFC performance is low due mainly to the slow EOR kinetics on the catalyst surface.

A fuel cell system can be evaluated based on its energy-conversion efficiency. Generally, three types of efficiency are used: thermodynamic efficiency (ε_{rev}), potential efficiency (ε_E), and faradaic efficiency (ε_F).

The thermodynamic efficiency (theoretical energy conversion efficiency) of a reaction is the total conversion of Gibbs free energy into electric energy, is derived from the thermodynamics of the overall combustion reaction of ethanol (eq.1.17): $E^\circ_{cell} = 1.14$ V, $\Delta G^\circ = -1325$ kJ mol^{-1}; $\Delta H^\circ = -1366$ kJ mol^{-1}. The ε_{rev} is a theoretical efficiency calculated using equation 1.18 (91, 92).

$$CH_3CH_2OH + 3O_2 \rightarrow 2CO_2 + 3H_2O \qquad (1.17)$$

The DEFC has a thermodynamic efficiency of 97% at ambient temperatures, which is similar to that of DMFC (97%) and higher than that of hydrogen fuel cells (83%) and internal combustion engines (43%) (55, 94).

$$\varepsilon_{rev} = \frac{\Delta G^\circ}{\Delta H^\circ} = 97\% \qquad (1.18)$$

Where ΔG° and ΔH° are the standard Gibbs free energy change and the standard enthalpy change for the complete combustion of the ethanol.

A DEFC's reversible cell potential (E_{rev}) can be calculated from the thermodynamics of ethanol combustion at equilibrium under standard conditions using equation 1.19 (92), where n is the number of transfer electrons from the complete ethanol oxidation, and F is the faradaic constant. The reversible cell potential is also called the equilibrium potential. It is the standard cell potential ($E°_{cell}$) in case the activities of both reactants and products are equal to one.

$$E_{rev} = -\frac{\Delta G°}{nF} = -\frac{-1325\ x\ 1000\ J\ mol^{-1}}{12\ x\ 96485} = 1.144\ V \qquad (1.19)$$

Potential efficiency (ε_E) is derived from the electrode overpotentials. Equation 1.20 calculates the potential efficiency, which is the ratio between the operation potential (E_{cell}) and the reversible cell potential (E_{rev}) (91).

$$\varepsilon_E = \frac{E_{cell}}{E_{rev}} \qquad (1.20)$$

The faradaic efficiency of the cell is the ratio between the average number of the generated electrons (n_{av}) to the maximum number of generated electrons from the complete ethanol oxidation (12 electrons), as shown in equation 1.16. Hence, incomplete oxidation of ethanol reduces faradaic efficiency (ε_F).

When applied to individual products, faradaic efficiency ($F_{product}$) is defined as the ratio of the amount of product (e.g. CO_2) to the amount that the total charge passed would produce, expressed as a fraction or percentage.

Based on the thermodynamic efficiency, the potential efficiency, the faradaic efficiency, and ethanol losses due to crossover through the membrane to the cathode (ε_{cross}), the overall efficiency of a DEFC (ε_{cell}) can be calculated through equation 1.21 (91).

$$\varepsilon_{cell} = \varepsilon_{rev} * \varepsilon_E * \varepsilon_F * \varepsilon_{cross} \qquad (1.21)$$

1.8. Thesis objectives

The overall goal of this thesis is to develop catalysts with high activity for the complete oxidation of methanol and ethanol in direct alcohol fuel cells and electrolysis cells. This study focused on preparing Pt-based catalysts with small sizes, narrow size distributions, low agglomerations, high crystallinity, and uniform distributions over carbon black supports. Their catalytic activities for methanol and ethanol oxidations in acidic media were investigated using cyclic voltammetry (CV) at ambient temperature and proton exchange membrane electrolysis cells (PEMEC) at 80 °C, to develop more efficient and cost-effective methanol and ethanol cells.

PtRu is one of the most effective anodic catalysts for methanol and ethanol oxidation reactions in direct methanol and ethanol fuel cells. Therefore, we added different amounts of Pt to the surface of this standard catalyst to form PtRu@Pt, aiming to increase its activity and selectivity for complete alcohol oxidations. We also tried rearranging these metals in Ru@Pt to increase active sites and stability. Last but not least, we replaced Ru with Rh because Rh was found to have a high ability to dissociate the C-C bond during ethanol oxidation, our primary goal for improving anodic catalysts in the direct ethanol fuel cell.

Chapter 3 describes the preparation of core-shell PtRu@Pt catalysts based on depositing different amounts of Pt on the surface of a state-of-the-art commercial PtRu catalyst. The effect of adding different amounts of Pt on the performance for methanol and ethanol oxidation was investigated in 1 M H_2SO_4 at ambient temperature and a PEMEC at 80 °C.

In Chapter 4, Ru@Pt core-shell catalysts with highly crystalline Ru cores were prepared using the polyol method without adding capping agents. Ru and Pt synergistic interactions were examined using XRD and XPS techniques. Their MOR and EOR catalytic activities were investigated using both CV and PEMEC experiments.

In Chapter 5, a series of Rh@Pt core-shell catalysts with different Pt thicknesses, small sizes, and highly crystalline structures were prepared. Using CV and PEMEC, their catalytic activity was investigated for MOR and EOR. This study investigates the selectivity of C-C bond dissociation during ethanol oxidation by measuring the faradaic yield of CO_2 in both normal and crossover modes of the fuel cell hardware. In this way, we can see how well they can function as anodic catalysts in DEFC.

In Chapter 6, a series of PtRh alloys with different (Pt:Rh) atomic ratios were prepared. Their catalytic activities were investigated using CV at ambient temperature and PEMEC at 80 °C. Using both normal and crossover modes, we investigated the effect of Rh on EOR activity and selectivity. In order to do this, an I-V curve was plotted, and n_{av} and CO_2 faradaic yields were measured at different potentials. This study clarifies the ability of these catalysts to generate electrons and hydrogen gas in both DEFC and PEMEC, respectively.

1.9. References

1. M. Zastempowski, Renewable and Sustainable Energy Reviews, **178**, 113262 (2023).
2. N. Abas, A. Kalair and N. Khan, Futures, **69**, 31-49 (2015).
3. S. Mohr, J. Wang, G. Ellem, J. Ward and D. Giurco, Fuel, **141**, 120-135 (2015).
4. S. Yi, K.R. Abbasi, K. Hussain, A. Albaker and R. Alvarado, Gondwana Research, **117**, 41-55 (2023).
5. R. York and S.E. Bell, Energy Research and Social Science, **51**, 40-43 (2019).
6. A. Kalair, N. Abas, M.S. Saleem, A.R. Kalair and N. Khan, Energy Storage, **3**, e135 (2021).
7. J.L. Holechek, H.M. Geli, M.N. Sawalhah and R. Valdez, Sustainability, **14**, 4792 (2022).
8. D. Wan, R. Xue, M. Linnenluecke, J. Tian and Y. Shan, Finance Research Letters, **43**, 101955 (2021).
9. P.J. Megía, A.J. Vizcaíno, J.A. Calles and A. Carrero, Energy and Fuels, **35**, 16403-16415 (2021).

10. J. Curtin, C. McInerney, B.Ó. Gallachóir, C. Hickey, P. Deane and P. Deeney, Renewable and Sustainable Energy Reviews, **116**, 109402 (2019).

11. A. Rehman, A. Rauf, M. Ahmad, A.A. Chandio and Z. Deyuan, Environmental Science and Pollution Research, **26**, 21760-21773 (2019).

12. K. Handayani, Y. Krozer and T. Filatova, Energy policy, **127**, 134-146 (2019).

13. D.J. Davidson, Nature Energy, **4**, 254-256 (2019).

14. M. Aminudin, S. Kamarudin, B. Lim, E. Majilan, M. Masdar and N. Shaari, International Journal of Hydrogen Energy, **48**, 4371-4388 (2023).

15. A. Pramuanjaroenkij and S. Kakaç, International Journal of Hydrogen Energy, **48**, 9401-9425 (2023).

16. J. Han, J. Feng, P. Chen, Y. Liu and X. Peng, Energy Conversion and Management: X, **15**, 100265 (2022).

17. J. Xu, C. Zhang, Z. Wan, X. Chen, S.H. Chan and Z. Tu, Renewable and Sustainable Energy Reviews, **155**, 111908 (2022).

18. S. Tanaka, K. Nagumo, M. Yamamoto, H. Chiba, K. Yoshida and R. Okano, ETransportation, **3**, 100046 (2020).

19. F. de Oliveira Gonçalves, E.S. Lopes, M.S. Lopes and R. Maciel Filho, International Journal of Hydrogen Energy, **46**, 36381-36397 (2021).

20. A. Ajanovic and R. Haas, Fuel cells, **19**, 515-529 (2019).

21. O. Korchagin, V. Bogdanovskaya, I. Vernigor, M. Radina, I. Stenina and A. Yaroslavtsev, Membranes, **13**, 669 (2023).

22. M.M. Hossen, M.S. Hasan, M.R.I. Sardar, J. bin Haider, K. Tammeveski and P. Atanassov, Applied Catalysis B: Environmental, **325**, 121733 (2023).

23. M.K. Singla, P. Nijhawan and A.S. Oberoi, Environmental Science and Pollution Research, **28**, 15607-15626 (2021).

24. R. Javaid and U.Y. Qazi, Energies, **16**, 5079 (2023).

25. E. Katz and P. Bollella, Israel Journal of Chemistry, **61**, 68-84 (2021).

26. M.L. Yusupovich, Texas Journal of Multidisciplinary Studies, **6**, 140-144 (2022).

27. Z. Zakaria and S.K. Kamarudin, International Journal of Energy Research, **45**, 4871-4887 (2021).

28. P. Colomban, Solid State Ionics, **334**, 125-144 (2019).

29. N. Bizon, Renewable and Sustainable Energy Reviews, **105**, 14-37 (2019).

30. A. Kirubakaran, S. Jain and R. Nema, Renewable and Sustainable Energy Reviews, **13**, 2430-2440 (2009).

31. U. Eberle and R. Von Helmolt, Energy and Environmental Science, **3**, 689-699 (2010).

32. A. Ajanovic, A. Glatt and R. Haas, Energy, **235**, 121340 (2021).

33. B.P. Tripathi and V.K. Shahi, Progress in Polymer Science, **36**, 945-979 (2011).

34. B. Ong, S. Kamarudin and S. Basri, International journal of hydrogen energy, **42**, 10142-10157 (2017).

35. X. Li and A. Faghri, Journal of Power Sources, **226**, 223-240 (2013).

36. C. Lamy, A. Lima, V. LeRhun, F. Delime, C. Coutanceau and J.-M. Léger, Journal of Power Sources, **105**, 283-296 (2002).

37. M. Kamarudin, S. Kamarudin, M. Masdar and W. Daud, International journal of hydrogen energy, **38**, 9438-9453 (2013).

38. S. Badwal, S. Giddey, A. Kulkarni, J. Goel and S. Basu, Applied Energy, **145**, 80-103 (2015).

39. E. Dogdibegovic, Y. Fukuyama and M.C. Tucker, Journal of Power Sources, **449**, 227598 (2020).

40. M. Ebrahimi, W. Kujawski, K. Fatyeyeva and J. Kujawa, International Journal of Molecular Sciences, **22**, 5430 (2021).

41. A. Abdollahipour and H. Sayyaadi, Energy, **260**, 124944 (2022).

42. Y. Wang, K.S. Chen, J. Mishler, S.C. Cho and X.C. Adroher, Applied Energy, **88**, 981-1007 (2011).

43. K. Jiao, J. Xuan, Q. Du, Z. Bao, B. Xie, B. Wang, Y. Zhao, L. Fan, H. Wang and Z. Hou, Nature, **595**, 361-369 (2021).

44. S. Ahmad, T. Nawaz, A. Ali, M.F. Orhan, A. Samreen and A.M. Kannan, International Journal of Hydrogen Energy, **47**, 19086-19131 (2022).

45. H. Li, H. Zhao, B. Tao, G. Xu, S. Gu, G. Wang and H. Chang, Nanomaterials, **12**, 4173 (2022).

46. Z. Li, Y. Wang, Y. Mu, B. Wu, Y. Jiang, L. Zeng and T. Zhao, Renewable and Sustainable Energy Reviews, **176**, 113182 (2023).

47. A. Navarro, M. Gómez, L. Daza and J. López-Cascales, Scientific Reports, **12**, 4219 (2022).

48. A. Hermann, T. Chaudhuri and P. Spagnol, International Journal of Hydrogen Energy, **30**, 1297-1302 (2005).

49. M.A. Abdelkareem, K. Elsaid, T. Wilberforce, M. Kamil, E.T. Sayed and A. Olabi, Science of The Total Environment, **752**, 141803 (2021).

50. F. Vigier, S. Rousseau, C. Coutanceau, J.-M. Leger and C. Lamy, Topics in Catalysis, **40**, 111-121 (2006).

51. H. Tian, Y. Yu, Q. Wang, J. Li, P. Rao, R. Li, Y. Du, C. Jia, J. Luo and P. Deng, International Journal of Hydrogen Energy, **46**, 31202-31215 (2021).

52. B. Braunchweig, D. Hibbitts, M. Neurock and A. Wieckowski, Catalysis Today, **202**, 197-209 (2013).

53. A.S. Moura, J.L. Fajín, M. Mandado and M.N.D. Cordeiro, Catalysts, **7**, 47 (2017).

54. S. Kwon, D.J. Ham, T. Kim, Y. Kwon, S.G. Lee and M. Cho, ACS Applied Materials and Interfaces, **10**, 39581-39589 (2018).

55. R.M. Altarawneh, Energy and Fuels, **35**, 11594-11612 (2021).

56. S. Mourdikoudis, J. Regner, R. Gusmão and Z. Sofer, Advanced Sustainable Systems, **6**, 2200163 (2022).

57. Q. Li, G. Zhang, B. Yuan, S. Zhong, Y. Ji, Y. Liu, X. Wu, Q. Kong, J. Han and W. He, Nano Select, **3**, 1459-1483 (2022).

58. P. Ochal, J.L.G. de la Fuente, M. Tsypkin, F. Seland, S. Sunde, N. Muthuswamy, M. Rønning, D. Chen, S. Garcia and S. Alayoglu, Journal of Electroanalytical Chemistry, **655**, 140-146 (2011).

59. V.K. Puthiyapura, W.-F. Lin, A.E. Russell, D.J. Brett and C. Hardacre, Topics in Catalysis, **61**, 240-253 (2018).

60. R.B. Moghaddam and P.G. Pickup, Electrochimica Acta, **65**, 210-215 (2012).

61. A.H. Ali and P.G. Pickup, ECS Advances, **2**, 024501 (2023).

62. G. Yang, Q. Zhang, H. Yu and F. Peng, Particuology, **58**, 169-186 (2021).

63. X. Wang, B. He, Z. Hu, Z. Zeng and S. Han, Science and Technology of Advanced Materials, **15**, 043502 (2014).

64. E.N. El Sawy, T.M. Brueckner and P.G. Pickup, Journal of the Electrochemical Society, **167**, 106507 (2020).

65. Y. Hu, A. Zhu, Q. Zhang and Q. Liu, International Journal of Hydrogen Energy, **41**, 11359-11368 (2016).

66. J. Zou, M. Wu, S. Ning, L. Huang, X. Kang and S. Chen, ACS Sustainable Chemistry and Engineering, **7**, 9007-9016 (2019).

67. J. Bai, X. Xiao, Y.-Y. Xue, J.-X. Jiang, J.-H. Zeng, X.-F. Li and Y. Chen, ACS Applied Materials and Interfaces, **10**, 19755-19763 (2018).

68. B.K. Devendra, B. Praveen, V. Tripathi, G. Nagaraju, D. Nagaraju and K. Nayana, Inorganic Chemistry Communications, **134**, 109065 (2021).

69. T. Imada, M. Chiku, E. Higuchi and H. Inoue, Journal of Physical Chemistry C, **125**, 14616-14626 (2021).

70. S.Y. Shen, T.S. Zhao and J.B. Xu, International Journal of Hydrogen Energy, **35**, 12911-12917 (2010).

71. F.H.B. Lima and E.R. Gonzalez, Electrochimica Acta, **53**, 2963-2971 (2008).

72. C.D. Silva, P.G. Corradini, V. Del Colle, L.H. Mascaro, F.H.B. de Lima and E.C. Pereira, Electrochimica Acta, **354**, 136674 (2020).

73. K. Bergamaski, E.R. Gonzalez and F.C. Nart, Electrochimica Acta, **53**, 4396-4406 (2008).

74. A. Bach Delpeuch, T. Asset, M. Chatenet and C. Cremers, Fuel Cells, **15**, 352-360 (2015).

75. F.H.B. Lima and E.R. Gonzalez, Applied Catalysis B: Environmental, **79**, 341-346 (2008).

76. Z.-B. Wang, G.-P. Yin, J. Zhang, Y.-C. Sun and P.-F. Shi, Journal of Power Sources, **160**, 37-43 (2006).

77. S. Beyhan, C. Coutanceau, J.-M. Léger, T.W. Napporn and F. Kadırgan, International Journal of Hydrogen Energy, **38**, 6830-6841 (2013).

78. A. Hoang, E. El Sawy, A. Blackburn, S. Ketabi, M. Goledzinowski, F.J.E. Comeau and V. Birss, ACS Applied Energy Materials, **3**, 8423-8436 (2020).

79. A.H. Ali and P.G. Pickup, Journal of the Electrochemical Society, **169**, 034523 (2022).

80. L. Fang, J. He, S. Saipanya and X. Huang, International Journal of Electrochemical Science, **10**, 5350-5357 (2015).

81. R. Wang, H. Wang, F. Luo and S. Liao, Electrochemical Energy Reviews, **1**, 324-387 (2018).

82. I.N. Leontyev, D.V. Leontyeva, A.B. Kuriganova, Y.V. Popov, O.A. Maslova, N.V. Glebova, A.A. Nechitailov, N.K. Zelenina, A.A. Tomasov, L. Hennet and N.V. Smirnova, Mendeleev Communications, **25**, 468-469 (2015).

83. E.N. El Sawy and P.G. Pickup, Electrocatalysis, **7**, 477-485 (2016).

84. S. Alayoglu, A.U. Nilekar, M. Mavrikakis and B. Eichhorn, Nature Materials, **7**, 333-338 (2008).

85. E.R. Zakirov, V.G. Kesler, G.Y. Sidorov, I.P. Prosvirin, A.K. Gutakovsky and V.I. Vdovin, Semiconductor Science and Technology, **34**, 065007 (2019).

86. T.M. Brueckner and P.G. Pickup, Journal of the Electrochemical Society, **164**, F1172-F1178 (2017).

87. R.M. Altarawneh, T.M. Brueckner, B. Chen and P.G. Pickup, Journal of Power Sources, **400**, 369-376 (2018).

88. R.M. Altarawneh and P.G. Pickup, Journal of the Electrochemical Society, **165**, F479-F483 (2018).

89. P. Ekdharmasuit, A. Therdthianwong and S. Therdthianwong, Fuel, **113**, 69-76 (2013).

90. Keoagile Mogorosi, M. Tunde Oladiran and E. Rakgati, Energy and Power Engineering, **12**, 653-670 (2020).

91. L. An, T. Zhao and Y. Li, Renewable and Sustainable Energy Reviews, **50**, 1462-1468 (2015).

92. S. Rousseau, C. Coutanceau, C. Lamy and J.-M. Léger, Journal of Power Sources, **158**, 18-24 (2006).

93. J.-H. Jung and S. Ahmed, Journal of Power Electronics, **10**, 739-748 (2010).

94. S. Fukuzumi and Y. Yamada, ChemElectroChem, **3**, 1978-1989 (2016).

Chapter 2: Experimental

This chapter provides an outline of the experiment methods employed and additional details of the methods described in Chapters 3-6.

Materials employed and catalyst preparation and characterization methods are described in each chapter. Thermogravimetric analysis, transmission electron microscopy, energy-dispersive X-ray spectroscopy, X-ray diffractometer, and X-ray absorption spectroscopy were used for physical characterization of catalysts, as described in detail in the following chapters. Details of the electrochemical methods are provided in the following sections.

2.1. Treatment method of Nafion-117 membrane

Nafion-117 membranes (7 mils thick, Ion Power Inc.), cut to 4.5×4.5 cm for use in our PEMEC, 20 films were stirred in 1 L of 3% H_2O_2 at 80 °C for 1 h with a glass rod. They were then washed with deionized water several times. Afterward, 1 L of 1 M H_2SO_4 was added to the membranes and stirred at 80 °C for one h. Finally, they were left in 1 L of deionized water at 80 °C for 3 h. The treated Nafion membrane was washed several times with deionized water and stored under deionized water at RT (1).

2.2. Cyclic voltammetry

Electrochemical measurements were conducted at ambient temperature using CV in 1.0 M sulfuric acid. This CV was set up in a three-compartment glass cell, as shown in Figure 2.1. A saturated calomel electrode (SCE) was used as the reference electrode, while a platinum wire served as the counter electrode. The results obtained with a Bio-Logic SP-50 potentiostat/galvanostat were recorded using EC-Lab electrochemical software. In order to remove O_2 from the solution, the solution was purged with N_2 gas for 15 min.

A blank CV was used to study the surface activity of the prepared catalyst. As well as demonstrating that the prepared core-shell catalysts contain Pt on the surface. 0.1 M alcohols in 1.0 M sulfuric acid at ambient temperature were used to evaluate the catalytic activity of the prepared catalysts for MOR and EOR at ambient temperature (2, 3).

The working electrode was prepared by sonicating 2 mg of catalyst in deionized water, 1-propanol, and 2-propanol (2:3:3) for 2 h. As a next step, a certain volume of catalyst ink was spread over the surface of a carbon fiber paper disk (0.24 cm^2) in order to obtain an amount of catalyst metals of 0.3 mg cm^{-2}. The disk was electrically connected to the potentiostat using a titanium clip as shown in Figure 2.1. Voltammograms for three catalyst electrodes were measured, and the median voltammogram is reported.

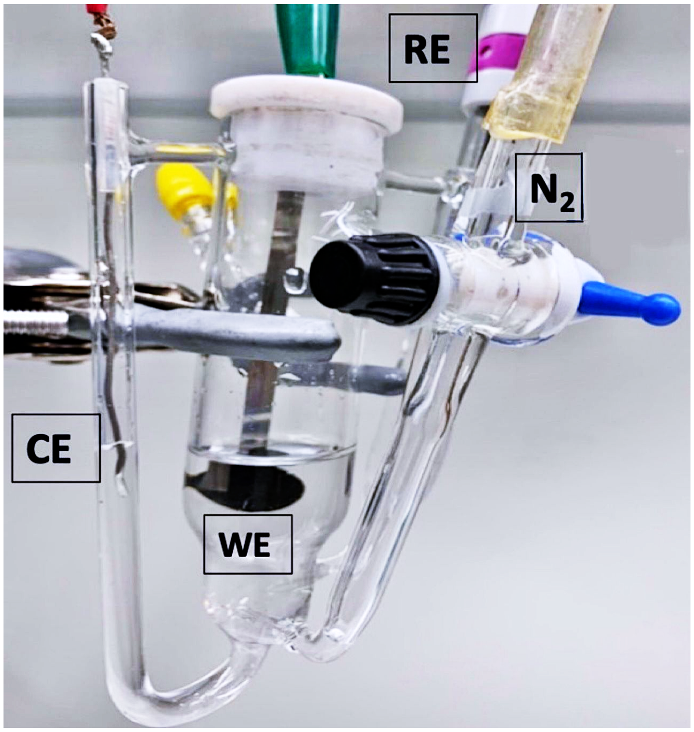

Figure 2.1. Photograph of the used three-compartment glass electrochemical cell.

2.3. Multi-anodes PEMEC

The use of multi-anode PEMEC enabled the investigation of the performance of many anodic catalysts simultaneously for the oxidation of alcohol. This study used an electrolysis cell capable of investigating nine anodes simultaneously (0.24 cm^2 per anode), as shown in Figure 2.2 (4). To determine reproducibility and precision, three catalysts were run simultaneously for each catalyst, and the average current and standard deviation is reported. It was decided to use a crossover mode in order to control the diffusion rate of ethanol to the anode during the operation of the cell and get the maximum cell efficiency. Modeling of kinetic and mass transport processes is simplified by utilizing the steady-state flow of fuel through the membrane to the anode (5). This mode involves purging the anode with 10 mL min^{-1} N_2 and pumping ethanol (0.10 M ethanol at 0.5 mL min^{-1}) at the cathode. A NE-300 syringe pump from Era Pump Systems supplied fuel.

A multi-channel potentiostat from Arbin Instruments was used to control the potentials. Torque wrenches (ca. 1.5 MPa) were used to press the membrane and electrode assemblies inside the cell. A Cole-Parmer temperature controller controlled the cell's temperature (type K thermocouple, model 89810-02). An Omega Engineering Inc., FMA1806A mass flow meter was also used to control the N_2 flow rate.

A polarization curves were measured at 80 °C in 50 mV steps between 0.90 V and 0 V. Anodes were first tested for methanol oxidation, then washed with DI water and tested for ethanol oxidation. The potential was held at 0.70 V for 1 hour before recording each polarization curve.

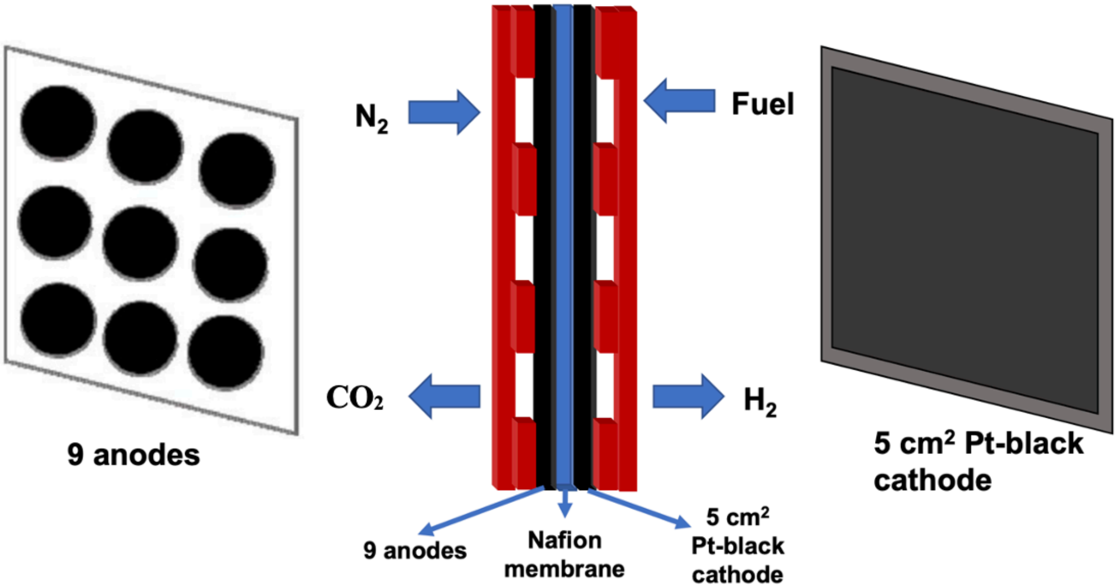

Figure 2.2. Schematic diagram of MEA of nine-anodes PEMEC operating in crossover mode, reprinted from (4). Open access to this article is granted under the terms of the Creative Commons Attribution 4.0 license.

Each anode electrode was prepared by suspending the prepared catalyst in a mixture of deionized water, 1-propanol, and 2-propanol (2:3:3). The mixture was sonicated at ambient temperature for 1 h. A certain amount of catalyst ink was deposited on a carbon fiber paper disk (0.24 cm^2) to provide 2.0 mg cm^{-2} of catalyst metal anode electrodes. An electrode was coated with 30% by mass Nafion solution (5%) and allowed to dry overnight in a fume hood at ambient temperature.

2.4. 5 cm^2 PEMEC

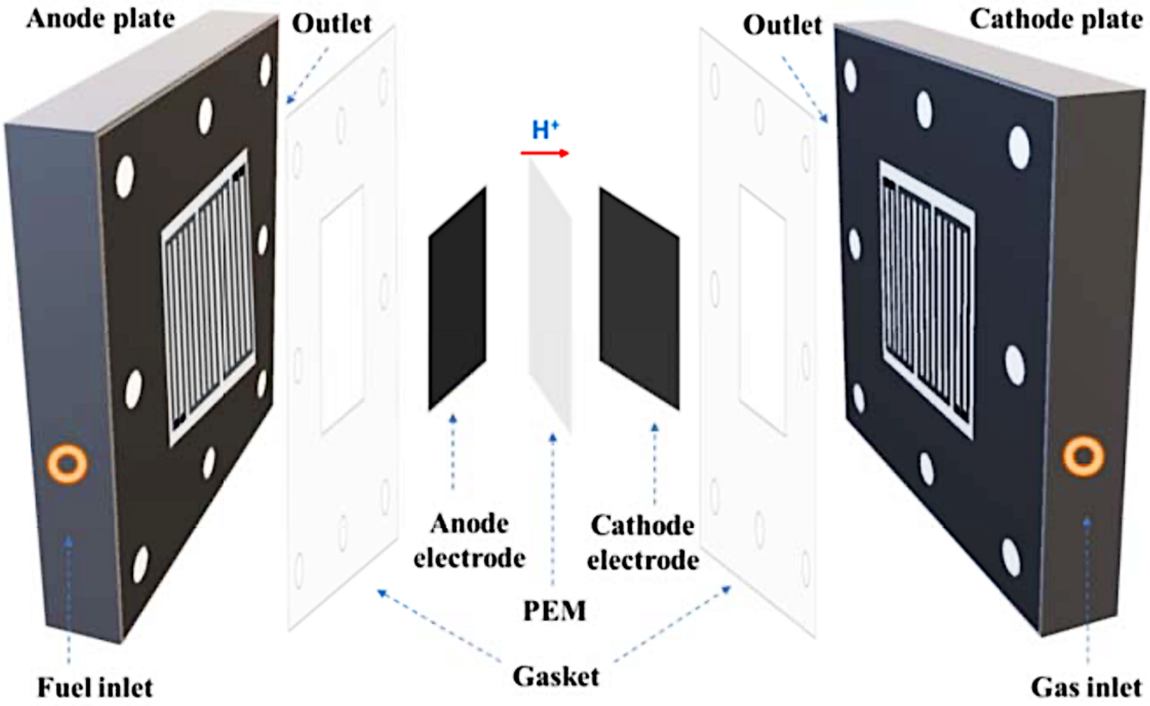

Figure 2.3. Schematic diagram of 5 cm^2 PEMEC operating in normal mode, reprinted from (6). Permission is granted by the main author.

Commercial fuel cell hardware (Fuel Cell Technology Inc.) was used for all types of PEMEC measurements. As a fuel cell-like condition, the cell operated in normal mode. The cathode was purged of 30 mL min^{-1} N_2, and the anode was pumped with 0.5 mL min^{-1} fuel. This cell was mainly used to study the catalytic activity of the prepared catalysts for ethanol oxidation. The cell was operated with a Hokuto Denko HA-301 potentiostat. In this study, polarization curves were measured using a potential range from 0 V to 0.70 V. Currents were averaged for 100 s and plotted against potential.

Anodes for 5 cm^2 PEMEC were prepared by suspending the catalyst in a mixture of deionized water, 2-propanol, and 1-propanol (2:3:3). After that, the ink was sonicated with Nafion solution (30% by mass) for another 1 h. The catalyst was spread on Toray carbon fiber paper cut to 5 cm^2 and dried overnight at ambient temperature. In Figure 2.3, one can see the 5 cm^2 PEMEC components and how it was connected. Pt black was used as the cathode electrode, and Nafion-117 membrane was used as the PEM. Gas leaks were sealed with gaskets with 5 cm^2 holes. The anode was first washed with DI water for at least 12 h then tested for ethanol oxidation. The potential was held at 0.70 V for 1 h before measuring each polarization curve, and the third data set is reported.

2.5. CO_2 measurements

Products from EOR were collected from the anode and cathode outlets of PEMEC in a trap. An NDIR CO_2 sensor (Telaire T6615 Series) operated with eCO_2View software was used for monitoring the CO_2, as shown in Figure 2.4. In 9-anode PEMEC, we only measure CO_2 at 0.50 V, whereas at 5 cm^2 PEMEC, we measure at a potential range of 0.30 - 0.70 V. The N_2 carrier gas flow rate was increased to 50 mL min^{-1} to flush gaseous products into the trap. It is important to monitor the CO_2 until the sensor measures a constant value. After applying constant potential, it takes around 8 min for the CO_2 concentration to reach a steady state.

Figure 2.4. The NDIR CO_2 sensor.

2.5.1. Calibration of the CO_2 sensor

The CO_2 sensor was calibrated by comparing the measured CO_2 from methanol oxidation with the expected CO_2 (f_{CO_2}) generated from the measured current at a given potential, using the Faraday law eq. 2.1 (7).

$$f_{CO_2} = \left(\frac{1\ CO_2 molecule}{6\ electrons}\right)\frac{I * V_m}{F * \upsilon_{N_2}} \qquad (2.1)$$

where, I is the measured current, V_m is the molar gas volume (22.4 L mol^{-1} at STP), F is the Faraday constant, and υ_{N_2} is the volume flow rate of N_2 (50 mL min^{-1}). A calibration curve measured with the 9-anode cell with 0.1 M methanol flowing from the cathode at 0.2 mL min^{-1} and N_2 at 50 mL min^{-1} is shown in Figure 2.5. The value, and validity, of this calibration method is established in Chapter 3.

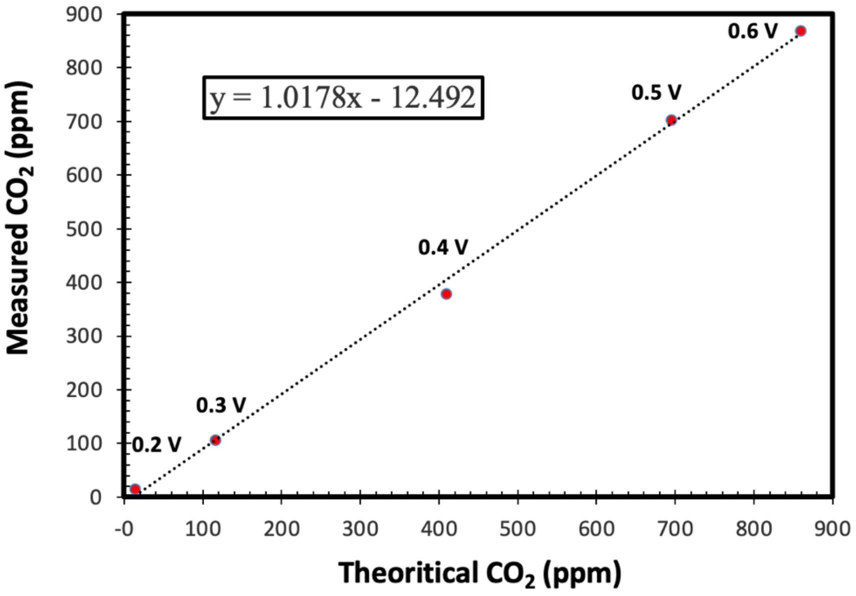

Figure 2.5. A calibration curve for the CO_2 sensor based on methanol oxidation at the three Ru@Pt electrodes of different compositions at 80 °C and different potentials.

2.5.2. CO_2 faradaic yield calculation

The faradaic yield of CO_2 (F_{CO_2}) from EOR in a PEMEC was calculated by dividing the measured CO_2, after subtracting the background and applying the calibration curve, by the maximum CO_2 generated (eq. 2.2). The maximum CO_2 is calculated using Faraday law (eq. 2.3), in which we assumed that the measured current (I) is generated from the complete oxidation of ethanol, where V_m is the molar gas volume (22.4 L mol^{-1} at STP), F is the Faraday constant, and υ_{N_2} is the volume flow rate of N_2 (50 mL min^{-1}).

$$F_{CO_2} = \frac{measured\ CO_2 (ppm)}{maximum\ CO_2\ (ppm)} * 100 \qquad (2.2)$$

$$Maximum\ CO_2 = (\frac{2\ CO_2 molecule}{12\ electrons}) \frac{I * V_m}{F * \upsilon_{N_2}} \qquad (2.3)$$

Minor corrections, based on the CO_2 yield for methanol oxidation at the same potential were made to account for any drift of the detector, as described in Chapter 3.

2.6. References

1. L. Napoli, M. Lavorante, J. Franco, A. Sanguinetti and H. Fasoli, Journal of New Materials for Electrochemical Systems, **16**, 151-156 (2013).
2. A.H. Ali and P.G. Pickup, Journal of the Electrochemical Society, **169**, 034523 (2022).
3. A.H. Ali and P.G. Pickup, ECS Advances, **2**, 024501 (2023).
4. T.M. Brueckner, E. Wheeler, B. Chen, E.N.E. Sawy and P.G. Pickup, Journal of the Electrochemical Society, **166**, F942-F948 (2019).
5. T.M. Brueckner and P.G. Pickup, Journal of the Electrochemical Society, **164**, F1172-F1178 (2017).
6. H. Hang, Support effects of metal oxides prepared by thermal decomposition on anode catalysts for direct ethanol fuel cells, in Chemistry, Faculty of science, Memorial University of Newfoundland (2022).
7. Q. Wan, Q. He, Y. Zhang, L. Zhang, J. Li, J. Hou, X. Zhuang, C. Ke and J. Zhang, Electrochimica Acta, **392**, 139023 (2021).

Chapter 3: Electrolysis of ethanol and methanol at PtRu@Pt catalyst

This Chapter has been published as:

Ali, A. H., and Pickup, P. G. (2022). Electrolysis of Ethanol and Methanol at PtRu@ Pt Catalysts. Journal of the Electrochemical Society, *169*(3), 034523.

The raw data are provided in Appendix A.

The main Principal author (Ahmed H Ali) contributed to all parts of this project, including the literature review, designing, and conducting all experiments, measuring, and analyzing the majority of results, and writing the publication.

The corresponding author (Peter G. Pickup) was responsible for funding, reviewing all my data analysis, writing the first draft of the manuscript, and completing it for submission.

3.1. Introduction

Electrolysis of organic fuels has attracted considerable attention as a method for generating hydrogen and value added chemicals from renewable resources (1-3), and in particular for generation of renewable hydrogen from bioethanol (2, 4-7). Cells with proton exchange membranes (PEM) such a Nafion™ are generally employed, with operating temperatures of typically 50-80 °C. The main challenge in the development of this technology is the activity and selectivity of the anode catalyst, which is also a major challenge in the development of direct organic (liquid) fuel cells (8). For ethanol oxidation, for example, Pt does not provide sufficient activity at low potentials and so its voltage efficiency is too low, while the faradaic efficiency (fuel efficiency) of PtRu is too low because it produces acetic acid as the main product (9). There are no reports of catalysts that have been shown to provide both high voltage and high faradaic efficiency in ethanol electrolysis or fuel cells.

The key difference between organic fuel cells and electrolysis cells is the cathode reaction, which is hydrogen evolution or oxygen reduction, respectively. Consequently, the study of anode catalysts in electrolysis cells also provides the knowledge required for developing better catalysts for fuel cells. In fact, the use of an electrolysis cell is preferable for characterization of anodes for fuel cells because it avoids errors in electrode potentials and product distributions that arise from the chemical reaction of the fuel with oxygen (10, 11).

Core shell nanoparticles in which a Pt shell is deposited onto a more electropositive core (M@Pt) are attractive catalysts for the oxidation of organic fuels in electrolysis cells and fuel cells because the core metal can be used to tune activity while reducing the amount of Pt that is required (12, 13). Ru@Pt catalysts are particularly attractive for the electrochemical oxidation of methanol

(14-21) and ethanol (18-20, 22-27) due to the electronic (ligand) effect of the Ru core, lattice strain, and the bifunctional (Langmuir–Hinshelwood) effect of surface oxides (19, 22, 23, 28, 29).

Despite their potential for improving performance and durability (30), the implementation of Ru@Pt catalysts in methanol and ethanol electrolysis and fuel cells has received little attention, with RuPt alloys still being most widely employed (8, 25). The first reported use of Ru@Pt in a direct methanol fuel cell employed a phosphoric acid doped PBI polybenzimidazole membrane (31). Although measurements in aqueous sulfuric acid showed significant improvements over Pt/C for concentrated methanol solutions at high temperatures and potentials, polarization curves in the fuel cell at 150 °C were not significantly different for Ru@Pt and Pt catalysts. In contrast, Ru@Pt nanoparticles with a 1.5 monolayer Pt shell were shown to greatly outperform both Pt and PtRu alloy catalysts in a PEM cell with a Nafion membrane (32). A Ru@Pt catalyst has also been shown to provide higher activity than Pt for methanol and ethanol oxidation at 80 °C in a PEMEC (26, 27).

From the limited data that is available, it is difficult to assess whether Ru@Pt catalysts provide significant benefits over PtRu alloy catalysts. To determine this, it is important to compare similar materials, and ensure that the baseline PtRu catalyst is representative of state-of-the-art commercial catalysts. Consequently, we report here on a systematic study of the effects of depositing Pt shells of varying thickness onto a high performance commercial, carbon supported PtRu alloy catalyst. In this way, modulation of the activity, and selectivity can be clearly attributed to the Pt shell, without significantly changing the nature of the catalyst in other ways.

Pt shells were deposited onto the commercial PtRu catalyst using ethylene glycol as the solvent and reductant (polyol method), without a stabilizing agent. Following characterization and cyclic voltammetry in aqueous sulfuric acid, the PtRu@Pt catalysts were evaluated for methanol and ethanol oxidation in a PEMEC at 80 °C.

3.2. Experimental

3.2.1. Materials

Methanol (HPLC Grade; Fisher Scientific), anhydrous ethanol (99.9%; Commercial Alcohols Inc.), sulfuric acid (Fisher Scientific), ethylene glycol (ACP), 5% Nafion^{TM} solution (Dupont), 1-propanol (J.T. Baker), 2-propanol (Caledon), dihydrogen hexachloroplatinate(IV) hexahydrate (Pressure Chemical Co.), and commercial 70% Pt on a high surface area advanced carbon support (Alfa Aesar), were used as received. All aqueous solutions were prepared using distilled and deionized water. The carbon supported PtRu alloy catalyst was HiSPEC® 12100, 50% Pt and 25% Ru on a high surface area advanced carbon support (Alfa Aesar).

3.2.2. Synthesis of the PtRu@Pt catalysts

Carbon supported PtRu@Pt catalysts were prepared using a polyol method as follows: The commercial PtRu catalyst (66.7 mg) was dispersed in 40 mL of pre-heated ethylene glycol and then the required amount of $H_2PtCl_6.6H_2O$ in ethylene glycol (10 mL) was added. The mixture was heated gradually to 185 °C and allowed to reflux for 2 h under stirring. The product was collected using a centrifuge, washed with hot deionized water several times, and dried in an oven at 80 °C for 8 h.

It should be noted that these PtRu@Pt core-shell nanoparticles were prepared without using any stabilizer agents, which avoids contamination of the catalyst surface. It was found that Pt was deposited preferentially onto the carbon supported PtRu nanoparticles, rather than as discrete Pt nanoparticles.

3.2.3. Analytical methods

Metal percentages were determined by using a TA Instruments Q500 thermogravimetric analyser (TGA) with a temperature ramp of 20 °C min^{-1} under an air atmosphere. An energy dispersive X-ray analyzer (EDX) attached to a FEI Quanta 400 scanning electron microscope (SEM) was used to determine Pt:Ru ratios. A Rigaku Ultima IV X-ray diffractometer (XRD), with a Cu K_α (0.154 nm) X-ray source and scintillation counter detector, was used to investigate the crystal structures of the catalysts. The electronic properties of the catalysts and their surface chemical states were measured by X-ray photoelectron spectroscopy (XPS) using a VG Micro-tech Multi-lab ESCA 2000 system at Dalhousie University (Halifax, Nova Scotia, Canada) by Andrew George. A Tecnai™ Spirit Transmission Electron Microscope (TEM) was used to investigate the dispersion of the metal nanoparticles on the carbon support and measure particle sizes.

3.2.4. Electrochemistry at ambient temperature in aqueous H_2SO_4

Cyclic voltammetry (CV) was performed in a three-electrode glass cell using a Biologic SP-50 potentiostat operated with EC-lab software. Carbon fiber paper (CFP, Toray TGP-H-090, 0.24 cm^2) working electrodes were used with a platinum wire auxiliary electrode and SCE reference electrode. Before use, the CFP was sprayed with an ethanol dispersion of Vulcan XC-72 carbon black (CB, 1.0 mg cm^{-2}, Cabot Corp.) to provide a support layer to improve utilization of the catalyst (CB/CFP). Desired volumes of catalyst inks were painted onto the CB/CFP to give metal loadings of 0.3 mg cm^{-2}, and left to dry overnight. Catalyst inks were prepared by dispersing 2.0 mg of catalyst in 60 μL of H_2O, 75 μL of 2-propanol and 75 μL of 1-propanol by sonication for 1 h.

Background CVs were recorded in 1 M H_2SO_4 which was first purged with ultra-high purity N_2 for at least 15 min. The alcohol was then added to give a 0.1 M solution, which was then purged with N_2 for at least 5 min before recording CVs for its oxidation. Background CVs were recorded from -0.25 V to 0.80 V (vs SCE) at a scan rate of 100 mV s^{-1} for 6 cycles, while CVs for oxidation of the alcohols were from -0.25 V to 0.80 V at a scan rate 10 mV s^{-1} for 4 cycles. The 3rd cyclic voltammogram has been shown in all cases.

3.2.5. Methanol and ethanol oxidation in a PEMEC

A commercial (ElectroChem Inc.) PEMFC, with a 5 cm^2 Pt black cathode and a Nafion-117 proton conducting membrane electrolyte, was modified to accommodate nine separate 0.24 cm^2 anodes as previously described (33). It was operated as an electrolysis cell, in crossover mode (33) at 80 °C, with 0.1 M aqueous methanol or ethanol pumped through the cathode flow field at 0.5 mL min^{-1} while the anode flow field was purged with nitrogen gas (10 mL min^{-1}).

The anodes were 0.24 cm^2 carbon fiber paper discs (TGP-H-090) coated with a catalyst ink (in a 2:3:3 mixture of deionized water, 1-propanol and 2-propanol) to give a metal loading of 2.0 mg cm^{-2}. The required volume of 5% Nafion solution was applied to the surface of each anode to give a Nafion loading of 30% by mass.

The potentials of the anodes (relative to the cathode) were controlled with a MSTAT potentiostat from Arbin Instruments. In the crossover mode employed, the fuel (methanol or ethanol) diffuses through the cathode and membrane and is oxidized at the anodes, while the cathode produces hydrogen. Potentials are referenced to the cathode, which acts as a dynamic hydrogen electrode (DHE). Polarization curves show the average current over 60 s, following a 120 s delay at each potential, starting at 0.90 V vs DHE. Prior to collection of the reported data, the cell was operated at 0.70 V for 1 h to activate the membrane and electrodes. Firstly, the cell was operated using 0.1 M methanol and the 4th polarization curve is shown. Then, the fuel was switched to 0.1 M ethanol and the 2nd polarization curve is shown.

Subsequently, faradaic yields for CO_2 formation were determined by operating the cell at 0.50 V for 10 min while CO_2 exiting the anode flow field was monitored with a nondispersive infrared CO_2 sensor (Telaire T6615 CO_2 Sensor Module) (34). Also, the N_2 flow rate was increased to 50 mL min^{-1}, while the alcohol flow rate was decreased to 0.2 mL min^{-1}.

3.3. Results and discussion

3.3.1. Characterization of the catalysts

The compositions of the catalysts were determined by using energy dispersive X-ray spectroscopy (EDX) to obtain the Pt:Ru ratio and thermogravimetric analysis to determine the metal loading on the carbon support. Target compositions and the measured values are given in Table 3.1. The formulas for the catalysts, PtRu@Pt_x, are based on the target compositions, where x is the atomic ratio of the Pt shell to Ru (or Pt) in the core. Consequently, the Pt:Ru ratio is $1+x$:1.

The Pt:Ru ratio measured for PtRu catalyst is in reasonable agreement with the expected (target) value for the nominal 2:1 mass ratio specified by the supplier, and the measured ratio for PtRu@$Pt_{0.3}$ is in excellent agreement with the target value. It is clear that a significant amount of Pt had been deposited on the PtRu catalyst, although the accuracy/precision of EDX is insufficient to determine whether quantitative deposition of the Pt was achieved. For the other PtRu@Pt catalysts, EDX indicated that there was more Pt than used in the synthesis. Since this is not feasible, it can be attributed to the absorption of the electron beam by the Pt shell, which results in decreased excitation of atoms in the core, and absorption of Ru X-rays generated in the core by the Pt shell.

The total metal (Pt+Ru) loadings determined by TGA are in good agreement with the expected values based on the target Pt:Ru ratios, rather than the values from EDX. Together, these observations provide good evidence that the Pt was deposited onto the PtRu nanoparticles to form core-shell structures.

Table 3.1. Target and measured compositions of the catalysts.

catalyst	Pt:Ru atomic ratio		Pt+Ru mass %	
	target	from EDX	expected[a]	from TGA
PtRu	1.00	1.08	75	80.1
PtRu@Pt$_{0.3}$	1.28	1.29	82.7	83.7
PtRu@Pt$_{0.6}$	1.57	1.85	84.7	85.6
PtRu@Pt$_{1.2}$	2.18	2.58	87.7	88.5
PtRu@Pt$_{1.4}$	2.40	2.77	88.6	89.3
PtRu@Pt$_{1.7}$	2.70	3.23	89.5	90.4

a. The expected Pt+Ru mass % for the PtRu@Pt catalysts is based on the measured value (80.1%) for the PtRu catalyst.

Figure 3.1 shows XRD patterns for the commercial PtRu catalyst and PtRu@Pt catalysts. It can be seen that deposition of Pt onto the PtRu nanoparticles shifted the positions of the peaks from the positions for the PtRu alloy, which are between the values for pure Pt and pure Ru, towards the lower values for pure Pt. This confirms that the Pt was deposited onto the PtRu nanoparticle, rather than being deposited as separate Pt particles. This is also confirmed by the sharpening of the peaks, which indicates that the PtRu@Pt particles increased in size as more Pt was deposited.

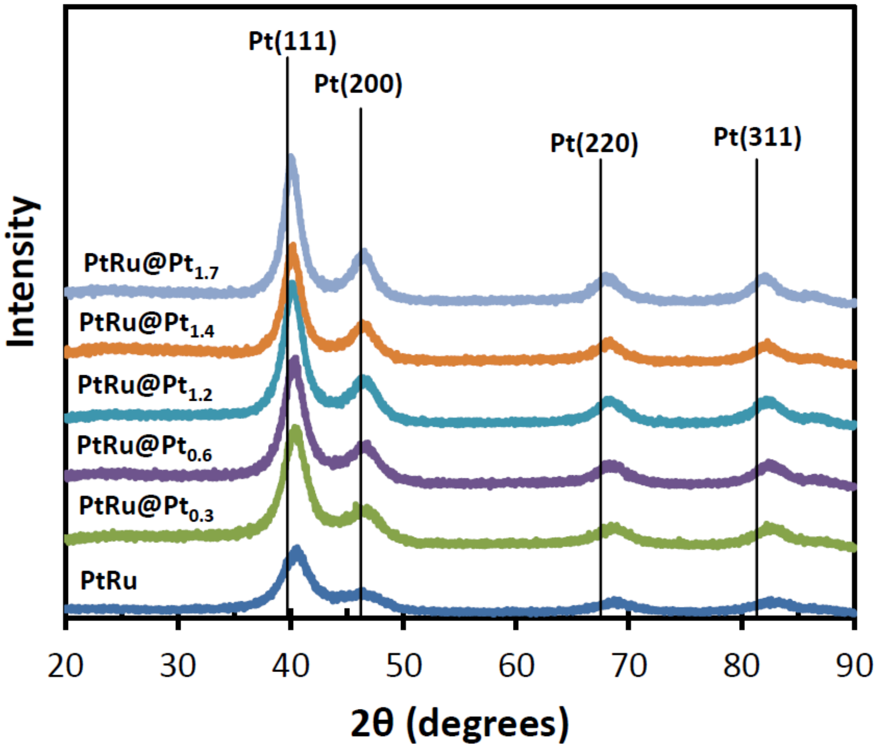

Figure 3.1. XRD patterns for the commercial PtRu catalyst and PtRu@Pt catalysts prepared by deposition of Pt shells onto the PtRu nanoparticles. The vertical lines show the positions of the peaks for pure Pt.

TEM images, provided in Appendix A as Figures A1-A5, show that the PtRu and PtRu@Pt nanoparticles were well dispersed on the carbon support. As shown in Table 3.2, the average diameter (d) of the metal particles increased as the Pt content was increased, and there is a reasonable correlation with the expected increases calculated by using equation 3.1(35),

$$d = d_c \sqrt[3]{(n_{Pt} + n_c)/n_c} \qquad (3.1)$$

where d_c is the diameter of the PtRu core, n_c is the number of atoms in the core, and n_{Pt} is the number of Pt atoms in the shell. This also allows estimation of the thickness of the Pt shell (36), which is given in monolayers of Pt in Table 3.2.

Table 3.2. Number of Pt monolayers and expected particle diameters calculated from the target compositions, and average particle sizes measured by TEM. Sizes were determined from the images in Figures A1-A5, plus two other images for each catalyst.

catalyst	Calculated monolayers of Pt	Average particle diameter (nm)	
		expected	from TEM
PtRu	0	2.7	2.6±0.4
PtRu@$Pt_{0.3}$	0.23	2.8	2.8±0.4
PtRu@$Pt_{0.6}$	0.44	2.9	2.9±0.4
PtRu@$Pt_{1.2}$	0.81	3.1	3.0±0.4
PtRu@$Pt_{1.4}$	0.95	3.2	3.5±0.5
PtRu@$Pt_{1.7}$	1.10	3.3	3.8±0.5

XPS of the original PtRu catalyst and two of the PtRu@Pt catalysts was used to investigate the distribution of the deposited Pt, and to probe electronic effects. Spectra were very similar for all three samples (Figure 3.2), with the most significant differences being seen in the measured Ru:Pt ratios (Table 3.3). The ratio of 1.17 obtained for the unmodified catalyst was somewhat higher than the expected 1:1 ratio, suggesting that there was some accumulation of Ru at the surface of the PtRu alloy nanoparticles. Addition of 0.6 equivalents of Pt (0.44 monolayers), resulted in a much larger decrease in the Ru:Pt ratio than expected for an alloy of the same composition. Since XPS is more sensitive to surface species, this indicates that the Pt was deposited on the surface of the PtRu particles (i.e. the Ru photoelectrons were absorbed by a Pt overlayer). An alternative catalyst structure, with discrete PtRu and Pt nanoparticles is ruled out by the low measured Ru:Pt ratio. Deposition of additional Pt decreased the measured Ru:Pt ratio further and increased the discrepancy with the ratio expected for an alloy, as expected for a core-shell structure.

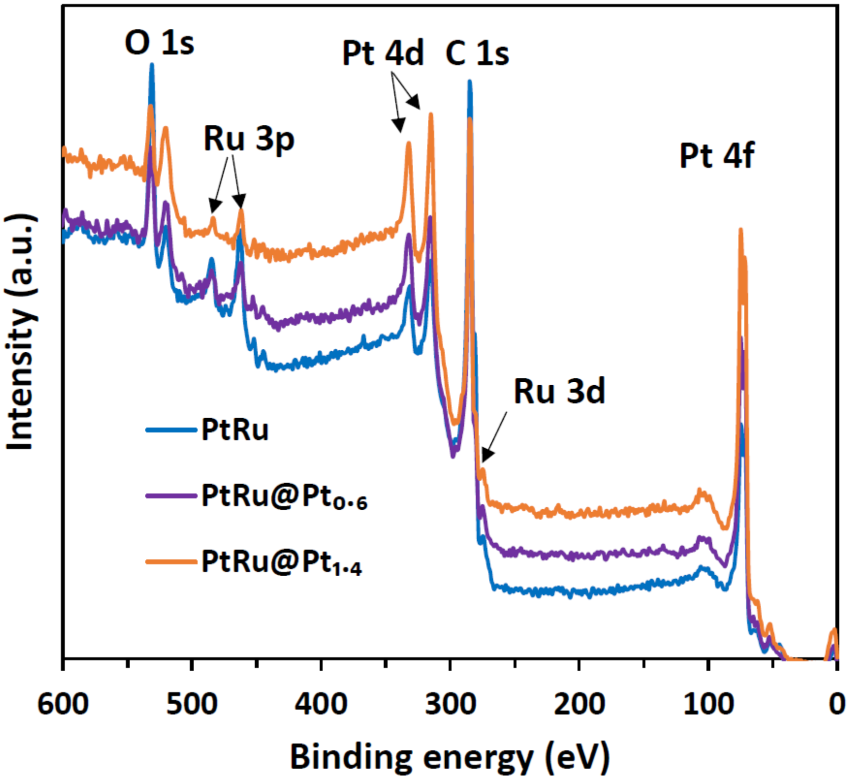

Figure 3.2. XPS spectra of the PtRu, PtRu@$Pt_{0.6}$ and PtRu@$Pt_{1.4}$ catalysts.

Interestingly, addition of Pt to the surface of the PtRu nanoparticles did not result in a significant change in the Pt 4f binding energies (Table 3.3). This is important because the electronic and strain effects of Ru in the PtRu alloy lower the energy of the d-band center and increase the Pt 4f binding energies relative to pure Pt (37, 38). This weakens the adsorption of CO, which is a significant factor in the enhanced activities for methanol and ethanol oxidation at PtRu alloys relative to Pt.

The O 1s region of the XPS, expanded in Figure 3.3, shows distinct changes as Pt was added to the PtRu core. Binding energies obtained from deconvolution of the peaks, as shown in Figures A6-A8, are summarized in Table 3.4. The PtRu catalyst gave a broad peak at 531.00 eV that could be deconvoluted into components at 529.63 eV, 530.73 eV, and 532.18, that are characteristic of O^{2-}, OH^- and H_2O species, respectively, at oxidized Ru sites (e.g. 529.40 eV, 530.80 eV, and 532.40 eV for hydrous Ru oxide (39)). However, the 532.18 eV component can be attributed primarily to oxygen species on the carbon support (40).

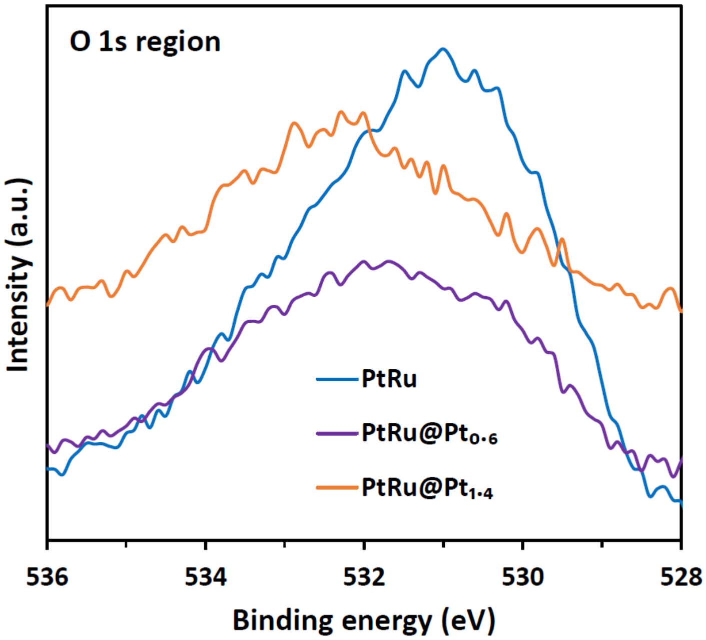

Figure 3.3. O 1s region of the XPS spectra of the PtRu, PtRu@$Pt_{0.6}$ and PtRu@$Pt_{1.4}$ catalysts.

Table 3.3. Ru:Pt atomic ratios and Pt $4f_{5/2}$ binding energies from XPS, and expected Ru:Pt ratios based on the target compositions.

catalyst	Ru:Pt atomic ratio		Pt $4f_{5/2}$ ($4f_{7/2}$) binding energy (eV)
	measured	expected	
PtRu	1.17	1.0	74.17 (70.84)
PtRu@$Pt_{0.6}$	0.36	0.62	74.27 (70.92)
PtRu@$Pt_{1.4}$	0.19	0.41	74.19 (70.84)

Table 3.4. O 1s binding energies from the deconvoluted spectra (Figures A6-A8) for PtRu, $PtRu@Pt_{0.6}$ and $PtRu@Pt_{1.4}$.

catalyst	O 1s binding energy/eV and (relative area)		
	$-O^{2-}$	$-OH^{-}$	$-H_2O$/C-O
PtRu	529.63 (10%)	530.73 (32%)	532.18 (58%)
$PtRu@Pt_{0.6}$	530.18 (27%)	531.57 (14%)	532.73 (59%)
$PtRu@Pt_{1.4}$	530.06 (7%)	absent	532.36 (93%)

Peaks at similar, but slightly higher binding energies were observed for $PtRu@Pt_{0.6}$, indicating that the same Ru-oxy species were present and suggesting that there was some electron donation to the added Pt layer. This electronic effect may also explain the increase in the area under the $Ru\text{-}O^{2-}$ component relative to $Ru\text{-}OH^{-}$.

In contrast, the $Ru\text{-}OH^{-}$ component was absent for $PtRu@Pt_{1.4}$ and the 530.06 eV component was very small, and can be attributed to Pt-O (40). The O 1s region was dominated by a single peak at 532.36 eV due to oxygen species on the carbon support. These observations provide strong evidence that the Pt coverage for $PtRu@Pt_{0.6}$ was sub-monolayer, while the surface Ru had been completely covered for $PtRu@Pt_{1.4}$, as expected based on the estimated Pt coverages of 0.44 and 0.95 monolayer, respectively (Table 3.2).

Cyclic voltammograms of the PtRu@Pt catalysts in aqueous H_2SO_4 are shown in Figure 3.4, together with voltammograms of the PtRu precursor, and a similar commercial Pt catalyst. Since a constant metal loading (0.3 mg cm^{-2} of Ru+Pt) was employed, and the PtRu@Pt nanoparticles increase in size with increasing Pt coverage, the main trend is for the currents to decrease with increasing Pt coverage, due to the decreasing area/mass ratio. However, it can also be seen that the peaks below 0 V, which are due to hydrogen underpotential deposition and reoxidation, became much more pronounced as the Pt shell was added. Their shape also changed, with distinct waves appearing at ca. –0.10 V and –0.20 V that are characteristic of the pure Pt surface seen for the Pt catalyst in Figure 3.4.

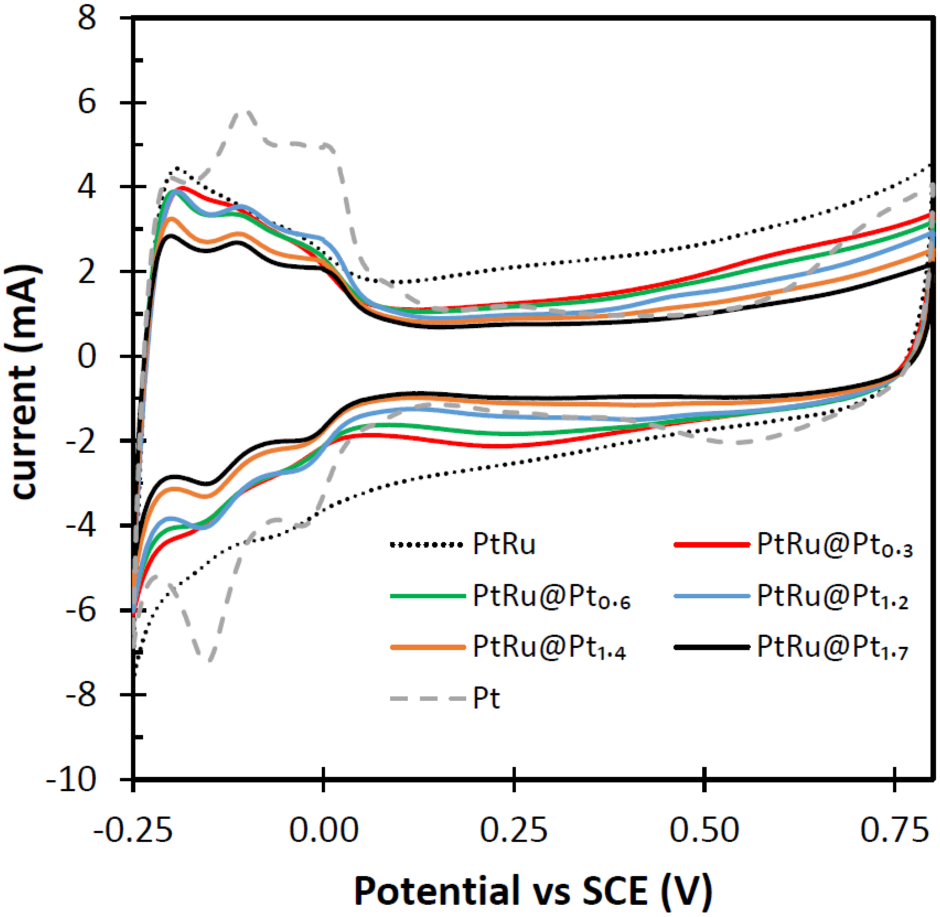

Figure 3.4. Cyclic voltammetry (100 mV s^{-1}) of PtRu, PtRu@Pt and Pt catalysts on CB/CFP electrodes in 1 M H_2SO_4 at ambient temperature. A constant metal loading of 0.3 mg cm^{-2} was used.

In addition, the large pseudo-capacitance due to surface Ru oxide, at potentials above ca. 0 V, diminished rapidly and became insignificant at the highest Pt coverage. Indeed, the height of the broad cathodic peak at ca. 0.25 V has been shown to provide a useful measure of the coverage of Pt on Ru nanoparticles (41). Its disappearance here at ca. 1 monolayer of Pt (PtRu@$Pt_{1.4}$) provides strong evidence that the Pt coverages provided in Table 3.2 are reasonable.

Finally, it is important to note that the oxide regions of the voltammograms for the PtRu@Pt catalysts do not show significant features in the 0.55 to 0.80 V region where an anodic shoulder and cathodic peak, due to Pt-OH formation and reduction, can be seen for the Pt catalyst. This indicates that the electronic and/or strain effects of the PtRu core exerts a significant effect on the Pt reactivity which persists at the highest Pt coverages employed. A similar suppression of the Pt oxidation waves can be seen in voltammograms of Ru@Pt core-shell nanoparticles (41).

3.3.2. Methanol oxidation in aqueous H_2SO_4

Figure 3.5 shows voltammograms for the oxidation of methanol at the PtRu, PtRu@Pt and Pt catalysts. Deposition of Pt onto the PtRu catalyst greatly increased its activity for methanol oxidation at all coverages, with relatively minor differences for coverages up to ca. 1 monolayer (PtRu@$Pt_{1.4}$). Optimum performance was obtained for PtRu@$Pt_{1.2}$, which produced the lowest half-wave potential and maximum peak current.

At higher Pt coverages, the half-wave and peak potentials shifted to higher potentials, and at 1.1 monolayers of added Pt the peak potential was closer to that of Pt than PtRu. This loss of low potential activity with increasing Pt coverage can be attributed to the loss of the bifunctional effect of surface Ru oxide as well as weakening of the electronic and strain effects of Ru in the PtRu core (19, 27).

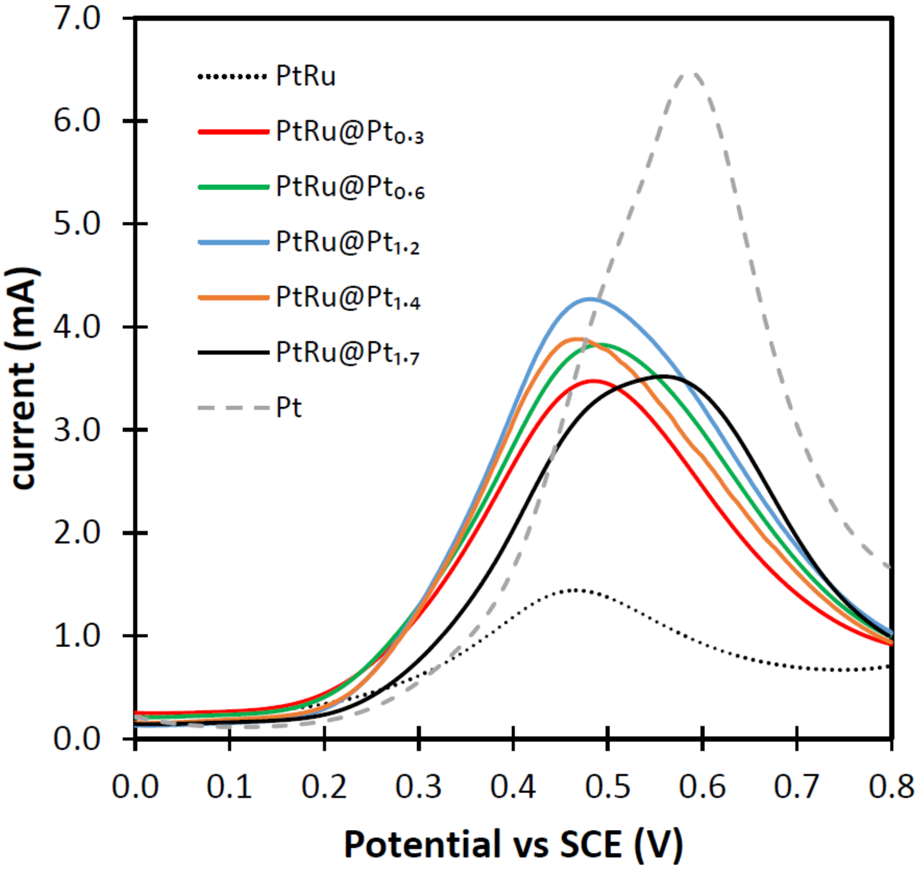

Figure 3.5. Linear sweep voltammetry (10 mV s^{-1}) of PtRu, PtRu@Pt, Pt catalysts on CB/CFP electrodes in 1 M H_2SO_4 + 0.1 M methanol at ambient temperature. A constant metal loading of 0.3 mg cm^{-2} was used.

Peak potentials for the PtRu@Pt catalysts with less than one monolayer of added Pt vary between 0.46 and 0.50 V vs SCE (ca. 0.70 V vs RHE), which is similar to the peak potential reported for methanol oxidation under similar conditions at a Ru@Pt catalyst with 0.1 monolayer of Pt. However, in that work, increasing the Pt coverage to increase the peak current produced a significant positive shift of the peak potential (e.g. to ca. 0.85 V vs RHE at 0.82 monolayer). Increasing the Pt coverage is crucial for optimizing activity because Ru sites are inactive for methanol oxidation, and the formation of larger ensembles of adjacent Pt atoms greatly increases the rate of methanol oxidation (42). Indeed, an increase in activity of Ru@Pt catalysts with increasing Pt coverage from 0.1 to 1.1 monolayer has been attributed to the increasing size of Pt islands on the Ru surface (19).

In light of these considerations, the observation in Figure 3.5 that the surface of PtRu nanoparticles can be completely covered with Pt (note that there is already Pt at the surface and so less than 1 additional monolayer is required), without increasing the peak potential for methanol oxidation is remarkable, and important for a number of reasons. Firstly, it indicates that the PtRu core employed here provides a better balance of bifunctional, electronic and strain effects than the Ru core employed in ref. (19). Secondly, since PtRu@Pt catalysts can provide much higher activities at lower potentials than the underlying PtRu alloy, the bifunctional effect is not a key requirement for optimum performance. Thirdly, a pure (or predominantly) Pt surface can potentially provide advantages in terms of durability (preventing loss of Ru) (30) and selectivity (9). Selectivity for complete oxidation is a crucial issue for higher alcohols and may also be a concern for methanol oxidation under some circumstances, particularly when the catalyst loading needs to be decreased to reduce costs.

3.3.3. Ethanol oxidation in aqueous H_2SO_4

Figure 3.6 shows linear sweep voltammograms for the oxidation of ethanol at the PtRu, PtRu@Pt, and Pt catalysts. Here the influence of adding Pt to the PtRu catalyst surface is more complicated than for methanol oxidation. Although the general trend is also an increase in activity with increasing Pt coverage, with optimum activity for the PtRu@$Pt_{1.2}$ catalyst, there are anomalies such as the small decrease in activity from PtRu@$Pt_{0.3}$ to PtRu@$Pt_{0.6}$, and the increase in activity from PtRu@$Pt_{1.2}$ to PtRu@$Pt_{1.4}$. Although these appear to be random, they are much larger than the variation between different electrodes prepared with the same catalyst. In addition, such anomalies were not observed for methanol oxidation (Figure 3.5) or in the absence of ethanol (Figure 3.4). In fact, the PtRu@Pt$_{1.2}$ catalyst was one of the most active in those experiments while it was one of the least active for ethanol oxidation.

The apparent anomalies in Figure 3.6 presumably arises from the complexity of the ethanol oxidation reaction, which involves multiple pathways, and three different major products with different numbers of electrons transferred (n); acetaldehyde (n = 2), acetic acid (n = 4) and CO_2 (n = 12) (43, 44). The relative rates of the pathways to these products are potential dependent (45) and for the PtRu@Pt catalysts employed here will depend differently on the coverage of Pt on the PtRu. Adding Pt will decrease the bifunctional, electronic, and strain effects and favor different pathways as the balance of the effects on ethanol adsorption, CO formation, CO adsorption strength, and CO oxidation change (27).

Despite these complexities, it is clear from the data in Figure 3.6 that PtRu@Pt catalysts are particularly attractive for ethanol oxidation. Not only can they provide higher currents at low potentials (0.25 to 0.50 V) than the PtRu precursor, they also provide a pure (or predominantly) Pt surface that can increase selectivity for the complete oxidation to CO_2 (27). The existence of this effect on selectivity here is suggested by the second wave seen in the voltammograms, at ca. 0.64 V, which is close to the peak for ethanol oxidation at the Pt catalyst.

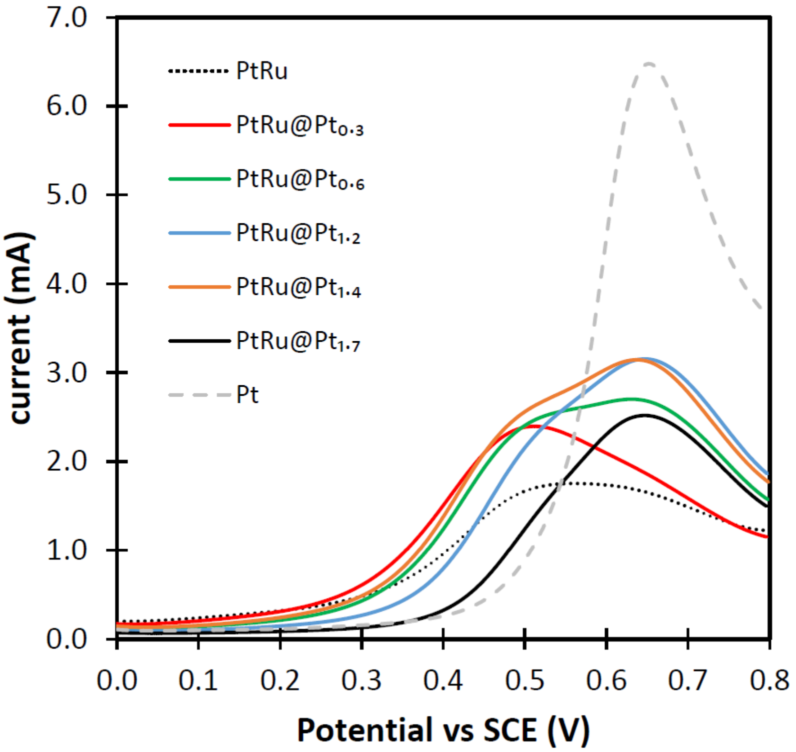

Figure 3.6. Linear sweep voltammetry (10 mV s^{-1}) of PtRu, PtRu@Pt, Pt catalysts on CB/CFP electrodes in 1 M H_2SO_4 + 0.1 M ethanol at ambient temperature. A constant metal loading of 0.3 mg cm^{-2} was used.

3.3.4. Methanol and ethanol oxidation in a PEMEC

Figure 3.7 shows polarization curves for electrolysis of 0.1 M methanol and 0.1 M ethanol at PtRu and PtRu@Pt anodes in a 9-anode PEM cell. In these experiments, methanol is oxidized to CO_2 at the anode, or ethanol is oxidized to a mixture of CO_2, acetic acid and acetaldehyde, while hydrogen is produced at the cathode. The crossover mode employed here, in which the methanol or ethanol diffuses through the polymer electrolyte membrane to the anode, provides the most useful way to study anode catalysts for application in both electrolysis and fuels cells (33). It provides data under steady state mass transport conditions, akin to the use of rotating disc voltammetry, and avoids the inaccuracies due to crossover effects and unstable/unknown cathode potentials that occur in fuel cells (46). Low concentrations were used in these experiments to increase the stoichiometry for ethanol oxidation since its complete oxidation is suppressed at higher concentrations (26). Maximizing the overall efficiency for ethanol oxidation requires limitation of the ethanol concentration at the catalyst surface. A comparison of the crossover mode of operation of the cell employed here with operation as a conventional electrolysis cell or a fuel cell is provided in ref. (46).

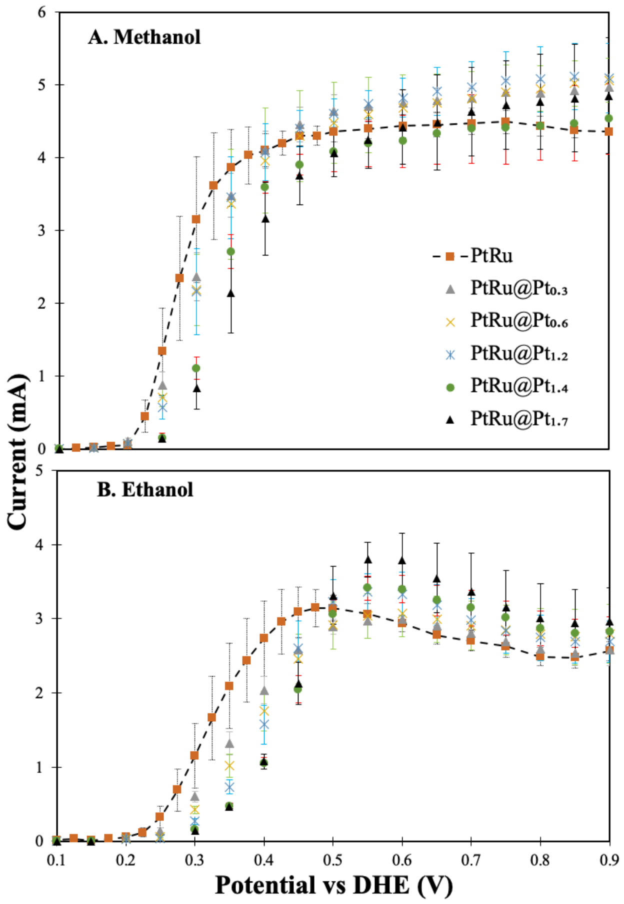

Figure 3.7. Polarization curves for the oxidation of 0.1 M methanol (A) and 0.1 M ethanol (B) at PtRu and PtRu@Pt catalysts on CFP electrodes, at 80 °C. A constant metal loading of 2.0 mg cm^{-2} was used.

For methanol oxidation (Figure 3.7A), the current densities at the PtRu and PtRu@Pt anodes reached a similar mass transport limited (33) current (i_{lim}) of ca. 4.5 mA (19 mA cm^{-2}) at high potentials. The half-wave potential, which is a measure of the reaction kinetics, was lowest (faster kinetics) for the PtRu anode and increased as Pt was added to the PtRu core. This is consistent with the much higher activity of PtRu for methanol oxidation relative to Pt at low potentials. However, it is notable that the activity was still very good with 0.81 monolayer of Pt added (PtRu@Pt$_{1.2}$), and this would be expected to produce a more durable catalyst (30).

For ethanol oxidation (Figure 3.7B), addition of Pt to the PtRu core had a more pronounced impact on the half-wave potential, and all of the polarization curves show a decrease in current with increasing potential in the mass transport limited region, following a peak at ca. 0.55 to 0.60 V. This decreasing current at high potentials is due to a potential dependence of the reaction stoichiometry (n; number of electrons transferred per ethanol molecule) (9). Whereas methanol oxidation consistently produces 6 electrons per molecule (n = 6) due to the complete oxidation to CO_2, the stoichiometry of ethanol oxidation depends on the relative rates of production of CO_2 (n = 12), acetic acid (n = 4), and acetaldehyde (n = 2). Consequently, it is possible to determine the stoichiometry of ethanol oxidation from the limiting currents observed in Figure 3.7B.

The limiting current is given by equation 3.2 (33),

$$i_{lim} = n_{av}FAmC \qquad (3.2)$$

where n_{av} is the product weighted average number of electrons transferred, A is the electrode area (0.24 cm^2), m is the mass transport coefficient (3.0×10^{-4} cm s^{-1} (33)), and C is the concentration of ethanol. At potentials above ca. 0.60 V, the electron transfer kinetics are so fast that the measured current can be taken to be i_{lim}, while at lower potentials the mass transport component needs to be separated from the kinetic component. This was accomplished as described in ref. (33)

by using the Tafel relationship to extrapolate the kinetic current from low potentials. Stoichiometries from this analysis are shown in Figure 3.8. Currents in the mass transport limited region are lower for ethanol than methanol because the stoichiometry (n_{av}) is lower in most cases, and the mass transport coefficient (m) is lower (33).

It is clear from the data in Figure 3.8, that adding a Pt shell to the PtRu can significantly increase the stoichiometry of ethanol oxidation. Whereas PtRu produces acetic acid (n = 4) as the main product (9), and the measured stoichiometry ranges between 3.6 to 4.6, the PtRu@$Pt_{1.7}$ catalyst transferred 6.1 electrons per ethanol molecule at 0.55 V. This indicates that PtRu@$Pt_{1.7}$ is much more selective for the complete oxidation to CO_2, which would increase fuel efficiency in an electrolysis cell (more efficient production of hydrogen) or fuel cell. It can be seen by comparing the data in Figure 3.7B and Figure 3.8 that the balance between activity (i.e. current and power density) and selectivity can be tuned by varying the thickness of the Pt shell.

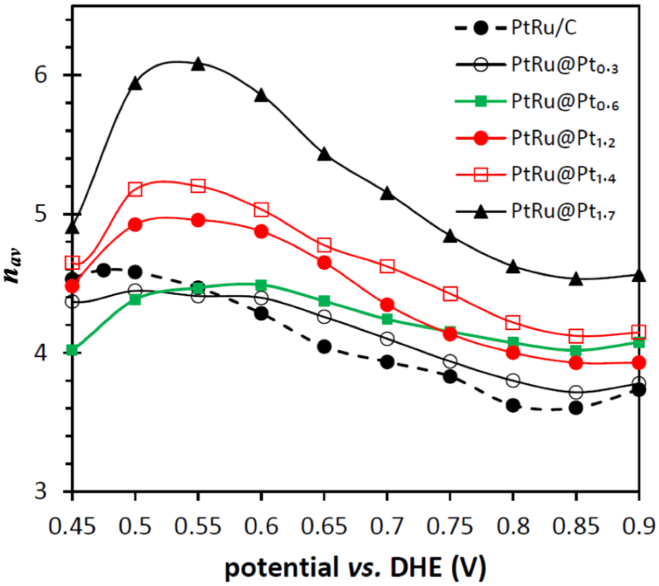

Figure 3.8. Stoichiometries (n_{av}) for the oxidation of 0.1 M ethanol at 80 °C determined from the polarization curve shown in Figure 3.7B.

Although the selectivity for complete oxidation of ethanol cannot be obtained from n alone, a range of possible values can be calculated by assuming either no acetic acid ($x_{acetic\ acid} = 0$) or no acetaldehyde ($x_{acetaldehyde} = 0$) is formed, by using equation 3.3,

$$n_{av} = \sum n_i x_i \qquad (3.3)$$

where n_i is the number of electrons transferred to form product i and x_i is the fraction of ethanol converted to product i. For the PtRu catalyst, the maximum n of 4.6 at 0.48 V corresponds to a chemical yield of CO_2 ($f_{\text{carbon dioxide}}$) in the range of 17±9%, while product analysis under the same conditions with a 5 cm^2 electrode has shown it to be 7% (9), which is not significantly different. In contrast, the PtRu@$Pt_{1.7}$ catalyst at 0.55 V produced a CO_2 yield in the range of 34±8%.

Table 3.5. Faradaic yields of CO_2 determined by monitoring CO_2 in the anode exhaust of a 9-anode PEM cell at 0.50 V vs DHE.

Catalyst	CO_2 yield (%)	
	methanol	ethanol
PtRu	107	20
PtRu@$Pt_{0.3}$	105	28
PtRu@$Pt_{0.6}$	102	43
PtRu@$Pt_{1.2}$	101	51
PtRu@$Pt_{1.4}$	99	55
PtRu@$Pt_{1.7}$	98	57
Pt	100	76

In order to assess the accuracy of this analysis, CO_2 produced during both methanol and ethanol electrolysis was measured in the exhaust stream by using a non-dispersive infrared monitor (34). Results obtained at a constant potential of 0.50 V are reported as faradaic yields in Table 3.5 (note that for ethanol oxidation, faradaic of CO_2 yields are higher than the chemical yields because of the 2:1 ratio of CO_2 produced to ethanol consumed, and that analysis of CO_2 can only provide the faradaic yield). The measured CO_2 yields for methanol oxidation were all close to the expected value of 100%. The minor deviations can be attributed to drift of the detector. In contrast, the measured CO_2 yield for ethanol oxidation was very low at the PtRu catalyst, but increased greatly as Pt was added. This is consistent with the much higher selectivity of Pt over PtRu for the complete oxidation of ethanol (9). The CO_2 yield of 20% for the PtRu catalyst is consistent with the previously reported faradaic yield of 18% (9), while the value of 57% for PtRu@$Pt_{1.7}$ is approaching the yield of 76% measured for Pt in this work and 75% previously reported for the same Pt catalyst (9).

The faradaic yields of acetic acid ($F_{acetic\ acid}$) and acetaldehyde ($F_{acetaldehyde}$) at 0.50 V can be calculated by using the measured CO_2 yields ($F_{carbon\ dioxide}$) and the stoichiometries from Figure 3.8, by using equation 3.4.

$$n = 12/(F_{carbon\ dioxide} + 3F_{acetic\ acid} + 6F_{acetaldehyde}) \qquad (3.4)$$

The results are shown Table 3.6, where the CO_2 yields have been corrected for drift of the detector by dividing them by the measured yields for methanol oxidation (i.e. the actual yield for methanol is assumed to be 100%). The negligible yield of acetaldehyde at the PtRu catalyst is consistent with previous data, while the increasing yields as Pt was added are consistent with the tendency for Pt to produce more acetaldehyde than PtRu (9). However, at 0.50 V the PtRu@Pt catalysts favour formation of acetaldehyde relative to both PtRu and Pt, indicating that selectivity is influenced by the subtle electronic and strain effects generated by the core-shell structure.

Table 3.6. Stoichiometries and faradaic yields of products for oxidation of 0.1 M ethanol at 0.50 V vs DHE in a PEMEC at 80 °C.

Catalyst	CO_2 yield[a]	n_{av} (Figure 3.8)	Acetic acid yield	Acetaldehyde yield
PtRu	19%	4.6	81%	0%
PtRu@$Pt_{0.3}$	27%	4.4	65%	9%
PtRu@$Pt_{0.6}$	42%	4.5	41%	17%
PtRu@$Pt_{1.2}$	50%	4.9	34%	15%
PtRu@$Pt_{1.4}$	56%	5.2	30%	14%
PtRu@$Pt_{1.7}$	58%	5.9	35%	7%

a. CO_2 yield is corrected for detector drift.

It is clear from the polarization curves in Figure 3.7 and the product distributions in Table 3.6 that PtRu@Pt core-shell structures can be used to tune both the activity and selectivity of ethanol oxidation catalysts. Although little data is available for comparison, a similar effect appears to occur with Ru@Pt catalysts (27), which have the economic advantage of requiring less Pt. However, the use of PtRu cores allows us to draw upon a vast resource of knowledge and methodology for manipulating the core (25, 47), as well as diverse and state-of-the-art commercial catalysts that can easily be tuned to suit specific applications. This offers many approaches for tuning strain and electronic effects by varying size, shape, and composition. It will be applicable to the electrocatalysis of diverse processes, including oxygen reduction, and anodic reactions in many different types of electrolysis and fuel cells (13, 26, 48, 49).

Interestingly, the trends in the activities of the catalysts with Pt coverage seen in the PEM cell show significant differences from those seen in cyclic voltammetry. For example, the original PtRu catalyst provided the best electrochemical performance for both methanol and ethanol oxidation in the PEM cell (Figure 3.7), while it was the worst catalyst for methanol oxidation in the H_2SO_4(aq) cell (Figure 3.5), and one of the worst for ethanol oxidation (Figure 3.6). These differences arise from the complex nature of these reactions, which involve many different adsorbed species and multiple pathways. The difference in operating temperature between the aqueous H_2SO_4 and PEM cells would play a major role in changing the balance of these processes, while the use of potentiodynamic vs potentiostatic conditions would also cause significant differences (27). In addition, sulphate adsorption may also be a significant factor in H_2SO_4 (27).

The important conclusion from these comparisons is that cyclic voltammetry in a liquid electrolyte at ambient temperature provides a poor indication of how a catalyst will perform for methanol or ethanol oxidation in a PEM electrolysis or fuel cell at elevated temperatures.

3.4. Conclusions

Highly active PtRu@Pt catalysts with core-shell structures have been easily prepared by chemical deposition of Pt onto a commercial carbon supported PtRu catalyst in ethylene glycol (polyol method). Variation of the amount of Pt deposited onto the PtRu core from less than one monolayer to ca. 1 monolayer allows the composition, electron density, and strain of the catalyst surface to be tuned, providing a wide range of activities for the oxidation of ethanol and methanol. This is particularly important for ethanol (and other multi-carbon alcohols (26)) where the selectivity, product distributions, and efficiency can be manipulated. Increasing the Pt coverage results in a shift of the half-wave potential for electrolysis of ethanol to higher potentials, towards the value for Pt, but increases the selectivity for the complete oxidation to CO_2, increasing the stoichiometry of the reaction (number of electrons transferred). Since the overall efficiency of an ethanol electrolysis cell or fuel cell depends on both the potential required and stoichiometry, optimum efficiency requires these two characteristics of the anode catalyst to be balanced for each application (45).

3.5. References

1. M. Simoes, S. Baranton and C. Coutanceau, ChemSusChem, **5**, 2106 (2012).

2. C. Coutanceau and S. Baranton, Wiley Interdisciplinary Reviews-Energy and Environment, **5**, 388 (2016).

3. B. Garlyyev, S. Xue, J. Fichtner, A. S. Bandarenka and C. Andronescu, ChemSusChem, **13**, 1 (2020).

4. V. Bambagioni, M. Bevilacqua, C. Bianchini, J. Filippi, A. Lavacchi, A. Marchionni, F. Vizza and P. K. Shen, ChemSusChem, **3**, 851 (2010).

5. A. Caravaca, A. de Lucas-Consuegra, A. B. Calcerrada, J. Lobato, J. L. Valverde and F. Dorado, Applied Catalysis, B Env., **134**, 302 (2013).

6. C. Lamy, T. Jaubert, S. Baranton and C. Coutanceau, Journal of Power Sources, **245**, 927 (2014).

7. A. Rodriguez-Gomez, F. Dorado, A. de Lucas-Consuegra and A. R. de la Osa, Journal of Energy Chemistry, **56**, 264 (2021).

8. N. Shaari, S. K. Kamarudin, R. Bahru, S. H. Osman and N. Ishak, International Journal of Energy Research, **45**, 6644 (2020).

9. R. M. Altarawneh and P. G. Pickup, Journal of Electrochemical Society, **164**, F861 (2017).

10. D. D. James and P. G. Pickup, Electrochimica Acta, **55**, 3824 (2010).

11. R. M. Altarawneh, P. Majidi and P. G. Pickup, Journal of Power Sources, **351**, 106 (2017).

12. M. B. Gawande, A. Goswami, T. Asefa, H. Z. Guo, A. V. Biradar, D. L. Peng, R. Zboril and R. S. Varma, Chemical Society Reviews, **44**, 7540 (2015).

13. J. S. Walker, N. V. Rees and P. M. Mendes, Journal of Experimental Nanoscience, **13**, 258 (2018).

14. T.-Y. Chen, T.-L. Lin, T.-J. M. Luo, Y. Choi and J.-F. Lee, ChemPhysChem, **11**, 2383 (2010).

15. D. Kaplan, M. Alon, L. Burstein, Y. Rosenberg and E. Peled, Journal of Power Sources, **196**, 1078 (2011).

16. T.-Y. Chen, T.-J. M. Luo, Y.-W. Yang, Y.-C. Wei, K.-W. Wang, T.-L. Lin, T.-C. Wen and C. H. Lee, Journal of Physical Chemistry C, **116**, 16969 (2012).

17. N. Muthuswamy, J. L. G. de la Fuente, D. T. Tran, J. Walmsley, M. Tsypkin, S. Raaen, S. Sunde, M. Ronning and D. Chen, International Journal of Hydrogen Energy, **38**, 16631 (2013).

18. N. M. Sanchez-Padilla, S. M. Montemayor, L. A. Torres and F. J. Rodriguez Varela, International Journal of Hydrogen Energy, **38**, 12681 (2013).

19. E. N. El Sawy, H. A. El-Sayed and V. I. Birss, Physical Chemistry Chemical Physics, **17**, 27509 (2015).

20. Y. M. Hu, A. M. Zhu, Q. G. Zhang and Q. L. Liu, International Journal of Hydrogen Energy, **41**, 11359 (2016).

21. A. Hoang, E. El Sawy, A. Blackburn, S. Ketabi, M. Goledzinowski, F. J. E. Comeau and V. Birss, Acs Applied Energy Materials, **3**, 8423 (2020).

22. F. H. B. Lima and E. R. Gonzalez, Applied Catalysis B: Environmetal, **79**, 341 (2008).

23. J. S. Zou, M. Wu, S. L. Ning, L. Huang, X. W. Kang and S. W. Chen, ACS Sustainable Chemistry and Engineering, **7**, 9007 (2019).

24. N. Kakati, J. Maiti, S. H. Lee, S. H. Jee, B. Viswanathan and Y. S. Yoon, Chemical Reviews, **114**, 12397 (2014).

25. Y. V. Tolmachev and O. A. Petrii, Journal of Solid State Electrochemistry., **21**, 613 (2017).

26. T. M. Brueckner, E. Wheeler, B. Chen, E. N. El Sawy and P. G. Pickup, Journal of Electrochemical Society, **166**, F942 (2019).

27. E. El Sawy, T. M. Brueckner and P. G. Pickup, Journal of Electrochemical Society, **167**, 106507 (2020).

28. E. N. El Sawy and P. G. Pickup, Electrocatalysis, **7**, 477 (2016).

29. J. Svendby, F. Seland, G. Singh, J. L. de la Fuente and S. Sunde, Journal of Electroanalytical Chemistry, **833**, 189 (2019).

30. P. Ochal, J. L. G. de la Fuente, M. Tsypkin, F. Seland, S. Sunde, N. Muthuswamy, M. Ronning, D. Chen, S. Garcia, S. Alayoglu and B. Eichhorn, Journal of Electroanalytical Chemistry, **655**, 140 (2011).

31. D. Bokach, J. L. G. de la Fuente, M. Tsypkin, P. Ochal, I. C. Endsjo, R. Tunold, S. Sunde and F. Seland, Fuel Cells, **11**, 735 (2011).

32. J. J. Wang, Y. T. Liu, I. L. Chen, Y. W. Yang, T. K. Yeh, C. H. Lee, C. C. Hu, T. C. Wen, T. Y. Chen and T. L. Lin, Journal of Physical Chemistry C, **118**, 2253 (2014).

33. T. M. Brueckner and P. G. Pickup, Journal of Electrochemical Society, **64**, F1172 (2017).

34. R. M. Altarawneh, T. M. Brueckner, B. Y. Chen and P. G. Pickup, Journal of Power Sources, **400**, 369 (2018).

35. G. Schmid, Chemical Reviews, **92**, 1709 (1992).

36. S. Alayoglu and B. Eichhorn, Journal of American Chemical Society, **130**, 17479 (2008).

37. R. J. K. Wiltshire, C. R. King, A. Rose, P. P. Wells, H. Davies, M. P. Hogarth, D. Thompsett, B. Theobald, F. W. Mosselmans, M. Roberts and A. E. Russell, Physical Chemistry Chemical Physics, **11**, 2305 (2009).

38. M. A. Rigsby, W. P. Zhou, A. Lewera, H. T. Duong, P. S. Bagus, W. Jaegermann, R. Hunger and A. Wieckowski, Journal of Physical Chemistry C, **112**, 15595 (2008).

39. A. Foelske, O. Barbieri, M. Hahn and R. Kotz, Electrochemical and Solid State Letters, **9**, A268 (2006).

40. A. S. Arico, A. K. Shukla, H. Kim, S. Park, M. Min and V. Antonucci, Applied Surface Science, **172**, 33 (2001).

41. E. N. El Sawy, H. A. El-Sayed and V. I. Birss, Chemical Communications, **50**, 11558 (2014).

42. S. E. Evarts, I. Kendrick, B. L. Wallstrom, T. Mion, M. Abedi, N. Dimakis and E. S. Smotkin, ACS Catalysis, **2**, 701 (2012).

43. Y. Wang, S. Z. Zou and W. B. Cai, Catalysts, **5**, 1507 (2015).

44. R. M. Altarawneh, Energy and Fuels, **35**, 11594 (2021).

45. R. M. Altarawneh and P. G. Pickup, Journal of Power Sources, **366**, 27 (2017).

46. P. Majidi, R. M. Altarawneh, N. D. W. Ryan and P. G. Pickup, Electrochimica Acta, **199**, 210 (2016).

47. A. S. Moura, J. L. C. Fajin, M. Mandado and M. Cordeiro, Catalysts, **7**, 47 (2017).

48. R. Y. Jiang, S. O. Tung, Z. Tang, L. Li, L. Ding, X. G. Xi, Y. Y. Liu, L. Zhang and J. J. Zhang, Energy Storage Materials, **12**, 260 (2018).

49. B. W. Zhang, H. L. Yang, Y. X. Wang, S. X. Dou and H. K. Liu, Advanced Energy Materials, **8**, 1703597 (2018).

Chapter 4: Efficient oxidation of ethanol at Ru@Pt core-shell catalysts in a proton exchange membrane electrolysis cell

The main Principal author (Ahmed H Ali) contributed to all parts of this project, including the literature review, designing and conducting all experiments, measuring and analyzing all the results, presenting the data, and writing the first draft of the publication.

The corresponding author (Peter G. Pickup) was responsible for funding, reviewing all my data analysis, editing my draft paper, and completing it for submission.

This Chapter has been published as:-

Ali, A. H., and Pickup, P. G. (2023). Efficient Oxidation of Ethanol at Ru@ Pt Core-Shell Catalysts in a Proton Exchange Membrane Electrolysis Cell. ECS Advances, *2*(2), 024501.

The raw data are provided in Appendix B.

Part of Chapter 3 and 4 was presented on the 241st ECS conference meeting, and the abstract of this poster was published as: (Ali, A. H., and Pickup, P. (2022, July). Ethanol and Methanol Electrolysis at Core-Shell Ru@ Pt and PtRu@ Pt Catalysts with Different Pt Shell-Thickness. In Electrochemical Society Meeting Abstracts 241 (No. 55, pp. 2316-2316). The Electrochemical Society, Inc.)

4.1. Introduction

There have been many studies reporting that oxidation of low molar mass alcohols in proton exchange membrane electrolysis cells (PEMEC) can produce hydrogen at much lower voltages than water electrolysis (1-5). The alcohol in a PEMEC is oxidized on the surface of an anodic catalyst. A proton exchange membrane (PEM) such as Nafion™ allows the protons formed to be transferred to the cathode and reduced to form hydrogen.

Many factors influence the choice of anodic catalyst, including their ability to adsorb the alcohol molecules and complete their oxidation to CO_2. The efficiency of the catalyst is determined by both the potential required (anode overpotential) and the amount of CO_2 generated (4, 6, 7). The formation of partial oxidation products, particularly acetic acid and acetaldehyde from ethanol oxidation, decreases the amount of hydrogen produced and requires methods for waste management and emission control. A key objective in the development of catalysts for ethanol oxidation is to improve the faradaic efficiency by increasing the yield of CO_2.

Platinum has a high ability to adsorb alcohol molecules and produce a high yield of CO_2 (6). However, modification of Pt catalysts (e.g. alloying with Ru or surface modification) is still required to remove strongly adsorbed CO that causes high anode overpotentials (8, 9). Deposition of a few monolayers of Pt onto a more active metal such as Ru to create core-shell nanoparticles (Ru@Pt) (10-12) can decrease the overpotential relative to Pt (13, 14), while improving selectivity for CO_2 formation relative to PtRu alloys (14). Ligand and lattice strain effects that result from interactions between the Pt shell and Ru core weaken the bonding of CO to the Pt surface (10, 11). The Pt shell can also increase stability and protect the Ru from dissolution during operation (15, 16). As a result, Ru@Pt catalysts have recently been used for the electrochemical oxidation of organic fuels, including methanol (14, 17-27) and ethanol (13, 14, 19, 20, 27-29).

Methanol electrooxidation has been studied more than ethanol because it occurs at lower overpotentials and methanol can be oxidized completely to CO_2 because it does not require cleavage of a C-C bond. However, ethanol is a much less toxic fuel than methanol and can be produced in large quantities from biomass. Additionally, a Ru@Pt catalyst capable of dissociating the C-C bond and oxidizing the adsorbed CO intermediate more easily could potentially produce higher current densities than for methanol.

Ru nanoparticle size (13, 18), crystallinity of the Ru core (13, 23, 29), and Pt shell thickness (14, 17, 18) are the main factors that affect the catalytic activity of Ru@Pt catalysts toward the oxidation of alcohols. In nanoparticle syntheses, capping agents such as polyvinyl pyrrolidone (PVP) serve as stabilizers to prevent their overgrowth (17). They can control the size distribution and produce uniform shell thickness. However, the active surface area of the catalyst can be significantly reduced due to the difficulty of removing capping agents (13, 19, 29).

Hseieh et al. (30) have reported atomically ordered Ru@Pt nanoparticles prepared by using ethanol as a reductant in an alkaline medium at a temperature lower than 100 °C. These crystalline core-shell nanoparticles prevented partial alloying at the Ru/Pt interface, which greatly increases the catalytic activity for methanol and ethanol oxidation (13, 29, 30). However, large particle sizes, broadening of the size distribution, less spherical shape and non-uniform Pt shells were identified as limitations of this method (13, 29).

Hu et al. (19) prepared Ru@Pt catalysts by using ethylene glycol as a reducing agent and a fast microwave technique. The resulting spherical nanoparticles had a small particle size with a narrow size distribution and uniform Pt shell thickness but had an amorphous structure. Their studies show higher reactivity for ethanol oxidation than methanol oxidation.

The development of more efficient anode catalysts for alcohol PEMEC also benefits the growth of direct alcohol fuel cells (PEMFC such as direct methanol fuel cells and direct ethanol fuel cells), which employ the same types of cells and anodes but produce electrical power through the spontaneous reaction of oxygen at the cathode (31-34). Chemical reaction between the fuel and the oxygen in a PEMFC due to fuel and oxygen crossover through the membrane makes it extremely challenging to determine the anode potential and the product distribution, resulting in inaccurate measurement of catalyst performance (35, 36). Consequently, anodic catalysts for fuel cells can be more accurately characterized in a PEMEC, where the anode potential is measured relative to hydrogen evolution at the cathode (dynamic hydrogen electrodes), and products from oxidation of the alcohol arise solely from the electrochemical reaction at the anode (6, 35, 36).

In this work, we prepared three Ru@Pt nanoparticle catalysts with different amounts (monolayers) of Pt deposited on the surface of highly crystalline, carbon-supported Ru nanoparticles (Ru/C) with a narrow particle size distribution. The aim of using crystalline Ru was to prevent partial alloying at the Ru/Pt interface, as previously reported (29, 30). Ethylene glycol was used as a reducing agent and solvent, without adding a capping agent, to form spherical nanoparticles of narrow size distribution, as shown in our previous work (37).

We report the catalytic activity of the new Ru@Pt catalysts toward ethanol electrooxidation in aqueous sulfuric acid at ambient temperature and in a PEMEC at 80 °C, in order to investigate the relationship between activities under these different conditions. Measurements in the PEMEC focus on the relationships between activity and efficiency, and how these change with the composition and structure of the catalyst. A low concentration (0.1 M) of ethanol was used in order to increase efficiency for the complete oxidation of ethanol, as discussed below. Data for methanol oxidation is also reported, in order to provide further insight into the mechanistic role of the core-shell structures.

All the Ru@Pt catalysts gave significantly higher currents at low potentials than a commercial Pt/C catalyst, which indicates that deposition of Pt onto the Ru core, using ethylene glycol as a reducing agent, promotes the activity of Pt at the nanoparticle surface. As a result, these catalysts are promising anodic catalysts for use in ethanol electrolysis cells and fuel cells.

4.2. Experimental

4.2.1. Materials

5% Nafion^{TM} solution (Dupont), 40% ruthenium supported on Vulcan XC-72 carbon (Ru/C; Fuel Cell Store), 40% Pt on carbon black (Pt/C; Alfa Aesar), 75% PtRu (1:1 atomic ratio) on carbon black (PtRu/C; Alfa Aesar), $H_2PtCl_6.6H_2O$ (Pressure Chemical Co.), sulfuric acid (95-98%; Fisher Scientific), methanol (HPLC grade; Fisher Scientific), anhydrous ethanol (99.9%; Commercial Alcohols Inc.), 1-propanol (J.T. Baker), ethylene glycol (EG; ACP) and 2-propanol (Caledon), were used as received. Deionized water was used to prepare all aqueous solutions.

4.2.2. Synthesis of Ru@Pt catalysts

500 mg of 40% Ru/C in 40 mL of EG was sonicated for ca. 40 min at 60 °C and then purged with hydrogen (5% in N_2) for 20 min to remove oxides and hydroxides from the Ru surface (38). The required amount of $H_2PtCl_6.6H_2O$ dissolved in 10 mL of EG was added dropwise at ambient temperature with vigorous stirring. The temperature was gradually increased to 185 °C and held at this temperature for 2 h. The catalyst was collected using a centrifuge (5 min at 9000 rpm), washed several times with boiling water and dried at 80 °C for 8 h. The catalysts are labelled as Ru@Pt$_{0.6}$, Ru@Pt$_{1.0}$ and Ru@Pt$_{1.4}$ according to their target atomic ratios.

4.2.3. Physical characterization

A Q500 thermogravimetric analyzer (TGA) was used to determine the metal loading (mass% of Ru+Pt) on the carbon black. Ca. 6 mg of the well-dried catalyst was used under air, and the temperature was increased with a ramp of 20 °C min^{-1} to 800 °C. Pt:Ru atomic ratios were determined using an energy-dispersive X-ray analyzer (EDX) attached to an FEI Quanta 400 scanning electron microscope (SEM). The catalysts (ca. 2 mg) were dispersed in a mixture of water, 1-propanol and 2-propanol (0.2 mL) for application to the SEM carbon tabs.

A Rigaku Ultima IV X-ray diffractometer (XRD) with a Cu Kα radiation source (0.154 nm) was used to study the crystal structure of the catalysts. The diffracted radiation was detected by using a scintillation counter analyzer. X-ray photoelectron spectroscopy (XPS) was conducted using a VG Micro-tech Multi-lab ESCA 2000 system at Dalhousie University (Halifax, Nova Scotia, Canada) by Andrew George.

A Tecnai TM Spirit transmission electron microscope (TEM, Faculty of Medicine at Memorial University) was used to determine the average particle size, size distribution and the degree of dispersion on the carbon support. An average nanoparticle size for each catalyst was obtained by measuring the diameters of at least 80 randomly selected nanoparticles using the Image J 1.53a program. TEM samples were prepared by dispersing 1 mg of catalyst in 200 μL of a water, 1-propanol, and isopropanol mixture by sonication for at least 1 h, then one droplet of the ink was placed on the TEM grid.

4.2.4. Electrochemical characterization at ambient temperature

An SP-50 Biologic potentiostat with EC-lab software was used for cyclic voltammetry (CV) in a three-electrode glass cell, with a Pt wire counter electrode and standard calomel reference electrode (SCE). Carbon fiber paper (CFP, 0.24 cm^2, Toray TGP-H-090) working electrodes were painted with the desired volume of catalyst ink to give a 0.3 mg cm^{-2} metal (Ru+Pt) loading. The catalyst ink was prepared by sonication of 2 mg of catalyst in 200 μL of a solvent mixture consisting of water, 1-propanol, and isopropanol at volume ratios of 2:3:3. All CV measurements were made in N_2 purged 1 M aqueous sulfuric acid. Following the recording of background CV (six cycles at 100 mV s^{-1}), methanol or ethanol was added to give a concentration of 0.1 M. The alcohol was homogeneously mixed by purging with N_2 for 3 min. CV for oxidation of the alcohols were obtained for three cycles from –0.25 V to 0.80 V at ambient temperature at a scan rate of 10 mV s^{-1}. The final anodic scan is shown in all cases.

4.2.5. PEMEC for alcohol oxidation studies at 80 °C

A commercial fuel cell (Electrochem Inc.) modified to accommodate an array of nine 0.24 cm^2 anodes was operated as an electrolysis cell in crossover mode at 80 °C, as previously described (39). This allowed the three Ru@Pt catalysts to be tested simultaneously using three electrodes for each catalyst to assess reproducibility. In the crossover mode employed, 0.1 M of methanol or ethanol was pumped through the cathode chamber at a flow rate of 0.5 mL min^{-1}, in order to provide controlled diffusion to the anode through the Nafion membrane. The anode was purged with N_2 gas at 10 mL min^{-1}.

A single 5 cm^2 Pt black on CFP cathode was employed with a Nafion-117 membrane. The cell was operated with an MSTAT potentiostat from Arbin instruments which controlled the potential applied to each anode relative to the cathode, which acts as a dynamic hydrogen electrode (DHE) (39).

Anodes were prepared by painting catalyst inks onto CFP disks (0.24 cm^2) to give a metal loading of 2.0 mg cm^{-2}. A 5% Nafion solution was then applied to the catalyst surface, equivalent to 30% of the total catalyst + Nafion mass. Catalyst inks were prepared by dispersion of 4 mg of catalyst in 200 µL of a mixture of water, isopropanol, and 1-propanol (2:3:3).

All anodes were set to a constant potential of 0.70 V (vs DHE) for at least 1 h before each polarization curve measurement. Polarization curves were obtained by measuring the current for 3 min at constant potentials, starting at 0.90 V. The average current for the last 60 s of each applied potential is reported. Initially, consecutive polarization curves for methanol oxidation (four) were recorded until they were consistent. Then two consecutive curves were recorded for ethanol oxidation. The final polarization curve is reported in all cases.

CO_2 generated by oxidation of the alcohols at 0.50 V was monitored using an infrared CO_2 sensor (Telaire T6615) as previously described (40). During CO_2 measurements, the N_2 flow rate was increased to 50 mL min^{-1} while the alcohol flow rate decreased to 0.2 mL min^{-1}.

4.3. Results and discussion

4.3.1. Characterization of the Ru@Pt catalysts

The total metal (Pt+Ru) content of each catalyst was determined through TGA as the residual mass percent at 800 °C as shown in Figure B 1 and reported in Table 4.1. As Pt was added, the residual mass percent increased as expected, and there was reasonable agreement with the target values. However, the measured values for Ru@Pt$_{0.6}$ and Ru@Pt$_{1.0}$ are a little higher than the target values, and this may be due to the loss of some of the carbon support during collection and washing of the catalysts.

EDX spectra for the catalysts, and SEM images the analysed areas, are shown in Figure B 2. All spectra show peaks for both Pt and Ru at 2.05 keV and 2.56 keV, respectively as expected. The Pt peak intensity increased relative to Ru as more Pt was deposited. The measured Pt:Ru atomic ratios are compared with the target ratios in Table 4.1and show that there was quantitative deposition of the Pt.

Table 4.1. Comparison of measured and target mass percentages of total metal and Pt:Ru atomic ratios.

Catalyst	Ru+Pt mass %		Pt:Ru atomic ratio	
	Target mass %	Residual mass % from TGA	Target	From EDX
Ru@Pt$_{0.6}$	59.0	66.5	0.60	0.63
Ru@Pt$_{1.0}$	66.1	68.2	1.00	1.00
Ru@Pt$_{1.4}$	71.2	69.5	1.40	1.38

TEM images and particles size distribution histograms of the Ru and Ru@Pt catalysts are shown in Figure B 3. The images show that the nanoparticles had an approximately spherical shape and were well dispersed on the carbon support with low agglomeration. The histograms indicate that the particle size distributions were relatively narrow, evidence of the formation of uniform Pt shells. The average diameters of the metal nanoparticles ($D_{Ru@Pt}$) are reported in Table 4.2, together with the expected sizes of the Ru@Pt core-shell nanoparticle calculated by using equation 4.1 (13, 41).

$$D_{Ru@Pt} = D_{Ru}\sqrt[3]{\frac{\frac{M_{Pt}P_{Ru}}{M_{Ru}P_{Pt}}n_{Pt}+n_{Ru}}{n_{Ru}}} \qquad (4.1)$$

where n_{Pt} and n_{Ru} are the target number of moles of Pt and Ru per particle, respectively, D_{Ru} is the measured diameter of the Ru core (3.9 nm), M_{Pt} and M_{Ru} are the molar mass of Pt and Ru, respectively, and P_{Pt} and P_{Ru} are the densities of Pt and Ru, respectively. It can be seen that the measure sizes agree well with the expected sizes, providing strong evidence that core-shell nanoparticle structures had been formed with the target compositions.

Table 4.2. Expected and measured average diameters of the Ru@Pt core-shell nanoparticles, and calculated monolayers of Pt in the shell.

Catalyst	Average particle diameter (nm)		ML of Pt
	Expected	Measured by TEM	
Ru	4.00[a]	3.9 ± 0.7	0.0
Ru@$Pt_{0.6}$	4.61	4.5 ± 0.4	1.3
Ru@$Pt_{1.0}$	4.98	4.9 ± 0.3	2.0
Ru@$Pt_{1.4}$	5.31	5.3 ± 0.2	2.5

a. Specified by the Fuel Cell Store.

The thicknesses of the Pt shells can be calculated in Pt monolayers (ML) from D_{Ru}, the diameter of a Pt atom ($D_{Pt\ atom}$) and $D_{Ru@Pt}$ by using equation 4.2. The resulting values are reported in Table 4.2.

$$Monolayers\ of\ Pt = \frac{D_{Ru@Pt} - D_{Ru}}{2\,D_{Pt\ atom}} \quad (4.2)$$

In all cases, more than one monolayer was deposited, which means that Pt atoms should have completely covered the surface of the Ru core. The highest coverage corresponds to more than 2 complete monolayers of Pt, which would significantly decrease the strain and ligand effects of the Ru core (42).

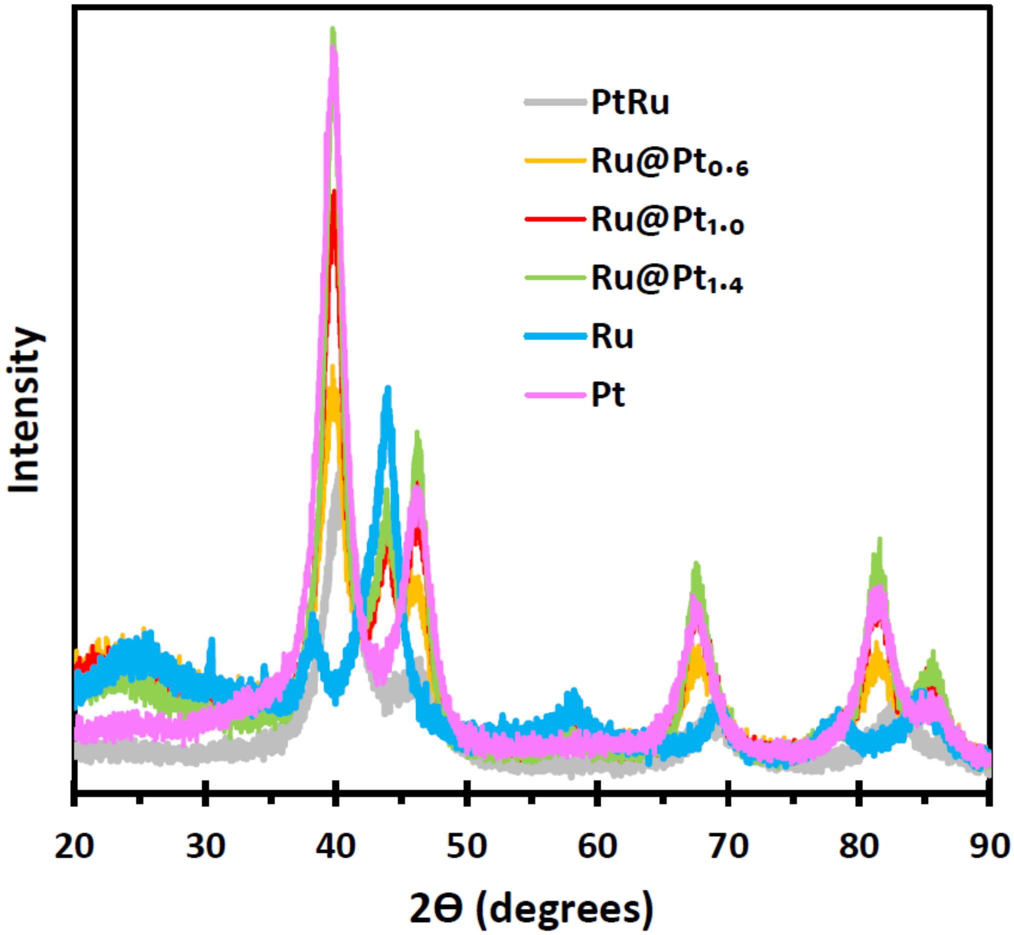

Figure 4.1. XRD patterns for the Ru@Pt catalysts and commercial Pt, Ru, and PtRu catalysts.

XRD spectra of the Ru@Pt catalysts are shown in Figure 4.1, together with spectra for the commercial Pt, Ru, and PtRu catalysts for comparison. For greater clarity, the Ru and Ru@Pt spectra are offset in Figure B 4, and peaks for each lattice plane are identified. Pt has an FCC structure, while the Ru core has an HCP structure. The XRD spectra of the Ru@Pt catalysts all show FCC peaks for Pt, which confirms the reduction of the H_2PtCl_6 to Pt metal. As the thickness of the Pt shell was increased, the intensity of the Pt diffraction peaks increased relative to the Ru peaks. In addition, the positions of the Pt diffraction peaks were close to the positions for pure Pt, as shown in Table 4.3, for the Pt (111) and (220) peaks. This is strong evidence for the deposition of Pt onto the surface of the Ru nanoparticles (13, 29).

Table 4.3. Peak position for the Pt(111) and Pt(220) lattice planes, and Pt-Pt intra-atomic strain.

Catalyst	2θ for Pt(111) peak	2θ for Pt(220) peak	Pt-Pt strain
Pt	39.70°	67.50°	0
Ru@Pt$_{1.4}$	39.74°	67.66°	–0.6%
Ru@Pt$_{1.0}$	39.90°	67.74°	–1.0%
Ru@Pt$_{0.6}$	39.96°	68.06°	–2.4%

A significant strain effect is induced by the mismatch between Ru and Pt lattices, which alters the Pt-Pt interatomic distance, and a method to calculate this has been established (42). Based on the strain values calculated from the positions of the Pt(111) peak (Table 4.3), the Ru@Pt catalysts show compression of the Pt lattice, which decreased as the thickness of the Pt shell was increased.

The Ru diffraction peaks for the Ru@Pt catalysts appear at the same positions as for the Ru/C catalyst. This indicates that the high crystallinity of the Ru core was maintained, and that there was not significant mixing with the Pt shell (38, 43). Moreover, as shown in Figure 4.1, the Pt diffraction peaks of the Ru@Pt catalysts are at significantly different positions than those of PtRu, which indicates that they were not alloys.

XPS spectra for the Ru@Pt catalysts were very similar to the spectrum for the PtRu catalyst (Figure 4.2). As expected, the ratio of the intensity of the Pt peaks to the Ru peaks increased as Pt was added to the Ru core. Compositions of the metal nanoparticles (atomic Pt percentage) calculated from the relative intensities of the Pt 4f$_{7/2}$ and Ru 3d$_{5/2}$ peaks are compared with the expected values for homogeneous mixtures of Pt and Ru in Table 4.4. Whereas the measured (apparent) Pt content was slightly lower than expected for the PtRu alloy, it was higher than expected for the Ru@Pt catalysts, indicating that Pt had been deposited onto the Ru cores. Although the measured Pt content increased as more Pt was added, the difference from the expected value decreased. This suggests Pt did not completely cover the Ru surface, and therefore was not deposited uniformly.

There were no significant differences between the Pt 4f binding energies of the three Ru@Pt catalysts and the PtRu catalyst (Figure B 5 and Table 4.4), indicating that the electronic effect of the Ru core did not vary significantly. The $4f_{7/2}$ binding energy is similar to a value of 71.06 eV reported for pure Pt nanoparticles (44).

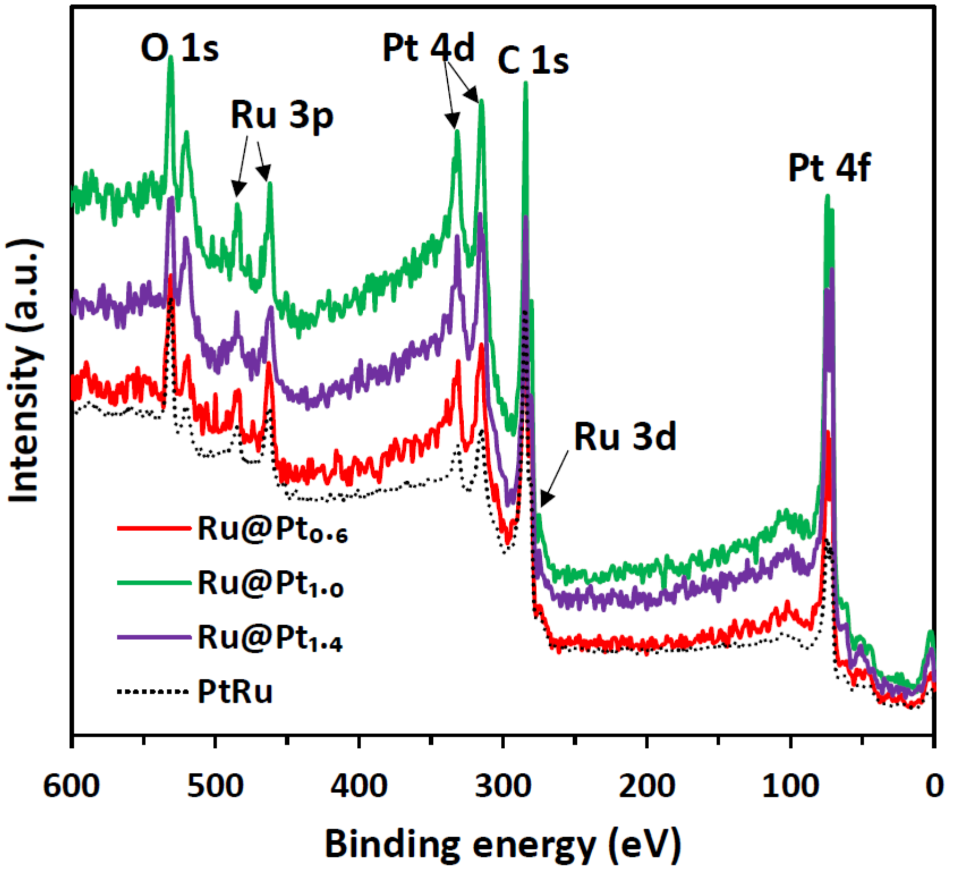

Figure 4.2. XPS spectra of the Ru@Pt and PtRu catalysts.

Table 4.4. Atomic percentage of Pt (%Pt) and Pt $4f_{5/2}$ binding energies from XPS, and %Pt based on the target compositions.

catalyst	%Pt		Pt $4f_{5/2}$ ($4f_{7/2}$) binding energy (eV)
	measured	expected	
PtRu	46%	50%	74.17 (70.84)
Ru@Pt$_{0.6}$	54%	38%	74.10 (70.73)
Ru@Pt$_{1.0}$	59%	50%	74.07 (70.71)
Ru@Pt$_{1.4}$	63%	58%	74.08 (70.74)

The O 1s regions of the XPS spectra are shown in Figure B 6. Components at 529.63 eV and 530.73 eV for the PtRu catalyst were previously assigned to O^{2-} and OH^- species, respectively, at oxidized Ru sites, while the 532.18 eV component is primarily due to C-O groups on the carbon support (37). The intensity of the O 1s peak decreased greatly relative to the Pt peaks as Pt was added to the core, indicating substantial coverage of the Ru surface. However, the persistence of the Ru-O/Ru-OH component ca. 530 eV indicates that there was incomplete coverage of the core (37). It is not clear why the O^{2-} and OH^- components are not resolved for the Ru@Pt catalysts, but it does suggest that there are some differences in the oxide species that are present relative to PtRu. Presumably, there is also an unresolved Pt-OH component at ca. 530 eV (45).

4.3.2. Cyclic voltammetry in aqueous sulfuric acid

Cyclic voltammograms of the Ru@Pt catalysts in 1 M sulfuric acid are shown in Figure 4.3, together with those for the Ru, Pt and PtRu catalysts. Similar features are seen for the three Ru@Pt catalysts, with decreasing currents as the Pt shell thickness was increased. Since a constant metal (Ru+Pt) loading was employed, this can be attributed to the decreasing surface area/mass ratio of the Ru@Pt nanoparticles.

The hydrogen desorption and adsorption region, below 0.15 V in the voltammograms, provides crucial information on the nature of the surface of the catalyst nanoparticles (37). The hydrogen desorption region for the Pt catalyst is characterized by two peaks/shoulders at ca. 0 V and –0.10 V. In contrast, the Ru and PtRu catalysts do not show these distinct features. However, all of the Ru@Pt catalysts show shapes that are characteristic of Pt with peaks at similar potentials, indicating that they had predominantly Pt surfaces. However, the persistence of higher currents than pure Pt in the 0.10 to 0.30 V region indicates that some Ru remained at the surface for even the highest Pt coverage (46). This is consistent with the XPS results and suggests that Pt may not have been deposited evenly on the Ru cores (13, 29).

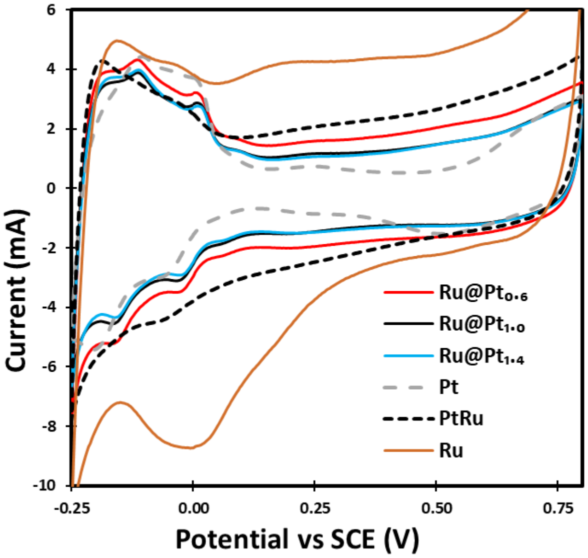

Figure 4.3. Cyclic voltammograms in 1 M aqueous sulfuric acid of the Ru@Pt, Pt, Ru, and PtRu catalysts at the same metal loading (0.3 mg cm^{-2} of Pt+Ru) and a scan rate of 100 mV s^{-1}.

Significantly, there is a cathodic peak at 0.52 V in the oxide region of the Pt voltammogram, which is due to the reduction of Pt-OH. The Ru@Pt catalysts do not possess this feature due to the electronic and/or strain effects of the Ru on the reactivity of the Pt surface (22, 37, 46).

4.3.3. Methanol and ethanol oxidation in aqueous sulfuric acid

Linear sweep voltammograms for methanol oxidation at the Ru@Pt, Pt and PtRu catalysts are shown in Figure 4.4. As expected from other reports, the Ru@Pt catalysts were much more active for methanol oxidation than the PtRu catalyst. However, their activities were lower than for the Pt catalyst at high potentials (18, 42). Changing the Pt shell thickness had relatively minor influences on the activities of the Ru@Pt catalysts, indicating dominance of the longer-range strain effects of the Ru core over electronic effects, which are much weaker for the second Pt monolayer, and the bifunctional effect of exposed Ru (18, 42).

Although the Pt catalyst produced the highest peak current, the Ru@Pt catalysts all gave lower half-wave potentials, indicating faster kinetics for methanol oxidation. This can be attributed to the interactions (ligand and strain) between the Pt shell and the Ru core (14, 18, 29). The Ru@$Pt_{1.4}$ catalyst (2.5 ML) gave the highest currents at potentials above ca. 0.43 V, indicating that it was most Pt-like. However, the Ru@$Pt_{0.6}$ catalyst (1.3 ML) showed the lowest onset potential and highest currents below ca. 0.42 V, which are more similar to the PtRu catalyst. The higher currents for the Ru@$Pt_{0.6}$ catalyst relative to PtRu at all potentials can be attributed to the higher coverage of surface Pt sites, which are required for methanol adsorption and dissociation. This clearly demonstrates the value of combining the ligand and strain effects of Ru with a Pt-rich surface.

Cyclic voltammograms for ethanol oxidation at the Ru@Pt, Pt and PtRu catalysts are shown in Figure 4.5. The Ru@Pt catalysts all produced much higher currents than the Pt catalyst at potentials below 0.50 V, and higher currents than PtRu above 0.40 V. Since optimizing the performances of ethanol PEMEC and PEMFC requires optimizing the balance between current at low and high potentials (6), the Ru@Pt catalysts employed here are particularly attractive. In addition, the Pt-like peak at ca. 0.65 V for the Ru@Pt catalysts suggests that there was improved selectivity for the complete oxidation of ethanol to CO_2 (14, 37). In contrast, PtRu is much more active than Pt for partial oxidation of ethanol to acetic acid at low potentials, but produces little CO_2 (6).

As for methanol oxidation, changing the Pt shell thickness had only minor influences on the activities of the Ru@Pt catalysts. This indicates that the strain effect of the Ru core has the dominant impact on activity at low potentials. The somewhat lower performance of the Ru@$Pt_{0.6}$ catalyst suggests that the combined electronic and strain effects may be too intense for efficient ethanol adsorption (14, 47).

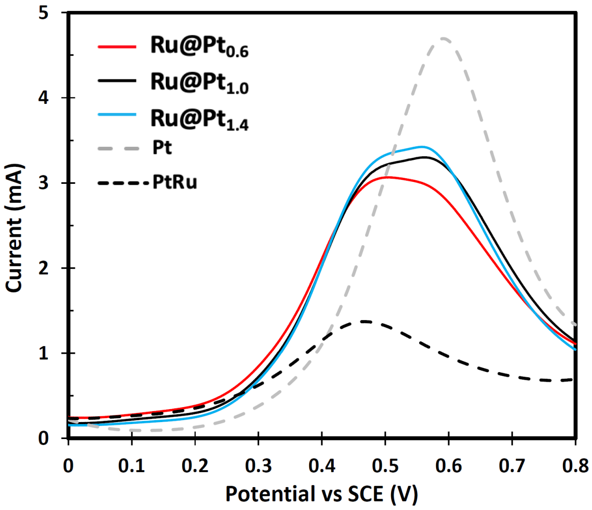

Figure 4.4. Linear sweep voltammetry for methanol oxidation in 1 M aqueous sulfuric acid at the Ru@Pt, Pt and PtRu and catalysts (0.3 mg cm^{-2} of Pt+Ru) at 10 mV s^{-1}.

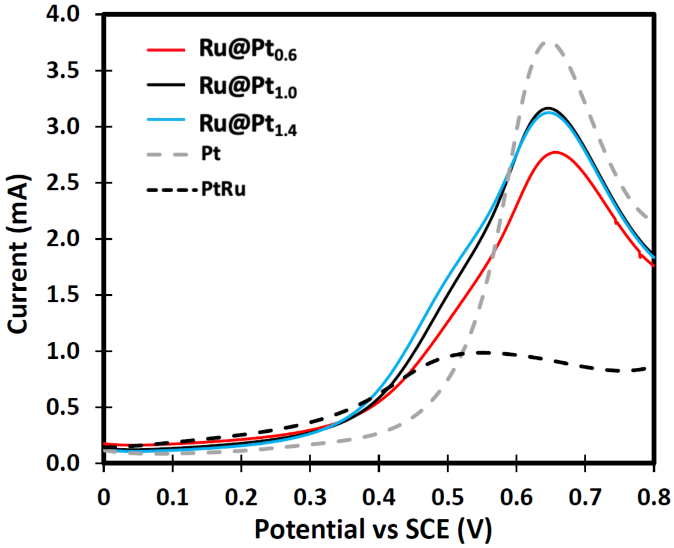

Figure 4.5. Linear sweep voltammetry for ethanol oxidation in 1 M aqueous sulfuric acid at the Ru@Pt, Pt and PtRu catalysts (0.3 mg cm^{-2} of Pt+Ru) at 10 mV s^{-1}.

4.3.4. Oxidation of methanol and ethanol in a PEMEC at 80 °C

Polarization curves for oxidation of 0.1 M methanol and ethanol in a PEMEC at 80 °C are shown in Figure 4.6. For all of the Ru@Pt catalysts, the onset and half-wave potentials were much lower than for the Pt catalyst, but higher than for PtRu. The improved performance relative to Pt can be attributed to the ligand, strain, and bifunctional effects of the Ru core which enhance the oxidation of the common adsorbed CO intermediate (14). As also seen in the voltammetric data in Figures 4.4-4.5, variation of the Pt shell thickness of the Ru@Pt catalysts had relatively minor effects on their performances in the PEMEC.

Since the PEMEC was operated in crossover mode, the currents are determined by the rate of steady-state mass transport at high potentials (39). For methanol oxidation (Figure 4.6A), the current became almost constant at high potentials, as expected for limitation of the current by the rate of methanol diffusion through the Nafion membrane. The variations seen for the different catalysts are due primarily to experiment uncertainty (39), although they may include contributions from variations in the product distribution between formaldehyde, formic acid, and CO_2.

For ethanol oxidation, it has been shown that variations in the yields of acetaldehyde, acetic acid, and CO_2 cause large variations in the mass transport limited current between catalysts, and variations with potential (14, 27, 37, 39). These effects can be quantified by using equations 4.3 and 4.4 (39),

$$I_{lim} = n_{av}AFmC \qquad (4.3)$$

$$n_{av} = \sum n_i x_i \qquad (4.4)$$

where I_{lim} is the mass transport limited current, n_{av} is the stoichiometry of the reaction (the average number of transferred electrons per molecule), C is the concentration of the alcohol solution, A is the electrode area, and m is the mass transport coefficient.

The stoichiometry is a weighted average of the stoichiometries for each product (equation 4.4), where n_i is the number of transferred electrons to form product i (for ethanol oxidation, $n_{acetaldehyde} = 2$, $n_{acetic\ acid} = 4$, and $n_{CO_2} = 12$) and x_i is the fraction of molecules that are converted to product i.

Equation 4.3 provides an explanation for the differences between the methanol and ethanol polarization curves at high potentials (> 0.50 V) in Figure 4.6. Whereas methanol is oxidized mainly to CO_2 ($n_{av} \sim n_{CO_2} = 6$), the main product from ethanol oxidation is acetic acid ($n_{acetic\ acid} = 4$), and there are considerable variations in product distribution between different catalysts (6). Mass transport limited currents for ethanol oxidation are usually lower than for methanol oxidation because of the typically lower stoichiometry and the lower diffusion coefficient (lower m) of ethanol (39). The decreasing mass transport limited currents for ethanol at high potentials are due to decreasing yields of CO_2 ($n_{co_2} = 12$) as the potential is increased (6).

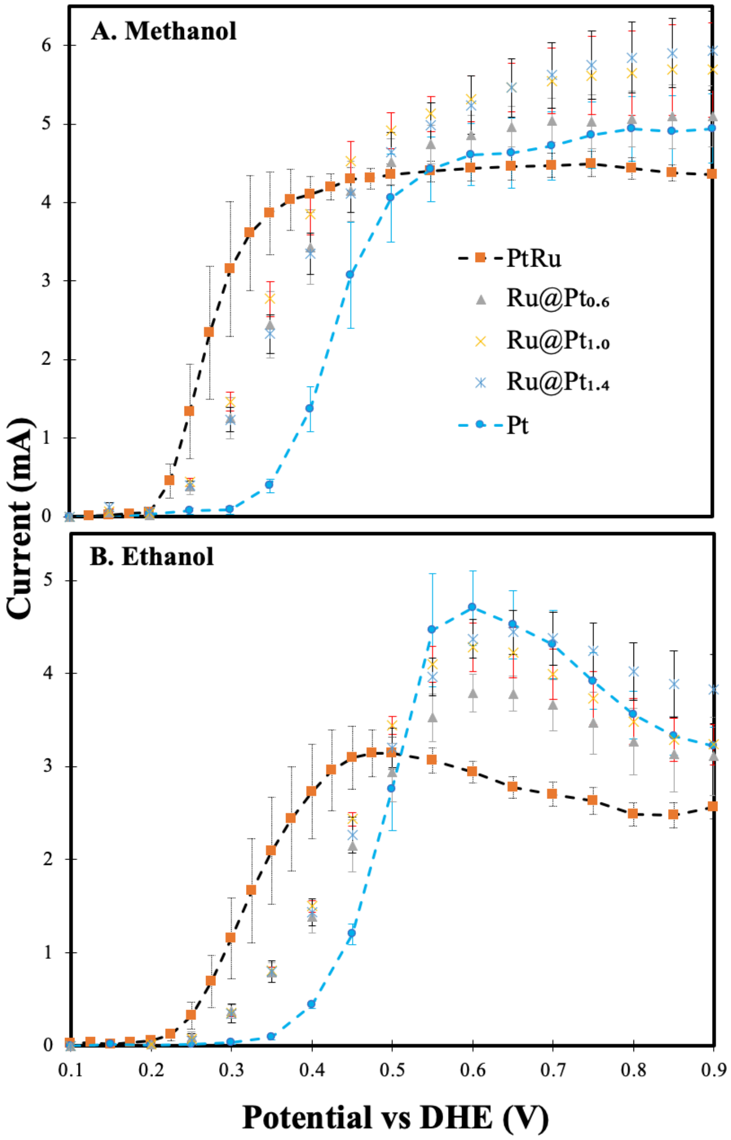

Figure 4.6. Polarization curves for methanol (A) and ethanol (B) oxidation at the Ru@Pt, Pt and PtRu catalysts (2.0 mg cm^{-2} of Pt+Ru) in a PEMEC at 80 °C.

Stoichiometries for ethanol oxidation, calculated from the polarization curves in Figure 4.6B by using equation 4.3 as previously described (39), are shown as a function of potential in Figure 4.7. Values below 0.50 V cannot be accurately determined because of uncertainty in the influence of the electron transfer kinetics (39). Stoichiometries for the Ru@Pt catalysts are intermediate between those of PtRu and Pt at most potentials, although values for the $Ru@Pt_{1.4}$ catalyst were significantly higher than both at potentials above 0.70 V. Whereas stoichiometry continuously decreased with potential above 0.50 V at the PtRu catalyst, it increased to a peak at the Ru@Pt and Pt catalysts. These differences show that selectivity for the complete oxidation of ethanol to CO_2 is very sensitive to the coverage of Pt at the catalyst surface, and the effect of the core on the surface electronic structure. The much higher stoichiometries at the Pt and Ru@Pt catalysts relative to the PtRu alloy clearly demonstrate the importance of a Pt-rich surface for breaking the C-C bond of ethanol.

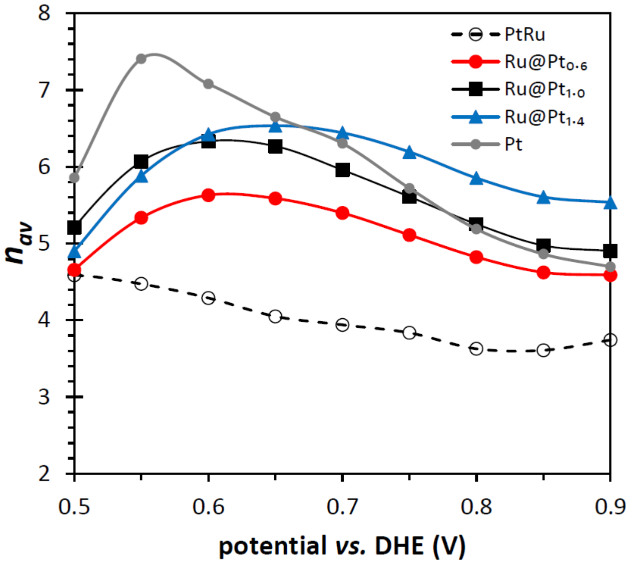

Figure 4.7. Stoichiometries calculated from the data in Figure 4.6B vs potential for ethanol oxidation at Ru@Pt, Pt and PtRu catalysts.

Determination of the stoichiometry for ethanol oxidation is vital for calculating the faradaic efficiency (and fuel efficiency) of electrolysis cells to produce hydrogen and fuel cells to provide electrical power (6, 48). It can also be used with other information to determine product distributions, by use of equation 4.5 (36),

$$n_{av} = 12/(F_{CO2} + 3F_{acetic\ acid}+6F_{acetaldehyde}) \qquad (4.5)$$

where F_i is the faradaic yield of product i. Since CO_2, acetic acid and acetaldehyde are the only products formed in significant quantities, their yields can be assumed to sum to 100%, and so the yield of only one needs to be measured if n_{av} is known. Here, the faradaic yield of CO_2 at 0.50 V was measured using a CO_2 monitor. The results are reported in Table 4.5, together with stoichiometries from Figure 4.7 and yields of acetic acid and acetaldehyde calculated by using equation 4.5.

Table 4.5. Faradaic yields of CO_2 (measured), stoichiometries (Figure 4.7), and calculated (equation 4.5) faradaic yields of acetaldehyde, and acetic acid at 0.50 V vs DHE.

catalyst	n_{av}	Faradaic yield		
		CO_2	Acetic acid	Acetaldehyde
Ru@Pt$_{0.6}$	4.7	38%	51%	11%
Ru@Pt$_{1.0}$	5.2	48%	43%	9%
Ru@Pt$_{1.4}$	4.9	46%	42%	12%
Pt	5.9	62%	28%	10%
PtRu	4.7	11%	89%	0%

Yields of CO_2 from the Ru@Pt catalysts (38-48%) were between the values obtained for PtRu (11%) and Pt (62%). Ru@Pt$_{1.0}$ provided the highest CO_2 yield for the core-shell catalysts, and also the highest n_{av}. The primary product (on a charge basis) was acetic acid at the PtRu and

Ru@Pt$_{0.6}$ catalysts, but CO_2 for Pt, Ru@Pt$_{1.0}$, and Ru@Pt$_{1.4}$. Acetaldehyde was a minor product ($\leq$ 12%) at all of the catalysts, and negligible for PtRu.

4.3.5. Anode performance and efficiency

All of the Ru@Pt catalysts reported here provided higher performances for ethanol oxidation than a previously reported Ru@Pt$_{0.85}$ catalyst that was used under the same conditions (14). For example, the new Ru@Pt$_{1.0}$ catalyst provided currents that were 33% and 18% higher at 0.40 V and 0.50 V, respectively. The enhanced activity can most likely be attributed to the higher crystallinity of the Ru core and/or the absence of a capping agent in the synthesis (13, 29), although the bifunctional effect of exposed Ru could also play a significant role.

The performances of the Ru@Pt catalysts for ethanol oxidation in the PEM cell are similar to those that have been reported for PtRu@Pt core-shell catalysts (37) and mixtures and bilayers of Pt and PtRu catalysts (48). They all yield polarization curves and stoichiometries that are intermediate between those of Pt and PtRu catalysts individually. This is important for ethanol electrolysis and fuel cells because it provides an optimum balance between voltage efficiency (low anode potential) and faradaic efficiency (high stoichiometry) (48). An added advantage of the Ru@Pt core-shell catalysts is that a lower Pt:Ru ratio is required to produce a similar balance. In addition, catalysts with a Pt shell are thought to be more durable than PtRu alloys, which suffer from dissolution of surface Ru (13, 15, 16).

4.4. Conclusions

Ru@Pt catalysts with high performances for methanol and ethanol oxidation have been conveniently prepared from a commercial carbon-supported Ru catalyst. Variation of the Pt:Ru ratio from 0.6 to 1.4 provided Pt shell thicknesses of 1.3 to 2.5 monolayers, with compressive strains ranging from 2.4% to 0.6%. Electrochemical activities for methanol and ethanol oxidation were intermediate between those for commercial Pt and PtRu alloy catalysts, providing much higher currents than Pt at low potentials, and much higher currents than PtRu at high potentials. This will optimize the efficiency of ethanol oxidation in electrolysis and fuel cells.

For ethanol oxidation, the use of a Pt shell on a Ru core greatly promotes the complete oxidation to CO_2 relative to PtRu alloys, which produce large amounts of acetic acid. Ru@Pt catalysts are particularly well suited for use in ethanol electrolysis and fuel cells to provide high activity at low potentials, control selectivity and enhance durability.

4.5. References

1. B. Garlyyev, S. Xue, J. Fichtner, A. S. Bandarenka and C. Andronescu, ChemSusChem, **13**, 1 (2020).
2. C. Coutanceau and S. Baranton, Wiley Interdisciplinary Reviews-Energy and Environment, **5**, 388 (2016).
3. A. Caravaca, A. de Lucas-Consuegra, A. B. Calcerrada, J. Lobato, J. L. Valverde and F. Dorado, Applied Catalysis: B Environmental, **134**, 302 (2013).
4. C. Lamy, T. Jaubert, S. Baranton and C. Coutanceau, Journal of Power Sources, **245**, 927 (2014).
5. A. Rodriguez-Gomez, F. Dorado, A. de Lucas-Consuegra and A. R. de la Osa, Journal of Energy Chemistry, **56**, 264 (2021).
6. R. M. Altarawneh and P. G. Pickup, Journal of Electrochemical Society, **164**, F861 (2017).
7. L. An, T. S. Zhao and Y. S. Li, Renewable and Sustainable Energy Reviews, **50**, 1462 (2015).

8. L. Yaqoob, T. Noor and N. Iqbal, RSC Advances, **11**, 16768 (2021).

9. G. X. Yang, Q. Zhang, H. Yu and F. Peng, Particuology, **58**, 169 (2021).

10. S. Alayoglu, A. U. Nilekar, M. Mavrikakis and B. Eichhorn, Nature Materials, **7**, 333 (2008).

11. S. Alayoglu, P. Zavalij, B. Eichhorn, Q. Wang, A. I. Frenkel and P. Chupas, ACS Nano, **3**, 3127 (2009).

12. M. B. Gawande, A. Goswami, T. Asefa, H. Z. Guo, A. V. Biradar, D. L. Peng, R. Zboril and R. S. Varma, Chemical Society Reviews, **44**, 7540 (2015).

13. A. Hoang, E. El Sawy, A. Blackburn, S. Ketabi, M. Goledzinowski, F. J. E. Comeau and V. Birss, ACS Applied Energy Materials, **3**, 8423 (2020).

14. E. El Sawy, T. M. Brueckner and P. G. Pickup, Journal of Electrochemical Society, **167**, 106507 (2020).

15. E. Antolini, Journal of Solid State Electrochemistry, **15**, 455 (2011).

16. P. Ochal, J. L. G. de la Fuente, M. Tsypkin, F. Seland, S. Sunde, N. Muthuswamy, M. Ronning, D. Chen, S. Garcia, S. Alayoglu and B. Eichhorn, Journal of Electroanalytical Chemistry, **655**, 140 (2011).

17. T.-Y. Chen, T.-L. Lin, T.-J. M. Luo, Y. Choi and J.-F. Lee, ChemPhysChem, **11**, 2383 (2010).

18. E. N. El Sawy, H. A. El-Sayed and V. I. Birss, Physical Chemistry Chemical Physics, **17**, 27509 (2015).

19. Y. M. Hu, A. M. Zhu, Q. G. Zhang and Q. L. Liu, International Journal of Hydrogen Energy, **41**, 11359 (2016).

20. N. M. Sanchez-Padilla, S. M. Montemayor, L. A. Torres and F. J. Rodriguez Varela, International Journal of Hydrogen Energy, **38**, 12681 (2013).

21. N. Muthuswamy, J. L. G. de la Fuente, D. T. Tran, J. Walmsley, M. Tsypkin, S. Raaen, S. Sunde, M. Ronning and D. Chen, International Journal of Hydrogen Energy, **38**, 16631 (2013).

22. D. Kaplan, M. Alon, L. Burstein, Y. Rosenberg and E. Peled, Journal of Power Sources, **196**, 1078 (2011).

23. T.-Y. Chen, T.-J. M. Luo, Y.-W. Yang, Y.-C. Wei, K.-W. Wang, T.-L. Lin, T.-C. Wen and C. H. Lee, Journal of Physical Chemistry C, **116**, 16969 (2012).

24. J. J. Wang, Y. T. Liu, I. L. Chen, Y. W. Yang, T. K. Yeh, C. H. Lee, C. C. Hu, T. C. Wen, T. Y. Chen and T. L. Lin, Journal of Physical Chemistry C, **118**, 2253 (2014).

25. A. B. Kashyout, A. A. A. Nassr, L. Giorgi, T. Maiyalagan and B. A. B. Youssef, International Journal of Electrochemical Science, **6**, 379 (2011).

26. Y. Y. Zheng, H. T. Zhan, Y. X. Fang, J. H. Zeng, H. Liu, J. Yang and S. J. Liao, Journal of Materials Science, **52**, 3457 (2017).

27. T. M. Brueckner, E. Wheeler, B. Chen, E. N. El Sawy and P. G. Pickup, Journal of Electrochemical Society, **166**, F942 (2019).

28. F. H. B. Lima and E. R. Gonzalez, Applied Catalysis B: Environmental, **79**, 341 (2008).

29. J. S. Zou, M. Wu, S. L. Ning, L. Huang, X. W. Kang and S. W. Chen, ACS Sustainable Chemistry and Engineering, **7**, 9007 (2019).

30. Y. C. Hsieh, Y. Zhang, D. Su, V. Volkov, R. Si, L. J. Wu, Y. M. Zhu, W. An, P. Liu, P. He, S. Y. Ye, R. R. Adzic and J. X. Wang, Nat. Communication, **4**, 9 (2013).

31. R. M. Altarawneh, Energy and Fuels, **35**, 11594 (2021).

32. N. Shaari, S. K. Kamarudin, R. Bahru, S. H. Osman and N. Ishak, International Journal of Energy Research, **45**, 6644 (2020).

33. S. S. Araya, V. Liso, X. T. Cui, N. Li, J. M. Zhu, S. L. Sahlin, S. H. Jensen, M. P. Nielsen and S. K. Kaer, Energies, **13**, 596 (2020).

34. D. M. Fadzillah, S. K. Kamarudin, M. A. Zainoodin and M. S. Masdar, International Journal of Hydrogen Energy, **44**, 3031 (2019).

35. D. D. James and P. G. Pickup, Electrochimica Acta, **55**, 3824 (2010).

36. R. M. Altarawneh, P. Majidi and P. G. Pickup, Journal of Power Sources, **351**, 106 (2017).

37. A. H. Ali and P. G. Pickup, Journal of Electrochemical Society, **169**, 8 (2022).

38. K. Tedsree and A. Thanatsiri, in 5th Thailand International Nanotechnology Conference (NanoThailand), p. 10954, Nakhon Ratchasima, THAILAND (2016).

39. T. M. Brueckner and P. G. Pickup, Journal of Electrochemical Society, **64**, F1172 (2017).

40. R. M. Altarawneh, T. M. Brueckner, B. Y. Chen and P. G. Pickup, Journal of Power Sources, **400**, 369 (2018).

41. J. N. Schwammlein, B. M. Stuhmeier, K. Wagenbauer, H. Dietz, V. Tileli, H. A. Gasteiger and H. A. El-Sayed, Journal of Electrochemical Society, **165**, H229 (2018).

42. A. Schlapka, M. Lischka, A. Gross, U. Kasberger and P. Jakob, Physical Review Letters, **91**, 016101 (2003).

43. J. Xie, Q. H. Zhang, L. Gu, S. Xu, P. Wang, J. G. Liu, Y. Ding, Y. F. Yao, C. W. Nan, M. Zhao, Y. You and Z. G. Zou, Nano Energy, **21**, 247 (2016).

44. M. A. Rigsby, W. P. Zhou, A. Lewera, H. T. Duong, P. S. Bagus, W. Jaegermann, R. Hunger and A. Wieckowski, Journal of Physical Chemistry C, **112**, 15595 (2008).

45. A. S. Arico, A. K. Shukla, H. Kim, S. Park, M. Min and V. Antonucci, Applied Surface Science, **172**, 33 (2001).

46. E. N. El Sawy, H. A. El-Sayed and V. I. Birss, Chemical Communications, **50**, 11558 (2014).

47. R. Costa-Amaral and J. L. F. Da Silva, Physical Chemistry Chemical Physics, **20**, 24210 (2018).

48. R. M. Altarawneh and P. G. Pickup, Journal of Power Sources, **366**, 27 (2017).

Chapter 5: Electrochemical oxidation of ethanol and methanol at Rh@Pt catalysts at 80 °C in proton exchange membrane (PEM) cell

The principal author (Ahmed H Ali) contributed to all parts of this Chapter, including the literature review and the experiments. He performed all the required physical and electrochemical measurements. In addition, he analyzed the data and wrote the first draft of this paper.

The corresponding author (Peter G. Pickup) was responsible for funding, reviewing all my data analysis, editing my draft paper, and completing it for submission to the Journal of ECS Advances.

Detailed raw data are provided in Appendix C.

5.1. Introduction

Electrochemical oxidation of alcohols in PEMEC and PEMFC is the basis for developing direct alcohol fuel cell technologies for producing sustainable power (1-3) and alcohol electrolysis cells for efficient production of hydrogen (4, 5). Direct methanol fuel cells (DMFC) (6) have already been commercialized, while development of direct ethanol fuel cells (DECF) (7, 8) is impeded by their lower performance and critically by the production of acetaldehyde and acetic acid by-products (9).

Although methanol is the most efficient alcohol as a fuel, DMFC still face some obstacles, including carbon monoxide poisoning of platinum-based catalysts, high methanol oxidation overpotentials, and high crossover rates which degrade cathode performance (10). Ethanol is potentially the best alternative to methanol, due to its more sustainable production, lower toxicity, higher energy density, and lower crossover (1, 10). However, dissociation of the C-C bond of ethanol presents a currently insurmountable challenge to the development of DEFC (9). Most catalytic materials are very inefficient at breaking the C–C bond and produce acetic acid (transfer of 4 electrons; ($n = 4$) and acetaldehyde ($n = 2$) as the major products, while the complete oxidation to CO_2 ($n = 12$) is required for maximum faradaic efficiency ($\varepsilon_F = n_{av}/12$), where n_{av} is the average number of electrons transferred (10, 11).

Pt is the most efficient catalyst for oxidation of ethanol to CO_2 in PEM cells, but its activity is insufficient for practical applications (12). Many Pt-based binary and ternary catalysts have therefore been developed (13-16). In the presence of metals (M) such as Ru, Rh, Cu, Ni, Sn, and Pd, the electronic properties, bond distances, and coordination numbers of surface Pt atoms are changed, weakening the adsorption energy of intermediates and resulting in increased catalytic activity (11, 13, 14).

Pt-coated core-shell nanoparticles (M@Pt) have attracted considerable attention as a new class of these catalysts. Typically, one to three monolayer Pt shells are deposited onto a more electropositive core in order to minimize Pt consumption and improve catalytic activity and stability (17-29). The core metal can increase the catalytic activity of the Pt surface while retaining Pt-like selectivity (27-29). The strain effect and electronic interaction between the core and shell atoms significantly influence catalytic performance (17, 25, 30-32).

Many studies have concentrated on Pt-Ru and Pt-Sn bimetallic electrocatalysts because these combinations show much lower onset potentials than Pt for ethanol oxidation. This is normally attributed to oxidation of the strongly adsorbed CO intermediate by oxidized surface Ru and Sn species via a Langmuir–Hinshelwood (bifunctional) mechanism (11, 14, 33). However, the major products are acetic acid and acetaldehyde due to disruption of the surface Pt ensembles (2-3 adjacent Pt atoms) required for breaking the C-C bond (34). Recent studies have shown that the deleterious effect of Ru on the selectivity of Pt for CO_2 formation can be mitigated by employing Ru@Pt (27, 29) or PtRu@Pt (28) nanoparticles with core-shell structures. These combine the beneficial effect of Ru in the core with the selectivity of a pure Pt surface for C-C bond cleavage.

There are many reports that PtRh alloy nanoparticles show enhanced selectivity for production of CO_2 from ethanol, relative to pure Pt, due to the strong ability of Rh to activate C-C bond dissociation (35-49). Additionally, PtRh nanoparticles are very stable in harsh operating environments (50). However, the effectiveness of Rh for promoting C-C bond cleavage during ethanol oxidation at ambient temperature has recently been questioned (9), and the relevance of these studies to ethanol oxidation in PEM cells at elevated temperatures is unclear.

There have been a number of reports of ethanol oxidation at Pt-Rh catalysts at elevated temperatures, in both aqueous acids (17, 40) and PEM cells (27, 51). Lima and Gonzalez compared activities for Pt, PtRu and PtRh alloy, and Ru@Pt and Rh@Pt core-shell catalysts in $HClO_4$(aq) at 25 °C and 60 °C (17). They found that both core-shell catalysts greatly decreased the onset potential for ethanol oxidation at 25 °C and were more effective than the alloys. However, the alloy catalysts were superior at 60 °C, and Pt was better than Rh@Pt. Overall, Ru was more effective at promoting ethanol oxidation at low potentials than Rh, and this correlates with its stronger effect on decreasing the potential for oxidation of adsorbed CO. The effects of Ru and Rh were attributed to strain and electronic effects, which lower the d-band center of surface Pt atoms and weaken the binding of adsorbates (17). In later work, it was shown by differential electrochemical mass spectrometry that Rh produced higher transient efficiencies for CO_2 formation than either Pt or Rh@Pt (40), but without sustained CO_2 production from bulk ethanol.

PtRh alloy nanoparticles with a preferential (100) orientation have been shown to be more active than Pt for ethanol oxidation, and more selective for producing acetic acid and CO_2 over acetaldehyde (51). There have also been other reports on the use of Rh@Pt catalysts for ethanol oxidation (19, 23, 27, 52). However, in the only study in a PEM cell, the performances of the Rh@Pt catalysts were inferior to both Pt and Ru@Pt catalysts, despite their superior performances in H_2SO_4(aq) at ambient temperature (27).

The purpose of the work described here was to provide a more detailed understanding of the effects of Rh@Pt catalysts on ethanol oxidation, and the relationships between behaviours observed in aqueous acid electrolytes and PEM cells. Specifically, the influence of the Rh core on both activity and selectivity for ethanol oxidation has been documented in PEM cells, as a function of the thickness of the Pt shell. In addition, the use of cyclic voltammetry at ambient temperature in an aqueous acid electrolyte has been evaluated as a tool for screening and selecting Rh@Pt catalysts for alcohol (methanol and ethanol) oxidation in PEM cells.

Carbon-supported Rh@Pt/C catalysts with Pt shell thicknesses ranging from 0.5 to 3.0 monolayers (ML) were prepared by deposition of Pt onto a commercial Rh/C catalyst using ethanol as the reductant and solvent. Their catalytic activities for ethanol and methanol oxidation were evaluated using cyclic voltammetry at ambient temperature and proton exchange membrane electrolysis cells (PEMEC) at 80 °C. Electrolysis cells were employed, rather than fuel cells, in order to avoid errors due to crossover of ethanol through the membrane and to provide a stable reference potential via hydrogen evolution at the cathode (53, 54).

5.2. Experimental

5.2.1. Materials

Rhodium supported on Vulcan XC-72 carbon (Rh/C; 20% Rh by mass; Fuel Cell Store), $H_2PtCl_6.6H_2O$ (Pressure Chemical Co.), Pt on Vulcan carbon XC-72 (Pt/C; 40% Pt by mass; Alfa Aesar), anhydrous ethanol (99.9%; Commercial Alcohols Inc.), sodium hydroxide (BHD Inc.), 5% Nafion ^{TM} solution (Dupont), sulfuric acid (95-98%; Fisher Scientific), methanol (HPLC grade; Fisher Scientific), 2-propanol (Caledon) and 1-propanol (J.T. Baker), were used as received. All the aqueous solutions were prepared using deionized water.

5.2.2. Synthesis of the Rh@Pt catalysts

Rh/C (40 mg) was dispersed in ethanol (20 mL) by sonication for 20 min, and then heated under reflux for 1 h to reduce oxide and hydroxide species at the Rh surface. The required amount (Table C 1) of $H_2PtCl_6.6H_2O$ in 5 mL of ethanol was injected dropwise, and reflux was continued for a further 1 h. NaOH(aq) (1 M) was then added in a molar ratio of 3:1 to Pt, and heating was continued for 2 h to ensure the complete reduction to Pt metal (26). The catalyst was collected using a centrifuge (10 min at 9000 rpm) and washed several times with boiling water until the absence of Cl^- was confirmed with silver nitrate. The catalysts were dried overnight in an oven at 80 °C. They are designated as Rh@Pt(0.5 ML), Rh@Pt(1.0 ML), Rh@Pt(1.5 ML), Rh@Pt(2.0 ML), and Rh@Pt(3.0 ML) according to the average number of platinum monolayers that should have been deposited onto the Rh nanoparticles.

5.2.3. Physical characterization

Pt:Rh atomic ratios were determined by energy dispersive X-Ray emission (EDX) with an FEI Quanta 400 scanning electron microscope (SEM). The catalysts (2.5 mg) were dispersed in a mixture of water, 1-propanol and 2-propanol (0.2 mL) at volume ratios of 2:3:3 for application to carbon tabs.

A Rigaku Ultima IV X-ray diffractometer (XRD) with a Cu Kα radiation source (0.154 nm) was used to study the crystal structure of the catalysts. The diffracted radiation was detected by using a scintillation counter analyzer.

X-ray photoelectron spectroscopy (XPS) using a VG Micro-tech Multi-lab ESCA 2000 system was conducted by Andrew George at Dalhousie University (Halifax, Nova Scotia, Canada).

A Tecnai TM Spirit transmission electron microscope (TEM, Faculty of Medicine at Memorial University) was used to determine the average particle size, size distribution and the degree of dispersion on the carbon support. An average nanoparticle size for each catalyst was obtained by measuring the diameters of ca. 80 randomly selected nanoparticles using the Image J 1.53a program. TEM samples were prepared by dispersing 1 mg of catalyst in 200 µL of water, 1-propanol, and 2-propanol mixture at volume ratios of 2:3:3 by sonication for at least 1 h, then one droplet of the ink was placed on the TEM grid.

5.2.4. Electrochemical characterization at ambient temperature

An SP-50 Biologic potentiostat with EC-lab software was used for cyclic voltammetry (CV) in a three-electrode glass cell, with a Pt wire counter electrode and saturated calomel reference electrode (SCE). Carbon fibre paper (CFP, 0.24 cm^2, Toray TGP-H-090) working electrodes were painted with the desired volume of catalyst ink to give a 0.3 mg cm^{-2} metal (Rh+Pt) loading. The inks were prepared by sonication of 2 mg of catalyst in 200 μL of a solvent mixture consisting of water, 1-propanol, and 2-propanol at volume ratios of 2:3:3. All CV measurements were made at ambient temperature in 1 M aqueous sulfuric acid that had been purged with UHP N_2. After recording background CVs (six cycles at 100 mV s^{-1}), methanol or ethanol was added to give a concentration of 0.1 M. The alcohol was homogeneously mixed by purging with N_2 for 3 min. CVs for oxidation of the alcohols were obtained for three cycles at a scan rate of 10 mV s^{-1}. The final anodic scan is shown in all cases.

5.2.5. Oxidation of methanol and ethanol at 80 °C in a multi-anode PEMEC

A commercial fuel cell (Electrochem Inc.) modified to accommodate an array of nine 0.24 cm^2 anodes was operated as an electrolysis cell in crossover mode at 80 °C, as previously described (28, 55). A single 5 cm^2 Pt black on CFP cathode was employed with a Nafion-117 membrane. Aqueous methanol or ethanol (0.1 M) was pumped through the cathode chamber at a flow rate of 0.5 mL min^{-1}, while the anode was purged with N_2 at 10 mL min^{-1}. Oxidation of alcohol that diffuses through the Nafion membrane to the anodes provides mass transport control of the current at high potential, which allows the stoichiometry of the reaction (n_{av}) to be determined (55). An MSTAT potentiostat from Arbin Instruments was used to control the potential applied to each anode relative to the cathode, which produces H_2 and therefore acts as a dynamic hydrogen electrode (DHE).

Anodes were prepared by painting catalyst inks onto CFP disks (0.24 cm^2) to give a metal loading of 2.0 mg cm^{-2}. A 5% Nafion solution was applied to the catalyst surface, equivalent to 30% of the total catalyst + Nafion mass. Catalyst inks were prepared by dispersion of 4 mg of catalyst in 200 μL of a mixture of water, 2-propanol, and 1-propanol (2:3:3).

All anodes were set to a constant potential of 0.70 V (vs DHE) for at least 1 h before each polarization curve measurement. Polarization curves were obtained by measuring the current for 3 min at constant potentials, starting at 0.90 V. The average current for the last 60 s of each applied potential is reported. Initially, consecutive polarization curves for methanol oxidation (four) were recorded until they were consistent. Then two consecutive curves were recorded for ethanol oxidation. The final polarization curve is reported in all cases.

As previously described (28, 56), CO_2 generated by oxidation of the alcohols at 0.50 V was monitored using a nondispersive infrared (NDIR) CO_2 sensor (Telaire T6615). During CO_2 measurements, the N_2 flow rate was increased to 50 mL min^{-1} while the alcohol flow rate was decreased to 0.2 mL min^{-1}.

5.2.6. Ethanol oxidation at 80 °C in a 5 cm^2 PEMEC

A commercial PEMFC (Fuel Cell Technologies, Inc.) was employed as an electrolysis cell with 0.1 M ethanol (at 0.5 mL min^{-1} for polarization curves) at the anode and N_2 (30 mL min^{-1}) at the cathode (12). Hydrogen production at the cathode provides a stable reference potential (DHE). Anodes prepared as described above, by spreading the catalyst ink onto a 5 cm^2 carbon fibre paper square to give a metal (Rh + Pt) loading of 2.0 mg cm^{-2} with 30 mass% Nafion, were separated from a 5 cm^2 Pt black cathode (4.0 mg cm^{-2} on wet-proofed CFP) by a Nafion-117 membrane.

Electrochemical measurements were made at 80 °C under steady-state conditions at constant cell potentials using a Hokuto Denko HA-301 potentiostat. The faradaic yield of CO_2 was measured at each potential with the Telaire T6615 NDIR CO_2 sensor.

5.3. Results

5.3.1. Physical characterization of the Rh@Pt catalysts

The Pt:Rh mole ratios of the Rh@Pt catalysts measured by EDX are compared with the target ratios in Table 5.1. The measured values agree with the expected values, or are slightly higher, which confirms the success of the synthetic method for complete deposition of the Pt. The increasing discrepancy for catalysts with more Pt, with EDX indicating a higher Pt:Rh ratio than expected, is consistent with the formation of core-shell structures in which electron and X-ray absorption by the Pt shell suppress the X-ray intensity from the Rh core. The higher measured ratios are inconsistent with incomplete deposition of Pt.

Pt:Rh ratios measured by XPS (see below), using the relative intensities of the Rh 3d and Pt 4f peaks, are also included in Table 5.1 for comparison. Since XPS is much more surface sensitive than EDX, the much higher Pt:Rh ratios observed by XPS confirm that Rh@Pt core-shell structures were formed.

Table 5.1. Comparison of measured (EDX and XPS) and target Pt:Rh atomic ratios for the Rh@Pt catalysts.

Catalyst	Pt:Rh atomic ratio		
	Expected	EDX	XPS
Rh@Pt(0.5 ML)	0.31	0.31	0.45
Rh@Pt(1.0 ML)	0.64	0.65	1.04
Rh@Pt(1.5 ML)	1.04	1.07	1.72
Rh@Pt(2.0 ML)	1.49	1.56	2.55
Rh@Pt(3.0 ML)	2.60	2.73	4.75

TEM images (Figure C 1) show that the metal nanoparticles were well dispersed over the carbon support. They have approximately spherical shapes with low agglomeration. Deposition of Pt did not noticeably change the appearance of the metal nanoparticles (i.e. relative to the Rh/C precursor), other than a steady increase in size as more Pt was added. Histograms of the particle size distributions (Figure C 2) show that the growth of the Rh@Pt particles occurred without significant broadening of the size distribution, and there is no evidence of a secondary distribution due to the formation of Pt nanoparticles.

The average diameters of ca. 80 randomly selected particles for each catalyst are compared with the expected diameters for Rh@Pt core-shell particles (eq. C1 (57)) in Table 5.2. The agreement between the measured and expected particle sizes confirms the formation of core-shell structures with the target compositions.

Table 5.2. Measured (TEM) and expected average diameters of the Rh@Pt and Rh nanoparticles, and specific strain of the Pt layers measured by XRD.

Catalyst	Average particle diameter (nm)		Strain
	Expected	TEM	
Rh	3.00 [a]	3.08 ± 0.33	N/A
Rh@Pt(0.5 ML)	3.39	3.38 ± 0.47	–2.7%
Rh@Pt(1.0 ML)	3.68	3.63 ± 0.56	–2.1%
Rh@Pt(1.5 ML)	3.97	3.88 ± 0.57	–1.5%
Rh@Pt(2.0 ML)	4.26	4.15 ± 0.60	–1.4%
Rh@Pt(3.0 ML)	4.83	4.67 ± 0.43	–0.72

a. Specified by the fuel cell store.

XRD patterns (Figure 5.1) show that all of the Rh@Pt catalysts have the same FCC crystalline structure as pure Rh and Pt. The diffraction peaks of the Rh@Pt nanoparticles were shifted from the positions for pure Rh toward the lower values for Pt as the thickness of the Pt layer was increased. This confirms the deposition of Pt onto the Rh nanoparticles and shows that there is a significant strain effect induced by the mismatch between Pt and Rh lattices.

The specific strain (S) of the Pt shell, calculated from the shift of the Pt(220) peak from the value for pure Pt (58), is shown in Table 5.2. The negative values show compressive strain of the Pt shell, which decreased as the shell thickness was increased. Previous reports have shown that varying the strain of Pt shells changes the adsorption energy of alcohol molecules and intermediates produced during their oxidation (30, 59, 60). Its effect on the oxidation of the adsorbed CO intermediate plays a major role in the activities of Ru@Pt and Rh@Pt catalysts (25, 27, 30, 60-63).

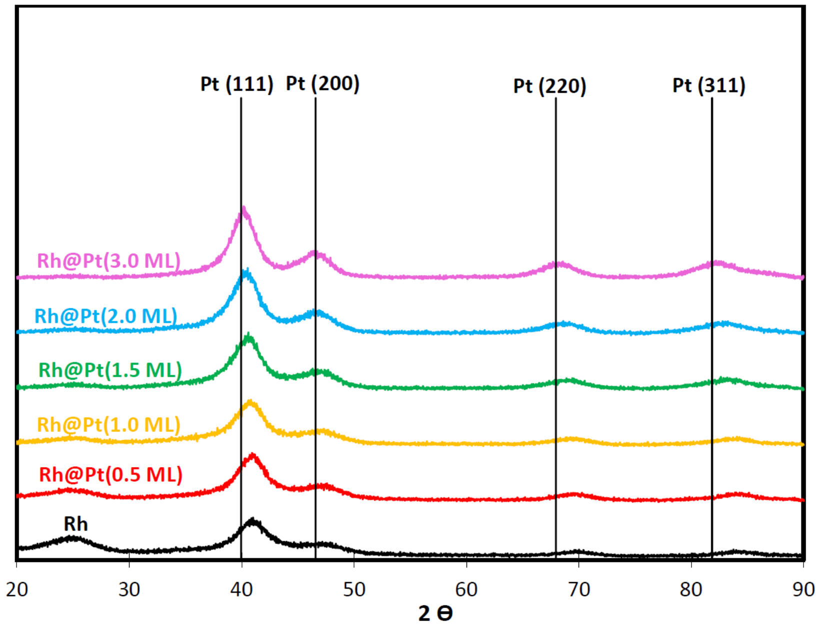

Figure 5.1. XRD patterns for the Rh and Rh@Pt catalysts. The vertical lines show the positions of the peaks for pure Pt.

The Rh 3d and Pt 4d regions of XPS spectra of the catalysts are shown in Figure 5.2, with survey spectra and deconvolution of the Rh 3d and Pt 4d peaks in Figure C 3 and Figure C 4, respectively. Deposition of Pt onto the Rh catalyst resulted in steady growth of Pt $4d_{5/2}$ (Figure 5.2) and Pt $4d_{3/2}$ (Figure C 4) peaks at binding energies (BE) of ca. 315 eV and 332 eV, respectively. This was accompanied by an increasing negative shift in the Rh 3d BE to lower values. The Pt 4f BE (Figure 5.3), which are more sensitive to changes than the 4d peak, were higher than for pure Pt, but shifted towards the Pt values as the Pt shell thickness was increased.

For PtRh alloy (64) and Rh@Pt (17) nanoparticles electron transfer from Pt (high BE) to Rh (lower BE), and the resulting downshift in the d-band center of Pt (higher Pt BE) has been attributed to lattice strain, since there is not a significant difference in electronegativity to cause an electronic effect (64).

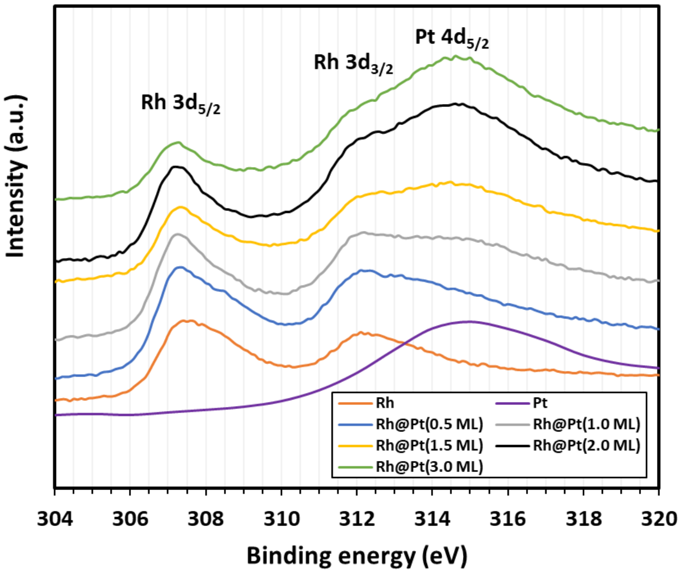

Figure 5.2. Rh 3d and Pt 4d region of XPS spectra of the Rh, Pt, and Rh@Pt catalysts.

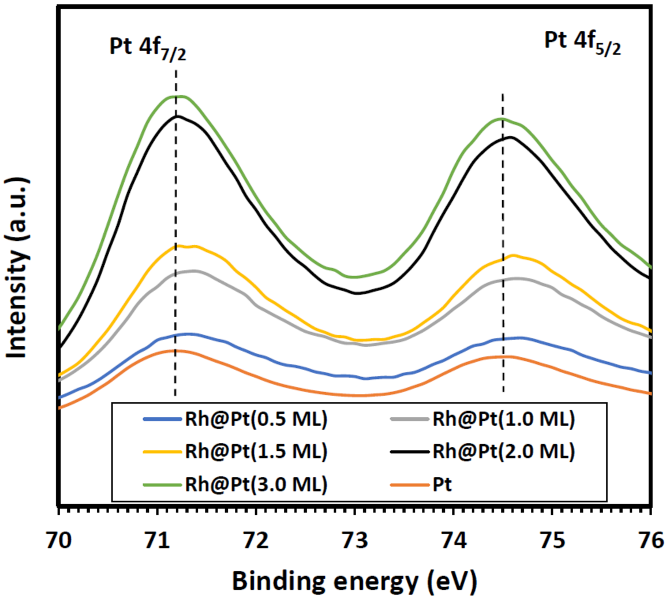

Figure 5.3. Pt 4f region of XPS spectra of the Pt and Rh@Pt catalysts.

5.3.2. Cyclic voltammetry in aqueous sulfuric acid

Cyclic voltammetry of the catalysts in aqueous acid (Figure 5.4) shows the evolution of the surface electrochemistry as Pt was added to the Rh core. In the hydrogen adsorption and desorption region below 0.10 V, addition of Pt suppressed activity of the Rh surface and split the single wave (41) into the two processes that are characteristic of a Pt surface. This region became more Pt-like as the shell thickness was increased. Similarly, the Rh oxide peaks at 0.63 V and 0.18 V were strongly suppressed by just 0.5 ML of Pt, and the voltammograms for the Rh@Pt catalysts became very similar to the Pt voltammogram at higher coverages. This indicates that the Rh surface became completely covered by Pt (60). With increasing Pt thickness, the rhodium oxide reduction wave shifted positively from 0.18 V to 0.51 V, which is close to the peak at 0.52 V for reduction of oxide on the Pt electrode.

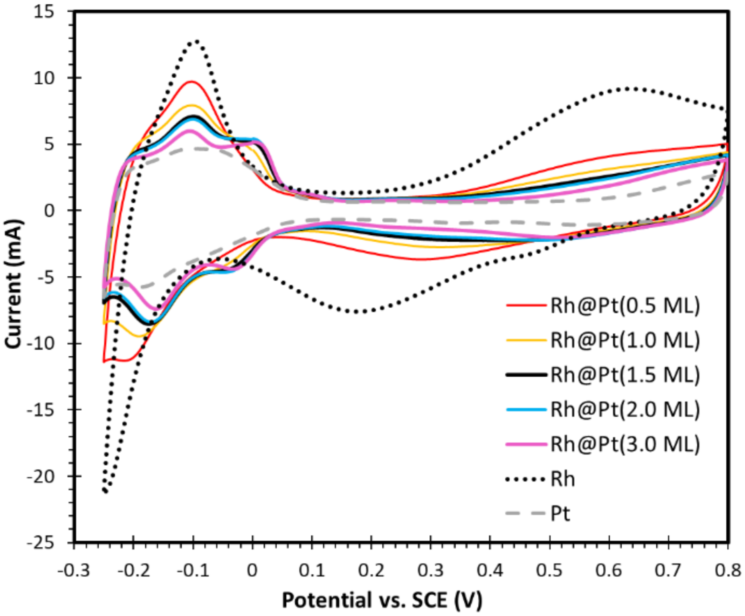

Figure 5.4. Cyclic voltammograms (100 mV s^{-1}) for Rh@Pt, Pt, and Rh catalysts (0.3 mg cm^{-2} of Pt+Rh) in 1 M H_2SO_4(aq) at ambient temperature.

5.3.3. Cyclic voltammetry for methanol and ethanol oxidation in aqueous sulfuric acid

Cyclic voltammetry for methanol oxidation at the Rh@Pt, Rh, and Pt catalysts at ambient temperature is shown in Figure 5.5. Deposition of Pt onto the Rh catalyst decreased the onset and peak potentials for methanol oxidation greatly and produced large increases in the peak current. The optimum Pt coverages were 1.5 ML at low potentials (< ca. 0.40 V) and 2.0 ML at higher potentials. The Rh@Pt catalysts also decreased the onset potential relative to the Pt catalyst, greatly increased the current at low potentials, decreased the peak potential, and increased the peak current for >1.0 ML of Pt. Overall, all of the Rh@Pt catalysts provided much higher performances for methanol oxidation than either Rh or Pt alone.

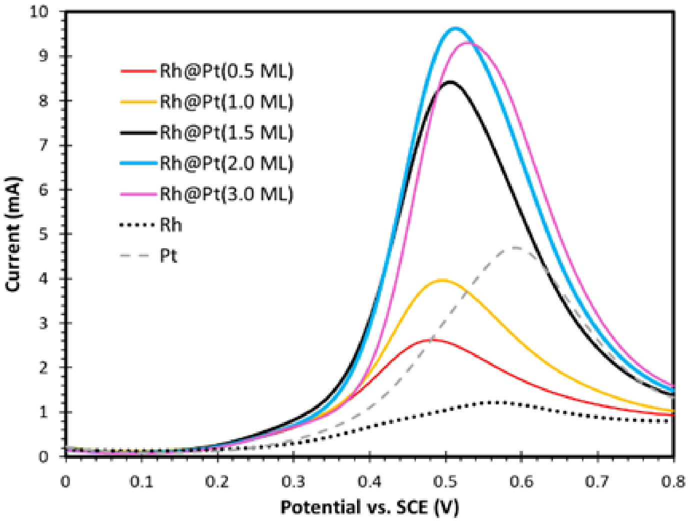

Figure 5.5. Linear sweep voltammetry (10 mV s^{-1}) for oxidation of 0.1 M methanol in 1 M H_2SO_4(aq) at Rh@Pt, Rh, and Pt catalysts (0.3 mg cm^{-2} of Pt+Rh) at ambient temperature.

The Rh core predominantly influences the electrocatalytic activity of the Pt shell via bifunctional, electronic, and strain effects (17, 52), which operate over significantly different distances (58, 65). The bifunctional effect requires surface Rh sites, so that Rh-OH species are available to oxidize the adsorbed CO intermediate to CO_2. It is most effective at sub-monolayer Pt coverages and should become insignificant at 1.0 ML if the Pt coverage is uniform. The much lower currents for the Rh@Pt(0.5 ML) and Rh@Pt(1.0 ML) catalysts in Figure 5.5, relative to those with higher coverages, clearly show that improvements in activity due to the bifunctional effect were relatively minor.

In contrast, the strain effect operates over a much larger distance (five or more monolayers), while the electronic effect becomes insignificant after a few monolayers (65). Consequently, the optimum performance seen for 1.5 ML of Pt over the full potential range in Figure 5.5 suggests that both electronic and strain effects influence the activities of the Rh@Pt nanoparticles. The persistence of the very strong effect on the peak current at 3.0 ML indicates that the strain effect plays the major role, while the shift to higher potential suggests that the electronic effect may play a significant role at potentials below ca. 0.45 V.

Deposition of Pt onto the Rh core also improved activity for the oxidation of ethanol over both Rh and Pt alone (Figure 5.6), although the effects are more complex than for methanol. Interestingly, the Rh catalyst was more active for ethanol oxidation than for methanol, with a higher peak current (1.35 mA vs 1.22 mA) and lower half-wave potential (0.37 V vs 0. 40 V). Consequently, it produced much higher currents than Pt at potentials below 0.50 V, and higher currents than most of the Rh@Pt catalysts below 0.48 V.

Deposition of 0.5 ML onto the Rh core shifted the onset potential for ethanol oxidation to lower potential and increased the current at all potentials, with a 2.1 fold increase in the peak current. This suggests that there was a significant bifunctional effect, although the ability of the surface Pt atoms to adsorb ethanol presumably plays a major role, and there may be a significant electronic effect. Increasing the Pt shell thickness to 1.0 ML produced the most active catalyst, with the lowest half-wave potential and almost double the peak current relative to 0.5 ML. However, it was less active than Rh@Pt(0.5 ML) at potentials below 0.35 V. This highlights the significance of the bifunctional effect for 0.5 ML of Pt at low potentials.

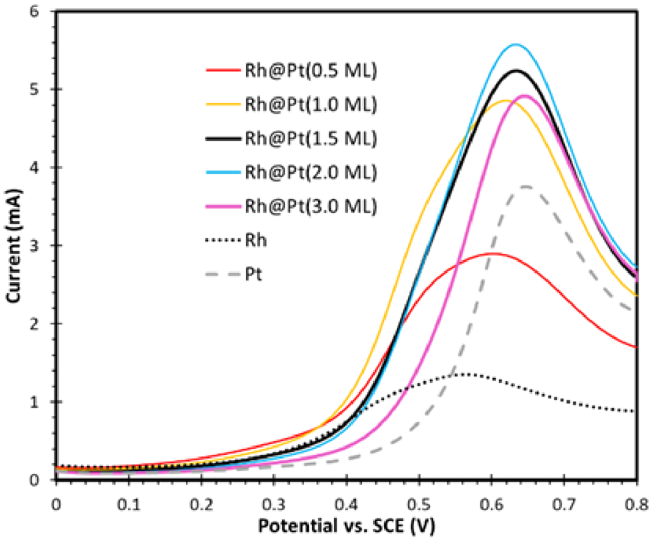

Figure 5.6. Linear sweep voltammetry (10 mV s^{-1}) for oxidation of 0.1 M ethanol in 1 M H_2SO_4(aq) at Rh@Pt, Rh, and Pt catalysts (0.3 mg cm^{-2} of Pt+Rh) at ambient temperature.

As the Pt shell thickness was increased further, there was a progressive shift of the ethanol oxidation wave to higher potentials. This is more pronounced than the similar effect seen for methanol (Figure 5.5), and persisted up to 3.0 ML. It is consistent with a combination of electronic and strain effects, with strain becoming dominant at higher coverages. All of the Rh@Pt catalysts provided higher currents than the Pt catalyst at all potentials, showing that there was still a significant strain effect at 3.0 ML.

5.3.4. Oxidation of methanol and ethanol in a 9-anode PEMEC at 80 °C

A PEMEC with nine separate anodes and a single cathode was used to characterize the performances of the catalysts under fuel cell-like conditions, measure CO_2 yields (56), and determine stoichiometries for ethanol oxidation (55). Three electrodes for each catalyst were run simultaneously to confirm the reproducibility (55).

Polarization curves for the oxidation of methanol and ethanol are shown in Figure 5.7. The relative performances of the catalysts in the PEM cell differ significantly from those seen in cyclic voltammetry at ambient temperature (Figures 5.5-5.6), demonstrating the importance of assessing catalysts under both conditions. Operation of the PEM cell in crossover mode provides steady-state currents that are limited by the rate of diffusion of the alcohol through the Nafion membrane (mass transport control, akin to rotating disc voltammetry) at high potentials (55). In contrast, cyclic voltammetry is strongly influenced by rapid changes in the mass transport conditions and populations of intermediates adsorbed on the catalyst surface.

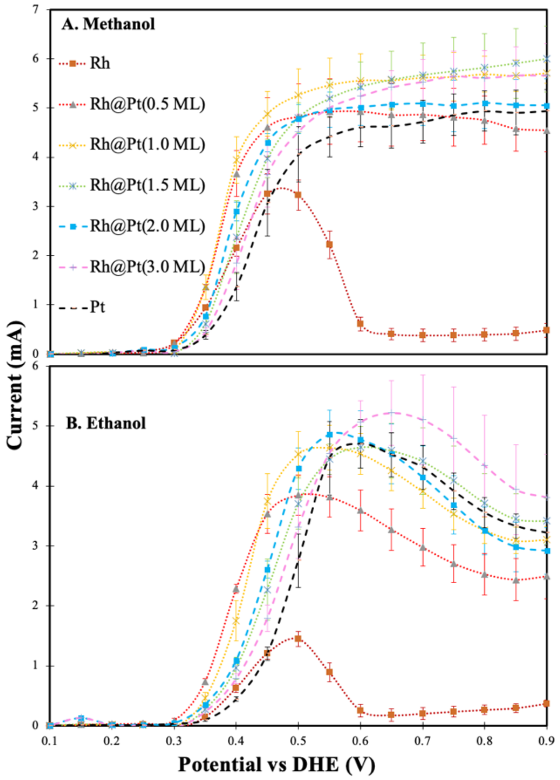

Figure 5.7. Polarization curves for methanol (A) and ethanol (B) oxidation at Rh@Pt, Rh, and Pt catalysts (2.0 mg cm^{-2} of Pt+Rh) in a 9-anode PEMEC at 80 °C in crossover mode.

For methanol oxidation (Figure 5.7A), all the Rh@Pt catalysts and the Pt catalyst reached a similar mass transport limiting current at high potential. The differences between the currents above 0.60 V for these catalysts are within the experimental uncertainty of the method (55). In contrast, the current at the Rh catalyst was very low at ≥ 0.60 V, indicating that it was limited by very slow kinetics in this region.

The limiting current (I_{lim}) in the PEM cell can be quantified using eq. 5.1, where C is the concentration of the alcohol solution, A is the electrode area, and m is the mass transport coefficient.

$$I_{lim} = n_{av}AFmC \qquad (5.1)$$

Since CO_2 is the only significant product from methanol oxidation at Pt catalysts under these conditions, $n_{av} \sim 6$. The similar limiting currents for the Rh@Pt catalysts show that they also oxidize methanol to CO_2 with high selectivity.

At lower potentials, where the current is under kinetic and mixed kinetic-mass transport control, the Rh@Pt catalysts were all much more active than Pt at all potentials, and the Rh@Pt(0.5 ML) and Rh@Pt(1.0 ML) catalysts were superior to Rh. Their activity decreased as the thickness of the Pt shell was increased. The superior activities of the Rh@Pt(0.5 ML) and Rh@Pt(1.0 ML) catalysts for methanol oxidation in the PEM cell are in stark contrast with their performances in cyclic voltammetry (Figure 5.5), where they gave much lower currents than the Rh@Pt catalysts with thicker Pt shells.

For ethanol oxidation (Figure 5.7B), the trend in activities in the kinetic region of the polarization curves (< 0.45 V) was similar to that for methanol, although more pronounced. Rh@Pt(0.5 ML) provided the highest currents at ≤ 0.40 V, suggesting that the bifunctional effect of exposed Rh-OH was significant. Currents in this region generally decreased as the thickness of the Pt shell was increased but remained higher than for Pt and Rh. The superiority of Rh@Pt(3.0 ML) over Pt in the kinetic region shows that the strain effect of the Rh core was a major factor in the increased activities of the Rh@Pt catalysts. At 0.40 V, the current at the Rh@Pt(0.5 ML) catalyst was five times higher than at Pt, making it very attractive for use in ethanol fuel and electrolysis cells.

In contrast to the polarization curves for methanol, which reach almost constant limiting currents, the ethanol polarization curves peak at potentials between 0.50 V and 0.65 V. The decreasing currents at higher potentials are due to changes in the reaction stoichiometry due to changes in the product distribution (eq. 5.2) (55),

$$n_{av} = \sum n_i x_i \qquad (5.2)$$

where n_i is the number of electrons transferred to form product *i,* and x_i is the fraction of ethanol that is converted to product *i*.

Stoichiometries for ethanol oxidation, calculated from the polarization curves in Figure 5.7B, by using eq. 5.1 as previously described (55), are shown as a function of potential in Figure 5.8 (data for Rh has been omitted because it clearly did not reach the mass transport limit). Significantly, the Rh@Pt catalysts with the highest Pt coverages (1.5-3.0 ML) provided higher stoichiometries than the Pt catalyst, indicating that the stain effect of the Rh core facilitates more complete oxidation of ethanol. In contrast, the significantly lower stoichiometries at Rh@Pt(0.5 ML) show that selectivity for breaking the C-C bond to form CO_2 (n_{CO2} = 12) was inhibited by Rh at the catalyst surface, due to the ensemble (third-body) effect (34).

In order to understand the differences in the activity and selectivity of the Rh@Pt and Pt catalysts it is necessary to determine the yields of acetaldehyde, acetic acid, and CO_2, which provide the rates for the main reaction pathways (66). Their faradaic yields (F_i) are related to the stoichiometry by eq. 5.3,

$$n_{av} = 12/(F_{carbon\ dioxide} + 3F_{acetic\ acid} + 6F_{acetaldehyde}) \qquad (5.3)$$

Since the sum of the yields of these three products can reasonably be assumed to be 100% (12), the yields of acetic acid and acetaldehyde can be calculated from $F_{carbon\ dioxide}$ (measured by using an NDIR CO_2 sensor) and n_{av}. Table 5.3 shows the yields of these products obtained at 0.50 V.

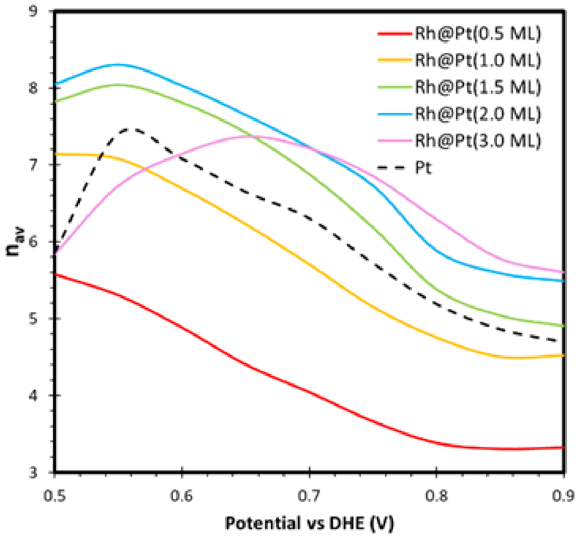

Figure 5.8. Stoichiometries for ethanol oxidation at Rh@Pt, Rh, and Pt electrodes from data in Figure 5.7B.

At 0.50 V, CO_2 was the major product (on a charge basis) for ethanol oxidation at all of the Rh@Pt catalysts, resulting in their high n_{av} values. CO_2 production increased as the Pt shell thickness was increased, reaching a maximum value of 73% at 2.0 ML. The yield of acetaldehyde was insignificant for 1.0 to 2.0 ML of Pt, but close to the value of 12% for Pt at the highest and lowest Pt coverages. The Rh@Pt(3.0 ML) catalyst produced essentially the same product distribution as the Pt catalyst at 0.50 V, but at a higher current (Figure 5.7).

Table 5.3. Stoichiometries (Figure 5.8) and faradaic yields of CO_2, acetaldehyde and acetic acid at 0.50 V vs DHE for ethanol oxidation at 80 °C.

Catalyst	n_{av}	Faradaic yield		
		CO_2	Acetic acid	Acetaldehyde
Rh@Pt(0.5ML)	5.6	56 %	35 %	9 %
Rh@Pt(1.0ML)	7.2	59 %	41 %	0 %
Rh@Pt(1.5ML)	7.8	61 %	39 %	0 %
Rh@Pt(2.0ML)	8.1	73 %	27 %	0 %
Rh@Pt(3.0ML)	5.8	65 %	23 %	12 %
Pt	5.9	66 %	22 %	12 %
Rh	Not determined	52 %		

5.3.5. Polarization curves and CO_2 yields for selected Rh@Pt catalysts in a 5 cm^2 PEMEC at 80 °C

Following initial assessment of the Rh@Pt catalysts in the 9-anode PEM cell, the best two were evaluated in a 5 cm^2 PEMEC with a single anode. This cell was operated as a normal ethanol electrolysis cell with the ethanol solution pumped through the anode flow field and N_2 at the cathode to exclude oxygen, and remove the hydrogen produced (54). CO_2 yields were measured using the NDIR CO_2 sensor.

Polarization curves for ethanol oxidation at the Rh@Pt(0.5 ML), Rh@Pt(1.5 ML) and Pt catalysts are compared in Figure 5.9. Rh@Pt(0.5 ML) gave the lowest onset potential and the highest currents up to 0.40 V, which can be attributed to the bifunctional effect of surface Rh.

Currents at the Rh@Pt(1.5 ML) electrode were higher than for Pt at all potentials, and higher than for Rh@Pt(0.5 ML) at potentials above 0.40 V, due to the ligand and strain effects of the Rh core.

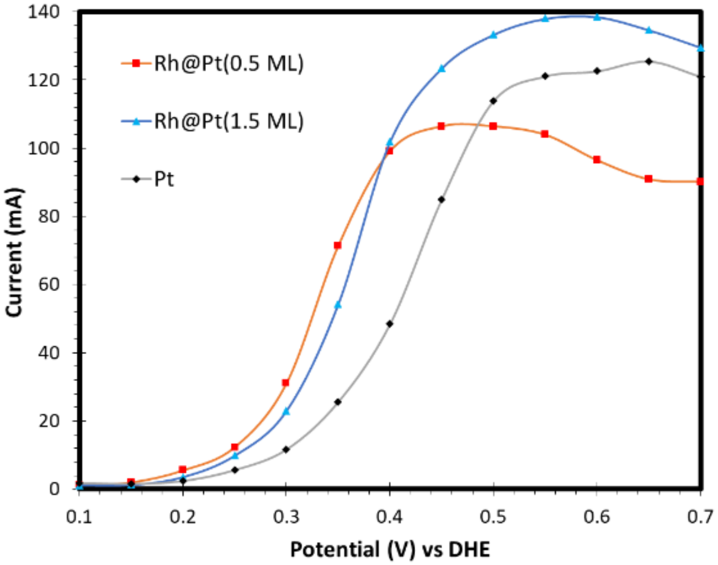

Figure 5.9. Polarization curves for ethanol oxidation at Rh@Pt(0.5 ML), Rh@Pt(1.5 ML), and Pt electrodes (2.0 mg cm^{-2} Rh+Pt) at 80 °C in a 5 cm^2 PEMEC.

Faradaic yields of CO_2 are shown as a function of potential in Figure 5.10. The values obtained at 0.50 V are consistent with those determined in the 9-anode cell (Table C 2), and confirm that the Rh@Pt(1.5 ML) catalyst is almost as efficient as Pt for breaking the C-C bond in ethanol at this potential, while Rh@Pt(0.5 ML) is less efficient. However, at lower potentials, which are most important for use of these catalysts in ethanol fuel and electrolysis cells, the Rh@Pt(0.5 ML) became more efficient, while the efficiency of both the Rh@Pt(1.5 ML) and Pt catalysts dropped off sharply. The highest faradaic yield of CO_2 was 67% for the Rh@Pt(0.5 ML) catalyst at 0.40 V.

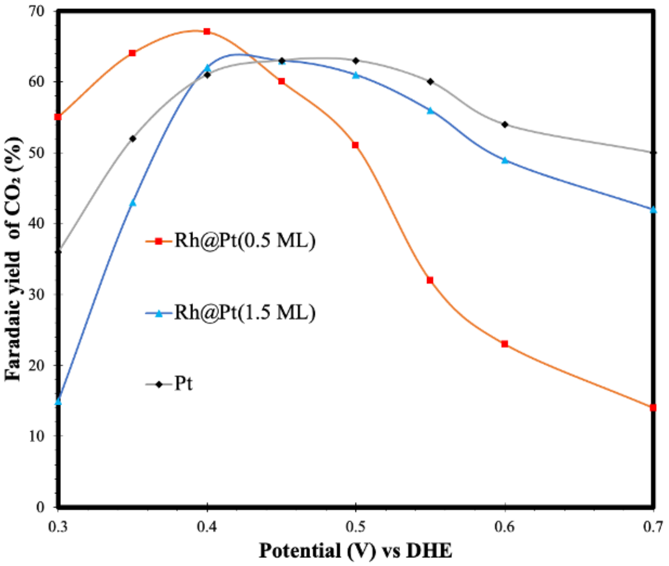

Figure 5.10. The faradaic yields of the CO_2 for oxidation of 0.1 M ethanol at Rh@Pt(0.5 ML), Rh@Pt(1.5 ML), and Pt electrodes, in a 5 cm^2 PEMEC at 80 °C.

5.4. Discussion

The activities of the Rh@Pt catalysts reported here for methanol and ethanol oxidation in aqueous H_2SO_4 are broadly consistent with previous studies that have demonstrated enhanced performances relative to Pt at low potentials (17, 19, 23, 27). The XRD and XPS results support the view that the influence of the Rh core is predominantly due to the strain that it induces in the Pt shell (17, 27). However, it is clear from the results in Figure 5.6 that the bifunctional effect of surface Rh atoms, and possibly electronic effects play important roles at low Pt coverages.

The Rh@Pt catalysts reported here also showed greatly enhanced activity over Pt in PEMEC at 80 °C, in contrast to a previous report that employed the same methodology (27). The catalysts used in that work were prepared in ethylene glycol with a polyvinylpyrrolidone capping agent (62), and so it is likely that the inferior performances obtained in both H_2SO_4(aq) and PEM cells were due to residual polyvinylpyrrolidone on the catalyst surface.

For ethanol oxidation, improving the activity of the catalyst is only part of the problem for their use in electrolysis and fuel cells. In both cases, the overall efficiency of the cell depends on both the overpotential required to drive the reaction and the stoichiometry.

For ethanol electrolysis to produce hydrogen, the energy required (W_e) is given by eq. 5.4 (67),

$$W_e = (33\ \text{kWh kg}^{-1})E_{cell}/1.23 \qquad (5.4)$$

where E_{cell} is the applied cell potential (i.e. the anode potential vs DHE), the energy density of the hydrogen produced is 33 kWh kg^{-1}, and the thermodynamic potential for electrolysis of water is 1.23 V. It can be seen from Figure 5.9 that the Rh@Pt(1.5 ML) electrode required less energy than the Pt electrode to produce hydrogen at all currents (rates), while the Rh@Pt(0.5 ML) electrode was most efficient at current densities below 100 mA (20 mA cm^{-2}). In addition, the Rh@Pt(0.5 ML) catalyst provided the highest yields of CO_2 at $E_{cell} \leq 0.40$ V and so would consume less ethanol.

For a DEFC, the overall efficiency (ε_{DEFC}), neglecting crossover and resistance losses, can be estimated by using eq. 5.5 (7, 12):

$$\varepsilon_{DEFC} = \varepsilon_{rev}(\eta_{cathode} - \eta_{anode})n_{av}/12E_{rev} \qquad (5.5)$$

where ε_{rev} is the theoretical efficiency of 96% at 80 °C, E_{rev} is the reversible cell potential of ca. 1.15 V, η_{anode} is the overpotential at the anode and $\eta_{cathode}$ is the overpotential at the cathode. Although the effects of the oxygen-reducing cathode of a DEFC ($\eta_{cathode}$) cannot be quantified here, it is clear from eq. 5.5 that the overall efficiency is proportional to n_{av}, increases with increasing CO_2 yield (eq. 5.3), and increases with decreasing η_{anode}. Consequently, we can see from Figures 5.9-5.10, that the Rh@Pt(0.5ML) catalyst will provide higher DEFC efficiencies at current densities below 20 mA cm^{-2} than either the Rh@Pt(1.5ML) or Pt catalyst, due to both the lower overpotential required (for the same current) and the higher CO_2 yield. The Rh@Pt(1.5ML) catalyst will also provide a much higher voltage efficiency ($(\eta_{cathode} - \eta_{anode})/E_{rev}$) than Pt in this region, but its faradaic efficiency ($n_{av}/12$) will be lower.

The data from the PEMEC employed in this work emphasize the need to evaluate catalysts under the conditions of their proposed applications, and to determine stoichiometries and CO_2 yields under steady-state conditions. Cyclic voltammetry in aqueous electrolytes is crucial for characterization of catalysts, and a mechanistic understanding of activity trends, but is not representative of performance and efficiency in fuel and electrolysis cells.

The application of PEM cells in this work has demonstrated conclusively that Rh can enhance *continuous* cleavage of the C-C bond of ethanol, which is crucial for DEFC applications. Although many studies have shown enhanced C-C bond cleavage in aqueous electrolytes at ambient temperature, this can be attributed in many cases to transient CO_2 formation from adsorbed CO produced during the initial adsorption of ethanol (9).

5.5. Conclusions

Rh@Pt core-shell catalysts prepared by deposition of Pt onto commercial carbon-supported Rh have shown enhanced performance over Pt and Rh catalysts for both methanol and ethanol oxidation in aqueous H_2SO_4 at ambient temperature and in PEM cells at 80 °C. The increased catalytic activity of the Pt shells relative to Pt nanoparticles is due primarily to the compressive strain induced by the Rh core. However, there is also a significant bifunctional effect (and/or an electronic effect) at low Pt coverages. These effects can also increase selectivity for cleavage of the C-C bond of ethanol in PEM cells, which will enhance the efficiencies of ethanol fuel and electrolysis cells.

5.6. References

1. N. Shaari, S. K. Kamarudin, R. Bahru, S. H. Osman and N. Ishak, International Journal of Energy Research, **45**, 6644 (2020).
2. D. M. Fadzillah, S. K. Kamarudin, M. A. Zainoodin and M. S. Masdar, International Journal of Hydrogen Energy, **44**, 3031 (2019).
3. B. C. Ong, S. K. Kamarudin and S. Basri, International Journal of Hydrogen Energy, **42**, 10142 (2017).
4. C. Coutanceau and S. Baranton, Wiley Interdisciplinary Reviews-Energy and Environment, **5**, 388 (2016).
5. A. Rodriguez-Gomez, F. Dorado, A. de Lucas-Consuegra and A. R. de la Osa, Journal of Energy Chemistry, **56**, 264 (2021).
6. M. S. Alias, S. K. Kamarudin, A. M. Zainoodin and M. S. Masdar, International Journal of Hydrogen Energy, **45**, 19620 (2020).
7. L. An, T. S. Zhao and Y. S. Li, Renewable and Sustainable Energy Reviews, **50**, 1462 (2015).
8. S. P. S. Badwal, S. Giddey, A. Kulkarni, J. Goel and S. Basu, Applied Energy, **145**, 80 (2015).
9. J. Piwowar and A. Lewera, Journal of Electroanalytical Chemistry, **875**, 114229 (2020).
10. E. Halim, S. Chemchoub, A. El Attar, F. E. Salih, L. Oularbi and M. El Rhazi, Frontiers in Energy Research, **10**, 843736 (2022).

11. M. Wala and W. Simka, Molecules, **26**, 2144 (2021).

12. R. M. Altarawneh and P. G. Pickup, Journal of Electrochemical Society, **164**, F861 (2017).

13. G. X. Yang, Q. Zhang, H. Yu and F. Peng, Particuology, **58**, 169 (2021).

14. L. Yaqoob, T. Noor and N. Iqbal, RSC Advances, **11**, 16768 (2021).

15. Y. Zheng, X. J. Wan, X. Cheng, K. Cheng, Z. F. Dai and Z. H. Liu, Catalysts, **10**, 166 (2020).

16. N. S. Marinkovic, M. Li and R. R. Adzic, Topics in Current Chemistry, **377** (2019).

17. F. H. B. Lima and E. R. Gonzalez, Applied Catalysis B: Environmental, **79**, 341 (2008).

18. N. M. Sanchez-Padilla, S. M. Montemayor, L. A. Torres and F. J. Rodriguez Varela, International Journal of Hydrogen Energy, **38**, 12681 (2013).

19. L. Fang, J. L. He, S. Saipanya and X. P. Huang, International Journal of Electrochemical Science, **10**, 5350 (2015).

20. Y. M. Hu, A. M. Zhu, Q. G. Zhang and Q. L. Liu, International Journal of Hydrogen Energy, **41**, 11359 (2016).

21. B. W. Zhang, T. Sheng, Y. X. Wang, X. M. Qu, J. M. Zhang, Z. C. Zhang, H. G. Liao, F. C. Zhu, S. X. Dou, Y. X. Jiang and S. G. Sun, ACS Catalysis, **7**, 892 (2017).

22. R. Rizo, R. M. Aran-Ais, E. Padgett, D. A. Muller, M. J. Lazaro, J. Solla-Gullon, J. M. Feliu, E. Pastor and H. D. Abruna, Journal of American Chemical Society, **140**, 3791 (2018).

23. P. T. Li, K. Liu, J. Y. Ye, F. Xue, Y. Cheng, Z. X. Lyu, X. Y. Liao, W. Wang, Q. B. Zhang, X. J. Chen, M. C. Liu and S. F. Xie, Journal of Materials Chemistry A, **7**, 17987 (2019).

24. Z. X. Liang, L. Song, S. Q. Deng, Y. M. Zhu, E. Stavitski, R. R. Adzic, J. Y. Chen and J. X. Wang, Journal of American Chemical Society, **141**, 9629 (2019).

25. J. S. Zou, M. Wu, S. L. Ning, L. Huang, X. W. Kang and S. W. Chen, ACS Sustainable Chemistry and Engineering, **7**, 9007 (2019).

26. A. Hoang, E. El Sawy, A. Blackburn, S. Ketabi, M. Goledzinowski, F. J. E. Comeau and V. Birss, ACS Applied Energy Materials, **3**, 8423 (2020).

27. E. El Sawy, T. M. Brueckner and P. G. Pickup, Journal of Electrochemical Society, **167**, 106507 (2020).

28. A. H. Ali and P. G. Pickup, Journal of Electrochemical Society, **169**, 034523 (2022).

29. A. H. Ali and P. G. Pickup, ECS Advances, **2**, 024501 (2023).

30. E. N. El Sawy, H. A. El-Sayed and V. I. Birss, Physical Chemistry Chemical Physics, **17**, 27509 (2015).

31. T.-Y. Chen, T.-L. Lin, T.-J. M. Luo, Y. Choi and J.-F. Lee, ChemPhysChem, **11**, 2383 (2010).

32. T.-Y. Chen, T.-J. M. Luo, Y.-W. Yang, Y.-C. Wei, K.-W. Wang, T.-L. Lin, T.-C. Wen and C. H. Lee, Journal of Physical Chemistry C, **116**, 16969 (2012).

33. E. Antolini and E. R. Gonzalez, Catalysis Today, **160**, 28 (2011).

34. S. E. Evarts, I. Kendrick, B. L. Wallstrom, T. Mion, M. Abedi, N. Dimakis and E. S. Smotkin, ACS Catalysis, **2**, 701 (2012).

35. J. P. I. de Souza, S. L. Queiroz, K. Bergamaski, E. R. Gonzalez and F. C. Nart, Journal of Physical Chemistry B, **106**, 9825 (2002).

36. S. Sen Gupta and J. Datta, Journal of Electroanalytical Chemistry, **594**, 65 (2006).

37. K. Bergamaski, E. R. Gonzalez and F. C. Nart, Electrochimica Acta, **53**, 4396 (2008).

38. A. Kowal, M. Li, M. Shao, K. Sasaki, M. B. Vukmirovic, J. Zhang, N. S. Marinkovic, P. Liu, A. I. Frenkel and R. R. Adzic, Nature Materials, **8**, 325 (2009).

39. Q. Yuan, Z. Y. Zhou, J. Zhuang and X. Wang, Chemistry of Materials, **22**, 2395 (2010).

40. D. A. Cantane, W. F. Ambrosio, M. Chatenet and F. H. B. Lima, Journal of Electroanalytical Chemistry, **681**, 56 (2012).

41. A. B. Delpeuch, T. Asset, M. Chatenet and C. Cremers, Journal of Electrochemical Society, **161**, F918 (2014).

42. L. Rao, Y. X. Jiang, B. W. Zhang, Y. R. Cai and S. G. Sun, Physical Chemistry Chemical Physics, **16**, 13662 (2014).

43. A. B. Delpeuch, F. Maillard, M. Chatenet, P. Soudant and C. Cremers, Applied Catalysis B: Environmental, **181**, 672 (2016).

44. J. Bai, X. Xiao, Y. Y. Xue, J. X. Jiang, J. H. Zeng, X. F. Li and Y. Chen, ACS Applied Materials and Interfaces, **10**, 19755 (2018).

45. F. C. Zhu, K. F. Tu, L. Huang, X. M. Qu, J. M. Zhang, H. G. Liao, Z. Y. Zhou, Y. X. Jiang and S. G. Sun, Electrochimica Acta, **292**, 208 (2018).

46. C. V. S. Almeida, D. S. Ferreira, H. L. Huang, A. C. Gaiotti, G. A. Camara, A. E. Russell, K. I. B. Eguiluz and G. R. Salazar-Banda, Applied Catalysis B: Environmental, **254**, 113 (2019).

47. Y. M. Zhu, L. Z. Bu, Q. Shao and X. Q. Huang, ACS Catalysis, **9**, 6607 (2019).

48. C. V. S. Almeida, H. L. Huang, A. E. Russell, K. I. B. Eguiluz and G. R. Salazar-Banda, Electrochimica Acta, **431**, 141089 (2022).

49. E. S. V. Neto, C. V. S. Almeida, H. L. Huang, A. E. Russell, K. I. B. Eguiluz and G. R. Salazar-Banda, ChemCatChem, e202300048 (2023).

50. T. Li, E. A. Marquis, P. A. J. Bagot, S. C. Tsang and G. D. W. Smith, Catalysis Today, **175**, 552 (2011).

51. N. G. Pereira, R. F. B. Souza, A. S. Ramos, R. M. Antoniassi, A. O. Neto and E. V. Spinace, International Journal of Electrochemical Science, **16**, 211253 (2021).

52. E. W. Harak, K. M. Koczkur, D. W. Harak, P. Patton and S. E. Skrabalak, ChemNanoMat, **3**, 815 (2017).

53. D. D. James and P. G. Pickup, Electrochimica Acta, **55**, 3824 (2010).

54. R. M. Altarawneh, P. Majidi and P. G. Pickup, Journal of Power Sources, **351**, 106 (2017).

55. T. M. Brueckner and P. G. Pickup, Journal of Electrochemical Society, **64**, F1172 (2017).

56. R. M. Altarawneh, T. M. Brueckner, B. Y. Chen and P. G. Pickup, Journal of Power Sources, **400**, 369 (2018).

57. J. N. Schwammlein, B. M. Stuhmeier, K. Wagenbauer, H. Dietz, V. Tileli, H. A. Gasteiger and H. A. El-Sayed, Journal of Electrochemical Society, **165**, H229 (2018).

58. P. Strasser, S. Koh, T. Anniyev, J. Greeley, K. More, C. Yu, Z. Liu, S. Kaya, D. Nordlund, H. Ogasawara, M. F. Toney and A. Nilsson, Nature Chemistry, **2**, 454 (2010).

59. S. Alayoglu, A. U. Nilekar, M. Mavrikakis and B. Eichhorn, Nature Materials, **7**, 333 (2008).

60. E. N. El Sawy, H. A. El-Sayed and V. I. Birss, Chemical Communications, **50**, 11558 (2014).

61. E. N. El Sawy and P. G. Pickup, Electrocatalysis, **7**, 477 (2016).

62. E. N. El Sawy and P. G. Pickup, Electrochimica Acta, **302**, 234 (2019).

63. S. P. Luo, L. Zhang, Y. J. Liao, L. X. Li, Q. Yang, X. T. Wu, X. Y. Wu, D. S. He, C. Y. He, W. Chen, Q. L. Wu, M. R. Li, E. J. M. Hensen and Z. W. Quan, Advanced Materials, 2008508 (2021).

64. F. Alcaide, G. Alvarez, P. L. Cabot, R. V. Genova-Koleva, H. J. Grande, M. V. Martinez-Huerta and O. Miguel, Journal of Electroanalytical Chemistry, **861**, 113960 (2020).

65. A. Schlapka, M. Lischka, A. Gross, U. Kasberger and P. Jakob, Physical Review Letters, **91**, 016101 (2003).

66. R. M. Altarawneh and P. G. Pickup, Journal of Power Sources, **366**, 27 (2017).

67. C. Lamy, T. Jaubert, S. Baranton and C. Coutanceau, Journal of Power Sources, **245**, 927 (2014).

Chapter 6: Methanol and ethanol oxidation on carbon-supported platinum-rhodium alloy nanoparticles using a proton exchange membrane electrolysis cell

The first author (Ahmed H Ali) contributed to all parts of this Chapter, including the literature review and the experiments. He performed all the required physical and electrochemical measurements. In addition, he analyzed the data and wrote the first draft of this paper.

The corresponding author (Peter G. Pickup) was responsible for funding, reviewing all my data analysis, editing my draft paper, and completing it for submission to the Journal of ECS Advances.

Detailed raw data are provided in Appendix D

6.1. Introduction

The most studied direct alcohol fuel cells (DAFC) are the direct methanol fuel cell (DMFC) and the direct ethanol fuel cell (DEFC) (1). These cells generate electricity by oxidizing the alcohol catalytically with oxygen (1). The maximum faradaic efficiency is obtained when the oxidation of these alcohols generates CO_2 as the only product. In that case, methanol oxidation generates 6 electrons ($n = 6$) while $n = 12$ for ethanol oxidation (1). In addition to CO_2, methanol electrooxidation also generates formaldehyde ($n = 2$) and formic acid ($n = 4$), while ethanol electrooxidation also produces acetaldehyde ($n = 2$) and acetic acid ($n = 4$) (1). Many products are formed during the electrooxidation of these alcohols, so the average number of electrons generated (n_{av}) is used to calculate the faradaic efficiency of these DAFCs.

Platinum catalysts are used widely to oxidize small organic molecules such as methanol and ethanol in low-temperature fuel cells due to their ability to bind and oxidize these molecules at high rates, even at low temperatures (2). Despite this, Pt is not an effective catalyst for DMFC and DEFC due to its surface being poisoned by the strongly adsorbed intermediate species formed during the oxidation of these alcohols, such as the adsorbed carbon monoxide (CO) (3). Modification of Pt by adding other metals is required to enhance the electronic properties of the Pt surface for removing the highly adsorbed CO and dissociating the C-C bond in the case of ethanol (4, 5).

Alloys of Pt with other metals such as Ru, Rh, Sn, Ir, Ni, Cu, Co, Re, Pb, and Fe have been used as catalysts for the methanol oxidation reaction (MOR) and ethanol oxidation reaction (EOR) (6-9). PtRu and PtSn are the most effective bimetallic alloy catalysts for the MOR and EOR in an acidic media (10). Ru and Sn increase the oxygenated species on the surface, such as OH, accelerating the rate of eliminating the strongly adsorbed CO by further oxidation to CO_2

(bifunctional effect) (11). Therefore, they improve the catalytic activity of the Pt surface and increase the overall reaction rate of the MOR and EOR. However, most studies have shown that they are less selective for CO_2 formation than Pt (10).

In another direction, it has been reported that PtRh catalysts have shown more selectivity for the generation of CO_2 compared to Pt. They showed a higher ability to dissociate the C-C bond in the EOR (8, 12-15). On the Rh surface, adsorbed ethanol forms an oxametallacyclic conformation that facilitates the dissociation of the C-C bond (10). Kleber et al. used differential electrochemical mass spectroscopy to study the ability of carbon-supported PtRh catalysts to enhance the EOR compared to Pt in $HClO_4$ (12). They found that these catalysts increased the selectivity for generating CO_2 and that the best Pt:Rh atomic ratio was 1:1. Compared with Pt, their CV results showed an unexpected decrease in the peak current density. Their explanation showed that the Rh surface underwent a slow alcohol dehydrogenation reaction. In addition, Rh was poisoned by CO more than Pt since the binding energy between Rh and CO is greater than that between Pt and CO (12).

Delpeuch. et al. studied the effect of temperature on increasing the rate of the overall EOR on the surface of the PtRh compared to Pt (16). Their CV results in H_2SO_4 showed slightly different onset potentials at room T. However, at 70 °C, the difference in onset potentials (Eonset) became notable. PtRh had E_{onset} = 0.59 V vs RHE at 25 °C and 0.42 V vs RHE at 70 °C, while Pt had E_{onset} = 0.62 V vs RHE at 25 °C and 0.49 V vs RHE at 70 °C. At higher temperatures, Rh formed more stable OH at much lower potentials than Pt, which accounted for the higher negative shifts in the onset potentials between PtRh and Pt (16). The strong bifunctional effect of PtRh at high T was reflected in the forward anodic scan, which had higher overall currents relative to Pt (16).

Proton exchange membrane electrolysis cells (PEMEC) are important for producing pure hydrogen gas from renewable sources such as water (14). They have many advantages over alkaline electrolysis cells, such as operating efficiently at high current densities and having low gas crossover and ohmic losses (17-19). Methanol and ethanol electrolysis produce more hydrogen at lower potentials than water electrolysis (20, 21). The hydrogen production rate is proportional to the generated electrons (n_{av}) from the catalytic oxidation of these alcohols (22). PEMEC have the same components and operational mechanism as a proton exchange membrane fuel cell (PEMFC) except for the half-reaction on the cathode (17, 18). Proton reduction occurs in the cathode of PEMEC, while spontaneous reduction of O_2 occurs in the case of PEMFC (17, 18).

A PEMEC was used to evaluate the catalytic activities of PtRh catalysts for the MOR and EOR. This evaluation is determined by measuring the polarization curves, average transfer of electrons (n_{av}), the faradaic yield of CO_2, and the overall rate of the MOR and EOR (5, 20, 23). These studies investigated their catalytic capacity for producing electricity from DAFCs (5).

In this work, we prepared carbon-supported PtRh alloy nanoparticles of different Pt:Rh atomic ratios using the formic acid method (12). The catalysts were characterized using an X-ray diffractometer (XRD), energy dispersive X-ray emission (EDX), transmission electron microscope (TEM), and X-ray photoelectron spectroscopy (XPS). Their catalytic activities for the MOR and EOR were studied using cyclic voltammetry (CV) at room temperature and a PEMEC at 80 °C.

6.2. Experimental

6.2.1. Materials

Vulcan carbon XC72 (CABOT), $RhCl_3.3H_2O$ (99%; Sigma Aldrich), $H_2PtCl_6.6H_2O$ (Pressure Chemical Co.), silver nitrate (ACP Chemicals Inc.), Rhodium supported on Vulcan XC72 (Rh/C; 20% Rh by mass; Fuel Cell Store), platinum supported on Vulcan XC72 (Pt/C; 40%

Pt by mass; Alfa Aesar), formic acid (98-100%; Sigma-Aldrich), anhydrous ethanol (99.9%; Commercial Alcohols Inc.), methanol (HPLC grade; Fisher Scientific), 5% Nafion ™ solution (Dupont), sulfuric acid (95-98%; Fisher Scientific), 2-propanol (Caledon) and 1-propanol (J.T. Baker), hydrogen peroxide (30%; ACP Chemicals Inc.), were used as received. All aqueous solutions were prepared using deionized water.

6.2.2. Synthesis of PtRh/C catalysts

Carbon black (see Table D 1) was dispersed in 50 mL of 2 M formic acid by sonication for 20 min. The mixture was refluxed for 1 h at 80 °C. An aqueous solution containing the required amounts (Table D 1) of $RhCl_3.3H_2O$ and $H_2PtCl_6.6H_2O$ was then added dropwise to the hot mixture, and the refluxing was continued for a further 4 h. Formic acid (5 mL; 2 M) was injected dropwise into the mixture after 2 h from the addition of salts to ensure the complete reduction to Pt(0) and Rh(0). The catalyst was collected using a centrifuge (5 min at 11000 rpm) and washed several times with hot water until Cl^- could not be detected in the mother liquor (i.e., no white ppt with silver nitrate). The catalysts were dried overnight in an oven at 80 °C. They are designated $Pt_{0.5}Rh/C$, $Pt_{1.0}Rh/C$, $Pt_{2.0}Rh/C$, $Pt_{3.0}Rh/C$, and $Pt_{4.0}Rh/C$ according to the targeted Pt:Rh atomic ratios.

6.2.3. Physical characterization

An X-ray diffractometer (Rigaku Ultimate IV; XRD) was used to detect the crystalline structure of the bimetallic particles. The radiation source was Cu Kα (0.154 nm), and the detector was a scintillation counter analyzer. The samples were analyzed in powder form.

The Pt:Rh atomic ratios of the bulk samples were measured by using energy dispersive X-ray emission (EDX) attached to an FEI Quanta 400 scanning electron microscope (SEM), which was used here for only selecting the area that will be used for the EDX measurements. The samples were prepared by dispersing 2 mg of catalyst in a mixture of 50 μL water, 75 μL 1-propanol, and 75 μL 2-propanol for application to carbon tabs.

A thermogravimetric analyzer (TGA) TA Instrument TGA 55 was used to determine metal percentages and catalyst thermal stability. Trios V5.6.0.87 software was used to operate this instrument. Samples weighing approximately 6 mg were loaded into a Platinum HT sample pan. Under an air atmosphere, the operation temperature ramp was 20 °C min^{-1}, and the final temperature was 800 °C.

The electronic properties of the surfaces of the catalysts were investigated using X-ray photoelectron spectroscopy (VG Micro-tech Multi-Lab ESCA 2000 system; XPS).

The nanoparticles were imaged using a Tecnai TM Spirit transmission electron microscope (TEM). These images could indicate the degree of dispersity of the nanoparticles on the carbon support and the degree of aggregation of the formed nanoparticles. The particle sizes of around 80 randomly selected nanoparticles were measured using the Image J 1.53a program to determine the average particle size and the size distribution. The TEM samples were prepared by dispersing 1 mg of catalyst in a 300 μL mixture of water, 1-propanol, and isopropanol (1:1:1) volume ratios. Then, only one droplet of the ink was placed on the lacey carbon film - Cu (electron microscopy sciences; 200 mesh, 50 micron CC).

6.2.4. Electrochemical characterization at ambient temperature

All cyclic voltammetry (CV) measurements were performed in 1 M H_2SO_4 at room temperature using an SP-50 Biologic potentiostat connected to EC-lab software. Three-electrode glass cells comprised a Pt wire counter electrode, saturated calomel reference electrode (SCE), and the catalyst as working electrode (WE). The WE was prepared by slowly painting a desired volume of the catalyst ink on carbon fiber paper (CFP, 0.24 cm^2, Toray TGP-H-090) to give a 0.3 mg cm^{-}

^{2} metal (Rh+Pt) loading. The background, ethanol, and methanol CV measurements were performed as described in (5). Before each CV measurement, the solution was purged with UHP N_2 for 5 min. Six cycles were run for the background CV at 100 mV s^{-1}, while three cycles at 10 mV s^{-1} were run in the presence of 0.1 M ethanol and methanol. The last cycle is drawn in all cases.

6.2.5. Oxidation of methanol and ethanol at 80 °C in a multi-anode PEMEC

A commercial fuel cell (Electrochem Inc.) was operated as an electrolysis cell in a crossover mode, as previously described (18). An MSTAT potentiostat from Arbin instruments was used to apply controlled potentials to each anode relative to the cathode. The cell was modified to measure 9- anodes simultaneously of size 0.24 cm^2. The cathode consists of Pt black on a single square (5 cm^2) of CFP, while the anodes consist of CFP discs painted with catalyst inks to give a metal loading of 2.0 mg cm^{-2}.

The catalyst inks were prepared by dispersion of 4 mg of catalyst in a solution of 50 µL water, 75 µL isopropanol, and 75 µL 1-propanol. Nafion solution (5%) was applied to the catalyst surface, equivalent to 30% of the total catalyst + Nafion mass. A treated 4.5 × 4.5 cm Nafion-117 membrane was employed between the anode and the cathode to transfer the generated proton to the cathode.

Aqueous methanol or ethanol (0.1 M) was pumped through the cathode compartment at a flow rate of 0.5 mL min^{-1}, while the anode was purged with N_2 at 10 mL min^{-1}. The ethanol that diffused through the Nafion membrane was oxidized to generate electrons and protons. The aim was to provide mass transport control of the current at high potential, which allows the n_{av} to be determined at those potentials. The cathode acts as a dynamic hydrogen electrode (DHE), in which hydrogen is produced in a Pt wire by applying a small cathodic current, which results in constant hydrogen coverage on the electrode, so a stable reference potential was obtained (24).

Polarization curves (PLs) were obtained by applying a constant potential for 3 min and measuring the current, starting at 0.90 V (vs DHE). The average current for the last 60 s of each applied potential is reported. Before each PL measurement, the anodes were set to a constant potential of 0.70 V (vs DHE) for at least 1 h. Initially, consecutive polarization curves for methanol oxidation (four) were recorded until they were consistent. Then, two successive curves were recorded for ethanol oxidation. The final polarization curve is reported in all cases. The CO_2 generated from ethanol oxidation at 0.50 V was measured using a nondispersive infrared (NDIR) CO_2 sensor (Telaire T6615), as previously described in (18). The N_2 flow rate was increased to 50 mL min^{-1} while the alcohol flow rate decreased to 0.2 mL min^{-1}.

6.2.6. Ethanol oxidation at 80 °C in a 5 cm^2 PEMEC

A commercial PEMFC (Fuel cell technology) was employed as an electrolysis cell with 0.1 M ethanol (at 0.5 mL min^{-1} for polarization curves) at the anode and N_2 (30 mL min^{-1}) at the cathode (25, 26). Hydrogen production at the cathode provides a stable reference potential (DHE).

Anodes were prepared as described above by spreading the catalyst ink onto a 5 cm^2 CFP square to give a metal (Rh + Pt) loading of 2.0 mg cm^{-2} with 30 mass % Nafion solution were separated from a 5 cm^2 Pt black cathode (4.0 mg cm^{-2} on wet-proofed CFP) by a Nafion-117 membrane. Electrochemical measurements were done at 80 °C under steady-state conditions at constant cell potentials using a Hokuto Denko HA-301 potentiostat. The faradaic yield of CO_2 was measured at each potential with the Telaire T6615 CO_2 sensor (27).

6.3. Results and discussion

6.3.1. Physical characterization of the PtRh/C catalysts

The measured Pt:Rh ratios using EDX agreed with the target ones, as summarized in Table 6.1. This is considered a good indication of the effectiveness of the synthesis method used for the complete reduction of the Pt and Rh precursors. EDX results indicated that Pt was not segregated on the surface of the PtRh, regardless of the Pt:Rh atomic ratio. If Pt were concentrated at the surface, there would be X-ray absorption from the X-rays emitted by Rh, resulting in a decrease in Rh intensity and a higher apparent Pt:Rh ratio (5, 20).

Table 6.1. The average atomic size was measured by TEM and XRD, the target and EDX measured Pt:Rh atomic ratios, the target, and TGA measured total metals (Rh+Pt) mass %, and the onset temperature (T_{onset}) of the prepared PtRh catalysts determined from their TGA curves (Figure 6.2).

Catalyst	Average atomic size		Pt:Rh ratios		Pt+Rh mass %		T_{onset} (°C)
	XRD	TEM	Target	EDX	Target	TGA	
$Pt_{0.5}Rh/C$	2.20	2.36 ± 0.47	0.50	0.54	40	42	354
$Pt_{1.0}Rh/C$	2.52	2.49 ± 0.57	1.00	1.10	40	34	418
$Pt_{2.0}Rh/C$	3.39	3.44 ± 0.56	2.00	2.10	40	36	418
$Pt_{3.0}Rh/C$	3.75	3.66 ± 0.42	3.00	2.99	40	39	421
$Pt_{4.0}Rh/C$	3.85	3.93 ± 0.72	4.00	3.99	40	38	419

Based on TEM measurements, the measured average particle sizes of the PtRh alloys were found between 2 – 4 nm, as shown in Table 6.1. The size of PtRh increased when the Pt content increased. The TEM images (Figure 6.1) show that the PtRh nanoparticles had an approximately spherical shape. Moreover, they were highly dispersed on the carbon support with low aggregation. Their histograms (Figure D 1) show relatively narrow particle size distributions. Accordingly, these catalysts were synthesized under well-controlled conditions, resulting in more uniform particle sizes, which enabled more consistent and reliable performance (28).

The metal loading on the carbon support was determined by thermogravimetric analysis (TGA). The target Pt + Rh mass % and measured values are shown in Figure 6.2 and summarized inTable 6.1. There is good agreement between the measured and the expected Pt+Rh mass %. This indicates that the Pt and Rh were successfully deposited onto the carbon support.Table 6.1 summarizes the onset temperatures (T_{onset}) for PtRh alloys based on their TGA curves (Figure 6.2). The determination of this factor is useful for determining the thermal stability of carbon supports, which can provide a preliminary indication of corrosion of the carbon support in fuel cell electrodes (29). A $Pt_{0.5}Rh$ catalyst showed the lowest onset temperature, indicating the highest corrosion rate on its carbon support. The carbon support stability of PtRh catalysts can be tuned by varying the Pt:Rh atomic ratio, in which the stability increases with increasing Pt content, reaching its maximum value at $Pt_{3.0}Rh$.

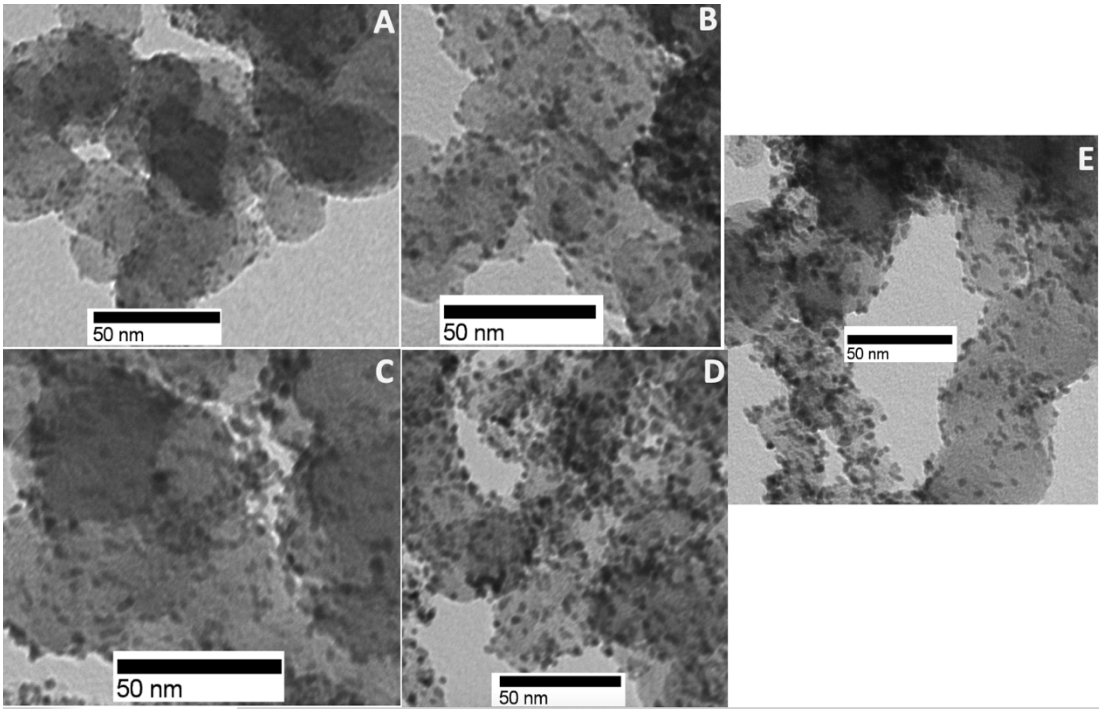

Figure 6.1. TEM images for (A) $Pt_{0.5}Rh/C$, (B) $Pt_{1.0}Rh/C$, (C) $Pt_{2.0}Rh/C$, (D) $Pt_{3.0}Rh/C$ and (E) $Pt_{4.0}Rh/C$.

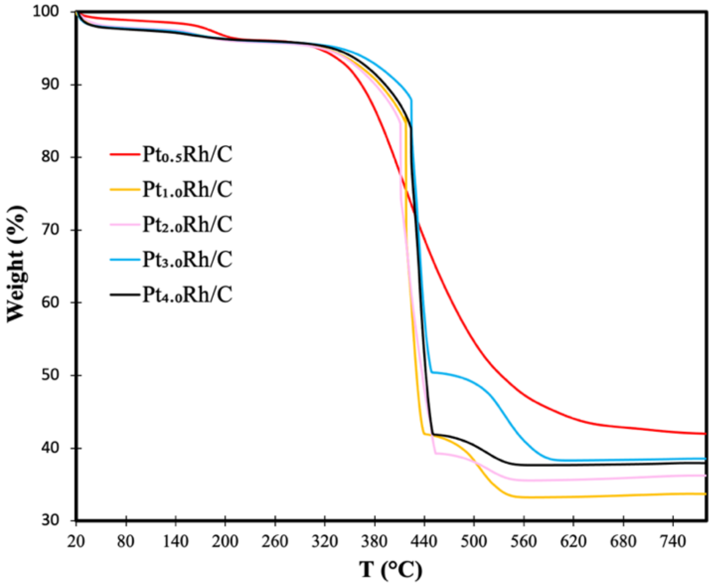

Figure 6.2. The mass loss (TGA) curves for the PtRh catalysts. The operation temperature ramp was 20 °C min $^{-1}$ under an air atmosphere.

The XRD diffractograms of the PtRh catalysts are shown in Figure 6.3. They have the same face-centered cubic (FCC) polycrystalline structure as Pt and Rh. However, their diffraction peaks lay between the positions of the same diffraction plane peaks for Pt and Rh. Moreover, there are negative shifts to lower 2θ for these peaks as the Pt:Rh ratios increase, indicating the formation of PtRh alloys instead of pure Rh and Pt (12). The crystallite size of these PtRh alloys was calculated using Scherrer's equation (30). Table 6.1 summarizes the results compared to the size measured by TEM. The crystallite size seems consistent with the average size measured by TEM, confirming that the PtRh catalysts are highly crystalline. The crystallinity of catalysts plays an important role in improving their ability for alcohol oxidation (31). In PtRh, the angles of the Pt (220) peaks shift upward as Rh content increases (Figure 6.3), confirming the presence of lattice strain contraction. This shift in Pt (220) suggests the formation of an alloy structure, as Lima et al. stated (32).

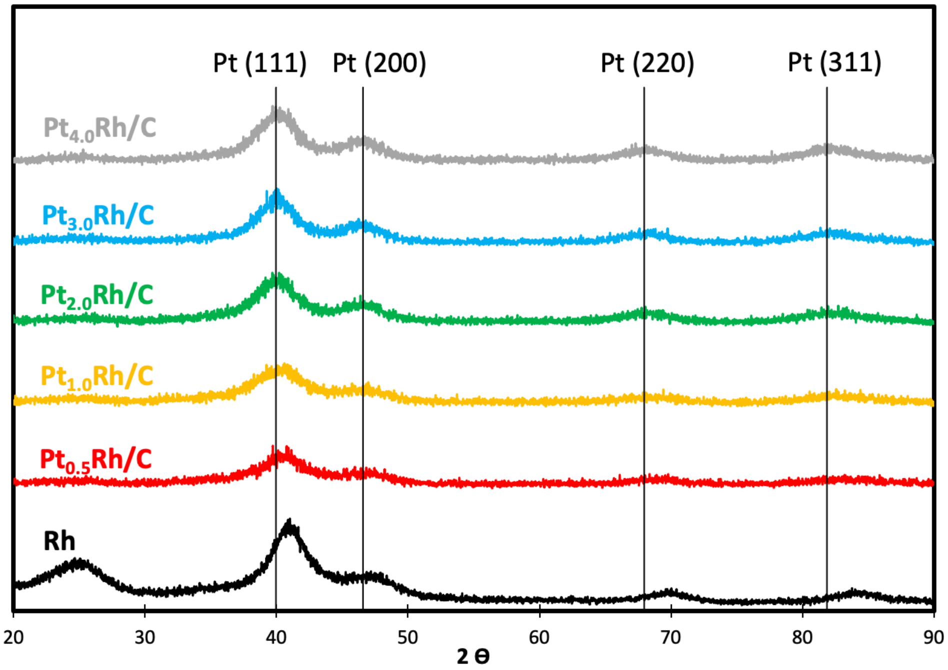

Figure 6.3. XRD patterns for the PtRh catalysts and commercial Rh. The vertical lines show the positions of the Pt diffraction peaks.

Bragg's law was employed to determine the experimental lattice parameters for the PtRh catalysts from the Pt (200) plane (12). Their values correlate well with the lattice parameters calculated using Vegard's law, as seen in Figure 6.4 (12). This confirms that the formed bimetallic PtRh catalysts are alloy structures (12, 33).

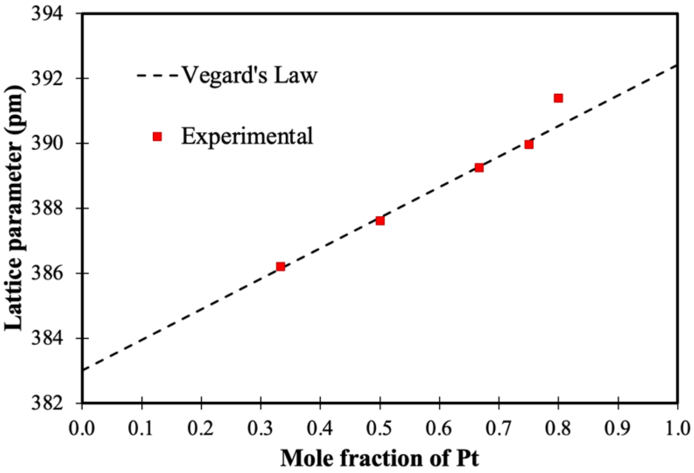

Figure 6.4. Dependence of the experimental lattice parameter (XRD) with the measured mole fraction of Pt (EDX) in the PtRh bimetallic catalysts. The dashed line represents lattice constants calculated by using Vegard's law.

The XPS spectra of the PtRh catalysts are shown in Figure D 2, in which they show peaks at almost the same binding energies (BE) as metallic Pt and Rh. This indicates that zero-valent Pt and Rh metallic states dominate the surface species of the prepared catalysts. The Rh 3d and Pt 4d peaks of the PtRh catalysts are compared with Rh and Pt in Figure 6.5. As the Pt:Rh atomic ratios increased, the Pt $4d_{5/2}$ BE peak intensity at ca. 315 eV increased. The Pt 4f BEs of the PtRh catalysts are slightly upshifted compared to Pt (Figure 6.6). This suggests that alloying Pt with Rh results in a significant Pt lattice strain that downshifts the Pt 5d-band center (34). This downshift enhances the electrocatalytic activities of PtRh alloys for alcohol oxidation by decreasing the adsorption strength of intermediates such as CO (32, 35).

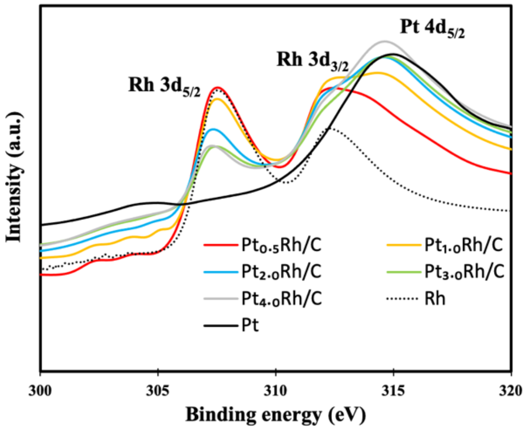

Figure 6.5. Rh 3d and Pt 4d regions of XPS spectra of Rh, Pt, and PtRh catalysts.

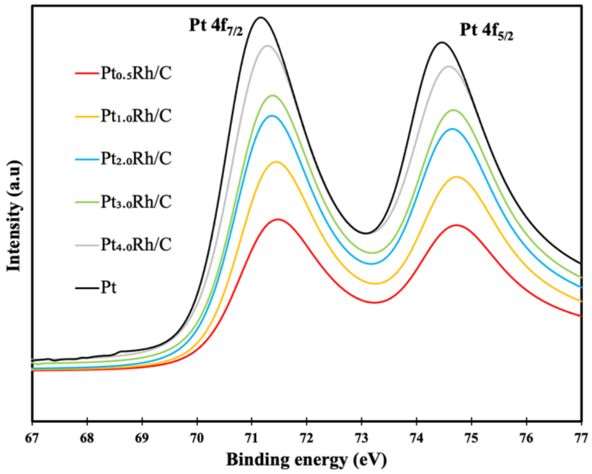

Figure 6.6. Pt 4f area of XPS spectra of Pt and PtRh catalysts.

Broad O 1s b bands are observed for all the PtRh catalysts, as shown in Figure 6.7, indicating the presence of surface platinum and rhodium-oxy species. Each broad O 1s peak consists of overlapping metals-oxide (-O^{2-}-), metals-hydroxides (-OH^{-}), adsorbed water, and carbon-oxy species (C-O) peaks (20, 36). Figure D 3 and Figure D 4 show the deconvolution of the metal-oxide peaks from the other overlapping oxygenated peaks. Their binding energies and the relative areas are summarized in Table 6.2.

There is an upshift in the binding energies for the -O^{2-} peaks of PtRh compared to Rh (Table 6.2), suggesting that Rh and Pt interact electronically (20). With increasing Pt content, the relative area of the O^{2-} peaks decreased (Table 6.2), indicating a decrease in the surface concentration of the more easily oxygenated Rh atoms, and the platinum oxides did not contribute significantly to the O^{2-} peak.

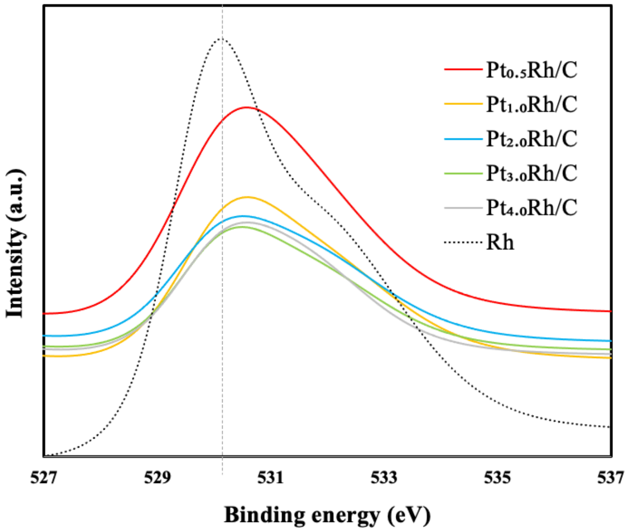

Figure 6.7. O 1s region of XPS spectra of Rh and Pt+Rh/C catalysts.

Table 6.2. O 1s binding energies and their relative areas from the deconvoluted XPS spectra (Figures D3-D4) for Rh and Pt:Rh alloys.

Catalyst	O 1s binding energy/eV and (relative area (%))	
	-O^{2-}-	-OH^- and -H_2O/C-O
Rh	530.05 (33)	531.62 (67)
$Pt_{0.5}Rh$/C	530.16 (41)	531.42 (59)
$Pt_{1.0}Rh$/C	530.21 (36)	531.61 (64)
$Pt_{2.0}Rh$/C	530.15 (33)	531.52 (67)
$Pt_{3.0}Rh$/C	530.11 (28)	531.46 (72)
$Pt_{4.0}Rh$/C	530.07 (26)	531.33 (74)

6.3.2. Cyclic voltammetry in aqueous sulfuric acid

The electrochemical responses of PtRh electrodes in 1 M H_2SO_4 at ambient temperature were investigated using the cyclic voltammetry ranging from –0.25 V to 0.80 V vs a standard calomel electrode (SCE). Steady-state voltammograms obtained after a few potential cycles are shown in Figure 6.8. In the hydrogen desorption region below 0.10 V, the hydrogen desorption peak split completely into strongly and weakly bound Pt-H-like peaks at ca. –0.10 V and 0 V on the surface of $Pt_{4.0}Rh$ (37). The electroactive surface area (*EASA*) was calculated using eq. 6.1, the hydrogen desorption method (38, 39). The *EASA* is also known as the real surface area.

$$EASA = \frac{C_m}{\theta C_{ML}} \qquad (6.1)$$

where C_m is the charge consumed in adsorbed hydrogen oxidation by integrating the voltammetric peaks, C_{ML} is the charge due to the oxidation of a monolayer of adsorbed hydrogen per unit area, and θ is the surface coverage of adsorbed hydrogen. A full monolayer ($\theta = 1$) cannot be formed because the hydrogen evolution charge dominates the hydrogen adsorption charge (38). However, we considered the surface fully covered with adsorbed hydrogen ($\theta = 1$) for the desorption wave (40-43). Moreover, we have assumed that the charging current in the double-layer region is constant without any faradaic contributions. For these reasons, the calculated *EASA* are estimated values. The accepted C_{ML} values for pure Pt and Rh are 0.210 mC cm^{-2} and 0.221 mC cm^{-2}, respectively, while the C_{ML} for PtRh alloys was calculated using eq. 6.2, where x_{Pt} and x_{Rh} are the mole fraction of Pt and Rh, respectively (38).

$$C_{ML} = 0.210\, x_{Pt} + 0.221\, x_{Rh} \qquad (6.2)$$

The values of *EASA*, the geometric surface area, and the surface utilization of each electrode are summarized in Table D2. Appendix D briefly describes the method for calculating geometric surface area and surface utilization. The $Pt_{1.0}Rh$ catalyst had the highest real surface area, reaching 91.62 cm^2, while Pt had the lowest value (37.09 cm^2). A similar large difference was observed in other work (44). Furthermore, the surface utilization of the prepared PtRh alloys exceeded 75%, while that of pure Pt and Rh was around 50%. The surface utilization order for the prepared PtRh catalysts was $Pt_{0.5}Rh < Pt_{1.0}Rh < Pt_{2.0}Rh = Pt_{3.0}Rh > Pt_{4.0}Rh$. It is likely that the alloying of Pt and Rh results in a more homogeneous surface, which makes it easier for reaction species to access the active sites. Moreover, their alloying increases the number of active sites, further enhancing the surface utilization of the PtRh catalysts (45).

Additionally, the double layer and metal oxide regions of PtRh alloys responded differently to changes in the Pt:Rh mole ratio. It is observed that the charging current of the double-layer area decreases as the mole fraction of Pt increases; in addition, the broad cathodic peaks of the PtRh alloys shift from potentials close to the Rh-oxide peak at 0.17 V to higher values close to the Pt-oxide at 0.53 V.

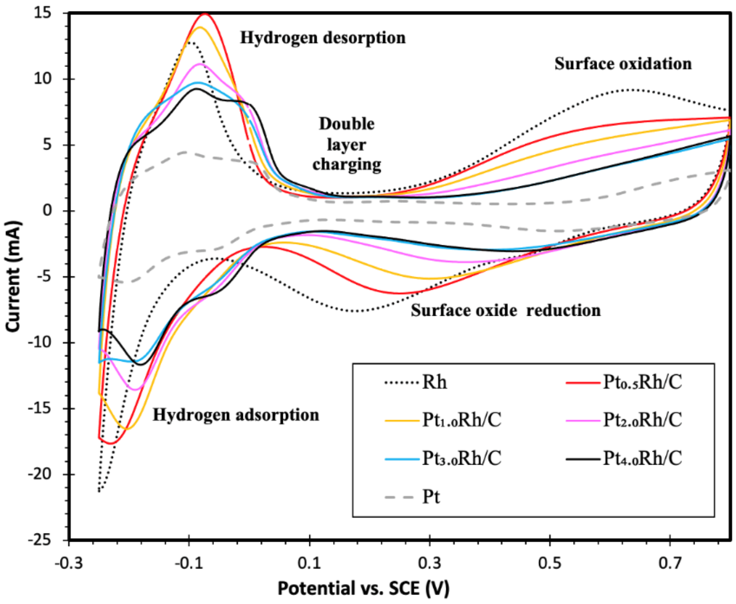

Figure 6.8. Background cyclic voltammograms (100 mV s^{-1}) of Pt, Rh, and PtRh electrodes (0.3 mg cm^{-2} of total metals) in 1 M sulfuric acid at ambient temperature.

6.3.3. Cyclic voltammetry for methanol and ethanol oxidation in aqueous sulfuric acid

Cyclic voltammograms of methanol oxidation on PtRh, Rh, and Pt catalysts at ambient temperature are shown in Figure 6.9. When Pt is alloyed with Rh, the methanol oxidation onset and peak potentials are shifted to lower values, and the peak current increases dramatically (Table 6.3). The enhanced catalytic activity of the PtRh catalysts can be attributed to the strong synergistic effect of Pt and Rh atoms in alloy structures. Peak current increased significantly as the Pt content in the PtRh alloy was increased, jumping from 5.67 mA for $Pt_{3.0}Rh$ to 8.84 mA for $Pt_{4.0}Rh$ (Table 6.3). This suggests that the bifunctional and strain effects of the $Pt_{4.0}Rh$ catalyst are still significant even when the Rh content is low (34, 46).

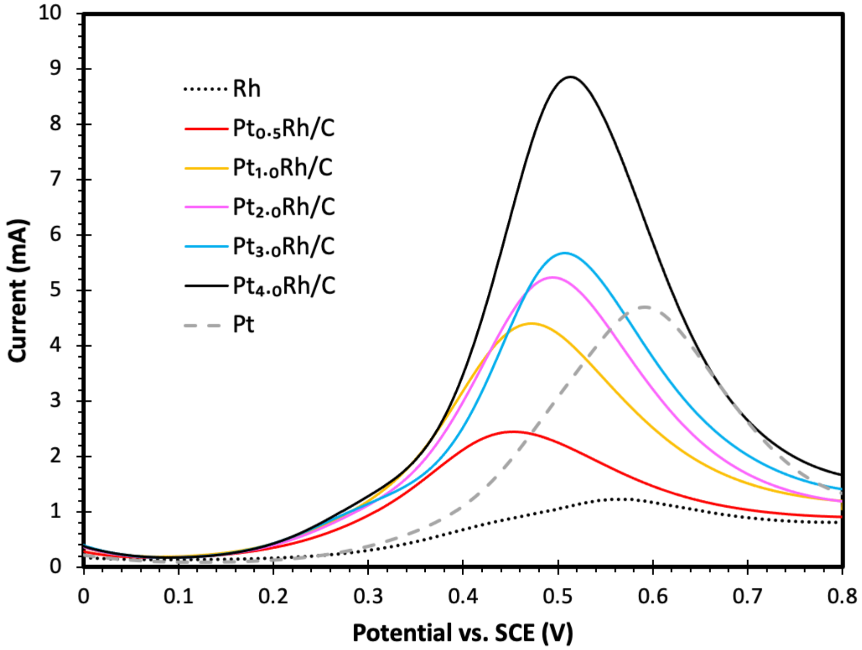

Figure 6.9. Linear sweep voltammetry (10 mV s^{-1}) for oxidation of 0.1 M methanol in 1 M H_2SO_4(aq) at PtRh, Rh, and Pt catalysts (0.3 mg cm^{-2} of Pt+Rh) at ambient temperature.

The PtRh alloys also improved ethanol oxidation activity over pure Rh and Pt, as shown in Figure 6.10. Rh catalyzed ethanol oxidation more efficiently than methanol, exhibiting a significantly higher peak current (1.36 mA vs 1.22 mA) and lower half-wave potential (0.37 V vs 0.40 V). Moreover, its current for ethanol oxidation was higher than for Pt at potentials below 0.50 V. This indicates that the Rh catalyst has a higher selectivity for ethanol oxidation over methanol oxidation and is more efficient than Pt for ethanol oxidation in an acidic medium. A low onset potential and high currents were observed for the $Pt_{0.5}Rh$ catalyst, indicating that the bifunctional effect is significant for PtRh alloys with high Rh contents. Interestingly, $Pt_{1.0}Rh$ had almost the same onset potential as $Pt_{0.5}Rh$ and almost the catalytic activity below 0.50 V. However, its peak current is 1.3 times greater at 0.50 V (Table 6.3). Therefore, the $Pt_{1.0}Rh$ catalyst must also exhibit significant lattice contraction.

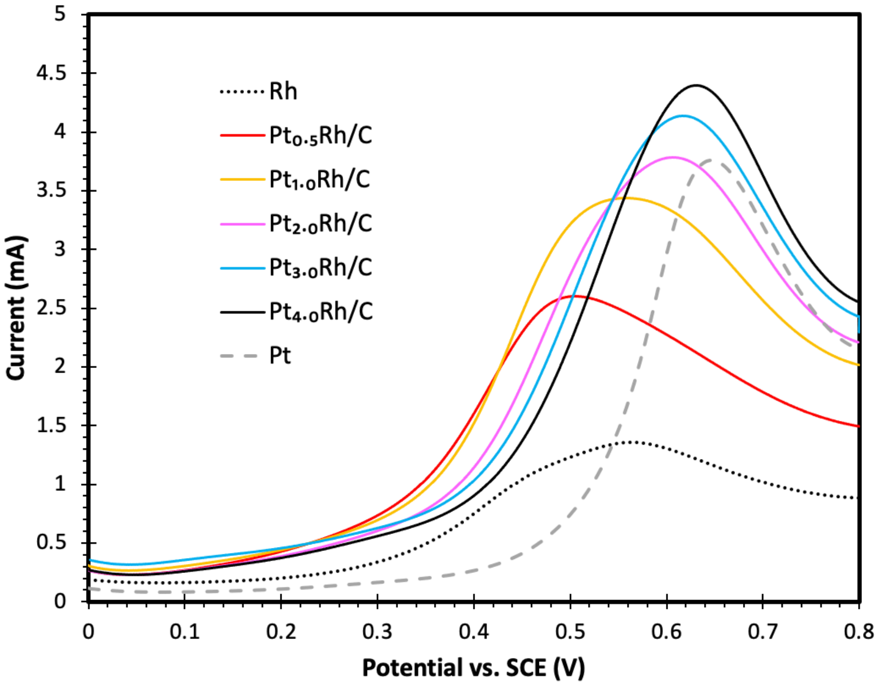

Figure 6.10. Linear sweep voltammetry (10 mV s^{-1}) for oxidation of 0.1 M ethanol in 1 M H_2SO_4(aq) at PtRh, Rh, and Pt catalysts (0.3 mg cm^{-2} of Pt+Rh) at ambient temperature.

The onset potentials and peak currents for the PtRh catalysts increased with increasing Pt content, similar to methanol (Figure 6.9); also, the highest forward anodic peak current was observed for $Pt_{4.0}Rh$. Its peak current reached 4.38 mA, while Pt reached 3.73 mA (Table 6.3). This indicates a strong synergistic interaction between Pt and low Rh content on the surface, with Pt being mostly responsible for increasing active sites.

Table 6.3. The forward anodic peak potential (E_f) and current (I_f) at 10 mV s^{-1} for the electrocatalytic activity of the PtRh catalysts for methanol and ethanol oxidation in 1 M H_2SO_4 (aq) at ambient temperature.

Catalyst	Methanol oxidation		Ethanol oxidation	
	E_f (V vs SCE)	I_f (mA)	E_f (V vs SCE)	I_f (mA)
Rh	0.56	1.22	0.56	1.36
$Pt_{0.5}Rh/C$	0.45	2.45	0.50	2.60
$Pt_{1.0}Rh/C$	0.47	4.40	0.55	3.44
$Pt_{2.0}Rh/C$	0.49	5.22	0.60	3.79
$Pt_{3.0}Rh/C$	0.50	5.67	0.61	4.13
$Pt_{4.0}Rh/C$	0.52	8.84	0.64	4.38
Pt	0.60	4.69	0.66	3.73

6.3.4. Oxidation of methanol and ethanol in a 9-anode PEMEC at 80 °C

Figure 6.11 shows the polarization curves for 0.1 M methanol and 0.1 M ethanol electrolysis at the surface of PtRh, Pt, and Rh anodes in a 9-anode PEMEC. The electrolysis cell was used to investigate the catalytic activities and selectivity of PtRh alloys for the generation of CO_2 under fuel cell-like conditions for methanol and ethanol oxidation compared to pure Pt and Rh (18, 23, 25). The PEM cell operates in a crossover mode to minimize the impact of ethanol crossing from the anode to the cathode without oxidizing at the anode catalyst. As a result, steady-state currents controlled by alcohol diffusion rates through the Nafion membrane are generated, with a stable cathodic potential due to H_2 evolution at a low overpotential (18, 25, 47).

For methanol oxidation (Figure 6.11A), the half-wave and onset potentials for the PtRh catalysts are much lower than for Pt. This indicates that Rh plays a role in enhancing methanol oxidation catalytic activity. All the PtRh catalysts have reached mass transport limits as Pt did at high potentials (20). The measured limiting currents (I_{lim}) were correlated with the average number of the generated electrons (n_{av}) eq. 6.3 (5, 20), in which F is the Faraday constant, m is the mass transport coefficient, A is the electrode area, and C is the fuel concentration.

$$I_{lim} = n_{av}FmAC \qquad (6.3)$$

At high potentials, the methanol is completely oxidized to CO_2 ($n_{av} \sim 6$) on the surface of Pt and PtRh catalysts except for $Pt_{0.5}Rh$ and $Pt_{1.0}Rh$ ($n_{av} \sim 5$).

For ethanol oxidation (Figure 6.11B), all PtRh electrodes had lower half-wave potentials than Pt electrode, meaning that the catalytic activity is higher due to the bifunctionality of Rh, which provides a stable hydroxide that further oxidizes the strongly adsorbed CO (34). The peak currents of PtRh alloys with a high Pt content are higher than that of Pt due to the strain effect of the alloying Rh (34). $Pt_{3.0}Rh$ electrode exhibits the highest peak current at 0.60 V, reaching 6.00 mA, while $Pt_{2.0}Rh$ has the highest peak current of 5.50 mA at ca. 0.50 V. Despite the similar currents for the $Pt_{4.0}Rh$ and Pt catalysts at 0.60 V, $Pt_{4.0}Rh$ is much more active at lower potentials, demonstrating that the presence of a small amount of Rh enhances the rate of ethanol oxidation by both bifunctional and strain effects. Rh alone showed no activity for ethanol oxidation, with a maximum current of only 1.00 mA at ca. 0.50 V. The reason for that is the slow rate of ethanol dehydrogenation and the slow rate of the further oxidation of the strongly adsorbed CO that results from the strong CO-Rh bonding (10).

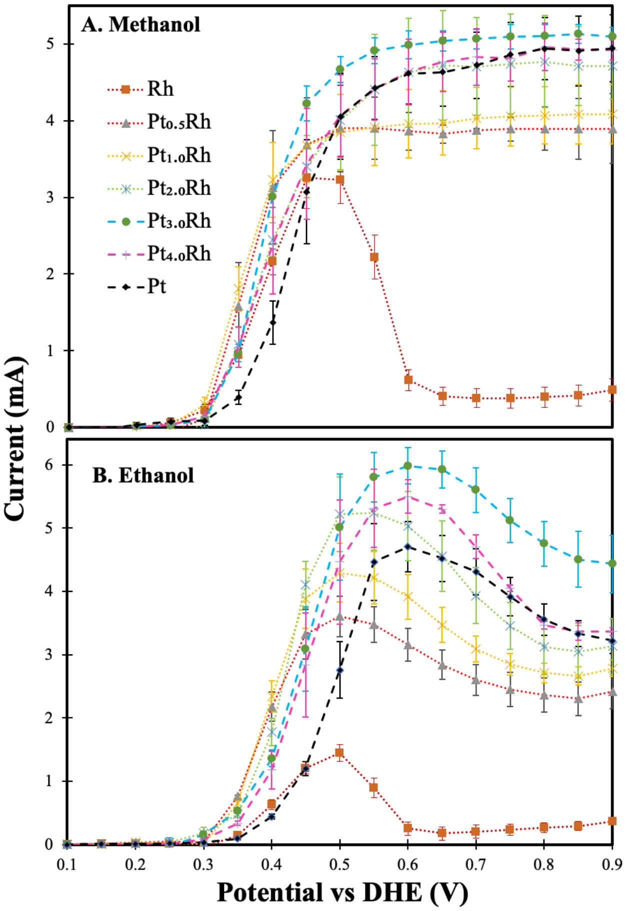

Figure 6.11. Polarization curves for the oxidation of 0.1 M methanol (A) and 0.1 M ethanol at Rh, PtRh, and Pt catalysts at 80 °C. A constant metal loading of 2.0 mg cm^{-2} on CFP electrodes was used.

It is observed that the limiting currents for ethanol oxidation decrease as the applied potential increases above 0.50 V (Figure 6.11B). However, the limiting currents remain constant for methanol oxidation at the same high potentials (Figure 6.11A). The reason for that is the change of the product distribution (i.e., change in the reaction stoichiometry (n_{av})) at each applied potential eq. 6.4 (5, 20), where n_i is the number of electrons transferred to form product *i,* and x_i is the fraction of ethanol converted to product *i*.

$$n_{av} = \sum n_i x_i \qquad (6.4)$$

The n_{av} at the mass transport limited area was calculated from the polarization curve (Figure 6.11B) using eq. 6.3, as previously described (18). The graph in Figure 6.12 shows the stoichiometries of ethanol oxidation at the surface of PtRh and Pt as a function of potentials.

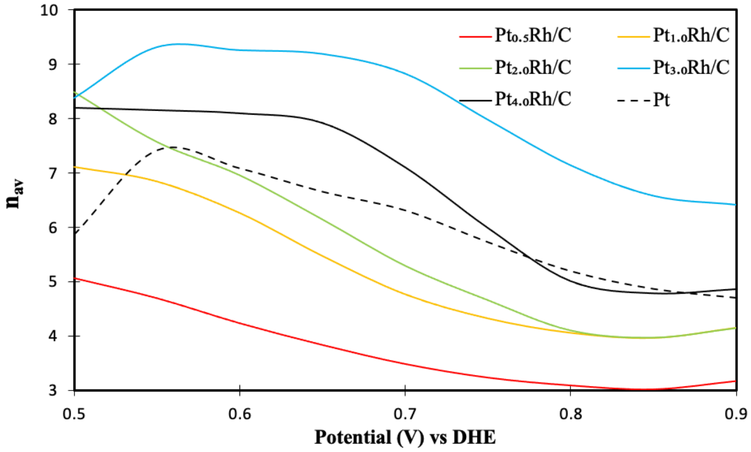

Figure 6.12. Stoichiometries for ethanol oxidation at PtRh and Pt electrodes from data in Figure 6.11B.

It is seen that the average number of electrons generated from ethanol oxidation on the surface of PtRh electrodes decreases as the applied potential increases. $Pt_{0.5}Rh$ has the lowest number of electrons generated above 0.50 V compared to Pt and other PtRh alloys, reaching 3.0 at 0.80 V, indicating that acetaldehyde (n = 2) and acetic acid (n = 4) are the primary products. The $Pt_{3.0}Rh$ and $Pt_{4.0}Rh$ catalysts had higher stoichiometries than the Pt catalyst. The maximum n_{av} was generated at $Pt_{3.0}Rh$ at all applied high potentials, with almost nine at 0.55 - 0.70 V. This indicates that CO_2 is its main product (n = 12) and acetic acid is its minor product (n = 4). Accordingly, the high Rh content in PtRh inhibits the selectivity for CO_2 generation due to the ensemble (third body) effect (48).

The catalytic selectivity for the generation of the CO_2 for ethanol oxidation on PtRh was further evaluated in the 9-anode PEMEC by measuring the faradaic yield of CO_2 ($F_{carbon\ dioxide}$)) at 0.50 V, using a previously described method (18). We measured at 0.50 V because all catalysts, including Rh, exhibit high catalytic activity at that potential for EOR at 80 °C (Figure 6.11B). The results are summarized in Table 6.4. CO_2 was the major product of ethanol oxidation at all Rh@Pt catalysts, resulting in their high n_{av} values.

The CO_2 yield increased with increasing the Pt content until reaching its maximum value of 80% at the $Pt_{3.0}Rh$ composition. As Pt content increases, CO_2 yield increases similarly to the calculated n_{av} (Figure 6.12) and the measured current (Figure 6.11B). PtRh catalysts, except $Pt_{0.5}Rh$, produced higher yields of CO_2 at 0.50 V than Pt catalysts. This indicates that the introduction of Rh facilitates the dissociation of the C-C bond, which generates CO_2. The highest efficiency of $Pt_{3.0}Rh$ for generating CO_2 in the anode corresponds to the highest H_2 yield in the cathode. Therefore, it is regarded as the best candidate for generating green hydrogen with a high yield. As well as being durable and corrosion-resistant (49), it has the lowest onset potential (Figure 6.11B), which means less energy is required for electrolysis.

The faradaic yield (F_i) of acetic acid and acetaldehyde, from the oxidation of ethanol on PtRh at 0.50 V can be calculated using eq. 6.5, where carbon dioxide, acetic acid, and acetaldehyde are assumed to be the only significant products during ethanol oxidation, and the sum of their faradaic yield can reasonably be assumed to be 100% (5).

$$n_{av} = 12/(F_{CO2} + 3F_{acetic\ acid} + 6F_{acetaldehyde}) \qquad (6.5)$$

According to Table 6.4, the PtRh catalysts do not produce significant amounts of acetaldehyde, except for $PtRh_{0.5}$, which yields 12% as Pt, confirming their high ability to dissociate the C-C bond and oxidize acetaldehyde to acetic acid further. $Pt_{1.0}Rh$ exhibits the highest acetic acid faradaic yield of 30% among PtRh and Pt. Thus, it is an excellent anodic catalyst for producing acetic acid beside green hydrogen from the EOR in PEMEC.

Table 6.4. Faradaic yields of CO_2, acetic acid, and acetaldehyde at 0.50 V vs DHE for ethanol oxidation at PtRh, Rh, and Pt at 80 °C.

Catalyst	Faradaic yield (%)		
	CO_2	Acetic Acid	Acetaldehyde
$Pt_{0.5}Rh/C$	61	19	20
$Pt_{1.0}Rh/C$	68	30	2
$Pt_{2.0}Rh/C$	78	22	0
$Pt_{3.0}Rh/C$	80	20	0
$Pt_{4.0}Rh/C$	77	23	0
Pt	66	22	12
Rh	52		

The polarization curve of EOR on the optimal PtRh composition ($Pt_{3.0}Rh$) is compared with data for a previously studied state-of-the-art PtRu catalyst (in the same 9-anode PEMEC at 80 °C with the same metal loading) in Figure D 5. (20). The EOR kinetics of PtRu were significantly faster than those of $Pt_{3.0}Rh$, since PtRu has an onset potential of 0.20 V, whereas $Pt_{3.0}Rh$ has an onset potential of 0.25 V. Additionally, PtRu has a half-wave potential of 0.30 V, whereas $Pt_{3.0}Rh$ has a half-wave potential of 0.45 V (Figure D 5). However, a significantly higher peak current was observed for $Pt_{3.0}Rh$, which reached 6.00 mA at 0.60 V, while PtRu reached 3.00 mA at 0.50 V (Figure D 5).

The overall efficiency of fuel cells depends on the overpotential needed to drive a reaction and the faradaic yield of CO_2 (50). Consequently, for optimum efficiency, the anode catalyst should possess both characteristics in balance. In this regard, $Pt_{3.0}Rh$ might be an attractive anodic catalyst in DEFC since it is highly selective for CO_2 generation compared with PtRu. $Pt_{3.0}Rh$ reaches 80% faradaic yield of CO_2 at 0.50 V compared to PtRu, which reaches 19% at 0.50 V.

6.3.5. Polarization curves and CO_2 yields for $Pt_{3.0}Rh$ catalysts in a 5 cm^2 PEMEC at 80 °C

In a 5 cm^2 PEMEC with a single anode, the best PtRh catalyst ($Pt_{3.0}Rh$) was evaluated using the normal electrolysis, after initial evaluation in the 9-anode PEM cell. That mode involves pumping ethanol through the anode, while N_2 is used at the cathode to exclude O_2.

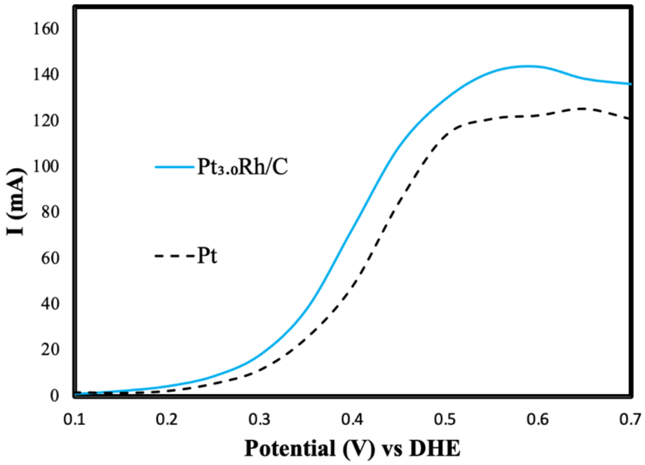

Figure 6.13. Polarization curves for ethanol oxidation at $Pt_{3.0}Rh$ and Pt electrodes using the same metal loading (2.0 mg cm^{-2}) in a 5 cm^2 PEMEC operated in a normal mode at 80 °C.

Figure 6.13 shows polarization curves for 0.1 M ethanol oxidation at the surface of the best-prepared catalyst $Pt_{3.0}Rh$ compared to the standard Pt operating in normal mode. $Pt_{3.0}Rh$ has a higher EOR reaction rate (lower onset potential) and higher generated currents than Pt, as shown at all applied potentials (Figure 6.13). This confirms the role of alloyed Rh for enhancing the electronic properties of the Pt by the strain effect and bifunctional mechanisms as described previously in the 9-anodes PEMEC part.

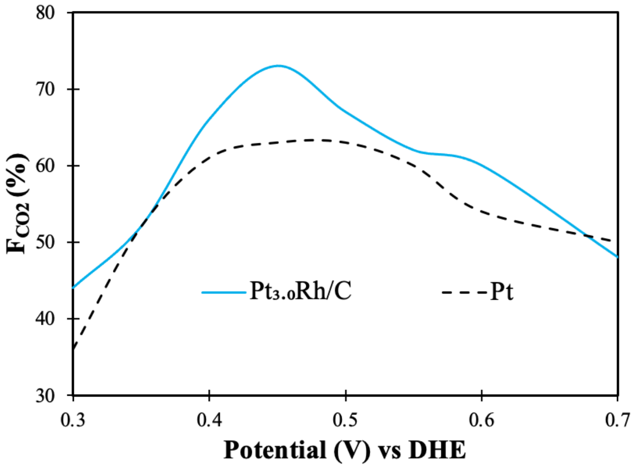

Figure 6.14. The CO_2 faradaic yields for 0.1 M ethanol oxidation at $Pt_{3.0}Rh$ and Pt electrodes using the same metal loading (2.0 mg cm^{-2}) in a 5 cm^2 PEMEC operated in a normal mode at 80 °C.

The faradaic yield of CO_2 at both $Pt_{3.0}Rh$ and Pt over a potential range of 0.30 V to 0.70 V for EOR was measured using the same method described previously Figure 6.14 (18). The faradaic yield in normal mode is expected to be lower than in crossover mode because some ethanol crosses to the cathode without oxidation. $Pt_{3.0}Rh$ has a higher selectivity for CO_2 generation than Pt at potentials below 0.70 V. However, at 0.70 V, its selectivity for CO_2 generation becomes slightly lower than Pt. At 0.45 V, the highest yield for CO_2 was obtained, with 73% for $Pt_{3.0}Rh$ and 63%

for Pt. Interestingly, these values are near the faradaic yield of CO_2 in the 9-anode PEMEC operated in a crossover mode at 0.50 V (Table 6.4). The results indicate that Rh facilitates the dissociation of the C-C bond and accelerates the oxidation of strongly adsorbed CO, resulting in the formation of CO_2.

6.4. Conclusions

In this study, we prepared high surface utilization PtRh alloy nanoparticles of different Pt:Rh atomic ratios using formic acid as a reducing agent. PtRh catalysts improved methanol and ethanol oxidation compared to Pt in aqueous H_2SO_4 at ambient temperature and PEM cells at 80 °C. As a result of the significant strain and bifunctional effects of Rh, it enhanced the electronic properties of the Pt surface for improving the fast removal of the highly adsorbed CO from the surface during methanol and ethanol oxidation. Also, it increases the selectivity for the generation of CO_2 during ethanol oxidation by facilitating the dissociation of the C-C bond compared to Pt.

The $Pt_{3.0}Rh$ composition is the optimal for increasing MOR activity and CO_2 selectivity for EOR in PEMEC. At 0.50 V, its stoichiometry (n_{av}) for EOR reaches 9.0, and its faradaic yield for CO_2 generation reaches 80%. The $Pt_{3.0}Rh$ catalyst is particularly well suited to the electrolysis of ethanol for generating green hydrogen and direct ethanol fuel cells for electricity generation by providing high activity at low potentials, high selectivity for CO_2 generation, and high durability and thermal stability of the carbon support.

6.5. References

1. Y.P. Liu, S.F. Zhao, S.X. Guo, A.M. Bond, J. Zhang, G. Zhu, C.L. Hill and Y.V. Geletii, Journal of the American Chemical Society, **138**, 2617-2628 (2016).

2. S.B. Han, Y.J. Song, J.M. Lee, J.Y. Kim and K.W. Park, Electrochemistry Communications, **10**, 1044-1047 (2008).
3. H.A. Asiri and A.B. Anderson, Journal of The Electrochemical Society, **162**, F115-F122 (2014).
4. G. Yang, Q. Zhang, H. Yu and F. Peng, Platinum-based ternary catalysts for the electrooxidation of ethanol, in Particuology, p. 169-186, Elsevier B.V. (2021).
5. A.H. Ali and P.G. Pickup, ECS Advances, **2**, 024501 (2023).
6. C.D. Silva, P.G. Corradini, V. Del Colle, L.H. Mascaro, F.H.B. de Lima and E.C. Pereira, Electrochimica Acta, **354**, 136674 (2020).
7. M.F. Azcoaga Chort, V.I. Rodríguez, S.R. de Miguel and N.S. Veizaga, Electrochimica Acta, **465**, 142948 (2023).
8. T. Imada, M. Chiku, E. Higuchi and H. Inoue, Journal of Physical Chemistry C, **125**, 14616-14626 (2021).
9. D.S. Santos, C.V.S. Almeida, G. Tremiliosi-Filho, K.I.B. Eguiluz and G.R. Salazar-Banda, Journal of Electroanalytical Chemistry, **879**, 114741 (2020).
10. S.Y. Shen, T.S. Zhao and J.B. Xu, International Journal of Hydrogen Energy, **35**, 12911-12917 (2010).
11. H. Liu, C. Song, L. Zhang, J. Zhang, H. Wang and D.P. Wilkinson, Journal of Power Sources, **155**, 95-110 (2006).
12. K. Bergamaski, E.R. Gonzalez and F.C. Nart, Electrochimica Acta, **53**, 4396-4406 (2008).
13. F.E. López-Suárez, M. Perez-Cadenas, A. Bueno-López, C.T. Carvalho-Filho, K.I.B. Eguiluz and G.R. Salazar-Banda, Journal of Applied Electrochemistry, **45**, 1057-1068 (2015).

14. B. Sawatmongkhon, K. Theinnoi, T. Wongchang, C. Haoharn, C. Wongkhorsub and E. Sukjit, Energy and Fuels, **35**, 4404-4417 (2021).
15. M. Li, W.P. Zhou, N.S. Marinkovic, K. Sasaki and R.R. Adzic, Electrochimica Acta, **104**, 454-461 (2013).
16. A. Bach Delpeuch, T. Asset, M. Chatenet and C. Cremers, Fuel Cells, **15**, 352-360 (2015).
17. R.M. Altarawneh, P. Majidi and P.G. Pickup, Journal of Power Sources, **351**, 106-114 (2017).
18. T.M. Brueckner and P.G. Pickup, Journal of the Electrochemical Society, **164**, F1172-F1178 (2017).
19. M. Carmo, D.L. Fritz, J. Mergel and D. Stolten, International Journal of Hydrogen Energy, **38**, 4901-4934 (2013).
20. A.H. Ali and P.G. Pickup, Journal of the Electrochemical Society, **169**, 034523 (2022).
21. C. Lamy, T. Jaubert, S. Baranton and C. Coutanceau, Journal of Power Sources, **245**, 927-936 (2014).
22. A. Ursua, L.M. Gandia and P. Sanchis, Proceedings of the IEEE, **100**, 410-426 (2011).
23. E.N. El Sawy, T.M. Brueckner and P.G. Pickup, Journal of the Electrochemical Society, **167**, 106507 (2020).
24. M. Carmo, T. Roepke, F. Scheiba, C. Roth, S. Moeller, H. Fuess, J.G.R. Poco and M. Linardi, Materials Research Bulletin, **44**, 51-56 (2009).
25. R.M. Altarawneh and P.G. Pickup, Journal of the Electrochemical Society, **164**, F861-F866 (2017).
26. R.M. Altarawneh, T.M. Brueckner, B. Chen and P.G. Pickup, Journal of Power Sources, **400**, 369-376 (2018).

27. R.M. Altarawneh and P.G. Pickup, Journal of the Electrochemical Society, **165**, F479-F483 (2018).

28. V.B. Venkatesh, G. Varghese, T.V. Joseph and P. Chippar, International Journal of Hydrogen Energy, **47**, 4018-4032 (2022).

29. I.N. Leontyev, D.V. Leontyeva, A.B. Kuriganova, Y.V. Popov, O.A. Maslova, N.V. Glebova, A.A. Nechitailov, N.K. Zelenina, A.A. Tomasov, L. Hennet and N.V. Smirnova, Mendeleev Communications, **25**, 468-469 (2015).

30. E.N. El Sawy, H.A. El-Sayed and V.I. Birss, Physical Chemistry Chemical Physics, **17**, 27509 (2015).

31. J. Zou, M. Wu, S. Ning, L. Huang, X. Kang and S. Chen, ACS Sustainable Chemistry and Engineering, **7**, 9007-9016 (2019).

32. F.H.B. Lima and E.R. Gonzalez, Electrochimica Acta, **53**, 2963-2971 (2008).

33. V. Petkov, Y. Maswadeh, J.A. Vargas, S. Shan, H. Kareem, Z.-P. Wu, J. Luo, C.-J. Zhong, S. Shastri and P. Kenesei, Nanoscale, **11**, 5512-5525 (2019).

34. F. Alcaide, G. Alvarez, P.L. Cabot, R.V. Genova-Koleva, H.-J. Grande, M.V. Martínez-Huerta and O. Miguel, Journal of Electroanalytical Chemistry, **861**, 113960 (2020).

35. Y. Kim, H.W. Kim, S. Lee, J. Han, D. Lee, J.R. Kim, T.W. Kim, C.U. Kim, S.Y. Jeong, H.J. Chae, B.S. Kim, H. Chang, W.B. Kim, S.M. Choi and H.J. Kim, ChemCatChem, **9**, 1683-1690 (2017).

36. M. Trzcinski, G. Balcerowska-Czerniak and A. Bukaluk, Catalysts, **10**, 617-627 (2020).

37. A.B. Delpeuch, T. Asset, M. Chatenet and C. Cremers, Journal of the Electrochemical Society, **161**, F918-F924 (2014).

38. M. Lukaszewski, M. Soszko and A. Czerwiński, International Journal of Electrochem, **11**, 4442-4469 (2016).

39. N.C. Röttcher, Y.-P. Ku, M. Minichova, K. Ehelebe and S. Cherevko, Journal of Physics: Energy, **5**, 024007 (2023).

40. J.M. Doña Rodríguez, J.A. Herrera Melián and J. Pérez Peña, Journal of Chemical Education, **77**, 1195-1197 (2000).

41. C. Cui, L. Gan, M. Heggen, S. Rudi and P. Strasser, Nature Materials, **12**, 765-771 (2013).

42. D. Chen, Q. Tao, L.W. Liao, S.X. Liu, Y.X. Chen and S. Ye, Electrocatalysis, **2**, 207-219 (2011).

43. M. Shao, J.H. Odell, S.-I. Choi and Y. Xia, Electrochemistry Communications, **31**, 46-48 (2013).

44. J. Bai, X. Xiao, Y.-Y. Xue, J.-X. Jiang, J.-H. Zeng, X.-F. Li and Y. Chen, ACS Applied Materials and Interfaces, **10**, 19755-19763 (2018).

45. C. Pettersen, A.O. Sjåstad and O. Ivashenko, The Journal of Physical Chemistry C, **125**, 25140-25147 (2021).

46. E.W. Harak, K.M. Koczkur, D.W. Harak, P. Patton and S.E. Skrabalak, ChemNanoMat, **3**, 815-821 (2017).

47. S.S. Pethaiah, J. Arunkumar, M. Ramos, A. Al-Jumaily and N. Manivannan, Bulletin of Materials Science, **39**, 273-278 (2016).

48. S.E. Evarts, I. Kendrick, B.L. Wallstrom, T. Mion, M. Abedi, N. Dimakis and E.S. Smotkin, ACS Catalysis, **2**, 701-707 (2012).

49. B.K. Devendra, B. Praveen, V. Tripathi, G. Nagaraju, D. Nagaraju and K. Nayana, Inorganic Chemistry Communications, **134**, 109065 (2021).

50. L. An, T. Zhao and Y. Li, Renewable and Sustainable Energy Reviews, **50**, 1462-1468 (2015).

Chapter 7: Summary and Future work

7.1. Methanol and ethanol oxidation activities on the PtRu@Pt core-shell catalysts

As illustrated in Chapter 3, highly active PtRu@Pt core-shell catalysts are easily prepared by chemically depositing different amounts of Pt on carbon-supported PtRu. Using this method, small-sized, dispersed, and low-agglomeration PtRu@Pt nanoparticles were prepared without stabilizers that negatively affected their catalytic activities.

PtRu@Pt had higher activity for the MOR in 1 M H_2SO_4 at ambient temperature than PtRu; however, they did not show an improvement over the state-of-the-art PtRu for methanol oxidation in PEMEC at 80 °C. The results of this study show that these catalysts improve ethanol oxidation compared to PtRu in PEMEC by increasing selectivity for the complete oxidation of ethanol to CO_2 and increasing the reaction stoichiometry (number of electrons transferred), leading to increased faradaic efficiency. Increasing the Pt coverage results in a higher half-wave potential for the electrolysis of ethanol. This results in a decrease in ethanol oxidation rate and, so, a reduction of potential efficiency.

The PtRu@$Pt_{1.7}$ is a promising catalyst for oxidizing ethanol in PEMEC to produce green hydrogen; its CO_2 faradaic yield is higher than PtRu (19%) and other PtRu@Pt reaching 58% at 0.50 V vs DHE.

7.2. Methanol and ethanol oxidation activities on the Ru@Pt core-shell catalysts

Using the same preparation method as Chapter 3, we could easily prepare Ru@Pt core-shell catalysts in Chapter 4. Our study focused on Pt shells with more than one monolayer for improving the activity and selectivity for ethanol oxidation, and the durability of the catalysts.

Pt shells on Ru cores promote the complete oxidation of ethanol to CO_2 more effectively than PtRu alloys and PtRu@Pt core-shell catalysts. In contrast to PtRu@Pt, higher potentials were required to overcome the reaction activation energy. In particular, these Ru@Pt catalysts are well-suited for ethanol electrolysis and hydrogen generation.

Methanol oxidation over $Ru@Pt_{0.6}$ in 1 M H_2SO_4 at ambient temperature produced lower onset potentials and higher peak currents than the state-of-art PtRu. Therefore, it can be used in direct methanol fuel cells to produce electricity.

7.3. Methanol and ethanol oxidation activities on the Rh@Pt core-shell catalysts

In Chapter 5, we prepared Rh@Pt core-shell catalysts ranging in thickness from half to three monolayers using an ethanol method. In an alkaline medium, this method produces small nanoparticles, narrow particle size distributions, high crystallinity, and uniform thicknesses of platinum.

The switch from Ru to Rh core proposed because Rh is more stable in acidic environments and more capable of selectively oxidizing ethanol to CO_2 (1-5). It was found that these catalysts performed better in aqueous H_2SO_4 at ambient temperature and PEMEC at 80 °C than Pt, Rh, and previous core-shell catalysts discussed in Chapters 3 and 4.

Rh@Pt(2.0 ML) exhibits the most increased ethanol oxidation activity and selectivity at higher potentials than Pt, PtRu, and other Rh@Pt preparations, with a faradaic yield of CO_2 of 73% at 0.50 V vs DHE, due to the high compressive strain caused by the Rh core. As a result, it can be used to produce green hydrogen from ethanol electrolysis.

Rh@Pt(0.5 ML) exhibits the highest catalytic activity at low applied potentials, nearing the most effective PtRu. In PEMEC operated in normal mode fuel cell conditions, Rh@Pt(0.5 ML) was examined for its catalytic activities and selectivity for CO_2 generation from ethanol oxidation. As a result of its high yield of CO_2 at low applied potentials, it makes a promising anodic catalyst for direct ethanol fuel cells.

7.4. Methanol and ethanol oxidation activities on PtRh alloys

The catalytic activities of PtRh alloys for ethanol oxidation in PEMEC at 80 °C were examined as a necessary step for studying their ability to act as anodic catalysts in direct ethanol fuel cells.

Surface electronic properties of Pt were enhanced through Rh's strain and bifunctional effects to enable the removal of CO during the oxidation of methanol and ethanol. In addition, it facilitates the dissociation of C-C bonds during ethanol oxidation, enhancing CO_2 generation.

$Pt_{3.0}Rh$ is the optimal composition for increasing MOR activity and CO_2 selectivity for EOR in PEMEC. In PEMEC under fuel cell-like conditions, its catalytic activities for ethanol oxidation were examined and compared with Pt. Its selectivity for generating CO_2 is much higher than that of Pt at all applied potentials. The $Pt_{3.0}Rh$ catalyst is particularly well suited to the electrolysis of ethanol for generating green hydrogen and direct ethanol fuel cells for electricity generation.

7.5. Brief list of Future work

Using our best catalysts, we will compare the overall efficiency of our ethanol electrolysis cell for hydrogen production with that of a water electrolysis cell using Pt as a state-of-the-art catalyst for hydrogen evolution. In this study, we plan to use PtRu@$Pt_{1.7}$ (1.0 ML), Ru@$Pt_{1.0}$ (2.0 ML), Rh@Pt(2.0 ML), and $Pt_{3.0}$Rh, which showed higher selectivity for CO_2 generation than PtRu and Pt at some applied potentials (6).

The best catalysts for EOR needed further study using a 5 cm^2 PEMEC in order to determine product distribution, stability at high potentials for long periods of time, kinetics, and efficiency at low applied potentials. The effect of increasing fuel concentrations on their selectivity for CO_2 generation for EOR will also be studied in PEMEC.

In addition, the catalytic activity of Ir@Pt of various Pt thicknesses has been planned to be investigated in PEMEC for the oxidations of methanol and ethanol due to their high ability to remove the CO and selective generation of CO_2, as previously described (7-9).

Our recent work indicates that the catalytic activity and selectivity of PtRh catalysts for ethanol oxidation can be enhancing by adding a third metal (ternary alloys) such as Ru, Ni, Fe, Sn, and Cu, due to their ability to remove strongly adsorbed CO from Pt surfaces (10-12).

The results for the PtRh alloys in Chapter 6 indicate that Rh and PtRh shells could be more active and selective than Pt shell. Consequently, PtRu@Rh and Ru@PtRh catalysts with different atomic ratios of the metals should be prepared to screen their effects on ethanol oxidation rate and CO_2 generation selectivity.

Finally, Ru@$Pt_{0.6}$ (1.5 ML), Rh@Pt(0.5 ML), and $Pt_{2.0}$Rh catalysts can be compared with state-of-the-art PtRu catalysts in direct methanol and ethanol fuel cells.

7.6. References

1. M. Kalyva, D.S. Wragg, H. Fjellvåg and A.O. Sjåstad, ChemistryOpen, **6**, 273-281 (2017).
2. J. Bai, X. Xiao, Y.-Y. Xue, J.-X. Jiang, J.-H. Zeng, X.-F. Li and Y. Chen, ACS Applied Materials and Interfaces, **10**, 19755-19763 (2018).
3. B.K. Devendra, B. Praveen, V. Tripathi, G. Nagaraju, D. Nagaraju and K. Nayana, Inorganic Chemistry Communications, **134**, 109065 (2021).
4. T. Imada, M. Chiku, E. Higuchi and H. Inoue, Journal of Physical Chemistry C, **125**, 14616-14626 (2021).
5. B. Sawatmongkhon, K. Theinnoi, T. Wongchang, C. Haoharn, C. Wongkhorsub and E. Sukjit, Energy and Fuels, **35**, 4404-4417 (2021).
6. L.M. Salonen, D.Y. Petrovykh and Y.V. Kolen'ko, Materials Today Sustainability, **11**, 100060 (2021).
7. M. Bekmezci, D.B. Subasi, R. Bayat, M. Akin, Z.K. Coguplugil and F. Sen, New Journal of Chemistry, **46**, 21591-21598 (2022).
8. N.S. Veizaga, G. Mendow, A.F. Quintero-Jaime, A. Berenguer-Murcia, S. de Miguel, E. Morallón and D. Cazorla-Amorós, Materials Chemistry and Physics, **275**, 125282 (2022).
9. G. Zhang, D. Cao, S. Guo, Y. Fang, Q. Wang, S. Cheng, W. Zuo, Z. Yang and P. Cui, Small, **18**, 2202587 (2022).
10. A.H. Ali and P.G. Pickup, Journal of the Electrochemical Society, **169**, 034523 (2022).
11. A.H. Ali and P.G. Pickup, ECS Advances, **2**, 024501 (2023).
12. N. Lu and Y. Wang, Computational and Theoretical Chemistry, **1228**, 114252 (2023).

Appendix A

Electrolysis of ethanol and methanol at PtRu@Pt catalyst

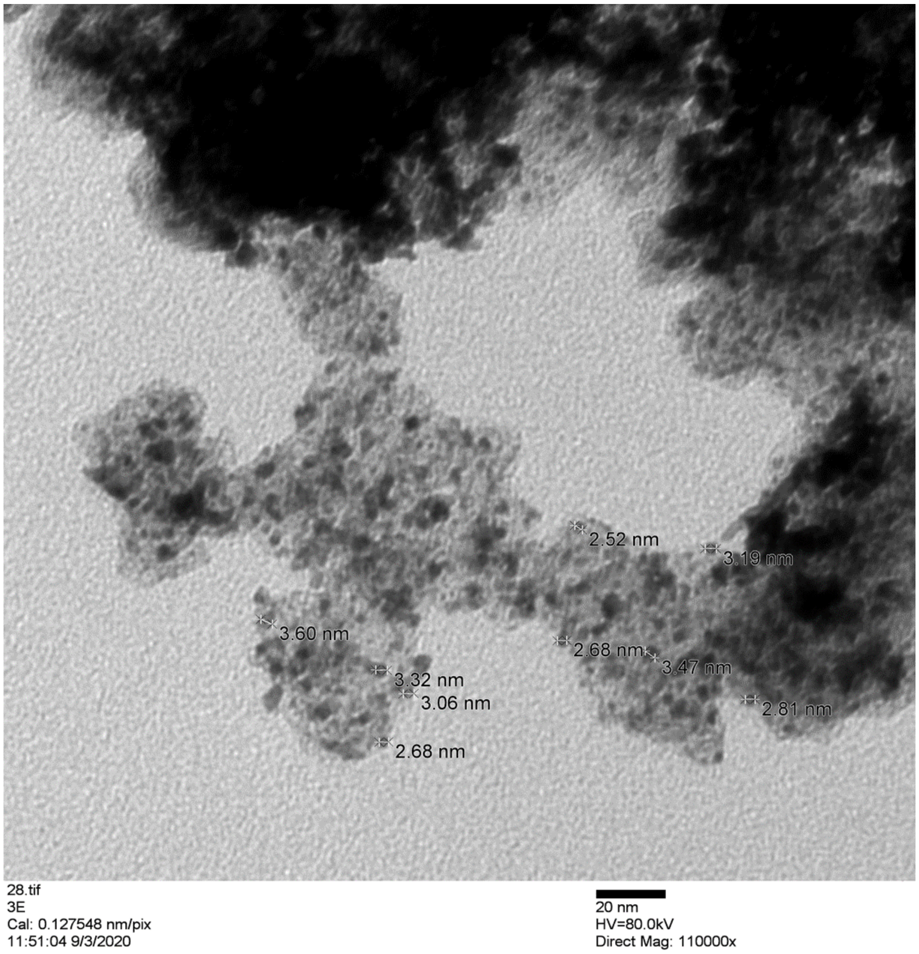

Figure A 1. TEM image of the PtRu@Pt$_{0.3}$ catalyst.

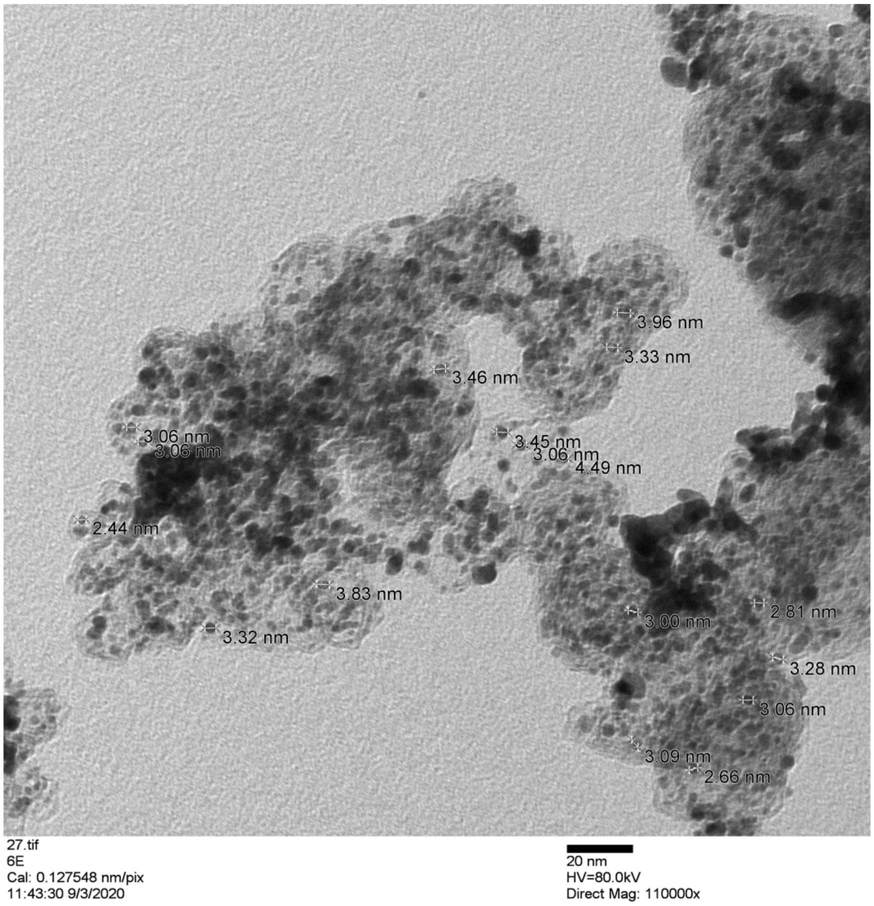

Figure A 2. TEM image of the PtRu@Pt$_{0.6}$ catalyst.

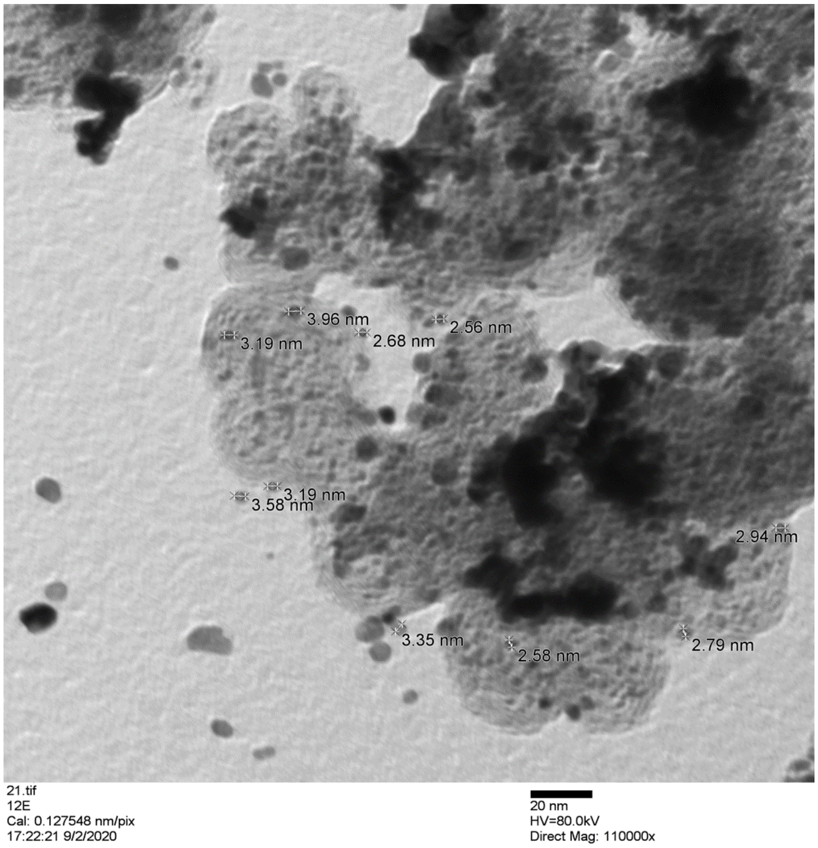

Figure A 3. TEM image of the PtRu@Pt$_{1.2}$ catalyst.

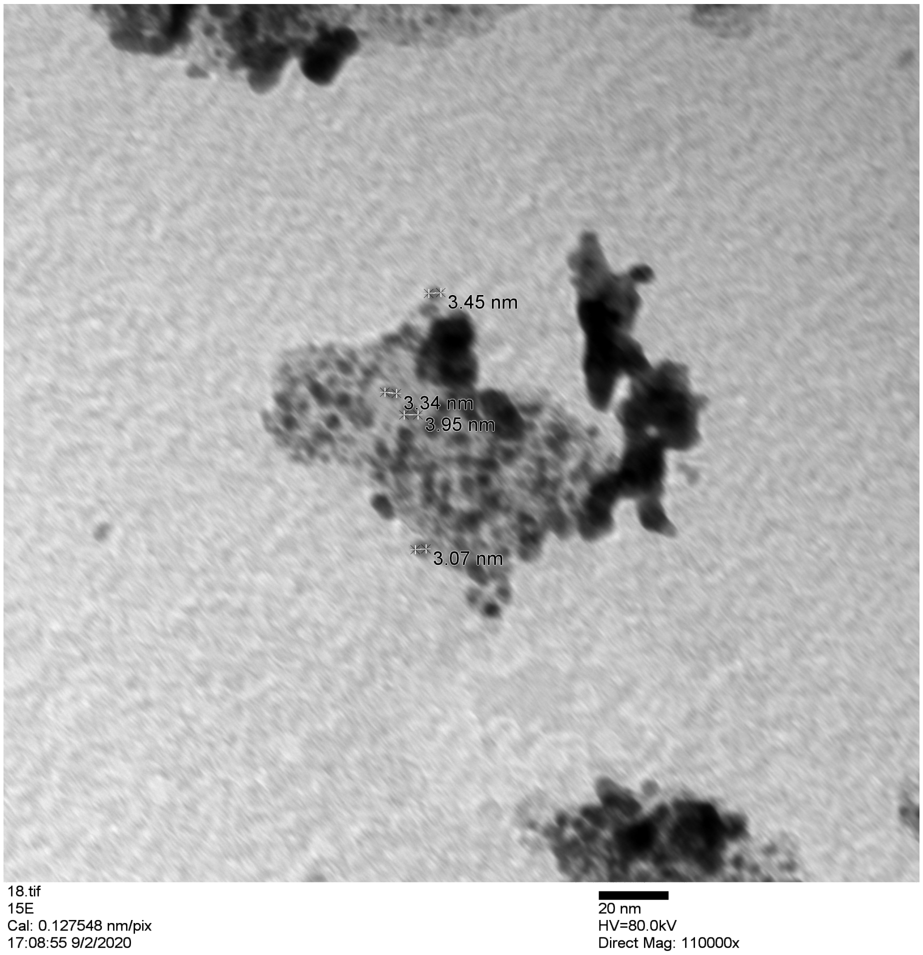

Figure A 4. TEM image of the PtRu@Pt$_{1.4}$ catalyst.

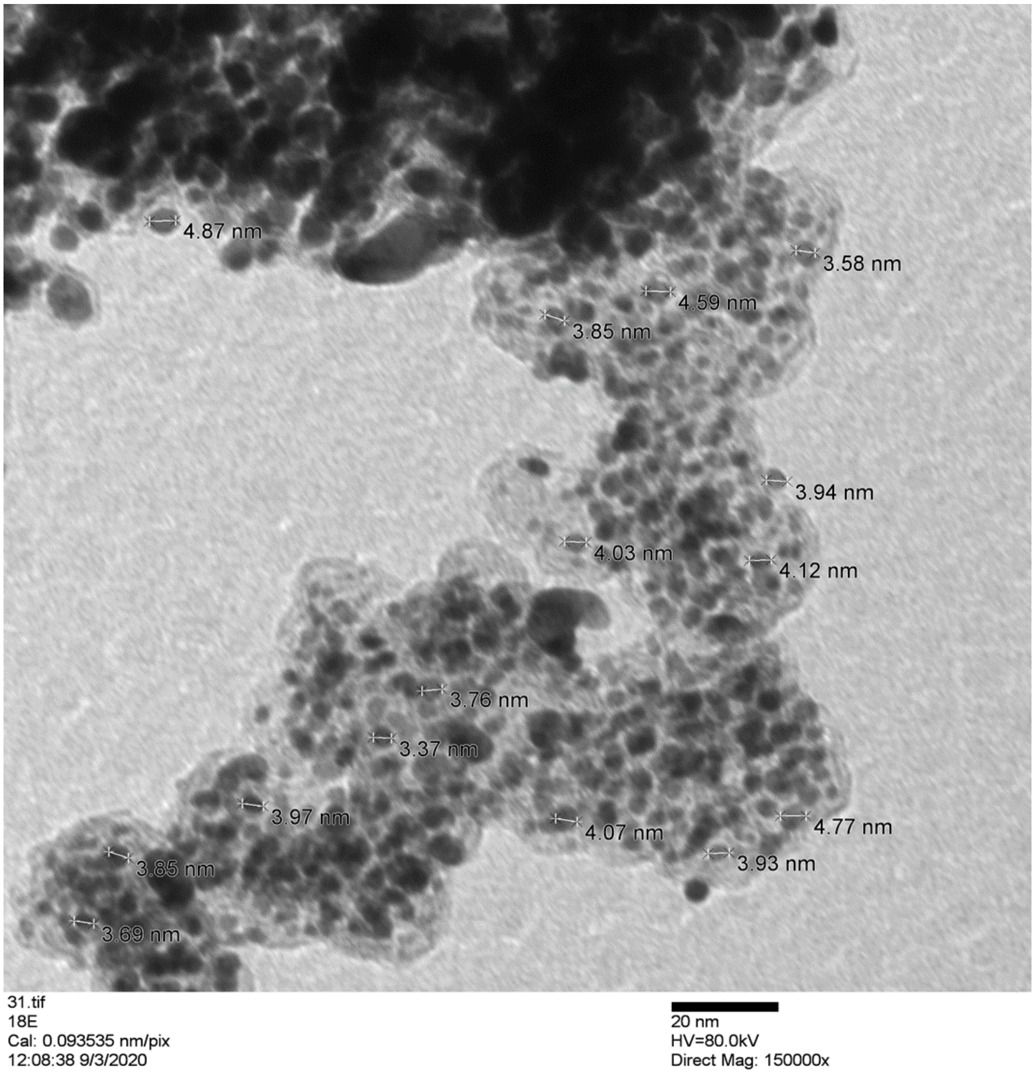

Figure A 5. TEM image of the PtRu@Pt$_{1.7}$ catalyst.

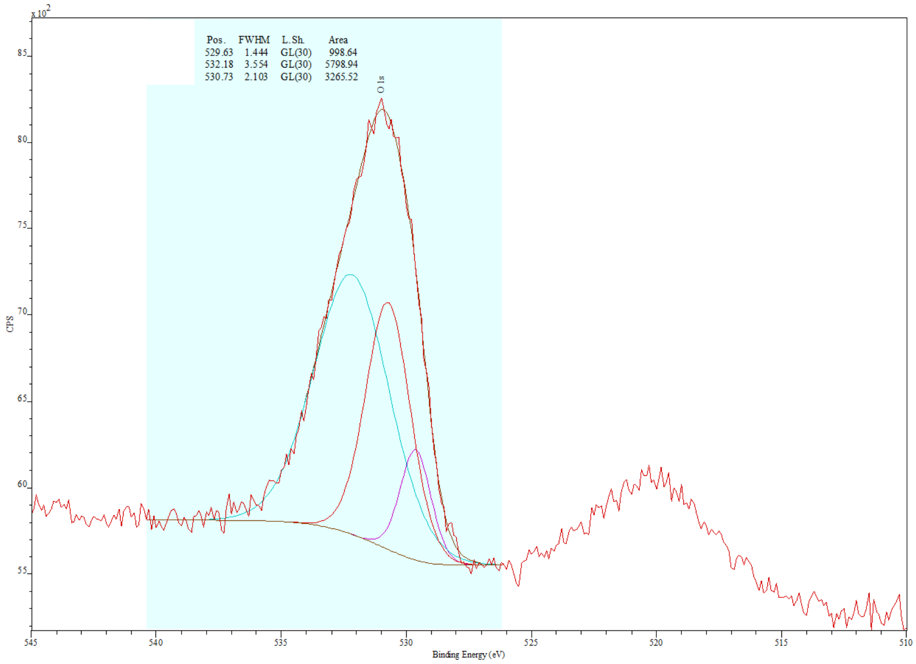

Figure A 6. Deconvoluted O 1s region of the XPS spectrum of the PtRu catalyst.

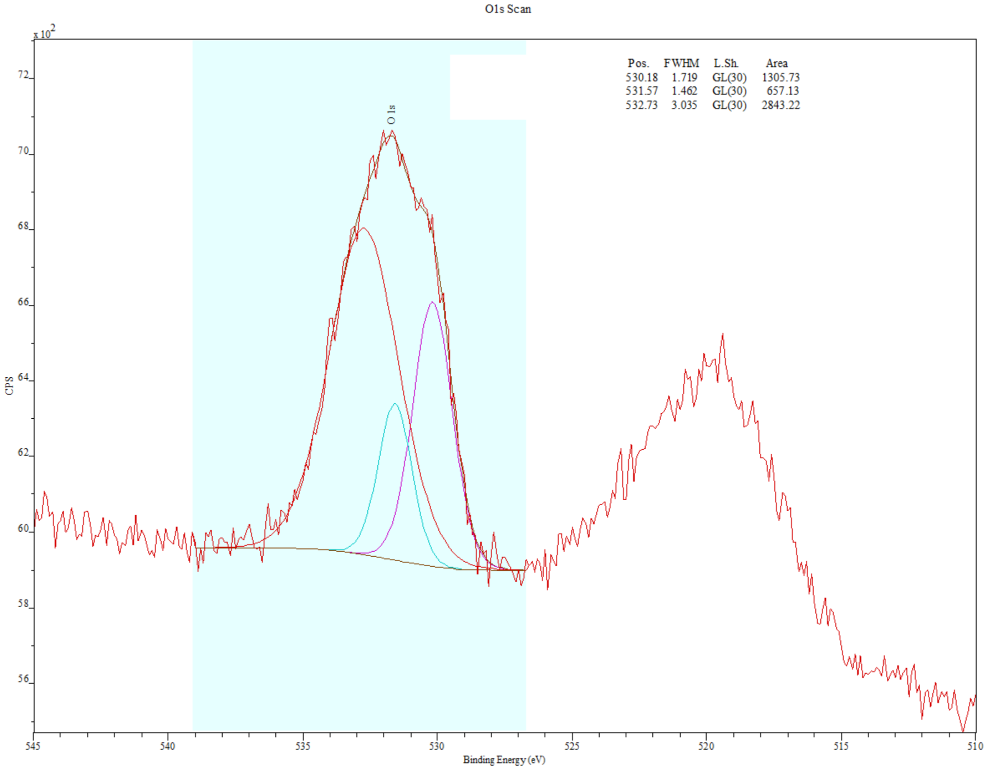

Figure A 7. Deconvoluted O 1s region of the XPS spectrum of the PtRu PtRu@Pt$_{0.6}$ catalyst.

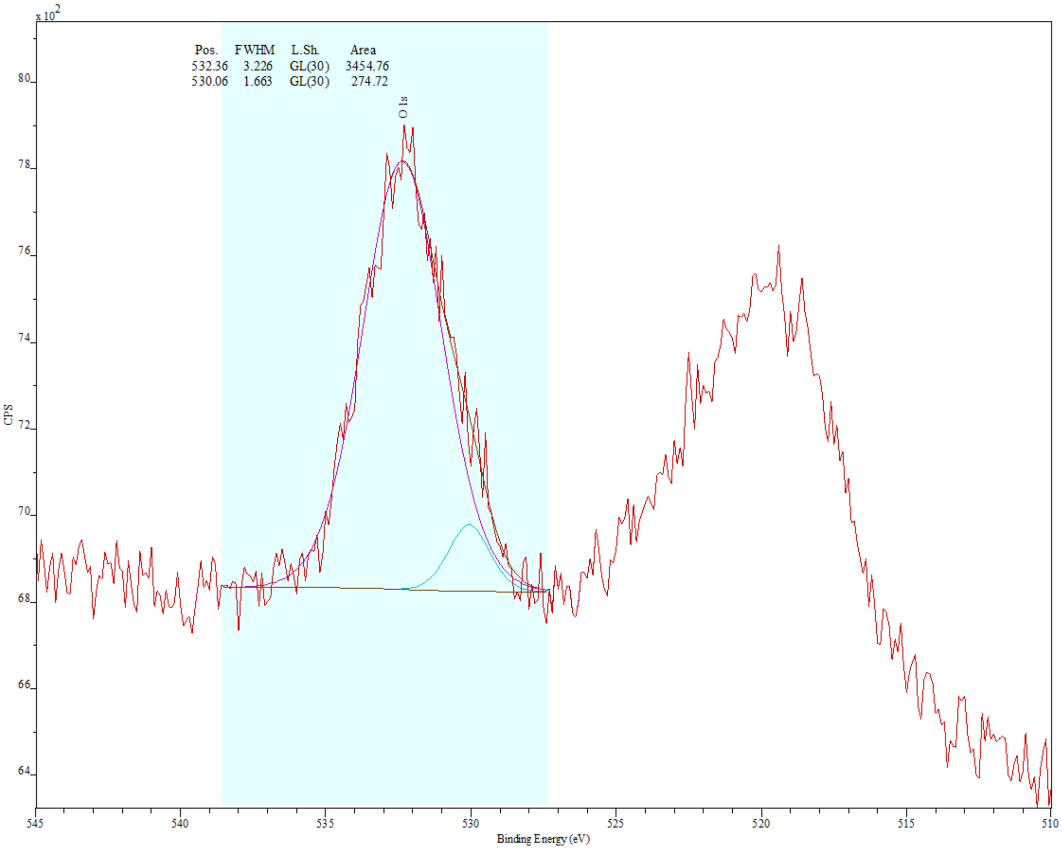

Figure A 8. Deconvoluted O 1s region of the XPS spectrum of the PtRu PtRu@Pt$_{1.4}$ catalyst.

Appendix B

Efficient oxidation of ethanol at Ru@Pt core-shell catalysts in a proton exchange membrane electrolysis cell

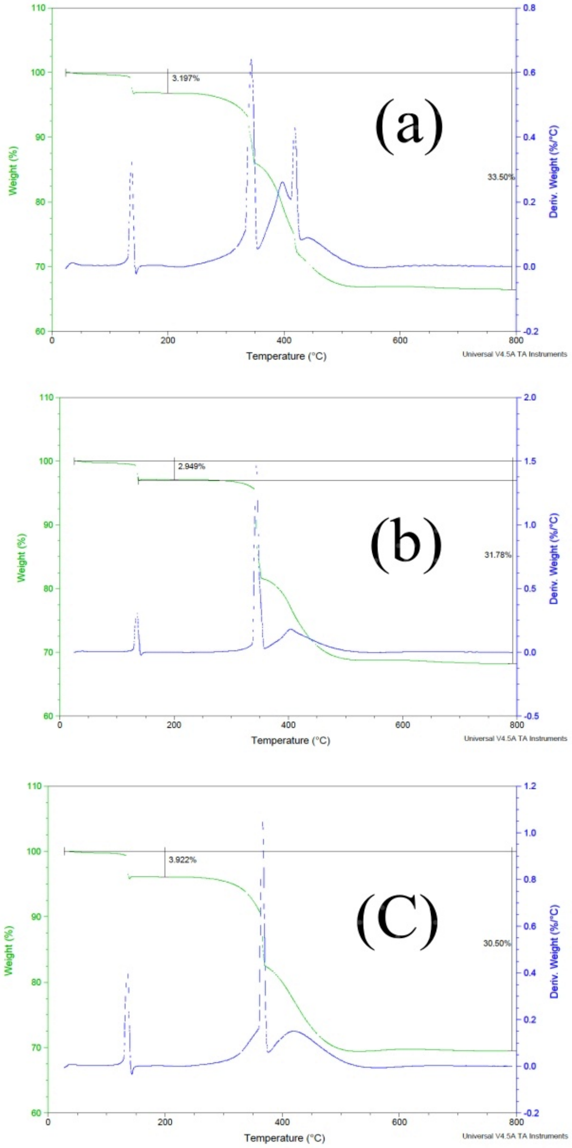

Figure B 1. TGA data for a) Ru@$Pt_{0.6}$, b) Ru@$Pt_{1.0}$ and c) Ru@$Pt_{1.4}$.

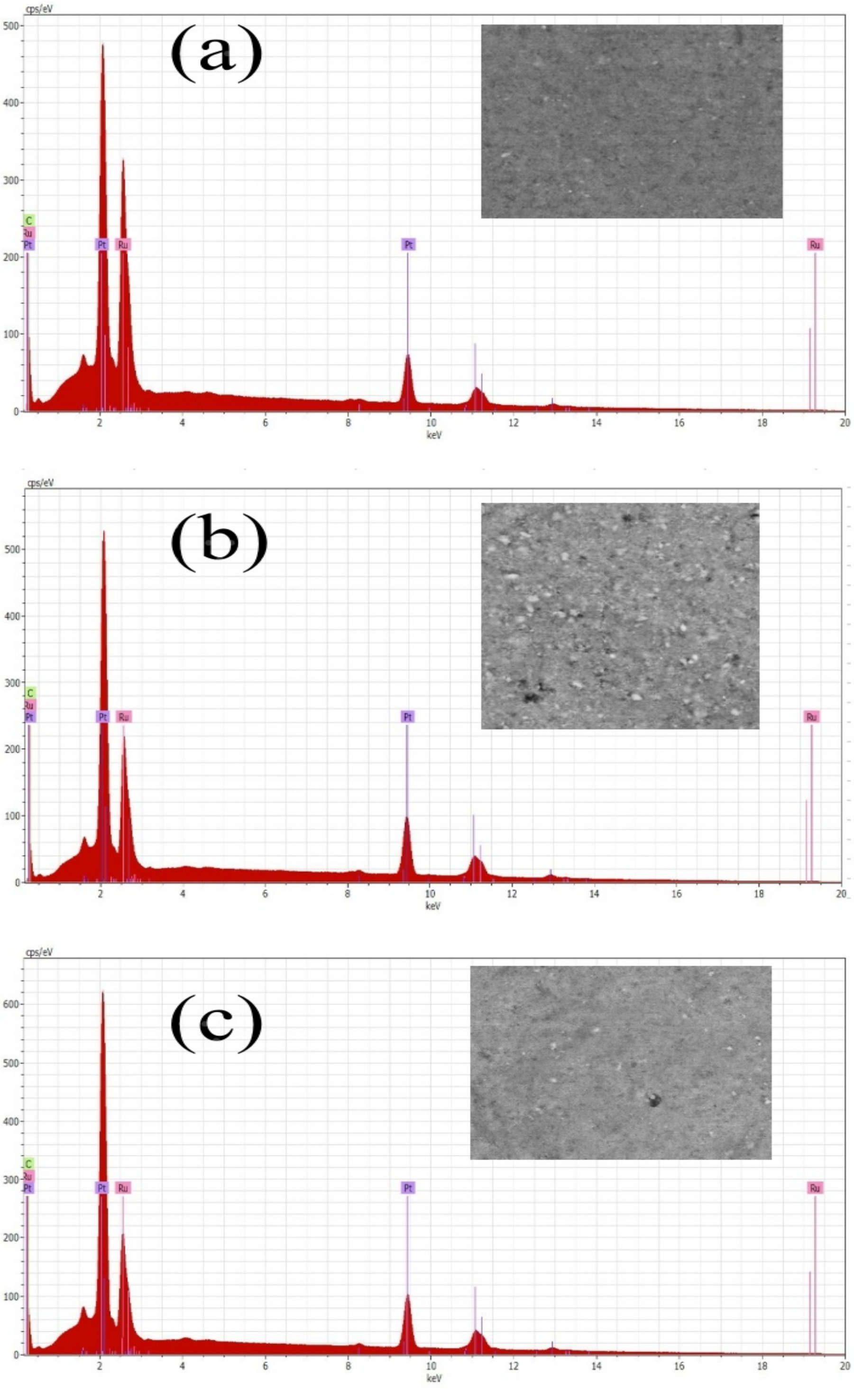

Figure B 2. EDX spectra for a) Ru@$Pt_{0.6}$, b) Ru@$Pt_{1.0}$ and c) Ru@$Pt_{1.4}$ and SEM images of the areas that were analyzed.

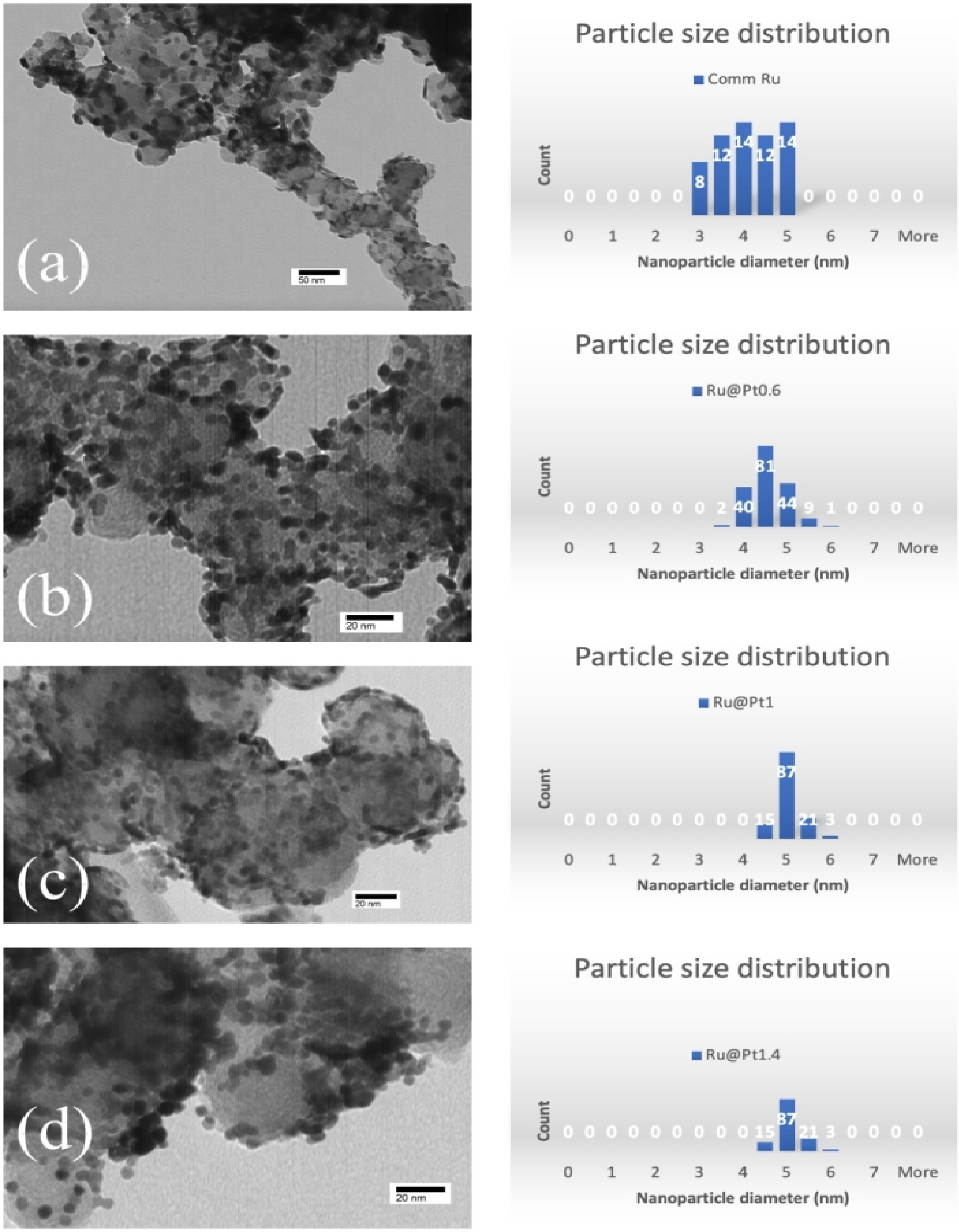

Figure B 3. TEM images and particle size distribution histograms of the catalysts: a) Ru, b) Ru@Pt$_{0.6}$, c) Ru@Pt$_{1.0}$ and d) Ru@Pt$_{1.4}$.

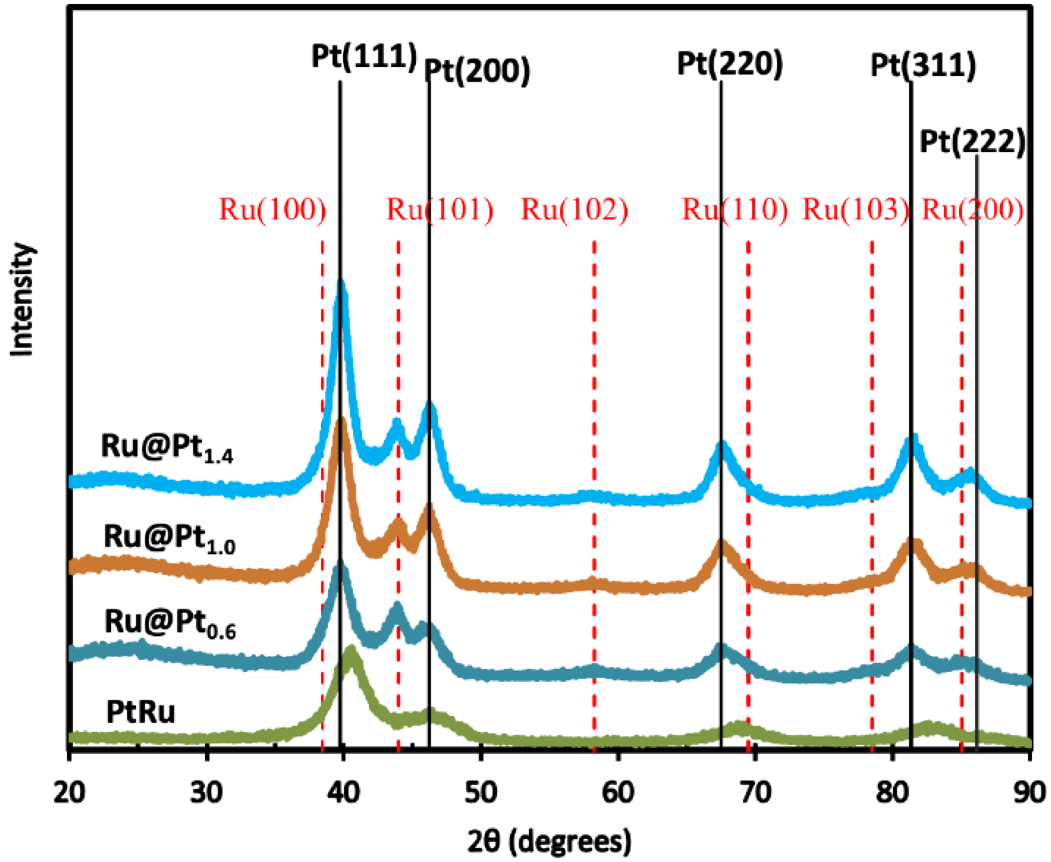

Figure B 4. XRD patterns for the Ru@Pt catalysts and a commercial PtRu catalyst. The vertical lines show peak positions for pure Pt and Ru.

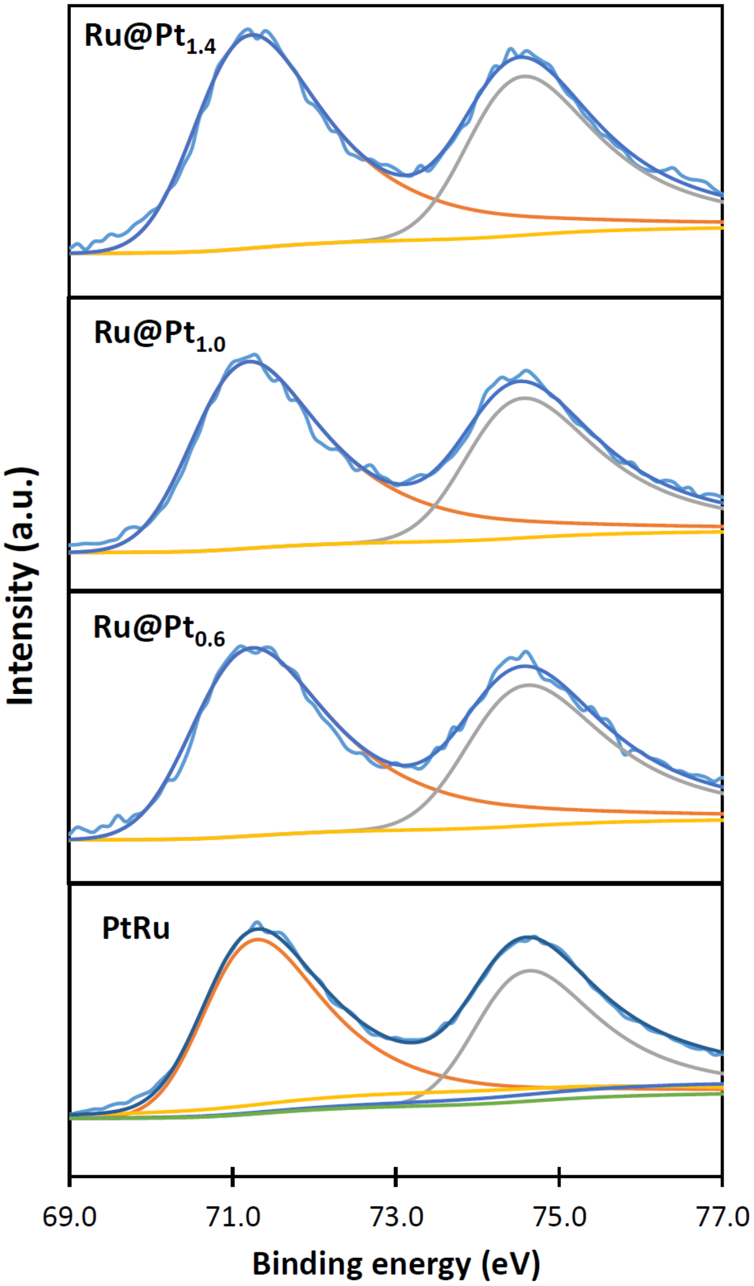

Figure B 5. Pt 4f XPS spectra for the Ru@Pt and PtRu catalysts.

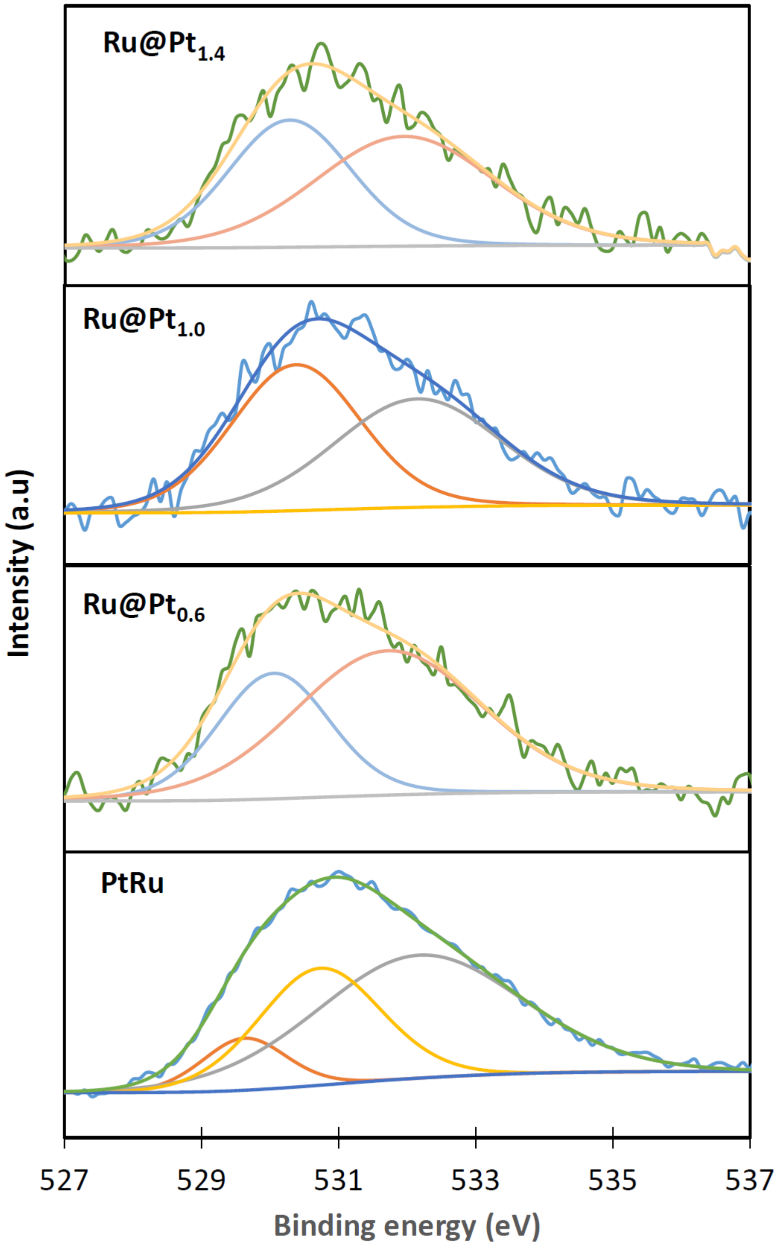

Figure B 6. O 1s XPS spectra for the Ru@Pt and PtRu catalysts.

Appendix C

Electrochemical oxidation of ethanol and methanol at Rh@Pt catalysts at 80 °C in proton exchange membrane (PEM) cell

Synthetic method Eqs. C1 and C2 (1) were used to calculate the amounts of $H_2PtCl_6.6H_2O$ required to prepare Rh@Pt nanoparticles with the targeted Pt shell thicknesses from 0.04 g of the commercial Rh/C catalyst, based on the specified Rh diameter of 3.0 nm (D_{Rh}). The required mass of $H_2PtCl_6.6H_2O$, the volume of 1 M NaOH required, expected total metal loading (Rh+Pt mass%), and expected diameter of Rh@Pt particles (Eq. C1) are provided in Table C1.

$$D_{Rh@Pt} = D_{Rh}\sqrt[3]{\frac{\frac{M_{Pt}P_{Rh}}{M_{Rh}P_{Pt}}n_{Pt}+n_{Rh}}{n_{Rh}}} \qquad \text{(C1)}$$

$$\text{Monolayers of Pt} = \frac{\mathrm{D_{Rh@Pt}} - \mathrm{D_{Rh}}}{2\ \mathrm{D_{Pt\,atom}}} \qquad \text{(C2)}$$

$D_{Rh@Pt}$ is the diameter of Rh@Pt core-shell nanoparticles, M_{Pt} and M_{Rh} are the molar masses of Pt and Rh, P_{Pt} and P_{Rh} are the densities of Pt and Rh, and n_{Pt} and n_{Rh} are the moles of Pt and Rh in a single Rh@Pt nanoparticle.

1. J. N. Schwammlein, B. M. Stuhmeier, K. Wagenbauer, H. Dietz, V. Tileli, H. A. Gasteiger and H. A. El-Sayed, Journal of Electrochemical Society, **165** (2018) H229-H239.

Table C 1. Required mass of $H_2PtCl_6.6H_2O$, volume of NaOH (V_{NaOH}) and expected Pt:Rh mole ratio, Rh+Pt mass% and particle diameter for each Rh@Pt catalyst.

Catalyst	Mass of $H_2PtCl_6.6H_2O$ (g)	Rh+Pt mass%	Pt:Rh mole ratio	V_{NaOH} (mL)	$D_{Rh@Pt}$ (nm)
Rh@Pt(0.5 ML)	0.0123	28.3 %	0.305	0.0711	3.39
Rh@Pt(1.0 ML)	0.0258	35.6 %	0.640	0.149	3.68
Rh@Pt(1.5 ML)	0.0417	42.6 %	1.04	0.241	3.97
Rh@Pt(2.0 ML)	0.0600	48.9 %	1.49	0.347	4.26
Rh@Pt(3.0 ML)	0.105	59.7 %	2.60	0.606	4.83

Table C 2. Comparison of faradaic yield of CO_2 measured at 0.50 V in the 9-anode and 5 cm^2 electrolysis cells.

Catalyst	Faradaic yield of CO_2	
	9-anode cell	5 cm^2 cell
Rh@Pt(0.5 ML)	56 %	51 %
Rh@Pt(1.5 ML)	61 %	61 %
Pt	66 %	63 %

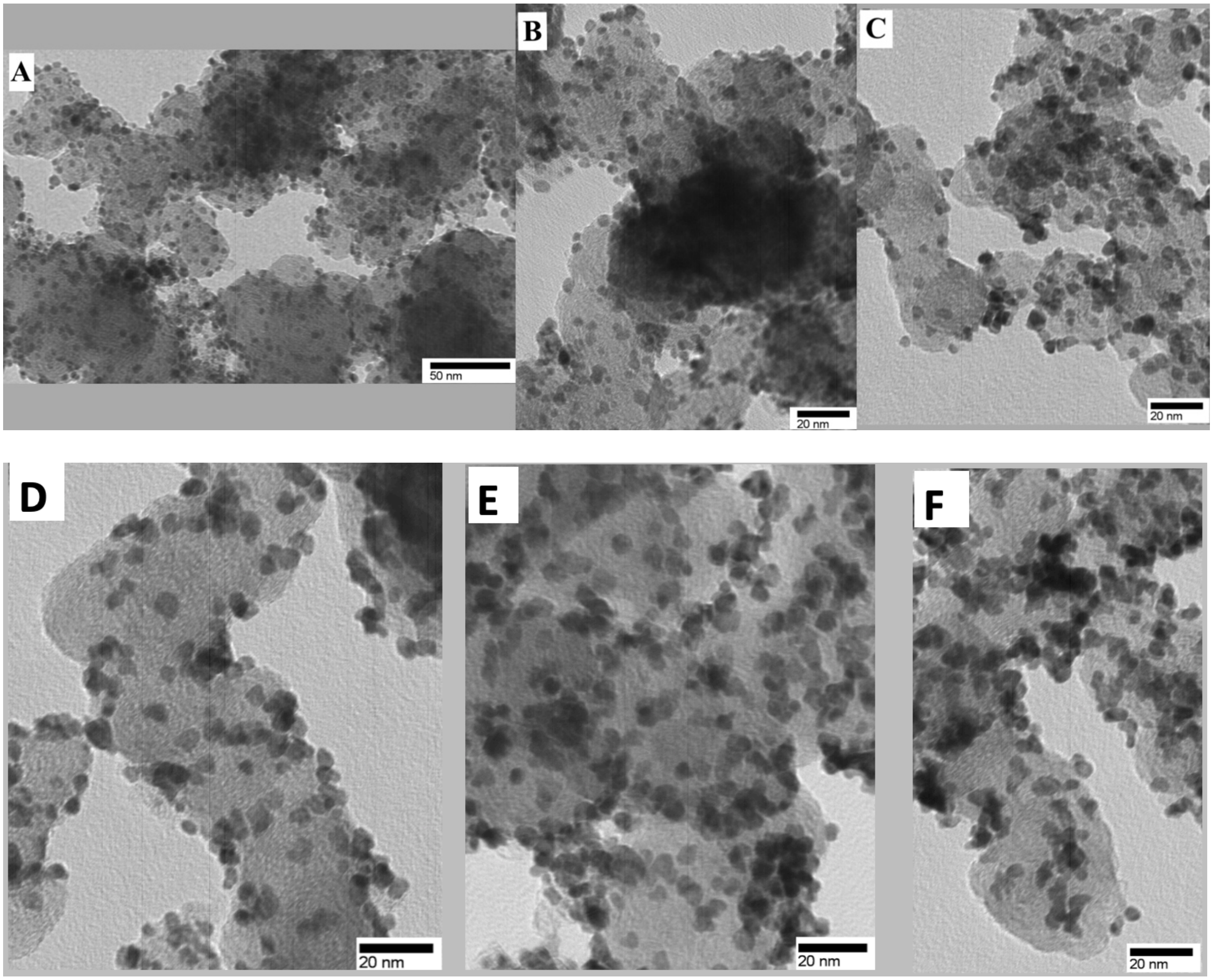

Figure C 1. TEM images of the Rh (A), Rh@Pt(0.5 ML) (B) and Rh@Pt(1.0 ML) (C), Rh@Pt(1.5 ML) (D), Rh@Pt(2.0 ML) (E), and Rh@Pt(3.0 ML) (F) catalysts.

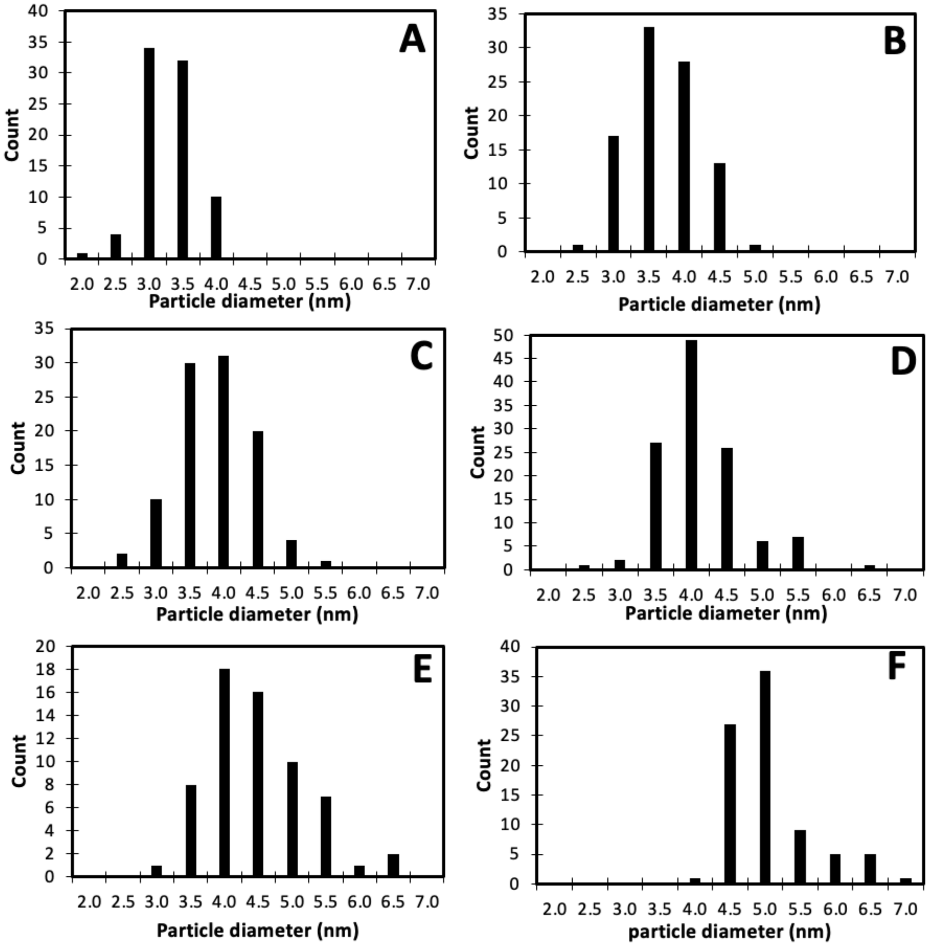

Figure C 2. The particle size distribution histograms of the Rh (A), Rh@Pt(0.5 ML) (B), Rh@Pt(1.0 ML) (C), Rh@Pt(1.5 ML) (D), Rh@Pt(2.0 ML) (E), and Rh@Pt(3.0 ML) (F) catalysts.

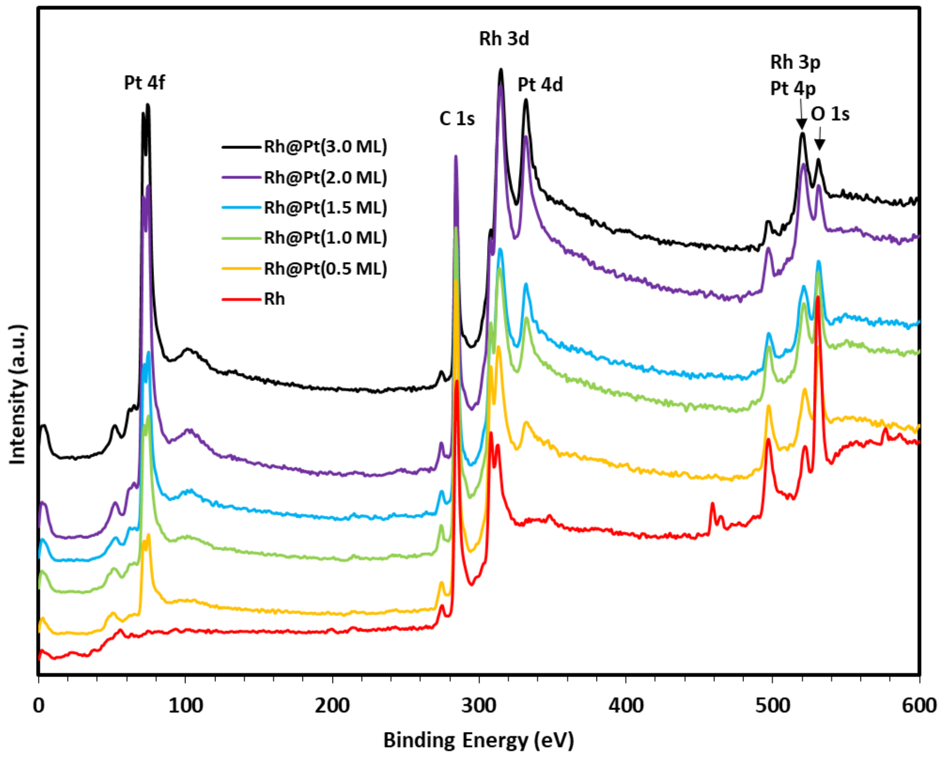

Figure C 3. XPS spectra of the Rh@Pt catalysts.

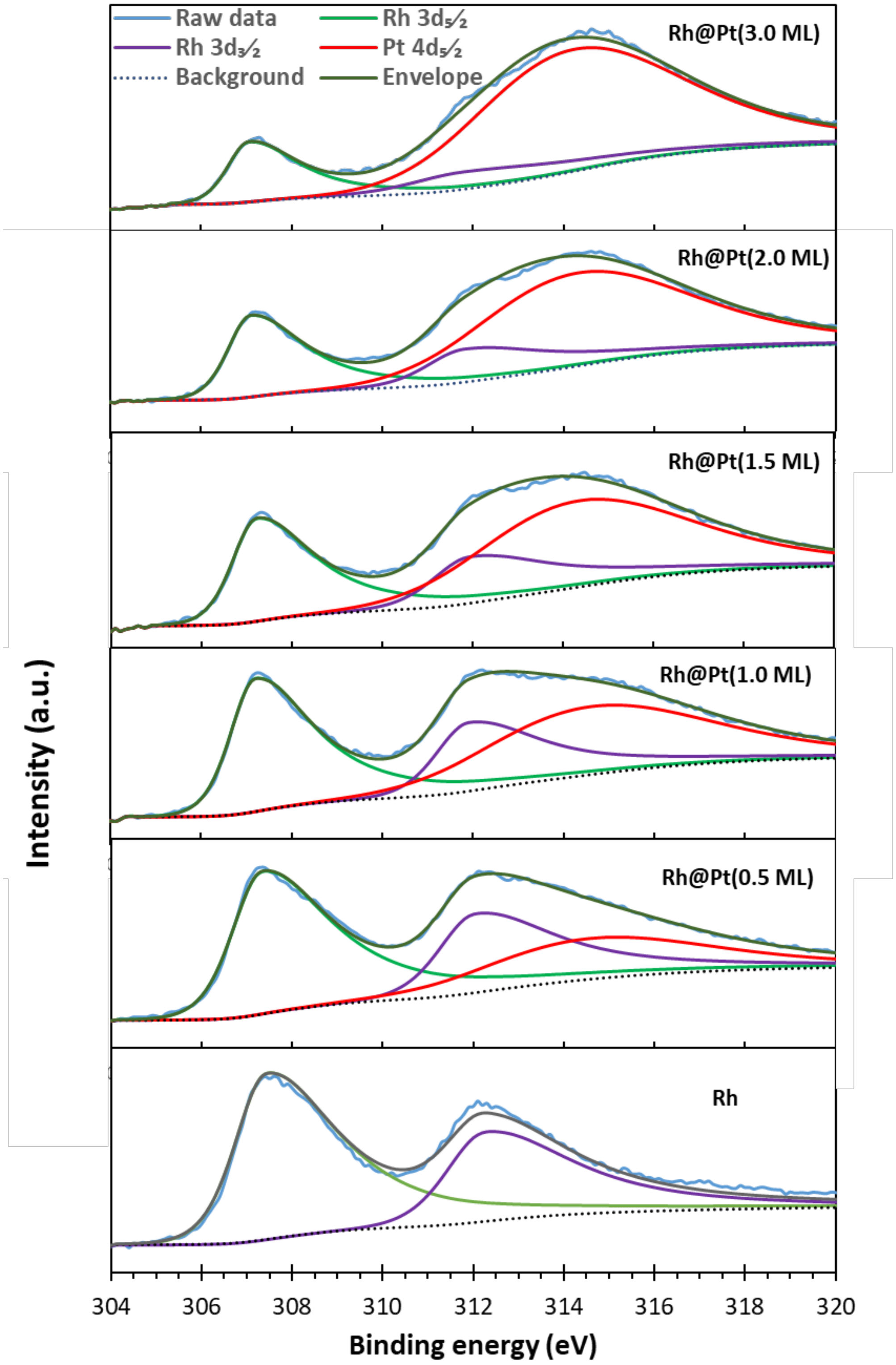

Figure C 4. Deconvolution of the Rh 3d and Pt 4d of the XPS spectra for the Rh and Rh@Pt catalysts.

Appendix D

Methanol and ethanol oxidation on carbon-supported platinum-rhodium alloy nanoparticles using a proton exchange membrane electrolysis cell

Table D 1. The required mass of $H_2PtCl_6.6H_2O$ and $RhCl_3.3H_2O$, the expected mole ratios of Pt:Rh, the required mass of carbon black-Vulcan XC-72, and the expected total metals (Rh+Pt) mass %, of each prepared PtRh/C catalyst.

Catalyst	mass			Rh+Pt mass %	Pt:Rh ratio
	$RhCl_3.3H_2O$ (g)	$H_2PtCl_6.6H_2O$ (g)	Carbon black (g)		
$Pt_{0.5}Rh/C$	0.050	0.049	0.057	40 %	0.5
$Pt_{1.0}Rh/C$	0.050	0.098	0.085	40 %	1.0
$Pt_{2.0}Rh/C$	0.050	0.197	0.141	40 %	2.0
$Pt_{3.0}Rh/C$	0.050	0.295	0.194	40 %	3.0
$Pt_{4.0}Rh/C$	0.050	0.393	0.250	40 %	4.0

Table D 2. The electroactive surface area (*EASA*) of the Rh, Pt, and PtRh nanoparticles.

Catalyst	*EASA*	Geometric surface area	Utilization (%)
Rh	62.7	115.2	54.4
$Pt_{0.5}Rh/C$	87.6	116.5	75.2
$Pt_{1.0}Rh/C$	91.6	100.7	91.0
$Pt_{2.0}Rh/C$	84.3	92.4	91.2
$Pt_{3.0}Rh/C$	81.1	88.9	91.2
$Pt_{4.0}Rh/C$	78.9	87.0	90.7
Pt	37.1	72.5	51.2

The geometric surface area is calculated as shown in eq. D1, where *N* is the number of particles, $4\,\pi r^2$ is the surface of particles. The surface utilization is calculated by dividing the *EASA* by the geometric surface area.

$$Geometric\ surface\ area\ = N * 4 * \pi * r^2 \qquad \text{(D1)}$$

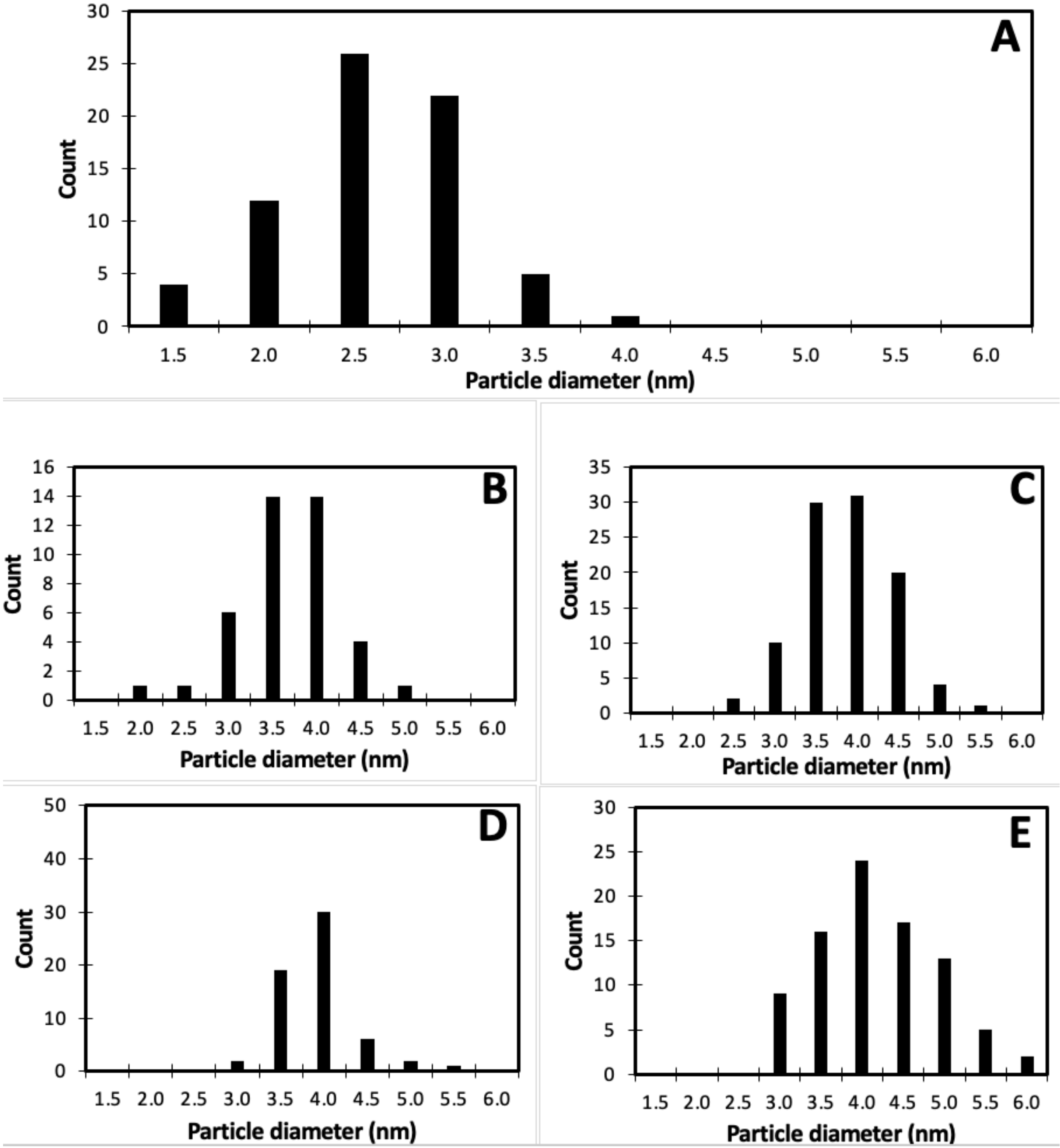

Figure D 1. TEM nanoparticle size distribution histograms of (A) $Pt_{0.5}Rh$ (B) $Pt_{1.0}Rh$, (C) $Pt_{2.0}Rh$, (D) $Pt_{3.0}Rh$, and (E) $Pt_{4.0}Rh$.

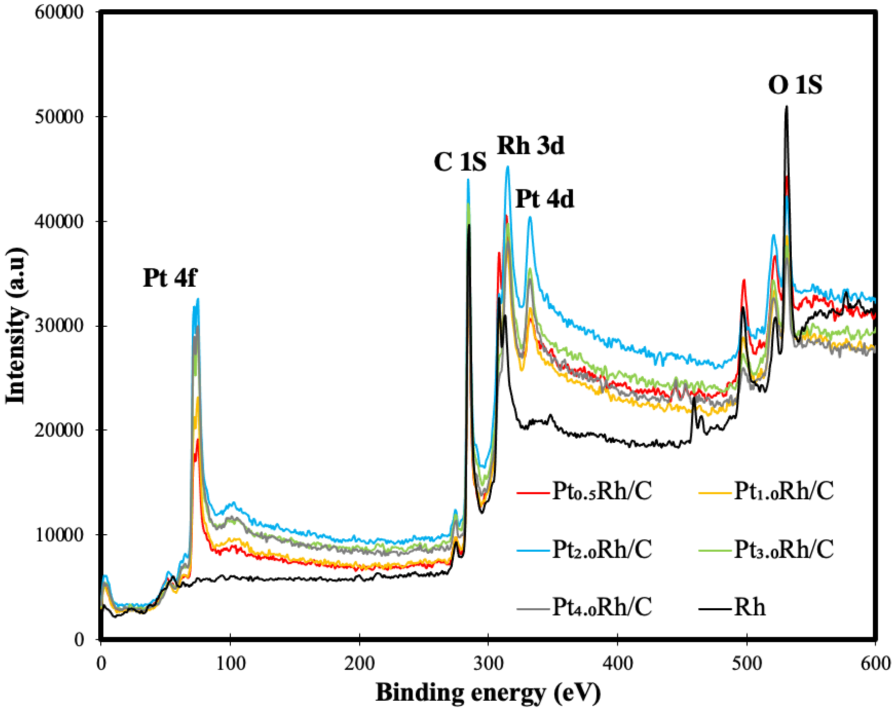

Figure D 2. XPS spectra of Rh and PtRh catalysts.

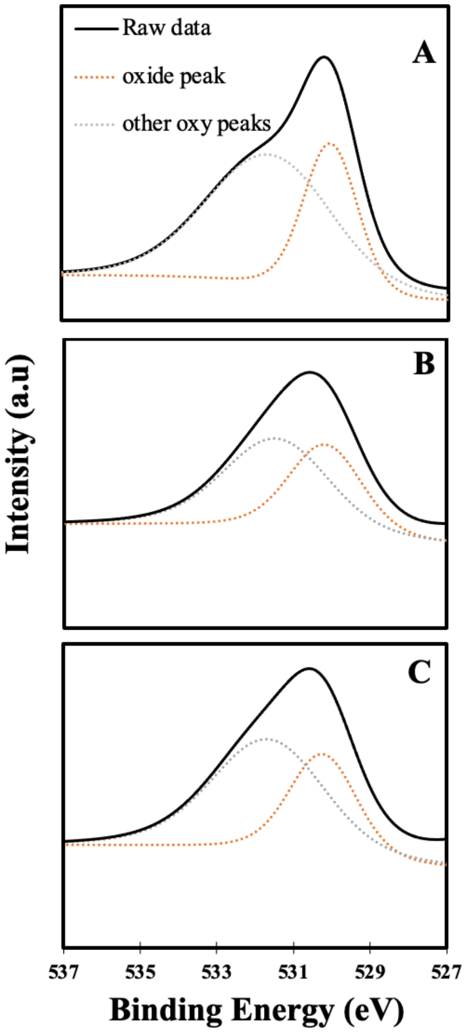

Figure D 3. Deconvoluted O 1s region of the XPS spectra of the (A) Rh, (B) $Pt_{0.5}Rh$, and (C) $Pt_{1.0}Rh$ catalysts.

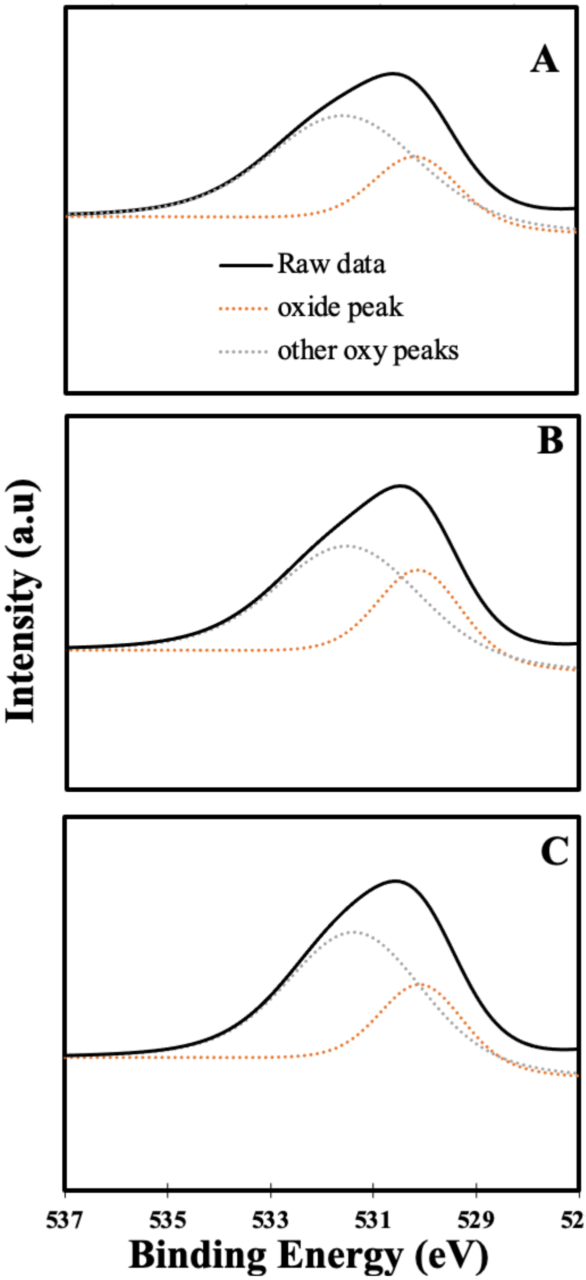

Figure D 4. Deconvoluted O 1s region of the XPS spectra of (A) $Pt_{2.0}Rh$, (B) $Pt_{3.0}Rh$, and (C) $Pt_{4.0}Rh$ catalysts.

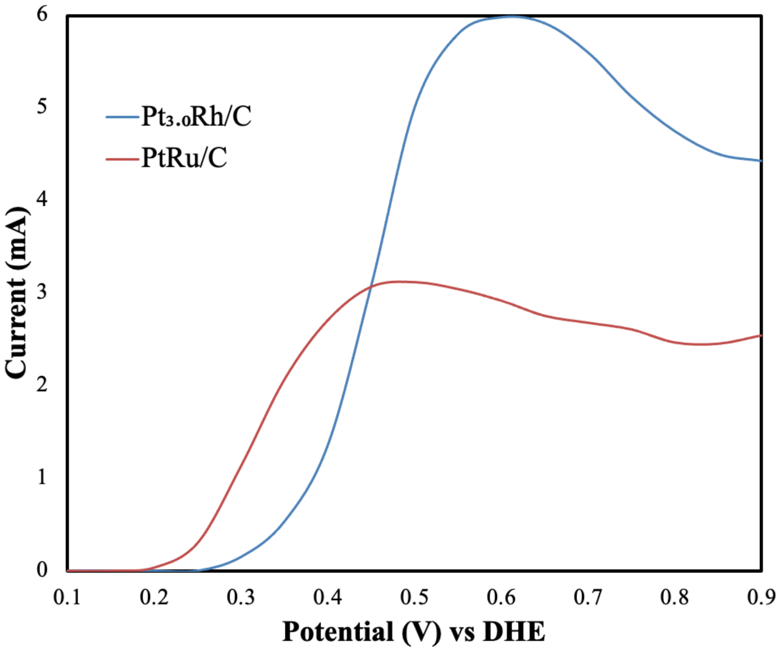

Figure D 5. Polarization curves for the oxidation of 0.1 M ethanol at $Pt_{3.0}Rh$ and PtRu (1), at 80 °C. A constant metal loading of 2.0 mg cm^{-2} on CFP electrodes was used.

1. A.H. Ali and P.G. Pickup, Journal of the Electrochemical Society, **169**, 034523 (2022).